

# Characterizing and Improving the Non-Collaborative and Collaborative Localization Problems

Benton K. Thompson

Thesis submitted to the Faculty of the  
Virginia Polytechnic Institute and State University  
in partial fulfillment of the requirements for the degree of

Master of Science  
in  
Electrical Engineering

R. Michael Buehrer, Chair  
Jeffrey H. Reed  
Claudio R. C. M. da Silva

August 23rd, 2011  
Blacksburg, Virginia

Keywords: localization, collaborative position location, cooperative indoor position  
location, iterative methods, wireless sensor networks

Copyright 2011, Benton K. Thompson

# Characterizing and Improving the Non-Collaborative and Collaborative Localization Problems

Benton K. Thompson

## ABSTRACT

This thesis focuses on the least-squares formulation of the non-collaborative and collaborative position location problems. For the non-collaborative problem, characterization encompassing the number of minima and the causes thereof is provided. Based on these efforts, we propose an improvement to the existing modified parallel projection method (MPPM), the reflected parallel projection method (RPPM). We show that the global minimum to the non-collaborative objective function can nearly always be found using the non-optimal reflected parallel projection method (RPPM).

For the collaborative position location problem, we provide a characterization that shows a heavy tail of root-mean-square (RMS) error due to a small percentage of simulated node/anchor layouts when solved by the iterative parallel projection method (IPPM). We provide an identification technique that successfully identifies most layouts that show large RMS error followed by a proposed solution to improve the accuracy in those problematic layouts.

Finally, we report the findings of a measurement campaign that validates our Gaussian model for line-of-sight (LOS) noise and shows that, for these particular measurements, non-line-of-sight (NLOS) noise is difficult to accurately model and can be very large.

This research was supported by a Bradley Fellowship from Virginia Tech's Bradley Department of Electrical and Computer Engineering, made possible by an endowment from the Harry Lynde Bradley Foundation.

# Acknowledgments

First, I want to acknowledge the guidance, patience, and expertise that my advisor Dr. Mike Buehrer was so gracious to give. From a professional standpoint, he defines proficiency and helpfulness. From a personal standpoint, a better mentor is not to be found. Thank you, Dr. Buehrer, for all your help.

The students, professors, and administrators of the MPRG lab at Virginia Tech are always willing to lend a helping hand, and I received my fair share of help from everyone. Thanks to you all and especially to Drs. Jeffrey Reed and Claudio da Silva for their assistance in finalizing this thesis. It was a great place to work.

Thank you to ENSCO, Inc., for supplying the radios used in our measurement campaign and to Luke Moser and Javier Schloemann for helping accomplish that campaign.

From the beginning, I have been blessed with *exceptional* teachers. Especially, thanks to Silvia Roca, Debbie West, Tom Shamblin, Lisa Berry, Sam Thomas, and Mike Brown for their math know-how that was passed to me during my days at Alcoa. Your hard work helped form my engineering foundation. Thank you, sincerely, to everyone at Alcoa.

This work would not have been possible without the generous support of the Bradley Fellowship from the Harry Lynde Bradley Foundation. I am appreciative of the confidence that the Foundation and Virginia Tech's ECE department placed in me. The freedom offered by the Bradley Fellowship has helped me pursue and achieve my goals; it has been quite a blessing. Thank you.

# Dedication

This thesis is dedicated both to my parents Bryan and Kathy, who have loved, supported, encouraged, and advised me as excellent parents will do, and to my grandfather H. Benton Thompson, a true engineer. I know you got a kick out of telling grad students that they didn't know what they were doing, Granddad, but I hope I broke the mold.

Thanks, Mom and Dad. Enough cannot be said.

# Contents

<b>1</b>	<b>Introduction</b>	<b>1</b>
1.1	Thesis Summary . . . . .	4
1.2	Problem Formulation . . . . .	5
<b>2</b>	<b>The Non-Collaborative Problem</b>	<b>7</b>
2.1	The Least Squares Formulation . . . . .	7
2.2	Finding the Global Minimum of $\Phi^{\text{ncl}}(\hat{\theta})$ . . . . .	10
2.2.1	Branch and Bound / Reformulation and Linearization Technique . . . . .	11
2.2.2	Interval Analysis . . . . .	11
2.3	Characterization of Number of Minima of $\Phi^{\text{ncl}}(\hat{\theta})$ . . . . .	14
2.3.1	Simulation Parameters . . . . .	15
2.3.2	Results . . . . .	16
2.3.3	Infeasibility of Optimal (Global) Solvers . . . . .	21
2.4	Modified Parallel Projection Method . . . . .	22
2.4.1	Identification of MPPM as Steepest Descent . . . . .	23
2.4.2	Guaranteed Convergence to a Stationary Point . . . . .	24

2.5	The Reflected Parallel Projection Method . . . . .	26
2.5.1	Motivation for the Reflected Parallel Projection Method . . . . .	26
2.5.2	RPPM Algorithm . . . . .	28
2.5.3	Comparison of RPPM to Optimal Solver . . . . .	31
2.5.4	The Weighted Least Squares Formulation . . . . .	36
<b>3</b>	<b>The Collaborative Problem</b>	<b>38</b>
3.1	The Collaborative Objective Function . . . . .	38
3.2	Finding the Global Minimum of $\Phi^{\text{col}}(\hat{\Theta})$ . . . . .	39
3.2.1	BB/RLT and Interval Analysis . . . . .	40
3.2.2	True Initialization Solution . . . . .	40
3.3	Iterative Parallel Projection Method . . . . .	41
3.4	Initialization Techniques . . . . .	43
3.4.1	Original Initialization Techniques . . . . .	43
3.4.2	Improved Initialization Techniques . . . . .	44
3.5	Motivation for the Reflected and Flipped Initialization Techniques . . . . .	45
3.5.1	Methodology for Characterization . . . . .	46
3.5.2	Comparison of Closest Anchor and True Initializations . . . . .	46
3.5.3	Experimental Evaluation of Number of Minima of $\Phi^{\text{col}}(\hat{\Theta})$ . . . . .	51
3.5.4	Summary of Motivations . . . . .	53
3.6	Identification of Problematic Layouts . . . . .	54
3.7	Solution Proposition for Problematic Layouts . . . . .	57

3.7.1	Improvement from Additional Initialization Techniques . . . . .	57
3.7.2	Performance Using Identification . . . . .	61
<b>4</b>	<b>Measurement Campaign</b>	<b>69</b>
4.1	Introduction . . . . .	69
4.1.1	Format of the Chapter . . . . .	70
4.1.2	Purpose . . . . .	70
4.1.3	Data Reported by the Radios . . . . .	70
4.1.4	Terminology . . . . .	71
4.1.5	Consistent Measurement Practices . . . . .	71
4.2	Calibration . . . . .	72
4.2.1	Purpose . . . . .	72
4.2.2	Scenario Setup . . . . .	73
4.2.3	Possible Cause of Calibration Error: Destructive Interference . . . . .	78
4.2.4	Gaussian Approximation for LOS Noise . . . . .	82
4.2.5	Standard Deviations of Data Sets . . . . .	84
4.3	LOS Indoor Scenarios . . . . .	85
4.3.1	Durham Hallway, Good LOS Performance Scenario . . . . .	86
4.3.2	Durham Hallway, Moderate LOS Performance Scenario . . . . .	91
4.4	NLOS Indoor Scenarios . . . . .	95
4.4.1	MPRG Offices Scenario . . . . .	96
4.4.2	MPRG Lab Scenario: A Dynamic Environment . . . . .	101

4.5	Apparent Multipath Effects . . . . .	106
4.6	Measurement Campaign Conclusions . . . . .	107
<b>5</b>	<b>Conclusions</b>	<b>110</b>
<b>Appendices</b>		<b>113</b>
<b>A</b>	<b>Derivation of Derivatives</b>	<b>114</b>
A.1	Derivatives of $\Phi^{\text{ncl}}(\hat{\theta})$ . . . . .	115
A.1.1	First Derivatives . . . . .	115
A.1.2	Second Derivatives . . . . .	116
A.1.3	Summary of Derivatives of $\Phi^{\text{ncl}}(\hat{\theta})$ . . . . .	118
A.2	Derivatives of $\Phi^{\text{col}}(\hat{\Theta})$ . . . . .	119
A.2.1	First Derivatives . . . . .	119
A.2.2	Second Derivatives . . . . .	120
A.2.3	Summary of Derivatives of $\Phi^{\text{col}}(\hat{\Theta})$ . . . . .	125
<b>B</b>	<b>Measurement Campaign Data</b>	<b>126</b>
B.1	Calibration Scenario . . . . .	126
B.2	Durham Hallway, Good LOS Performance Scenario . . . . .	148
B.3	Durham Hallway, Moderate LOS Performance Scenario . . . . .	151
B.4	MPRG Offices Scenario . . . . .	160
B.5	MPRG Lab Scenario . . . . .	176



# List of Abbreviations

BB/RLT	Branch and bound, reformulation-linearization technique
CDF	Cumulative distribution function
IPPM	Iterative parallel projection method
LBS	Location based service
LOS	Line-of-sight
MPPM	Modified parallel projection method
MPRG	Mobile and portable radio research group
NLOS	Non-line-of-sight
PDF	Probability density function
PPM	Parallel projection method
RMS	Root mean square
RPPM	Reflected parallel projection method
RSS	Received signal strength
TOF	Time of flight
WLS	Weighted least squares

# List of Figures

2.1	Noiseless range estimates . . . . .	8
2.2	Noisy range estimates . . . . .	9
2.3	Standard deviation $\sigma$ of $n_k$ , given distance and $K_E$ . . . . .	16
2.4	Number of minima against number of anchors ( $K_E = 0.0144$ ) . . . . .	17
2.5	Example layout with multiple minima ( $K_E = 0.0144$ ) . . . . .	18
2.6	Number of minima; $K_E = 0.0144$ . . . . .	19
2.7	Probability of multiple minima; node outside convex hull . . . . .	19
2.8	Number of minima; $K_E = 0.0144$ . . . . .	20
2.9	MPPM: Moving from one iteration to the next . . . . .	23
2.10	Heavy tail of error when multiple minima exist ( $K_E = 0.0025$ , three anchors) . . . . .	28
2.11	MPPM can settle to non-global minimum even in the absence of noise. . . . .	29
2.12	Minimum pairs show symmetry for two example layouts. . . . .	30
2.13	RPPM example . . . . .	33
2.14	RPPM performs almost identically to interval analysis. ( $K_E = 0.0144$ ) . . . . .	34
2.15	RPPM performs almost identically to interval analysis. (3 anchors) . . . . .	35

2.16	Minimizing $\Phi^{\text{ncl}}(\hat{\theta})$ does not always minimize $\Omega$ . . . . .	35
2.17	CDF of error for weighted least squares ( $K_E = 0.0144$ ) . . . . .	37
3.1	CDF of RMS error ( $K_E = 0.0144$ ) . . . . .	47
3.2	RMS error against objective value . . . . .	48
3.3	Mean RMS error against $K_E$ for closest anchor and true initializations . . .	48
3.4	Example layout where closest anchor initialization fails ( $K_E = 0.0144$ ) . . .	49
3.5	Example layout with small objective value and large RMS error ( $K_E = 0.0144$ )	50
3.6	Percentage of layouts where closest anchor found same minimum as true .	51
3.7	Number of minima found experimentally using IPPM . . . . .	52
3.8	Number of minima found experimentally using IPPM, separated by number of anchors/nodes ( $K_E = 0.0144$ ) . . . . .	53
3.9	RMS error . . . . .	56
3.10	RMS error against objective value . . . . .	56
3.11	CDF of RMS error for additional initialization techniques, 0% NLOS . . . .	59
3.12	CDF of RMS error for additional initialization techniques, 10% NLOS . . . .	59
3.13	CDF of RMS error for additional initialization techniques, 80% NLOS . . . .	60
3.14	RMS error against objective value ( 0% NLOS ) . . . . .	62
3.15	Mean RMS error against $K_E$ for all initialization techniques ( 0% NLOS ) . .	63
3.16	Mean RMS error against $K_E$ for all initialization techniques ( 10% NLOS ) .	63
3.17	Mean RMS error against $K_E$ for all initialization techniques ( 80% NLOS ) .	64
3.18	Mean $\Phi^{\text{col}}(\hat{\Theta})$ against $K_E$ for all initialization techniques ( 0% NLOS ) . . . .	64

3.19	Identification improvement ( $\beta > 0.9, 0\% \text{ NLOS}$ ) . . . . .	65
3.20	Identification improvement ( $\beta > 0.9, 0\% \text{ NLOS}$ ) . . . . .	65
3.21	Identification improvement ( $\beta > 0.9 \cup P < 21, 0\% \text{ NLOS}$ ) . . . . .	66
3.22	Identification improvement ( $\beta > 0.9 \cup P < 21, 0\% \text{ NLOS}$ ) . . . . .	66
3.23	CDF of eccentricity of layouts . . . . .	67
3.24	Identification of layouts by eccentricity and percentage of node estimations in anchors' convex hull . . . . .	68
4.1	Calibration scenario (on the Drillfield) . . . . .	74
4.2	Calibration group, mean measurements . . . . .	75
4.3	Calibration group, median measurements . . . . .	75
4.4	Calibration group error (mean) . . . . .	76
4.5	Calibration group error (median) . . . . .	76
4.6	Ground bounce diagram . . . . .	79
4.7	Destructive interference . . . . .	81
4.8	PDFs of calibration data sets . . . . .	84
4.9	Kurtosis values of calibration data sets . . . . .	85
4.10	Standard deviations of data sets against actual distance . . . . .	86
4.11	Durham hallway, good LOS performance scenario . . . . .	87
4.12	Durham hallway, good LOS performance group, mean measurements . . . . .	89
4.13	Durham hallway, good LOS performance group, median measurements . . . . .	89

4.14	Durham hallway, good LOS performance groups, error from mean measurements . . . . .	90
4.15	Durham hallway, good LOS performance groups, error from median measurements . . . . .	90
4.16	Durham hallway, moderate LOS performance scenario . . . . .	91
4.17	Durham hallway, moderate LOS performance groups, mean measurements	93
4.18	Durham hallway, moderate LOS performance groups, median measurements	94
4.19	Durham hallway, moderate LOS performance groups, error from mean measurements . . . . .	94
4.20	Durham hallway, moderate LOS performance groups, error from median measurements . . . . .	95
4.21	MPRG offices scenario . . . . .	97
4.22	MPRG offices groups, mean measurements . . . . .	99
4.23	MPRG offices groups, median measurements . . . . .	99
4.24	MPRG offices, error from mean measurements . . . . .	100
4.25	MPRG offices, error from median measurements . . . . .	100
4.26	MPRG lab scenario . . . . .	102
4.27	MPRG lab groups, mean measurements . . . . .	104
4.28	MPRG lab groups, median measurements . . . . .	104
4.29	MPRG lab, error from mean measurements . . . . .	105
4.30	MPRG lab, error from median measurements . . . . .	105
4.31	Multipath effect corrupts Gaussian approximation . . . . .	106

4.32	Multipath effect nullified . . . . .	107
B.1	Calibration, location pair T1, set # 1 . . . . .	128
B.2	Calibration, location pair T1, set # 2 . . . . .	128
B.3	Calibration, location pair T1, set # 3 . . . . .	129
B.4	Calibration, location pair T2, set # 1 . . . . .	129
B.5	Calibration, location pair T2, set # 2 . . . . .	130
B.6	Calibration, location pair T2, set # 3 . . . . .	130
B.7	Calibration, location pair T3, set # 1 . . . . .	131
B.8	Calibration, location pair T3, set # 2 . . . . .	131
B.9	Calibration, location pair T3, set # 3 . . . . .	132
B.10	Calibration, location pair T4, set # 1 . . . . .	132
B.11	Calibration, location pair T4, set # 2 . . . . .	133
B.12	Calibration, location pair T4, set # 3 . . . . .	133
B.13	Calibration, location pair T4, set # 4 . . . . .	134
B.14	Calibration, location pair T4, set # 5 . . . . .	134
B.15	Calibration, location pair T4, set # 6 . . . . .	135
B.16	Calibration, location pair T5, set # 1 . . . . .	135
B.17	Calibration, location pair T5, set # 2 . . . . .	136
B.18	Calibration, location pair T5, set # 3 . . . . .	136
B.19	Calibration, location pair T6, set # 1 . . . . .	137
B.20	Calibration, location pair T6, set # 2 . . . . .	137

B.21	Calibration, location pair T6, set # 3 . . . . .	138
B.22	Calibration, location pair T7, set # 1 . . . . .	138
B.23	Calibration, location pair T7, set # 2 . . . . .	139
B.24	Calibration, location pair T7, set # 3 . . . . .	139
B.25	Calibration, location pair T8, set # 1 . . . . .	140
B.26	Calibration, location pair T8, set # 2 . . . . .	140
B.27	Calibration, location pair T8, set # 3 . . . . .	141
B.28	Calibration, location pair T9, set # 1 . . . . .	141
B.29	Calibration, location pair T9, set # 2 . . . . .	142
B.30	Calibration, location pair T9, set # 3 . . . . .	142
B.31	Calibration, location pair T10, set # 1 . . . . .	143
B.32	Calibration, location pair T10, set # 2 . . . . .	143
B.33	Calibration, location pair T10, set # 3 . . . . .	144
B.34	Calibration, location pair T11, set # 1 . . . . .	144
B.35	Calibration, location pair T11, set # 2 . . . . .	145
B.36	Calibration, location pair T11, set # 3 . . . . .	145
B.37	Calibration, location pair T12, set # 1 . . . . .	146
B.38	Calibration, location pair T12, set # 2 . . . . .	146
B.39	Calibration, location pair T12, set # 3 . . . . .	147
B.40	Durham hallway, good LOS performance, location pair T1 . . . . .	148
B.41	Durham hallway, good LOS performance, location pair T2 . . . . .	149

B.42	Durham hallway, good LOS performance, location pair T3 . . . . .	150
B.43	Durham hallway, moderate LOS performance, location pair T1, group # 1 .	152
B.44	Durham hallway, moderate LOS performance, location pair T1, group # 2 .	152
B.45	Durham hallway, moderate LOS performance, location pair T1, group # 3 .	153
B.46	Durham hallway, moderate LOS performance, location pair T2, group # 1 .	153
B.47	Durham hallway, moderate LOS performance, location pair T2, group # 2 .	154
B.48	Durham hallway, moderate LOS performance, location pair T2, group # 3 .	154
B.49	Durham hallway, moderate LOS performance, location pair T3, group # 1 .	155
B.50	Durham hallway, moderate LOS performance, location pair T3, group # 2 .	155
B.51	Durham hallway, moderate LOS performance, location pair T3, group # 3 .	156
B.52	Durham hallway, moderate LOS performance, location pair T4, group # 1 .	156
B.53	Durham hallway, moderate LOS performance, location pair T4, group # 2 .	157
B.54	Durham hallway, moderate LOS performance, location pair T4, group # 3 .	157
B.55	Durham hallway, moderate LOS performance, location pair T5, group # 1 .	158
B.56	Durham hallway, moderate LOS performance, location pair T5, group # 2 .	158
B.57	Durham hallway, moderate LOS performance, location pair T5, group # 3 .	159
B.58	MPRG offices, location pair T1, group # 1 . . . . .	162
B.59	MPRG offices, location pair T1, group # 2 . . . . .	162
B.60	MPRG offices, location pair T1, group # 3 . . . . .	163
B.61	MPRG offices, location pair T2, group # 1 . . . . .	163
B.62	MPRG offices, location pair T2, group # 2 . . . . .	164

B.63 MPRG offices, location pair T2, group # 3 . . . . .	164
B.64 MPRG offices, location pair T3, group # 1 . . . . .	165
B.65 MPRG offices, location pair T3, group # 2 . . . . .	165
B.66 MPRG offices, location pair T3, group # 3 . . . . .	166
B.67 MPRG offices, location pair T4, group # 1 . . . . .	166
B.68 MPRG offices, location pair T4, group # 2 . . . . .	167
B.69 MPRG offices, location pair T4, group # 3 . . . . .	167
B.70 MPRG offices, location pair T5, group # 1 . . . . .	168
B.71 MPRG offices, location pair T5, group # 2 . . . . .	168
B.72 MPRG offices, location pair T5, group # 3 . . . . .	169
B.73 MPRG offices, location pair T6, group # 1 . . . . .	169
B.74 MPRG offices, location pair T6, group # 2 . . . . .	170
B.75 MPRG offices, location pair T6, group # 3 . . . . .	170
B.76 MPRG offices, location pair T7, group # 1 . . . . .	171
B.77 MPRG offices, location pair T7, group # 2 . . . . .	171
B.78 MPRG offices, location pair T7, group # 3 . . . . .	172
B.79 MPRG offices, location pair T8, group # 1 . . . . .	172
B.80 MPRG offices, location pair T8, group # 2 . . . . .	173
B.81 MPRG offices, location pair T8, group # 3 . . . . .	173
B.82 MPRG offices, location pair T9, group # 1 . . . . .	174
B.83 MPRG offices, location pair T9, group # 2 . . . . .	174

B.84 MPRG offices, location pair T9, group # 3 . . . . .	175
B.85 MPRG lab, location pair T1, group # 1 . . . . .	176
B.86 MPRG lab, location pair T1, group # 2 . . . . .	178
B.87 MPRG lab, location pair T2, group # 1 . . . . .	179
B.88 MPRG lab, location pair T2, group # 2 . . . . .	179
B.89 MPRG lab, location pair T3, group # 1 . . . . .	180
B.90 MPRG lab, location pair T3, group # 2 . . . . .	180
B.91 MPRG lab, location pair T4, group # 1 . . . . .	181
B.92 MPRG lab, location pair T4, group # 2 . . . . .	181
B.93 MPRG lab, location pair T5, group # 1 . . . . .	182
B.94 MPRG lab, location pair T5, group # 2 . . . . .	182
B.95 MPRG lab, location pair T6, group # 1 . . . . .	183
B.96 MPRG lab, location pair T6, group # 2 . . . . .	183
B.97 MPRG lab, location pair T7, group # 1 . . . . .	184
B.98 MPRG lab, location pair T7, group # 2 . . . . .	184
B.99 MPRG lab, location pair T8, group # 1 . . . . .	185
B.100MPRG lab, location pair T8, group # 2 . . . . .	185

# List of Tables

- 2.1 Seconds to process layouts,  $K_E = 0.0144$  . . . . . 21
  
- 4.1 Calibration Statistics . . . . . 77
- 4.2 Durham Hallway, Good LOS Performance Statistics . . . . . 88
- 4.3 Durham Hallway, Moderate LOS Performance Statistics . . . . . 92
- 4.4 MPRG Offices Statistics . . . . . 98
- 4.5 MPRG Lab Statistics . . . . . 103
  
- B.1 Calibration Statistics . . . . . 127
- B.2 Durham Hallway, Good LOS Performance Statistics . . . . . 148
- B.3 Durham Hallway, Moderate LOS Performance Statistics . . . . . 151
- B.4 MPRG Offices Statistics . . . . . 161
- B.5 MPRG Lab Statistics . . . . . 177

# Chapter 1

## Introduction

Position location information has and will continue to be used in many different ways. Recently, the proliferation of wireless devices (namely cellular phones) has led to an explosion of location based services (LBS). Applications such as targeted and improved marketing strategies [1], urban vehicular traffic monitoring [2], cooperation among first responders/military personnel [3], and many more take advantage of location information. Some companies have used recorded location information to assist in future GPS fixing times [4], earning worldwide attention for saving this information without notifying customers. The importance of location information leads to the need to research fast, efficient methods of obtaining it.

The term *localization* refers to the act of geo-locating objects. A familiar problem is the localization of one *node* or object, such as when an emergency 911 phone call triggers the localization of the calling cell phone to assist first responders. In this scenario, only one node is being used; all other information comes from *anchors*, objects with known locations such as cell base stations. This one-node scenario is labeled in this thesis as *non-collaborative position location*.

Collaborative position location, sometimes referred to by other names such as cooperative

position location, wireless sensor location, or position localization, is the localization of nodes in space when the nodes rely on information from other unlocalized nodes. Thus, the estimate of each node's location can be improved by leveraging information from neighboring nodes, even though those neighbors are not guaranteed to be correctly localized.

Collaborative position location has recently become very popular for addressing the issue of localizing wireless devices in environments with limited infrastructure support from GPS or a cellular system. An indoor environment is one such scenario. The basic concept is to use the additional measurements among unlocalized nodes to increase location coverage and improve localization accuracy. In fact, many algorithms and experimental systems have already been developed, both those that use centralized computations [5, 6, 7] and those using distributed algorithms [8, 9, 10, 11, 12]. A more detailed survey of collaborative position location approaches can be found in [13, 14, 15].

In this thesis, we focus on improving the recently-developed modified parallel projection method (MPPM) [16] for non-collaborative localization and its collaborative extension, the iterative parallel projection method (IPPM), which has been demonstrated to achieve comparable and often better localization accuracy than existing methods such as SDP (semi-definite programming) and MDS (multi-dimensional scaling) with substantially less computational complexity [17]. We show that our proposed improvement to MPPM identifies and mitigates the heavy tail of error resulting from non-global minima (shown in Figure 2.10) of the objective function  $\Phi$  and nearly matches the performance of the interval analysis method, an optimal but slow and computationally expensive solver.

Turning to the collaborative problem, we show that a small percentage of simulated layouts contribute a disproportionately large amount to the average RMS error. We develop an identification mechanism, based on the colinearity of anchors, to accurately predict which layouts are likely to be solved incorrectly by the iterative parallel projection method (IPPM). Finally, we develop a solution technique that specifically targets those

layouts that contribute most to average RMS error. Our improved solution technique shows significant performance gains as compared to IPPM.

### **Methods of Localization Measurements**

Different types of information can be leveraged towards the ultimate goal of localization. Time, frequency, power, and angle of incoming wireless signals can all be used. Time is probably the most widely-used method of obtaining information for localization because of the relative reliability compared to other measurements. Multipath scenarios can corrupt information obtained by timing, so care must be taken to account for line-of-sight (LOS) signals as opposed to non-line-of-sight (NLOS) signals. Doppler shifts provide information on the velocity of objects which can assist with localization. Received signal strength (RSS) is likely the easiest measure available for localization because of the nearly ubiquitous availability of signal power information in wireless devices, but the variability in signal power due to environmental effects renders RSS measurements less reliable than time measurements. Finally, the angle of arrival of signals can be measured, providing lines-of-bearing. However, it cannot generally be guaranteed that the angle at which the incoming signal arrives is the angle towards the signal's emitter.

### **Assumptions about Distance Estimates**

The work in this thesis is based upon distance (range) estimates obtained between wireless devices. The manner in which these estimates are obtained is not the focus of this work, although round trip time of flight measurements performed during the Spring 2011 semester (described in Chapter 4) confirm the reasonability of our Gaussian noise assumption for LOS environments. Throughout this work, the presence of range estimates is assumed, and the focus of this work is how to best leverage the range estimates rather than how they were obtained.

## 1.1 Thesis Summary

### Chapter 2: The Non-Collaborative Problem

The non-collaborative localization problem is introduced in Chapter 2 along with the associated least squares formulation. Using the optimal interval analysis solver, we are able to confirm that performance degrades when the node’s estimated location is outside the anchors’ convex hull *because* the number of minima of our objective function  $\Phi^{\text{ncl}}(\hat{\theta})$  usually increases when the node’s estimated location is outside the convex hull of the anchors.

Starting with the previously-developed modified parallel projection method (MPPM) [16], we show that it is, in fact, a steepest descent algorithm and therefore is only guaranteed to converge to a stationary point. Using the information gained from characterization, we develop the reflected parallel projection method (RPPM) that uses intelligent initializations of MPPM to achieve nearly optimal performance (as measured against the optimal interval analysis solver). Finally, we demonstrate that minimizing the objective function  $\Phi^{\text{ncl}}(\hat{\theta})$  will not necessarily minimize the root mean square (RMS) error of the layout.

### Chapter 3: The Collaborative Problem

Chapter 3 focuses on the collaborative problem and the associated objective function  $\Phi^{\text{col}}(\hat{\Theta})$ . We provide an analysis of the number of minima of the objective function. Based on our simulations, multiple minima are more likely in layouts with nearly colinear anchors (which, in turn, causes most node location estimates to be outside the anchors’ convex hull) and in layouts with a large number of nodes. Again, the well known performance degradation when nodes are outside the convex hull of the anchors is confirmed, and we submit that the reason is that multiple minima exist more often in these situations.

The iterative parallel projection method (IPPM) [16] was developed to minimize  $\Phi^{\text{col}}(\hat{\Theta})$ , and we use the aforementioned characterization to propose improved initialization techniques and show incremental performance increases for each more complicated initialization technique. Additionally, we propose techniques that accurately identify which node/anchor layouts are likely to have multiple minima, allowing the user to be selective in which layouts need additional initializations. Also, we confirm that minimizing  $\Phi^{\text{col}}(\hat{\Theta})$  will not necessarily minimize the RMS error of the network, a result matched in the non-collaborative scenario.

#### **Chapter 4: The Measurement Campaign**

Chapter 4 describes a measurement campaign with the purpose of assisting in noise modeling for both LOS and NLOS situations. ENSCO, Inc. ®, provided two radios designed specifically for ranging. The radios use 22MHz of the Wi-Fi band to measure the time-of-flight between themselves, returning range estimates at a rate of 217Hz. By keeping the radios stationary and recording the measurements taken at one known distance, we obtained distributions of range estimates. Using these distributions, we conclude that LOS ranging noise can accurately be modeled as Gaussian. We also conclude that NLOS ranging noise is highly variable depending on the environment but nearly always shows a considerable positive bias. Expectedly, the radios performed poorly when people or substantial walls separated them, and they performed well in open, clean, LOS environments. We appreciate ENSCO's allowing us to use the radios for our research purposes.

## **1.2 Problem Formulation**

Consider a 2D square network consisting of  $K \geq 3$  anchors at known locations and  $N$  unlocalized nodes whose locations are to be estimated. In the applications of interest,

$N \gg K$ , but this is not necessary for the developed algorithms to be effective. The true locations of the unlocalized nodes are denoted by  $\Theta = [\theta_1, \theta_2, \dots, \theta_N]$ , and the known locations of the anchors are denoted by  $A = [\theta_{N+1}, \theta_{N+2}, \dots, \theta_{N+K}]$ , where  $\theta_i = [x_i \ y_i]^T$  is the 2D coordinate of the  $i$ th node, for  $i = 1, 2, 3, \dots, N + K$ , and  $(\cdot)^T$  is the matrix transpose operation. If the distance between the  $i^{\text{th}}$  and  $j^{\text{th}}$  nodes, denoted by  $d_{ij}$ , is less than the physical communication range  $R$ , we say the two nodes neighbor each other and thus can communicate and obtain a (noisy) range estimate  $r_{ij}$  of their true distance  $d_{ij}$ . (In practice, due to non-line-of-sight (NLOS) obstruction, there is a possibility that two nodes may not communicate even if their physical distance is within the communication range.) Furthermore, we assume range estimates are symmetric, i.e.,  $r_{ij} = r_{ji}$ ,  $\forall i, j$ . The task is to obtain an estimate  $\hat{\Theta}$  of the true locations  $\Theta$ .

We assume that range estimates are corrupted by independent zero-mean Gaussian noise. In particular, the range estimate between the  $i^{\text{th}}$  and  $j^{\text{th}}$  nodes is modeled as  $r_{ij} = d_{ij} + n_{ij} + b_{ij}$ , where  $d_{ij} = \sqrt{(x_i - x_j)^2 + (y_i - y_j)^2}$  is the true inter-node distance.  $n_{ij} \sim \mathcal{N}(0, \sigma_{ij}^2)$  is a zero-mean Gaussian random variable with a variance of  $\sigma_{ij}^2 = K_E d_{ij}^{\beta_{ij}}$ , where  $K_E$  is a proportionality constant capturing combined physical layer and receiver effects.  $b_{ij}$  is a positive uniform random variable representing an added bias for NLOS noise.  $\beta_{ij}$  is the path loss exponent. For this thesis, we assume  $\beta_{ij} = 2 \forall i, j$ .

To compare different localization methods, the RMS localization error (for one noise realization) is defined as

$$\Omega = \sqrt{\frac{1}{N} \sum_{i=1}^N \|\hat{\theta}_i - \theta_i\|^2}, \quad (1.1)$$

where  $\|\cdot\|$  denotes the Euclidean norm (distance).

# Chapter 2

## The Non-Collaborative Problem

The non-collaborative localization problem is defined with  $K$  anchors and  $N = 1$  unlocalized nodes. The knowledge of all  $K$  anchor locations  $A = \{A_1, A_2, A_3, \dots, A_k\}$  and range estimates  $r_k$  from each  $k^{\text{th}}$  anchor to the node provides ranging circles that help determine the location of the node.

### 2.1 The Least Squares Formulation

If the range estimates are noiseless such that  $r_k$  is the true distance between the node and anchor  $k$ , then all ranging circles will intersect at the true node location as shown in Figure 2.1. In general, to remove ambiguity between intersection points of ranging circles (with noiseless range estimates), at least three unique ranging circles are required to define the true node location. This can be seen in Figure 2.1 where each of the three circles intersects each of the other circles at exactly two points, and the third ranging circle is required to identify the true node location.

With three anchors and noiseless range estimates, the solution of the true node location can be found by simultaneously solving the system of Equations 2.1-2.3. These equations

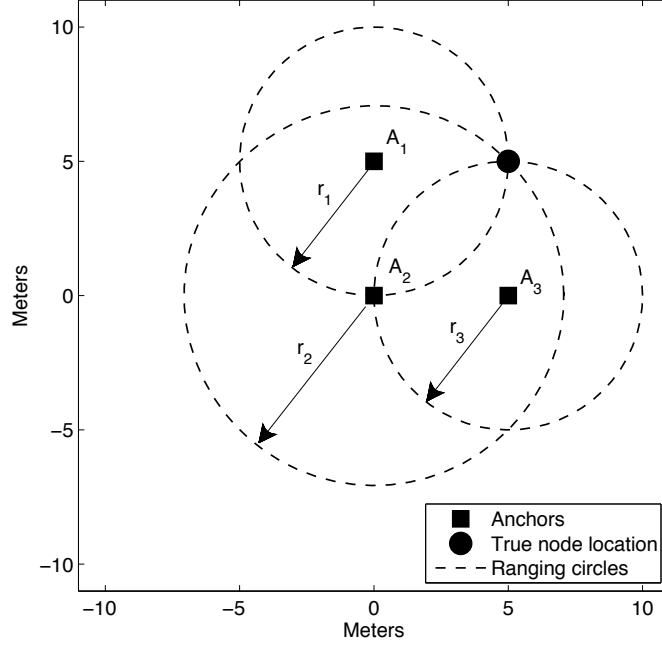


Figure 2.1: Noiseless range estimates

define the range estimates, where  $[x, y]^T$  is the node's location and  $[x_k, y_k]^T$  is the  $k^{\text{th}}$  anchor's location.

$$r_1 = \sqrt{(x - x_1)^2 + (y - y_1)^2} \quad (2.1)$$

$$r_2 = \sqrt{(x - x_2)^2 + (y - y_2)^2} \quad (2.2)$$

$$r_3 = \sqrt{(x - x_3)^2 + (y - y_3)^2} \quad (2.3)$$

If the range estimates are noisy such that  $r_k = d_k + n_k$ , the true distance plus noise, the ranging circles defined by  $r_k$  are not guaranteed to intersect, and thus Equations 2.1-2.3 may be an inconsistent system. Figure 2.2 shows a scenario with noisy range estimates that lead to an inconsistent system of range estimate equations. Because of this inconsistent system, we rely upon the minimization of a cost function to determine the best estimate of the node's location. Combettes proposes the least squares metric in [18]

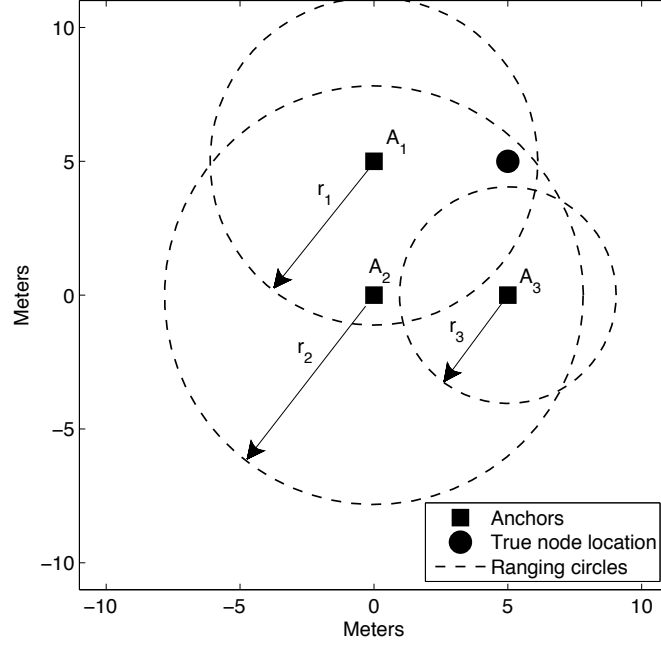


Figure 2.2: Noisy range estimates

(modified in [16]) as

$$\begin{aligned}
 \Phi^{\text{ncl}}(\hat{\theta}) &= \frac{1}{K} \sum_{k=1}^K \left( r_k - \|\hat{\theta} - A_k\| \right)^2 \\
 &= \frac{1}{K} \sum_{k=1}^K \left( r_k - \sqrt{(x - x_k)^2 + (y - y_k)^2} \right)^2,
 \end{aligned} \tag{2.4}$$

where  $\theta^{\text{ncl}}$  represents the non-collaborative location estimation,  $\hat{\theta}$  is the unlocalized node's current estimated location,  $A_k$  represents its  $k$ th connecting anchor, and  $r_k$  denotes the range estimate between the unlocalized node and  $A_k$ .  $\|\hat{\theta} - A_k\|$  represents the Euclidean distance between  $\hat{\theta}$  and  $A_k$ .  $K$  is the number of anchors, and the term  $1/K$  normalizes the objective function.

Thus,  $\Phi^{\text{ncl}}(\hat{\theta})$  represents the normalized sum of the squared errors between the range estimates  $r_k$  and the actual distances between  $\hat{\theta}$  and  $A_k$ . It can be seen that if  $\hat{\theta} = \theta$ , the true node location, and  $r_k$  are all noiseless range estimates,  $\Phi^{\text{ncl}}(\hat{\theta}) = 0$ . Essentially, the

objective of Equation 2.4 is the sum of the weighted squared difference between range estimates and the distances calculated using the estimated location, which is, in fact, the same as the objective of the maximum likelihood estimator [19].

With noisy range estimates, then, we turn from solving the simultaneous system of equations for  $r_k$  to solving the minimization of the least squares formulation

$$\min \left\{ \Phi^{\text{ncl}}(\hat{\theta}) = \frac{1}{K} \sum_{k=1}^K \left( r_k - \|\hat{\theta} - A_k\| \right)^2 \right\}. \quad (2.5)$$

The difficulty in solving this minimization has been the unknown error surface and, consequently, the number of minima for a given layout. Without prior knowledge of the error surface, designing a solution method specifically for this objective function has been only moderately successful. By characterizing the the non-collaborative problem (focusing on the number of minima) for many different layouts and improving upon the modified parallel projection method (discussed in Section 2.4), we propose a solution method that nearly always discovers and returns the global minimum of  $\Phi^{\text{ncl}}(\hat{\theta})$ .

## 2.2 Finding the Global Minimum of $\Phi^{\text{ncl}}(\hat{\theta})$

The global minimization of the non-collaborative objective function  $\Phi^{\text{ncl}}(\hat{\theta})$  does *not* guarantee the minimization of RMS error  $\Omega$  for a given layout. Figure 2.14 shows that in some cases, solutions (minima) with lower  $\Omega$  values than the solution with the lowest objective value exist. However, equipped only with the anchors' locations  $A$  and the range estimates  $r_i$  between the  $i^{\text{th}}$  anchor and the node, minimizing  $\Phi^{\text{ncl}}(\hat{\theta})$  is our best effort at minimizing  $\Omega$ . Therefore, knowing where the global minimum of  $\Phi^{\text{ncl}}(\hat{\theta})$  lies and how many non-global minima exist for a given layout will help us determine the best approach for finding the global minimum. Two solution methods, specifically tailored to solving  $\min\{\Phi^{\text{ncl}}(\hat{\theta})\}$ , are described in Sections 2.2.1 and 2.2.2.

### 2.2.1 Branch and Bound / Reformulation and Linearization Technique

In [20], Jia and Buehrer develop a branch and bound (BB) technique, using the reformulation and linearization technique (RLT) described in [21]. Jia and Buehrer show, using their BB/RLT, that the optimal solution to the collaborative position location problem is solvable. The non-collaborative case is a subset of the collaborative problems, so the BB/RLT could be used to find the global solution to the non-collaborative problem, also. However, BB/RLT does not easily return the non-global minima of  $\Phi^{\text{ncl}}(\hat{\theta})$ , so we employ interval analysis, another solution technique.

### 2.2.2 Interval Analysis

Another method of finding the global minimum of  $\Phi^{\text{ncl}}(\hat{\theta})$  is interval analysis. Rump's INTLAB [22], a MATLAB<sup>1</sup> library developed specifically for interval analysis, is leveraged by Hargreaves in [23] to guarantee the identification of all solutions of a nonlinear system of equations that lie within a given bounding box.

Interval analysis is simply the use of intervals rather than specific values in mathematical systems. For instance, the equation  $10 - 3 = 7$  can be generalized using intervals to 10 less the interval  $[2, 4]$ , where  $10 - 2 = 8$  and  $10 - 4 = 6$ , so  $10 - [2, 4] = [6, 8]$ . Therefore, the equation  $10 - 3 = 7$  is fully contained within the interval equation  $10 - [2, 4] = [6, 8]$ .

Hargreaves, in [23], describes the use of the Krawczyk operator in solving nonlinear systems of equations.

A benefit of using interval analysis to solve nonlinear equations is that the Krawczyk and Hansen-Sengupta operators can be used to test the existence and uniqueness of a zero in an interval  $x$ .

In our case, the interval of interest is two dimensional (a rectangular box); we are

---

<sup>1</sup>MATLAB®, ©2009 by TheMathWorks™

searching over the  $x$  and  $y$  directions to determine the optimal value of the node's location  $\hat{\theta}$ . The Krawczyk operator allows us to find all the roots of a continuous nonlinear function (in our case the derivative of  $\Phi^{\text{ncl}}(\hat{\theta})$ ), and in doing so, we find all the stationary points of  $\Phi^{\text{ncl}}(\hat{\theta})$ , including all the minima.

As given by Hargreaves in [23] (with the nomenclature  $\mathbf{K}$  substituted out in this thesis with  $\mathbf{Z}$ ), the Krawczyk operator  $\mathbf{Z}(v, \mathbf{V})$  operates on the interval  $\mathbf{V} = [l, u]$  and on  $v$ , the midpoint of  $\mathbf{V}$ , as described in Equation 2.6.  $\mathbf{Z}$  is returned as an interval.

$$\mathbf{Z}(v, \mathbf{V}) = v - Cf(v) \pm (I - CJ(\mathbf{V}))(v - \mathbf{V}) \quad (2.6)$$

In Equation 2.6,  $C$  is "an arbitrary non-singular real matrix" [24]. Hargreaves advises using the inverse of the midpoint matrix of  $J(\mathbf{V})$  as  $C$ , where  $J(\mathbf{V})$  is the interval Jacobian matrix of  $f(\mathbf{V})$ . The midpoint is defined as the average of  $u$  and  $l$ , the upper and lower bounds of an interval. Thus,  $\text{mid}(J(\mathbf{V}))$  is simply the midpoint of each of the intervals of  $J(\mathbf{V})$ , and  $C = [\text{mid}(J(\mathbf{V}))]^{-1}$ .  $f$  is the function of interest, and, for our application,  $f = \Phi'^{\text{ncl}}(\hat{\theta})$ .  $I$  is the identity matrix. The  $\pm$  is also arbitrary because the last term  $(v - \mathbf{V}) = -(v - \mathbf{V}) = (\mathbf{V} - v)$ . Note that  $v$  is the midpoint of  $\mathbf{V}$ , such that  $v = \frac{l+u}{2}$ , so

$$(v - \mathbf{V}) = \frac{u+l}{2} - [l, u] = \left[ \frac{-u+l}{2}, \frac{u-l}{2} \right] = [l, u] - \frac{u+l}{2} = (\mathbf{V} - v). \quad (2.7)$$

Note that  $\frac{u+l}{2} - [l, u] = \left[ \frac{-u+l}{2}, \frac{u-l}{2} \right]$ , not  $\left[ \frac{u-l}{2}, \frac{-u+l}{2} \right]$ , because  $u \geq l$ , so  $a - u \leq a - l \quad \forall a$ .

Also, for interval  $\mathbf{V} = [l, u]$ , the radius of  $\mathbf{V}$  is defined as  $\text{rad}(\mathbf{V}) = \frac{u-l}{2}$ .

Theorem 7.1 in Hargreaves' thesis [23] (proven by Neumaier in [25]) states

Let  $f : \mathbb{R}^n \rightarrow \mathbb{R}^n$  be a (set of) nonlinear continuous function(s), and let  $v \in \mathbf{V}$ .

- If  $f$  has a root  $r \in \mathbf{V}$ , then  $r \in \mathbf{Z}(v, \mathbf{V}) \cap \mathbf{V}$ .
- If  $\mathbf{Z}(v, \mathbf{V}) \cap \mathbf{V} = \emptyset$ , then  $f$  contains no zero in  $\mathbf{V}$ .
- If  $\emptyset \neq \mathbf{Z}(v, \mathbf{V}) \subseteq \text{interior of } \mathbf{V}$ , then  $f$  contains a unique zero in  $\mathbf{V}$ .

In this thesis, we use the first derivative of  $\Phi^{\text{ncl}}(\hat{\theta})$  as  $f$  because interval analysis will return the roots of  $f$ , and this allows us to find all the stationary points (the roots of the derivative) of  $\Phi^{\text{ncl}}(\hat{\theta})$ . The number of inputs to and outputs of  $f$  is  $n = 2$ . The inputs are  $\hat{\theta} = [x, y]^T$ , and the outputs are the partial derivatives of  $\Phi^{\text{ncl}}(\hat{\theta})$ , one each with respect to  $x$  and  $y$ .

Hargreaves lists in [23] an algorithm for finding all the roots of a given function  $f$  using the above theorem, and his MATLAB function “allroots.m” serves as the basis for our optimal solver for  $\min \left\{ \Phi^{\text{ncl}}(\hat{\theta}) \right\}$ . Modifications were necessary, notably where  $f = \Phi^{\text{ncl}}(\hat{\theta})$  is not continuous.

Appendix A.1 shows the derivatives of  $\Phi^{\text{ncl}}(\hat{\theta})$ , and

$$f = \Phi^{\text{ncl}}(\hat{\theta}) = \frac{-2}{K} \sum_{k=1}^K \left[ \frac{\hat{\theta} - A_k}{\|\hat{\theta} - A_k\|} r_k + A_k - \hat{\theta} \right]. \quad (2.8)$$

$\Phi^{\text{ncl}}(\hat{\theta})$  is discontinuous when  $\|\hat{\theta} - A_k\| = 0$ , that is, when the guessed node location  $\hat{\theta}$  is at an anchor location  $A_k$ . Avoiding this problem requires that the cases where  $\|\hat{\theta} - A_k\| = 0$  be explicitly checked, and, when found, the result  $\frac{\hat{\theta} - A_k}{\|\hat{\theta} - A_k\|}$  is not returned as  $\infty$  but as some sufficiently large number  $M$ . For our work,  $M = 1 \times 10^6$ .

Using interval analysis (Algorithm 1), all the roots of  $\Phi^{\text{ncl}}(\hat{\theta})$  can be found inside a chosen bounding box  $\mathbf{V}$ , giving us the stationary points  $S = \{S_1, S_2, S_3, \dots\}$  of  $\Phi^{\text{ncl}}(\hat{\theta})$ . If the Hessian matrix (the second derivative matrix) of  $\Phi^{\text{ncl}}(S_i)$  is positive semidefinite, then  $S_i$  is a minimum of  $\Phi^{\text{ncl}}(\hat{\theta})$ . (The first and second derivatives of  $\Phi^{\text{ncl}}(\hat{\theta})$  can be found in Section A.1). In this manner, we not only are able to find the global minimum of  $\Phi^{\text{ncl}}(\hat{\theta})$  but also all the local minima in  $\mathbf{V}$ . This allows the characterization of the number of minima of  $\Phi^{\text{ncl}}(\hat{\theta})$  based upon different parameters, an important piece of information for developing effective algorithms for position location.

---

**Algorithm 1** : Optimal Solver for  $\min \{ \Phi^{\text{ncl}}(\hat{\theta}) \}$  Using Interval Analysis
 

---

- 1: Choose  $\mathbf{V} = \begin{pmatrix} [l_x, u_x] \\ [l_y, u_y] \end{pmatrix}$   $\triangleright 2 \times 1$  interval vector over which to search (in the  $x$  and  $y$  directions)
- 2: Choose  $\epsilon$  as a small number denoting how small an interval bounding box must be in its largest dimension to “sufficiently” bound a root of  $\Phi^{\text{ncl}}(\hat{\theta})$ .
- 3: Initialize list of discovered stationary points.
- 4: Explicitly check each anchor location  $A_k$  to see whether they are stationary points.
- 5:  $v \leftarrow \text{mid}(\mathbf{V})$   $\triangleright v$  is a  $2 \times 1$  vector of scalars.
- 6:  $f \leftarrow [\Phi^{\text{ncl}}(v), \Phi^{\text{ncl}}(v)]$   $\triangleright$  Equations 2.12-2.13;  $f$  is a  $2 \times 1$  interval vector with identical bounds.
- 7:  $f' \leftarrow \Phi'^{\text{ncl}}(\mathbf{V})$   $\triangleright$  Equations A.25-A.28;  $f'$  is a  $2 \times 2$  interval matrix.
- 8:  $C \leftarrow [\text{mid}(f')]^{-1}$ ; Set values of  $C$  that  $== \infty$  to 0.  $\triangleright C$  is a  $2 \times 2$  matrix of scalars.
- 9:  $\mathbf{Z}(v, \mathbf{V}) \leftarrow v - Cf + (I - Cf')(v - \mathbf{V})$   $\triangleright$  Equation 2.6;  $\mathbf{Z}$  is a  $2 \times 1$  interval vector.
- 10:  $\mathbf{X} \leftarrow \mathbf{Z} \cap \mathbf{V}$   $\triangleright \mathbf{X}$  is a  $2 \times 1$  interval vector.
- 11: **if**  $\mathbf{X} == \emptyset$  **then**
- 12:     **Return** nothing.  $\triangleright$  No root of  $\Phi^{\text{ncl}}$  exists in  $\mathbf{V}$ .
- 13: **else if**  $\max \{ \text{rad}(\mathbf{V}) - \text{rad}(\mathbf{X}) \} \leq \frac{\max \{ \text{rad}(\mathbf{X}) \}}{2}$  **then**  $\triangleright$  if  $\mathbf{X}$  is sufficiently smaller than  $\mathbf{V}$
- 14:     **if**  $\max \{ \text{rad}(\mathbf{X}) \} < \epsilon$  **then**  $\triangleright$  if  $\mathbf{X}$  is sufficiently small
- 15:         **Return**  $\text{mid}(\mathbf{X})$  as a stationary point.  $\triangleright$  A root of  $\Phi^{\text{ncl}}$  has been found.
- 16:     **else**
- 17:          $\dagger$  Bisect  $\mathbf{X}$  along a chosen dimension into two new  $2 \times 1$  intervals,  $\mathbf{X}_1$  and  $\mathbf{X}_2$ .
- 18:         **Goto** Step 7, using  $\mathbf{X}_1$  as  $\mathbf{V}$ .
- 19:         **Goto** Step 7, using  $\mathbf{X}_2$  as  $\mathbf{V}$ .
- 20:     **end if**
- 21: **else**
- 22:     **Goto** Step 7, using  $\mathbf{X}$  as  $\mathbf{V}$ .
- 23: **end if**

$$\dagger T_j = \text{rad}(\mathbf{V}_j) \sum_{i=1}^2 |f'_{ij}|; \text{ Bisect along } r^{\text{th}} \text{ dimension for } T_r \geq T_j, j = 1, 2.$$

Note: This algorithm was adapted from Hargreaves’ “allroots.m” in his thesis [23].

---

## 2.3 Characterization of Number of Minima of $\Phi^{\text{ncl}}(\hat{\theta})$

Using the global interval analysis solver for  $\min \{ \Phi^{\text{ncl}}(\hat{\theta}) \}$  described in Section 2.2.2, we are able to describe all the local minima given a particular anchor/node layout and a noisy range estimate realization. To analyze the likelihood of multiple minima being present and the factors which cause multiple minima, simulations in MATLAB were run.

### 2.3.1 Simulation Parameters

A *layout* is defined as a set of anchors and, in the non-collaborative case, one true node location. Based upon this information, noisy range estimates are generated, creating the last piece of information necessary for simulation. For the characterization of multiple minima in differing layouts, the following parameters were used.

- 30m × 30m area in which all anchors and the node are constrained to lie
- Number of anchors uniformly distributed on [3, 10].
- Different realizations of the random variable  $L$ , where  $L$  is uniform on  $[-15, 15]$ , were used for all anchors' and the node's  $x$  and  $y$  coordinates.
- True distances between the node and anchor were taken as the Euclidean distances  $d_k = \sqrt{(x - x_k)^2 + (y - y_k)^2}$ , where  $x$  and  $y$  are the coordinates of the node, and  $x_k$  and  $y_k$  are the coordinates of the  $k^{\text{th}}$  anchor.
- Range estimates between the  $k^{\text{th}}$  anchor and the node were corrupted with noise  $n_k$ , a zero-mean Gaussian random variable described as  $n_k \sim \mathcal{N}(0, \sigma_k^2)$ , where  $\sigma_k^2 = K_E d_k^{\beta_k}$ .
- $K_E$  is the “noise constant,” and layouts were simulated at  $K_E = \{0, 0.0025, 0.0144, 0.0361, 0.0676, 0.1089, 0.1600\} = \text{MATLAB's } [0, (\text{linspace}(0.05, 0.40, 6)).^2]$ .
  - For reference, Figure 2.3 shows the relationship between  $\sigma$ , the standard deviation of  $n_k$ , given a distance and a  $K_E$  value.
- $\beta_k$  is the path loss exponent and is held constantly at  $\beta_k = 2$  for all LOS simulations.
- 100,000 different layouts per  $K_E$  value were created, giving a total of 700,000 layouts and simulations.

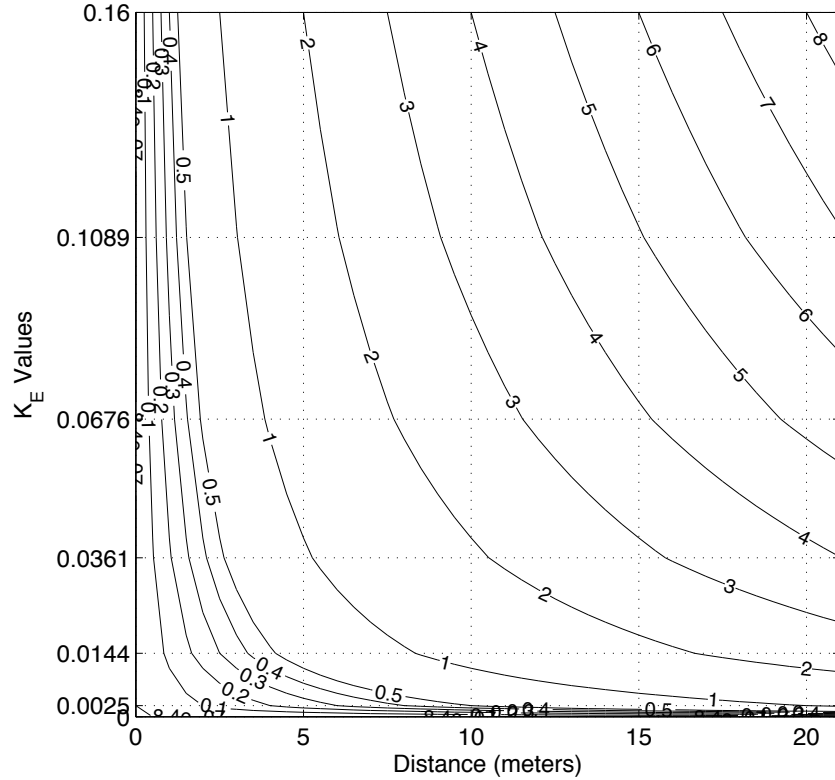


Figure 2.3: Standard deviation  $\sigma$  of  $n_{k_r}$ , given distance and  $K_E$

### 2.3.2 Results

Counting the number of minima for each layout was the first task in determining how to improve performance. Layouts that only have one minima in the first place are already solvable by minimum-finding algorithms (e.g. steepest descent). Figure 2.4 shows the percentage of layouts that have multiple minima (and how many), plotted against the number of anchors in the layout. Notably, for the layouts with only three anchors, there is more than a 50% chance that multiple minima will exist. This underscores the necessity of finding the correct minimum, not just the first available minimum. However, the possibility of having more than two anchors is rare.

Investigating many of the layouts that created multiple minima of  $\Phi^{\text{nl}}(\hat{\theta})$ , we discovered the trend that most minima tended to be approximately spatially divided by the bulk of

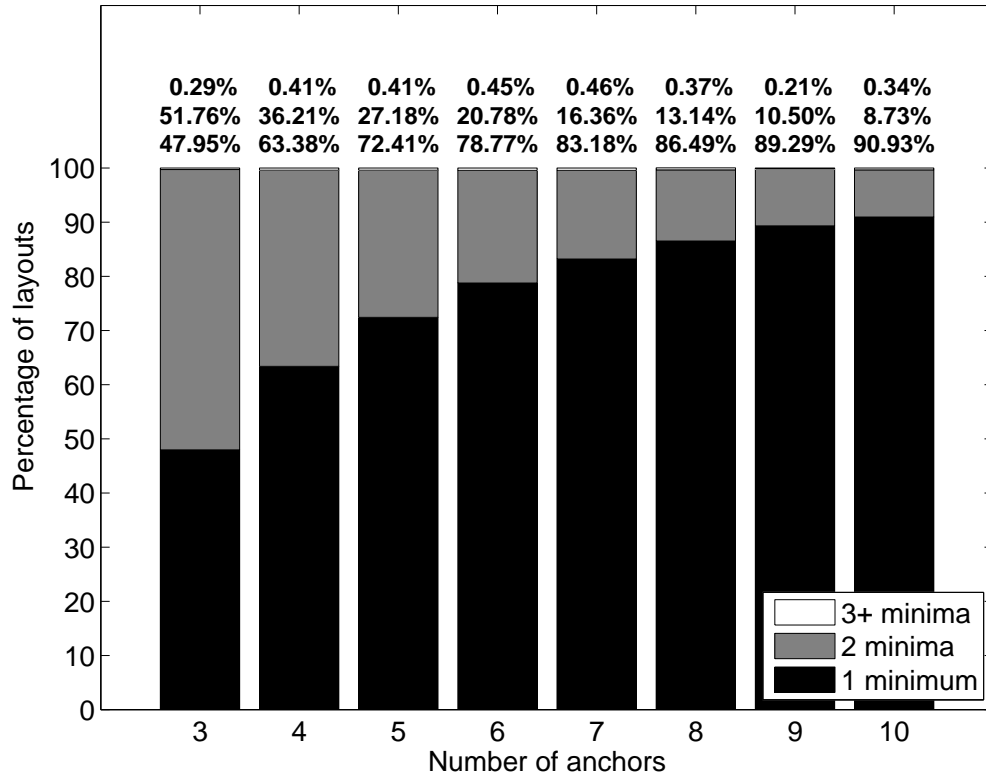


Figure 2.4: Number of minima against number of anchors ( $K_E = 0.0144$ )

the anchors. Also, we identified most of the layouts with multiple minima as having one characteristic in common: the estimated node location was outside of the anchors' convex hull. Figure 2.5 shows an example layout with  $K_E = 0.0144$  and multiple minima. The three minima are all outside the convex hull of the anchors, as is the true node location. Also, note that the minima are approximately separated by the bulk of the anchors.

Leveraging the information about multiple minima occurring more often when the node is outside the convex hull of the anchors, and ruling out other possibilities for the main cause of multiple minima, we draw this conclusion: The most important factor determining whether or not multiple minima of  $\Phi^{\text{ncl}}(\hat{\theta})$  exist is whether or not the node is inside or outside the convex hull of the anchors. Other criteria tested were the colinearity of the anchors, noise amount, and number of anchors. Figure 2.6 shows the dramatic increase in probability of multiple minima when the node is inside the convex hull as

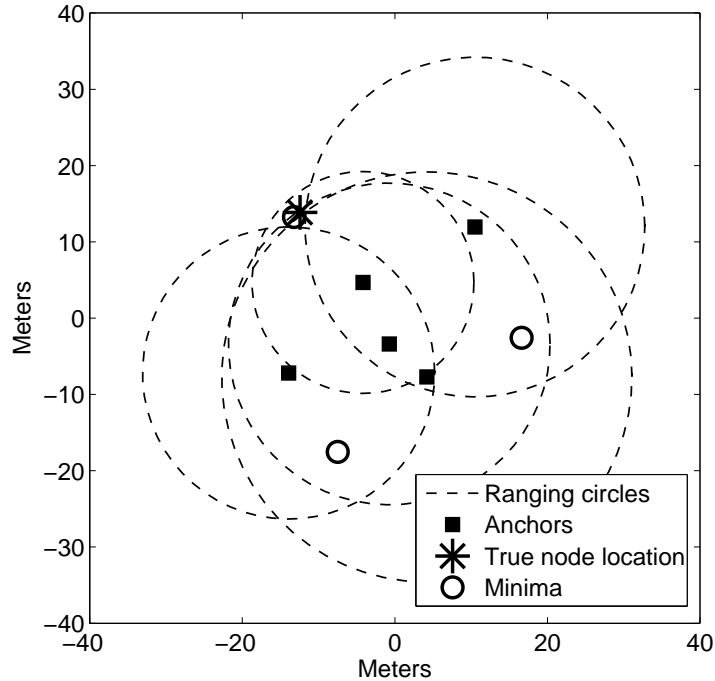


Figure 2.5: Example layout with multiple minima ( $K_E = 0.0144$ )

opposed to when it is not. Figure 2.6 also shows that with an increasing number of anchors, the probability of multiple minima understandably decreases. In this case, more information is available to assist in localizing the node. Therefore, performance increases as the number of minima decreases. Figure 2.7 shows the same trends for other values of  $K_E$ .

Our simulations show that the two factors most affecting the number of minima of  $\Phi^{\text{ncl}}(\hat{\theta})$  are whether or not the node's estimated location is inside the convex hull of the anchors and the number of anchors. Overall, the probability of multiple minima occurring when the true node location is inside the convex hull of the anchors is low, and the probability of the node being randomly placed inside the convex hull of the anchors increases directly with the number of anchors. The degradation of localization performance when nodes and/or their location estimates are outside the anchors' convex hull is a well known problem [6, 26, 27, 28, 29, 30, 31]. Our contribution is to note that performance for our objective function degrades when the node is outside of the convex hull because multiple

minima of  $\Phi^{\text{ncl}}(\hat{\theta})$  are much more likely to exist than when the node is inside the convex hull.

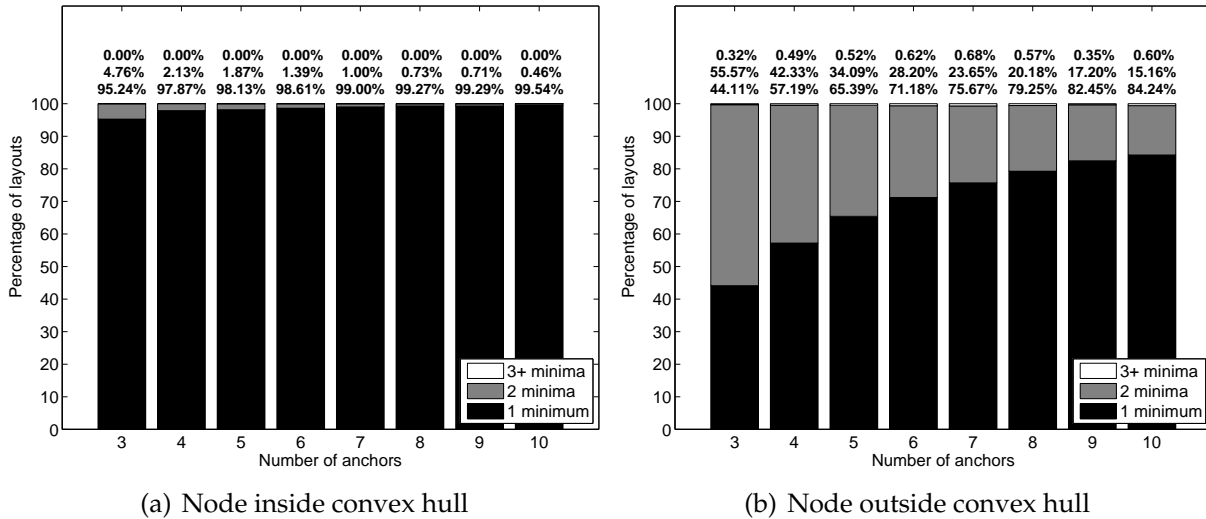


Figure 2.6: Number of minima;  $K_E = 0.0144$

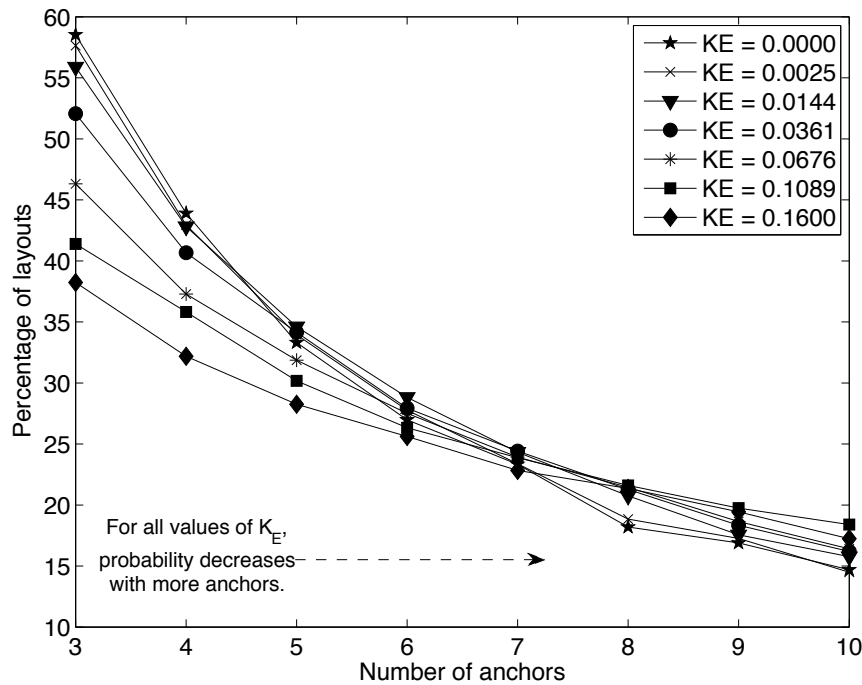


Figure 2.7: Probability of multiple minima; node outside convex hull

Figure 2.8 shows error plotted against anchor linearity (eccentricity, explained in Sec-

tion 3.6). Here, it can be seen that the layouts with nearly colinear anchors are also likely the layouts that produce high error. This is intuitive as the probability of the node being outside the convex hull grows as the anchors become more aligned. However, a large enough percentage of layouts with low anchor eccentricity and high error exist, making eccentricity insufficient for identifying those layouts with high error. This reaffirms our conclusion that whether the node is inside or outside the convex hull is the largest identifying factor with regard to error.

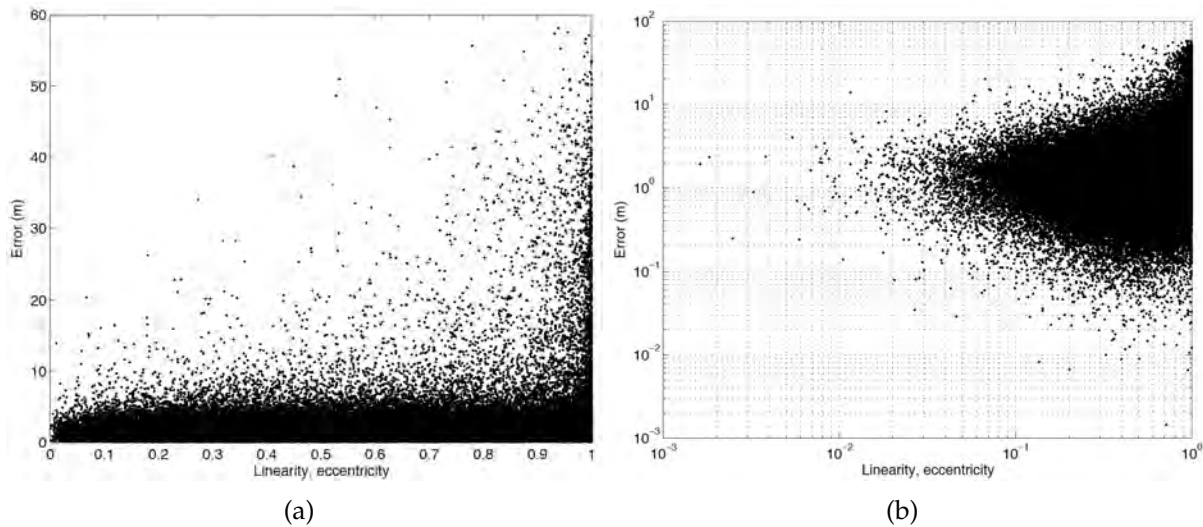


Figure 2.8: Number of minima;  $K_E = 0.0144$

The simulation results clearly show three facts:

- The true node location being inside or outside of the convex hull has the greatest effect on the number of minima for a given layout.
- An increasing number of anchors decreases the possibility of multiple minima.
- The amount of noise on the ranging estimates has some, but not an overwhelming, effect on the probability of multiple minima.
- When multiple minima of  $\Phi^{\text{ncl}}(\hat{\theta})$  exist, there are nearly always exactly two.

With these facts in mind, we describe and analyze the modified parallel projection method in Section 2.4 and develop an improvement specifically designed to address the layouts identified above that have multiple minima in Section 2.5.

### 2.3.3 Infeasibility of Optimal (Global) Solvers

Having an optimal solver available, e.g. BB/RLT or interval analysis, is helpful, but the computational complexity and computation time involved in using these solvers renders them infeasible for our applications of interest. The modified parallel projection method (MPPM) and the reflected PPM (RPPM) are described in detail in Sections 2.4 and 2.5. These solvers are non-optimal, but it will be shown that the RPPM achieves nearly equal performance to the optimal interval analysis solver. To compare the complexity of using the interval analysis solver against that of using MPPM and RPPM, runtimes were recorded for each solver as they operated on the same layouts. Simulations were performed on a computer running Mac OS<sup>2</sup> 10.6.8 and MATLAB R2010a (7.10.0.499), 64-bit, with 4 GB of RAM. Table 2.1 shows the seconds elapsed for each of the solvers when processing 100 layouts. The three orders of magnitude increase in time required for the interval analysis solver to complete explains why sub-optimal solvers are desired. For a more thorough comparison of the MPPM and RPPM solvers, the times elapsed for each of them to process 10,000 layouts are also listed.

100 layouts			10,000 layouts	
MPPM	RPPM	Interval analysis	MPPM	RPPM
0.5210	1.6685	$8.6507 \times 10^3$ (nearly 2.5 hours)	45.2084	166.3948

Table 2.1: Seconds to process layouts,  $K_E = 0.0144$

---

<sup>2</sup>Mac OS<sup>TM</sup>, © 2011 by Apple Inc.

## 2.4 Modified Parallel Projection Method

In [16], the authors modify the the parallel projection method (originally developed for signal recovery [18]) to obtain an iterative approach for position location, here labeled the *modified parallel projection method* (MPPM). A starting location  $\hat{\theta}$  is chosen, and the MPPM iteratively updates  $\hat{\theta}$  until convergence is achieved. The authors define a projection function in Equation 2.9.

$$P_k^{\text{ncl}}(\hat{\theta}) = A_k + r_k \frac{\hat{\theta} - A_k}{\|\hat{\theta} - A_k\|} \quad (2.9)$$

$P_k^{\text{ncl}}(\hat{\theta})$  simply represents the intersection point on the  $k^{\text{th}}$  anchor's ranging circle that is closest to the current guessed location  $\hat{\theta}$ .  $\frac{\hat{\theta} - A_k}{\|\hat{\theta} - A_k\|}$  is the vector of unit length pointing from the  $k^{\text{th}}$  anchor to  $\hat{\theta}$ . Multiplying this by  $r_k$  gives the vector the desired length (the radius of the  $k^{\text{th}}$  ranging circle), and adding the vector to  $A_k$  translates it from the origin to the anchor's location. Therefore, Step 3 of Algorithm 2 simply updates the node's guessed location to be the average of the points on each of the  $K$  ranging circles that are closest to  $\hat{\theta}$ . Figure 2.9 shows, for an example layout, the intersection points as circles and the average of these points, the next guess of  $\hat{\theta}$ , as a star.

The authors of [16] use Equations 2.4 and 2.9 to estimate location as described in Algorithm 2.

---

### Algorithm 2 : Modified PPM

---

- 1: Initialize the unlocalized node at  $\hat{\theta}$ ;  $l \leftarrow 0$ ;  
 $\Phi_l^{\text{ncl}} \leftarrow \Phi^{\text{ncl}}(\hat{\theta})$ ;  $\delta \leftarrow$  a small positive number
  - 2: **repeat**
  - 3:  $\hat{\theta} \leftarrow (1/K) \sum_{k=1}^K P_k^{\text{ncl}}(\hat{\theta})$  ▷ Update estimated location.
  - 4:  $\Phi_{l+1}^{\text{ncl}} \leftarrow \Phi^{\text{ncl}}(\hat{\theta})$  ;  $l \leftarrow l + 1$  ▷ Calculate objective value.
  - 5: **until**  $|\Phi_{l+1}^{\text{ncl}} - \Phi_l^{\text{ncl}}| \leq \delta$  ▷ Compare difference in objective values over subsequent iterations.
  - 6: **return**  $\hat{\theta}$
-

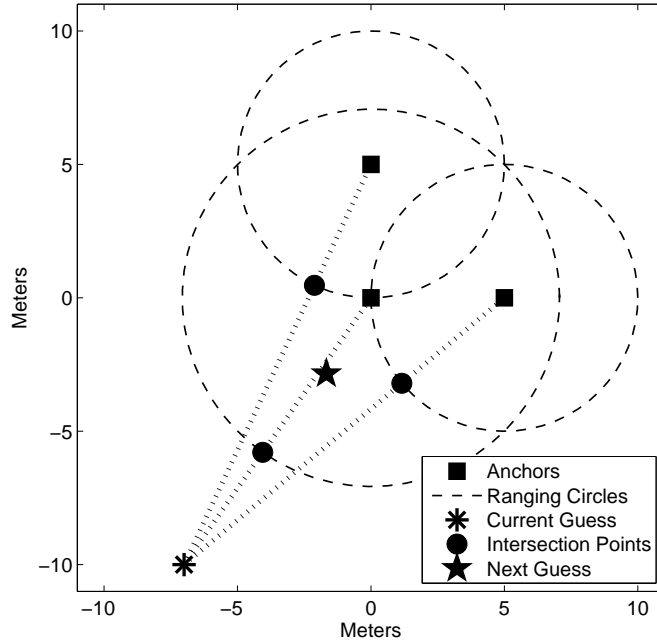


Figure 2.9: MPPM: Moving from one iteration to the next

### 2.4.1 Identification of MPPM as Steepest Descent

Convergence of steepest descent algorithms with constant stepsize only guarantees that the algorithm will converge to a stationary point [32]. The modified parallel projection method is shown in this section to be a steepest descent (gradient) solution method. Therefore, convergence to a local minimum of the objective function  $\Phi^{\text{ncl}}(\hat{\theta})$  is probable but not guaranteed.

Recall that the objective function

$$\Phi^{\text{ncl}}(\hat{\theta}) = \frac{1}{K} \sum_{k=1}^K \left( r_k - \|\hat{\theta} - A_k\| \right)^2 \quad (2.10)$$

$$= \frac{1}{K} \sum_{k=1}^K \left( r_k - \sqrt{(x - x_k)^2 + (y - y_k)^2} \right)^2. \quad (2.11)$$

Then, from Appendix A.1, the negated (for descent) first derivative of  $\Phi^{\text{ncl}}(\hat{\theta})$  is

$$-\Phi'^{\text{ncl}}(\hat{\theta}) = \begin{bmatrix} \frac{2}{K} \sum_{k=1}^K \left( r_k \left[ (x - x_k)^2 + (y - y_k)^2 \right]^{-\frac{1}{2}} - 1 \right) (x - x_k) \\ \frac{2}{K} \sum_{k=1}^K \left( r_k \left[ (x - x_k)^2 + (y - y_k)^2 \right]^{-\frac{1}{2}} - 1 \right) (y - y_k) \end{bmatrix} \quad (2.12)$$

$$= \frac{2}{K} \sum_{k=1}^K \left[ \frac{\hat{\theta} - A_k}{\|\hat{\theta} - A_k\|} r_k + A_k - \hat{\theta} \right]. \quad (2.13)$$

Note that in Algorithm 2, Step 3, the next guessed node location  $\hat{\theta}^{i+1}$  is the average of all the projection points (on each of the ranging circles)

$$\hat{\theta}^{i+1} = \frac{1}{K} \sum_{k=1}^K P_k^{\text{ncl}}(\hat{\theta}^i) = \frac{1}{K} \sum_{k=1}^K \frac{\hat{\theta}^i - A_k}{\|\hat{\theta}^i - A_k\|} r_k + A_k, \quad (2.14)$$

and subtracting  $\hat{\theta}^i$  from Equation 2.14 yields the vector from  $\hat{\theta}^i$  to the next guessed location  $\hat{\theta}^{i+1}$ .

$$\hat{\theta}^{i+1} - \hat{\theta}^i = \frac{1}{K} \sum_{k=1}^K \left[ \frac{\hat{\theta}^i - A_k}{\|\hat{\theta}^i - A_k\|} r_k + A_k - \hat{\theta}^i \right] = -\Phi'^{\text{ncl}}(\hat{\theta})/2 \quad (2.15)$$

Thus, the modified parallel projection method iteratively updates the guessed node location, always updating in the direction of steepest descent and with a distance equal to half the magnitude of the derivative vector.

## 2.4.2 Guaranteed Convergence to a Stationary Point

Because the MPPM is a gradient descent (and a steepest descent) solution method, the question of convergence arises. Bertsekas provides a proof of convergence to a stationary point of a gradient descent method with a constant stepsize in Proposition 1.2.3 in [33].

The proposition states:

Let  $x^k$  be a sequence generated by a gradient method  $x^{k+1} = x^k + \alpha^k d^k$ , where  $d^k$  is gradient related. Assume that for some constant  $L > 0$ , we have

$$\|\nabla f(x) - \nabla f(y)\| \leq L \|x - y\|, \quad \forall x, y \in \mathbb{R}^n, \quad (2.16)$$

and that for all  $k$ , we have  $d^k \neq 0$  and

$$\epsilon \leq \alpha^k \leq \frac{(2 - \epsilon) \left| \nabla f(x^k)^\top d^k \right|}{L \|d^k\|^2}, \quad (2.17)$$

and  $\epsilon$  is a fixed positive scalar. Then, every limit point of  $x^k$  is a stationary point of  $f$ .

It is generally difficult, according to Bertsekas in [33], to prove satisfaction of Equation 2.16. However, for our objective function  $\Phi^{\text{ndl}}(\hat{\theta})$  (labeled  $f$  in the proposition), Equation 2.16 is satisfied by simply dividing  $f$  by a sufficiently large number. The purpose of the objective function is to compare one minimum against another. Dividing both objective values by the same number will not affect this comparison.

Equation 2.17 can be transformed by recognizing that  $d^k = -\nabla f(x^k)$  is the steepest descent vector. Thus,

$$\left| \nabla f(x^k)^\top d^k \right| = \left| - (d^k)^\top d^k \right| = (d^k)^\top d^k = \|d^k\|^2, \quad (2.18)$$

and Equation 2.17 becomes  $\epsilon \leq \alpha^k \leq (2 - \epsilon)/L$ . We know that the step size  $\alpha^k = 1/2 \forall k$  (as shown in Equation 2.15), and we arrive at  $\epsilon \leq 1/2 \leq (2 - \epsilon)/L$ . The right hand inequality yields  $L \leq 2(2 - \epsilon)$ , and maximizing  $\epsilon$  to  $1/2$  forces  $L \leq 3$ . However, as explained above, Equation 2.16 can be satisfied for an arbitrarily small  $L$  by dividing  $f$  by a sufficiently large number. Thus, Equations 2.16 and 2.17 can both be satisfied by using  $0 < \epsilon \leq 1/2$  and  $L \leq 3$ . Therefore, Proposition 1.2.3 from [33] proves that the modified parallel projection method's limit point is a stationary point of the objective

function  $\Phi^{\text{ncl}}(\hat{\theta})$ .

The likelihood of MPPM converging to a non-minimum stationary point was not explored because of the excellent performance achieved in the first place. In certain test cases, it can be shown that MPPM does settle to a saddle point rather than a minimum given a specifically chosen initialization point. MPPM will not converge to a maximum, but the remote possibility exists that MPPM's iterations will force it to iterate exactly to a maximum of  $\Phi^{\text{ncl}}(\hat{\theta})$ . While MPPM always follows the descent direction, it is conceivable that the magnitude of the gradient vector will pass over the non-maximum stationary point and will point MPPM exactly to a maximum. In this scenario, the gradient vector would have zero length, and MPPM would stop. The possibility of initializing MPPM to a maximum of  $\Phi^{\text{ncl}}(\hat{\theta})$  is also conceivable. In all these scenarios, though, where MPPM might converge to a non-minimum stationary point, the reflected parallel projection method (RPPM) (explained in Section 2.5) mitigates the possibility of never finding any minimum of  $\Phi^{\text{ncl}}(\hat{\theta})$  by using multiple initialization points.

An analysis of how often the MPPM settles in a non-global minimum appears in Section 2.5 along with our proposed solution method for remedying those cases.

## 2.5 The Reflected Parallel Projection Method

This section details the development and performance of the reflected parallel projection method (RPPM), a method which nearly matches the performance of the optimal interval analysis solver while using much fewer computer resources and much less time.

### 2.5.1 Motivation for the Reflected Parallel Projection Method

From the characterization of the non-collaborative location problem, we built a library of layouts, noise realizations, and the minima of  $\Phi^{\text{ncl}}(\hat{\theta})$  associated with these layouts.

While the optimal interval analysis solver works well, it is slow and computationally expensive. One of the main applications of collaborative position location is in the low-power wireless sensor arena, so a computationally expensive algorithm is prohibitive and unwieldy. Here, we develop a sub-optimal solver for  $\min \{ \Phi^{\text{ncl}}(\hat{\theta}) \}$  that shows nearly optimal performance at a much lower cost, the reflected parallel projection method (RPPM).

Because the parallel projection method is an iterative algorithm, its performance is, like most other iterative algorithms, dependent upon initialization. In particular, performance improves as more initialization points are used, but cost and time grow accordingly. The objective of the RPPM is to limit the number of initialization points required to achieve nearly optimal performance by intelligently choosing one initialization point based upon the solution of the MPPM from a different initialization point.

Figure 2.10 shows the performance of the MPPM in situations with only one minimum (as found by the interval analysis method) compared to those situations with multiple minima. Performance in multiple-minima situations is noticeably worse than the single-minima situations at least 40% of the time, and performance in multiple-minima situations is severely worse about 30% of the time. In some cases where multiple minima exist, MPPM will converge to  $\min \{ \Phi^{\text{ncl}}(\hat{\theta}) \}$ . When it does not, RMS error  $\Omega$  can increase dramatically, as shown in Figure 2.10. This heavy tail of error in multiple-minima situations is what the RPPM is designed to address and correct.

Figure 2.11 shows that, even in the absence of noise, multiple minima of  $\Phi^{\text{ncl}}(\hat{\theta})$  can exist, and, depending upon the choice of starting location, MPPM may settle in a non-global minimum.

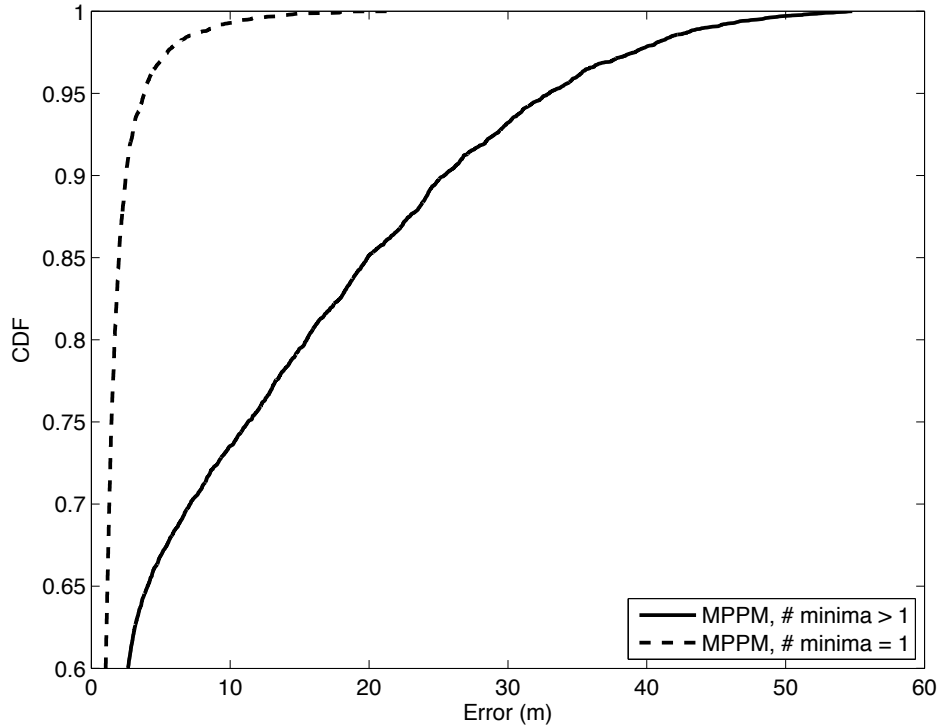


Figure 2.10: Heavy tail of error when multiple minima exist ( $K_E = 0.0025$ , three anchors)

## 2.5.2 RPPM Algorithm

The characterization of the number of minima likely for a given layout in Section 2.3 leads us to the conclusion that, under typical circumstances, ideally we need only three initialization points to find the possible three minima of  $\Phi^{\text{ncl}}(\hat{\theta})$ . Figure 2.6 shows that the probability of finding more than three minima is negligible. If all the minima of  $\Phi^{\text{ncl}}(\hat{\theta})$  are found, then a simple comparison of the minima's objective value will yield the solution to  $\min \{ \Phi^{\text{ncl}}(\hat{\theta}) \}$ . The interval analysis method described in Section 2.2.2 yields all the minima, and we show that the RPPM, a sub-optimal solver, nearly matches the performance of the interval analysis method.

Using the results of the characterization of the minima of  $\Phi^{\text{ncl}}(\hat{\theta})$ , we discovered that the multiple minima were nearly always spatially divided by the bulk of the anchors. This phenomenon is similar to the well known flip ambiguity. Taking advantage of this,

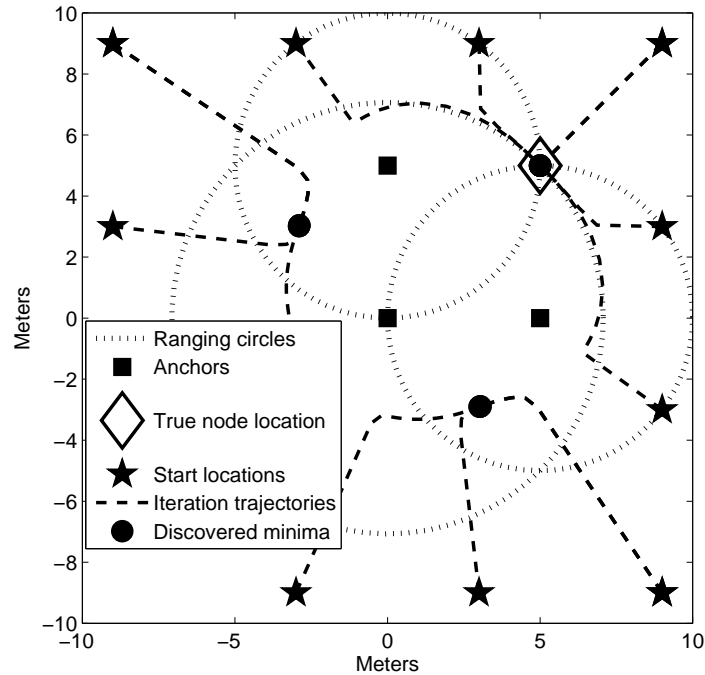


Figure 2.11: MPPM can settle to non-global minimum even in the absence of noise.

we choose as the next initialization point the reflection of the prior solution about the centroid of the anchors. Thus, the next initialization point is likely to be nearer a different minimum than the prior solution, and this process is repeated until one minimum is found twice. Then, all the discovered minima's objective values are compared, and the minimum with the lowest objective value is returned.

In addition to discovering that minima are usually spatially divided by the anchors, we show in Figure 2.12 that, given a set of anchors, minima pairs occur with some amount of symmetry. Figure 2.12 shows two example noiseless layouts where the true node is plotted in different locations (in the lower left corner for Figure 2.12(a) and in the lower right corner for Figure 2.12(b)). For each true node location, a second (non-global) minimum occurs and is plotted as another circle, linked to the true node location with a dashed line. As the true node moves upward in the  $y$  direction, the second minimum moves in a matching fashion. This phenomenon appears in many layouts; Figure 2.12 contains two examples.

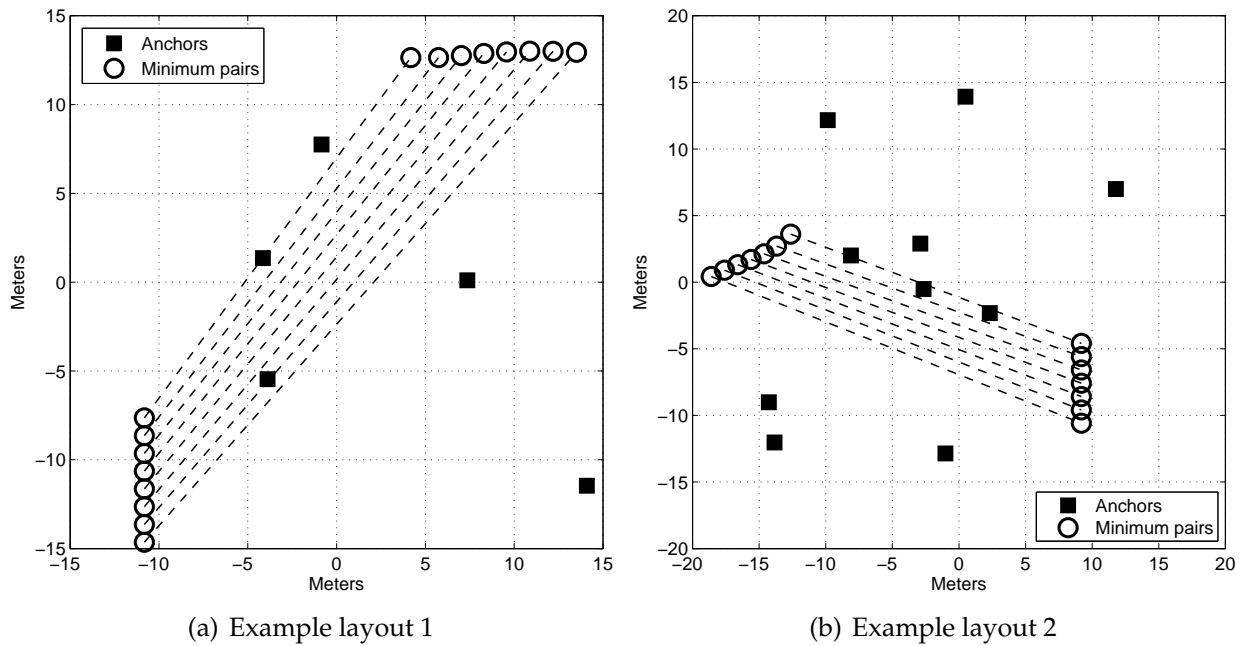


Figure 2.12: Minimum pairs show symmetry for two example layouts.

Using the RPPM on the randomly generated layouts used for the characterization of  $\Phi^{\text{ncl}}(\hat{\theta})$ , we found that the RPPM ran the MPPM algorithm an average of 2.3 times for each layout (as opposed to the 1 time it would have been run without reflecting). This is reasonable because the RPPM has to run MPPM at least twice. If it is only run twice, the RPPM finds the same minimum two times in a row and returns it as the only minimum of  $\Phi^{\text{ncl}}(\hat{\theta})$ . When multiple minima exist, the RPPM must run at least three times to find two minima. In general, the RPPM runs the MPPM algorithm  $n + 1$  times, where  $n$  is the number of discovered minima. The last MPPM run finds a minimum that has already been discovered, telling the RPPM algorithm when to terminate.

In the RPPM algorithm (Algorithm 3),  $M = [m_1, m_2, \dots, m_i]$ , where  $m_i = [x_i, y_i]^T$  is the 2D coordinate of the  $i^{\text{th}}$  minimum of  $\Phi^{\text{ncl}}$ .  $\bar{\theta}_i$  is the initialization point for the  $i^{\text{th}}$  iteration.  $A$  is the set of 2D coordinates of the anchors neighboring the unlocalized node, and  $\partial(H(A))$  is the boundary of the convex hull of  $A$ .  $f$  is the 2D reflection point, the average of  $A \subset \partial(H(A))$ .  $|\cdot|$  denotes cardinality, so  $\bar{\theta}_{i+1}$  is the reflection of  $m_i$  about  $f$ , weighted by the

number of neighboring anchors. The algorithm stops when a minimum that has already been found is found again and then returns the minimum with the lowest objective value.

---

**Algorithm 3** : Reflected PPM

---

```

1:  $i \leftarrow 0$ ;  $M \leftarrow \emptyset$ ;  $\bar{\theta}_1 \leftarrow$  closest anchor
2:  $f \leftarrow A \subset \partial(H(A))$  ▷ Find reflection point  $f$ .
3: repeat
4:    $i \leftarrow i + 1$ 
5:    $m_i \leftarrow$  PPM (initialized to  $\bar{\theta}_i$ ) solution ▷ Run MPPM and store solution.
6:    $\bar{\theta}_{i+1} \leftarrow m_i + |A|(f - m_i)$  ▷ Reflect about  $f$ .
7: until  $m_i = m_j$ , for any  $j = \{1, 2, 3, \dots, i - 1\}$  ▷ Stop when a minimum is discovered twice.
8: return  $m_k : m_k \in M, \Phi(m_k) \leq \Phi(m_j) \forall j \neq k$  ▷ Return min with lowest objective value.

```

---

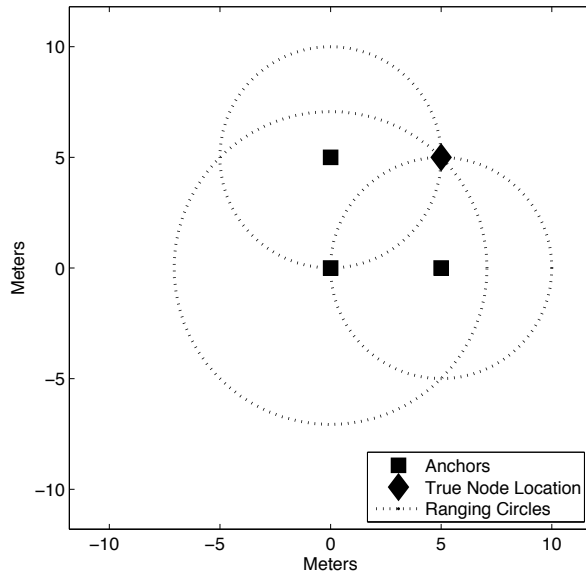
Figure 2.13 shows the an example of the RPPM algorithm.

### 2.5.3 Comparison of RPPM to Optimal Solver

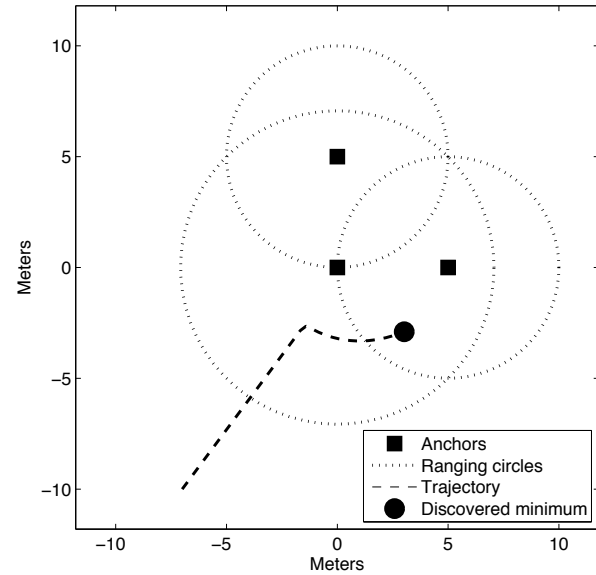
Figures 2.14 and 2.15 show the gains in performance that RPPM provides compared to MPPM and the nearly identical performance of RPPM to interval analysis. Figure 2.14 shows the cumulative distribution function of error for all layouts with  $K_E = 0.0144$ . The reduction of the heavy tail of RMS error gained by using RPPM as opposed to only MPPM is significant, and the optimal performance of interval analysis is nearly indistinguishable from RPPM. Thus, RPPM, a non-optimal solver, almost always returns the same minimum as the global interval analysis solver.

It can also be seen in Figure 2.14 that sometimes, the lowest objective value does *not* correspond to the minimum with the lowest RMS error  $\Omega$ . This is shown by the upper “Best from interval analysis” and “Best from RPPM” plotlines. If it were possible to distinguish the best (lowest RMS error) minimum from all those returned by interval analysis or RPPM, the upper plotlines’ performance would be achievable.

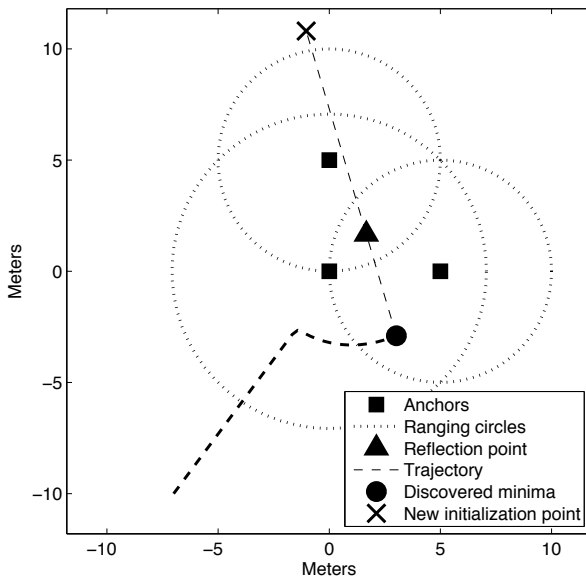
Figure 2.15 shows the RMS error for MPPM, RPPM, and interval analysis on layouts with exactly three anchors and variable amounts of noise (variable  $K_E$ ). Again, performance



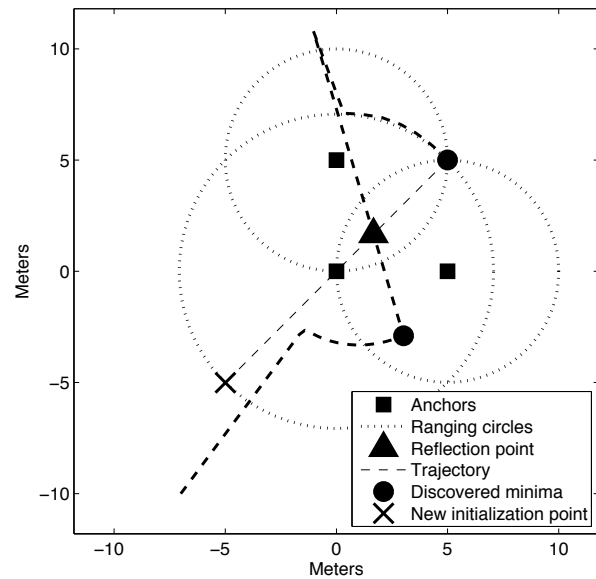
(a) Layout



(b) First discovered minimum



(c) First reflection



(d) Second discovered minimum and reflection

(Figure continued on next page.)

is noticeably improved by using RPPM, and the optimal performance of interval analysis is nearly matched. More dramatic, though, is the difference between the minimum displaying the least error out of all minima found and the minimum with the lowest

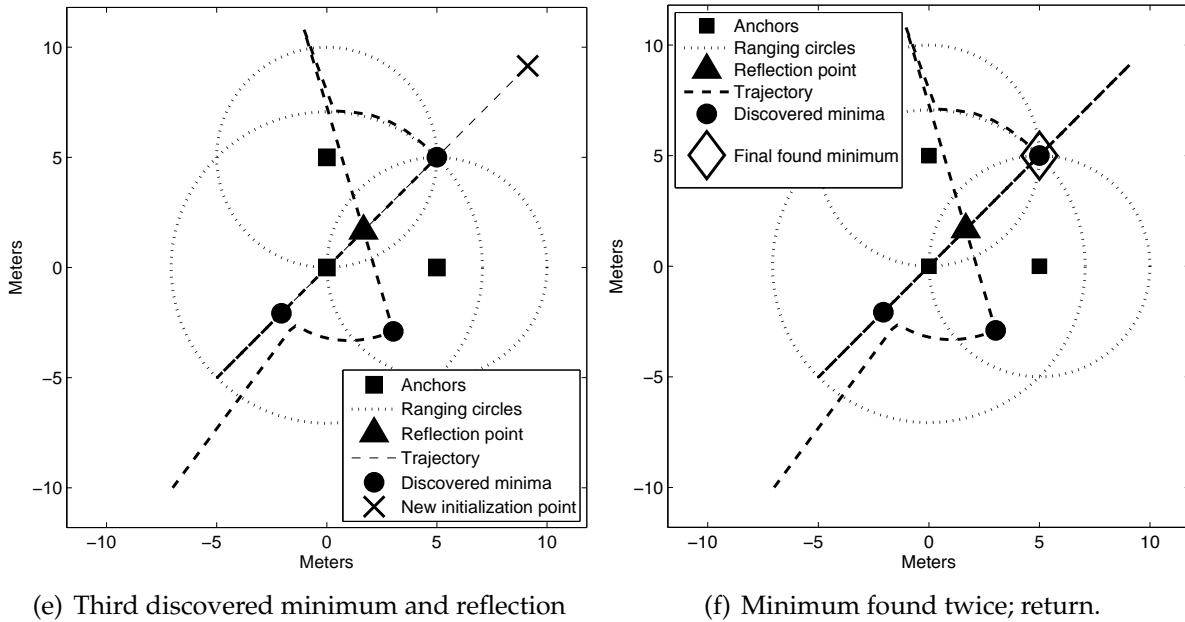


Figure 2.13: RPPM example

objective value. Figure 2.15 shows, in dashed lines, the minimum error out of all minima, as discovered by RPPM and by interval analysis. This reaffirms that the minimum of  $\Phi^{\text{ncl}}(\hat{\theta})$  with the lowest objective value is not guaranteed to minimize  $\Omega$ . While Figure 2.15 only displays results for layouts with exactly three anchors, it shows the potential for improvement beyond minimizing  $\Phi^{\text{ncl}}(\hat{\theta})$ .

Ideally, RPPM would always find all the minima of  $\Phi^{\text{ncl}}(\hat{\theta})$ , allowing us to identify the global minimum in all cases. While such a guarantee is not possible, the interval analysis method does guarantee the identification of all minima of  $\Phi^{\text{ncl}}(\hat{\theta})$ . Interval analysis is a computationally expensive and slow method for finding minima, but it does provide a lower bound on the error performance of RPPM in the sense that it allows us to know whether RPPM found the global minimum of  $\Phi^{\text{ncl}}(\hat{\theta})$ .

Figure 2.16 is an example of one layout and noise realization that yields multiple minima and where the minimum with the lowest objective value does not have the lowest RMS error. It can easily be seen that the minimum with lowest RMS error is nearly at the true

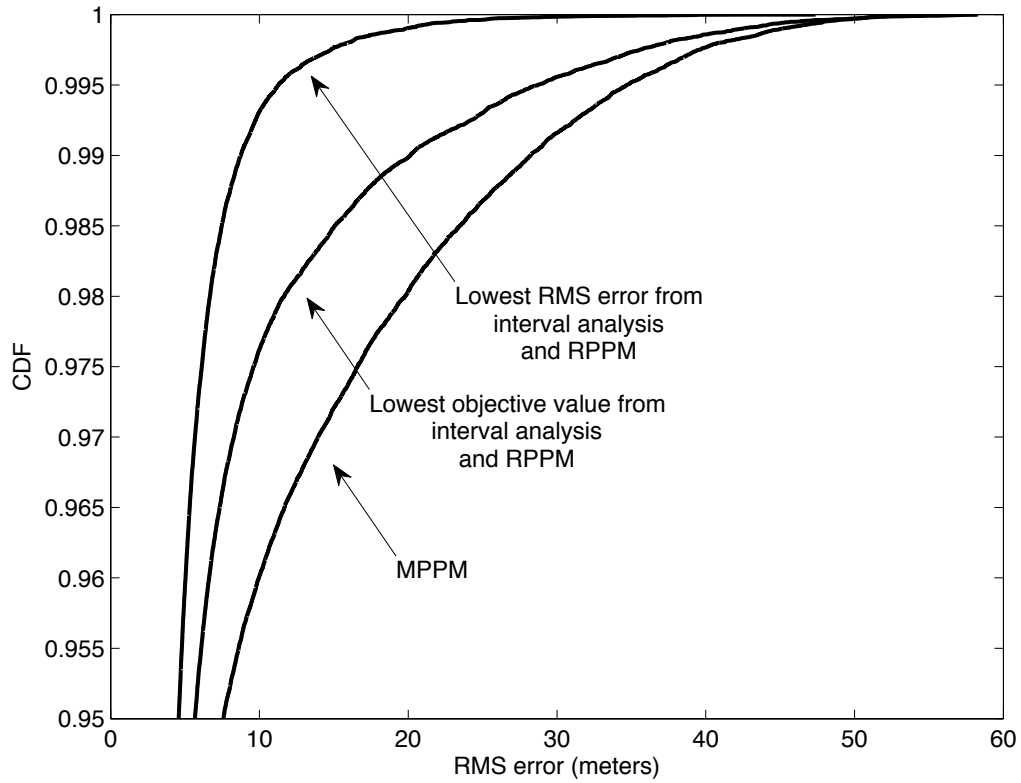


Figure 2.14: RPPM performs almost identically to interval analysis. ( $K_E = 0.0144$ )

node location, but the flip ambiguity of the anchor layouts along with this specific noise realization force the minimum on the opposite side to have a lower objective value.

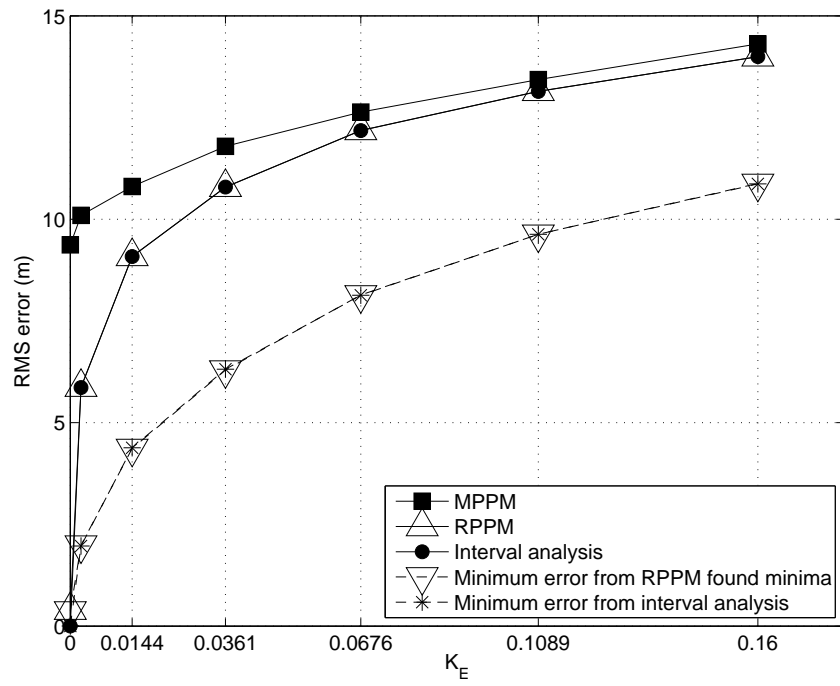


Figure 2.15: RPPM performs almost identically to interval analysis. (3 anchors)

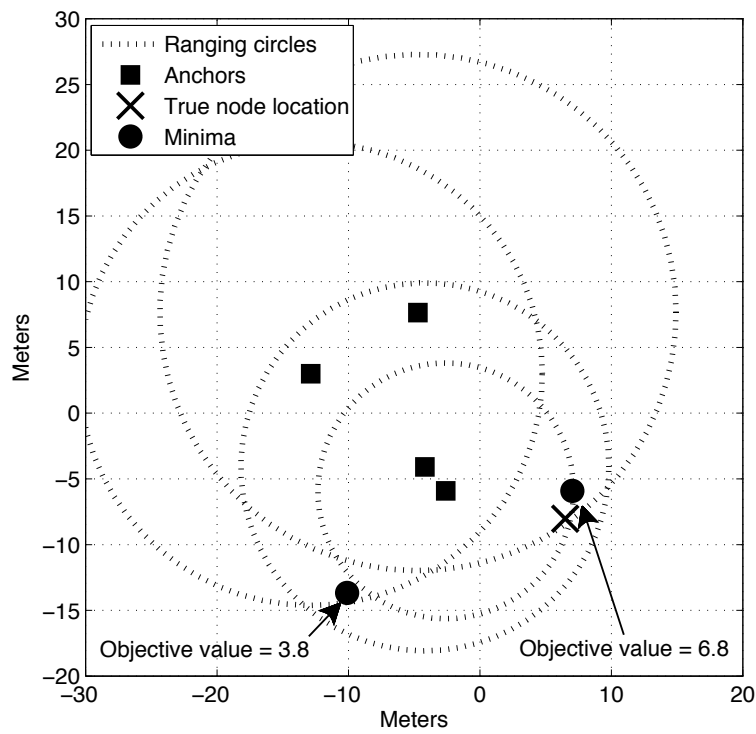


Figure 2.16: Minimizing  $\Phi^{ncl}(\hat{\theta})$  does not always minimize  $\Omega$ .

### 2.5.4 The Weighted Least Squares Formulation

The MPPM as described uses non-weighted projections. Incorporating weights would simply change the update step to be

$$\hat{\theta} \leftarrow \frac{\sum_{k=1}^K w_k P_k^{\text{ncl}}(\hat{\theta})}{\sum_{k=1}^K w_k} \quad (2.19)$$

instead of

$$\hat{\theta} \leftarrow (1/K) \sum_{k=1}^K P_k^{\text{ncl}}(\hat{\theta}), \quad (2.20)$$

where  $w_k$  would be the reciprocal of the variance of range estimate noise for each range estimate. If the variance of each range estimate noise value was known, incorporating the weights into the MPPM formulation would improve average performance. Some layouts returned a lower RMS error with MPPM than with the weighted least squares (WLS) formulation, but the gain in performance shown by Figure 2.17 when using WLS is significant. The RMS error returned by WLS is actually smaller, on average, than the minimum RMS error of all minima found by interval analysis/RPPM. This indicates that the WLS formulation returns a node location estimate that is *not* necessarily a minimum of  $\Phi^{\text{ncl}}(\hat{\theta})$ . However, knowledge of  $w_k$  is difficult without multiple range estimates between the same node/anchor pair. This operation would consume valuable battery power in the applications of interest. Thus, the weighted least squares formulation was not tested as thoroughly as the non-weighted version.

The performance gain possible through weighted least squares, though, motivates the researching of how to weight each term in the update step. For this particular formulation of noise, where  $\sigma^2 = K_E d_k^{\beta_k}$ , knowledge that the variance is directly related to the distance is helpful. However, this particular model of noise may not be accurate for real-life scenarios.

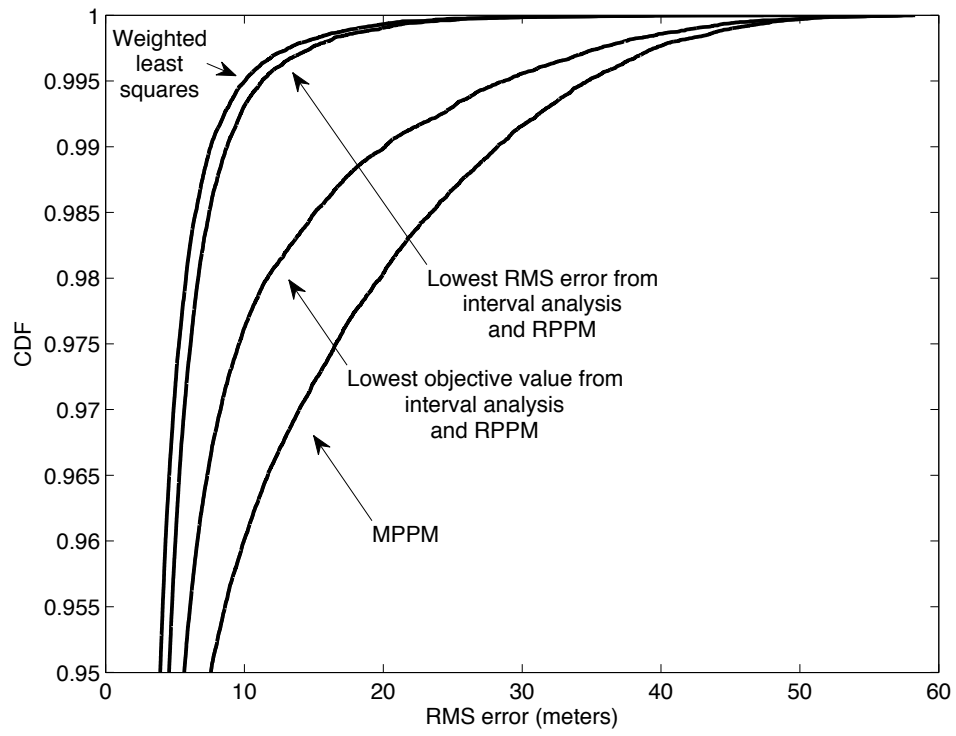


Figure 2.17: CDF of error for weighted least squares ( $K_E = 0.0144$ )

# Chapter 3

## The Collaborative Problem

In the non-collaborative case, only one node and multiple anchors exist. In the collaborative problem, multiple nodes communicate with each other, assisting each other in localization, particularly by providing range measurements and node location estimates.

### 3.1 The Collaborative Objective Function

Recall that the non-collaborative objective function is

$$\Phi^{\text{ncl}}(\hat{\theta}) = \frac{1}{K} \sum_{k=1}^K \left( r_k - \|\hat{\theta} - A_k\| \right)^2 \quad (3.1)$$

$$= \frac{1}{K} \sum_{k=1}^K \left( r_k - \sqrt{(x - x_k)^2 + (y - y_k)^2} \right)^2, \quad (3.2)$$

where  $K$  is the number of anchors,  $r_k$  is the range estimate between the node and the  $k^{\text{th}}$  anchor,  $\hat{\theta}$  is the supposed node location, and  $A_k$  is the location of the  $k^{\text{th}}$  anchor.

$\hat{\Theta} = \{\hat{\theta}_1, \hat{\theta}_2, \dots, \hat{\theta}_N, \theta_{A_1}, \theta_{A_2}, \dots, \theta_{A_K}\} = \{\hat{\theta}_1, \hat{\theta}_2, \dots, \hat{\theta}_N, \theta_{N+1}, \theta_{N+2}, \dots, \theta_{N+K}\}$  is a list, for the collaborative case, of the unlocalized nodes' locations *followed* by a list of the anchors' known locations. The range estimates vector in the non-collaborative case becomes an  $N \times N + K$  matrix in the collaborative case, where  $N$  is the number of nodes and  $K$  is the number of anchors. Multiple nodes exist, and, depending on the radio range, some nodes may not be connected to other nodes. Then, the collaborative objective function becomes

$$\begin{aligned} \Phi^{\text{col}}(\hat{\Theta}) &= \frac{1}{C} \sum_{i=1}^N \sum_{j=i+1; j \in \mathcal{N}_i}^{N+K} \left( r_{ij} - \|\hat{\theta}_i - \hat{\theta}_j\| \right)^2 \\ &= \frac{1}{C} \sum_{i=1}^N \sum_{j=i+1; j \in \mathcal{N}_i}^{N+K} \left( r_{ij} - \sqrt{(x_i - x_j)^2 + (y_i - y_j)^2} \right)^2, \end{aligned} \quad (3.3)$$

where  $r_{ij}$  is the range estimate between the  $i^{\text{th}}$  and  $j^{\text{th}}$  nodes and  $\mathcal{N}_i$  is the set of neighboring nodes/anchors to the  $i^{\text{th}}$  node.  $C$  is the total number of connections (node/node and node/anchor) in the network, which is equal to the number of terms in the entire summation. The  $j = i+1$  beginning index of the second summation is included to ensure that the connection from node  $i$  to node  $j$  is only contributing to the objective value once rather than twice. The first summation of Equation 3.3 sums only over the unlocalized nodes while the second summation sums over nodes and anchors. Note that the non-collaborative objective function  $\Phi^{\text{ncl}}(\hat{\theta})$  can be obtained from the collaborative objective function  $\Phi^{\text{col}}(\hat{\Theta})$  by setting neglecting  $N$  and  $i$  (as there is only one node), and setting  $\mathcal{N} = A$ , the set of anchors.

### 3.2 Finding the Global Minimum of $\Phi^{\text{col}}(\hat{\Theta})$

As is the case with the non-collaborative problem, described in Section 2.2, our approach is to find the global minimum of  $\Phi^{\text{col}}(\hat{\Theta})$ , compare the existing iterative parallel projection

method's performance to that of the global solver, and target the layouts which cause large RMS error. Sections 3.2.1 and 3.2.2 explain our techniques for finding the global minimum of  $\Phi^{\text{col}}(\hat{\Theta})$ .

As the global minimization of the non-collaborative objective function  $\Phi^{\text{ncl}}(\hat{\theta})$  does *not* guarantee the minimization of RMS error  $\Omega$  for a given layout, neither does the minimization of  $\Phi^{\text{col}}(\hat{\Theta})$  guarantee minimal RMS error. Figure 3.11 shows that in some cases, minima with lower RMS values than the minimum with the lowest objective value exist.

### 3.2.1 BB/RLT and Interval Analysis

Similarly to Sections 2.2.1 and 2.2.2, the global minimum of  $\Phi^{\text{col}}(\hat{\Theta})$  can theoretically be found by using either the branch and bound/reformulation-linearization technique (BB/RLT) or interval analysis. Implementation of both of these methods, however, proved considerably more difficult than for the non-collaborative case. Specifically, the time required to run a sufficient number of layouts to provide useful results is prohibitive to actual execution. For testing cases with only two nodes, the interval analysis solver would return the correct minima but would not terminate in a reasonable amount of time.

To circumvent these restrictions, we sacrifice a small amount of certainty regarding the optimality of our solution. This technique is described in Section 3.2.2.

### 3.2.2 True Initialization Solution

Because the optimal BB/RLT and interval analysis solvers proved unwieldy for finding the global minimum of our collaborative problem, we turn to a non-realizable initialization of an existing solver. Jia and Buehrer in [17] describe the iterative parallel projection

method (IPPM), a method of iteratively using the modified parallel projection method, as shown in Section 2.4, to modify each node's location until a minimum of  $\Phi^{\text{col}}(\hat{\Theta})$  is achieved. Just like the MPPM, the IPPM requires an initialization of  $\hat{\Theta}$ , and the minimum of  $\Phi^{\text{col}}(\hat{\Theta})$  returned by the IPPM is dependent upon the initialization. The IPPM is described in detail in Section 3.3.

To find our best guess as to the optimal minimum of  $\Phi^{\text{col}}(\hat{\Theta})$ , we simply initialize  $\hat{\Theta}$  to the true locations of the nodes. While this is impossible in practice, it provides a high level of confidence that the minimum returned by IPPM will be the minimum with lowest RMS error  $\Omega$ . While this minimum may not be the global minimum of  $\Phi^{\text{col}}(\hat{\Theta})$  (because minimizing  $\Phi^{\text{col}}(\hat{\Theta})$  does not guarantee minimized  $\Omega$ ), it provides a reliable lower bound on achievable RMS error for the least squares formulation. For zero noise, the minimum returned by true node initialization will be both the global minimum of  $\Phi^{\text{col}}(\hat{\Theta})$  and the minimum with the least amount of error (zero).

### 3.3 Iterative Parallel Projection Method

The iterative parallel projection method (IPPM) uses the modified PPM as a basic element and extends it to an iterative and distributed numerical framework. IPPM involves an initialization step and an iterative update step, where local communications between nodes are necessary in both steps.

In the initialization step, each unlocalized node obtains an initial solution for its location. The specific method is described in detail in [16]. A more complete summary is found in Section 3.4.1. Each node is initialized to its closest anchor or a combination of its neighbors' initializations. In the iterative update step, each unlocalized node uses MPPM (from Section 2.4) to update its location estimate, based on its range estimates to neighboring nodes/anchors. In particular, if the  $i^{\text{th}}$  and the  $j^{\text{th}}$  nodes are neighbors, the

projection of  $\hat{\theta}_i$  onto the feasibility set (ranging circle) given by the range estimate  $r_{ij}$  is

$$P_{ij}^{\text{col}}(\hat{\theta}_i) = \hat{\theta}_j + r_{ij} \frac{\hat{\theta}_i - \hat{\theta}_j}{\|\hat{\theta}_i - \hat{\theta}_j\|}. \quad (3.4)$$

Just as in Equation 2.9,  $P_{ij}^{\text{col}}(\hat{\theta}_i)$  is simply a point on the ranging circle given by neighbor  $\hat{\theta}_j$  that is closest to current guess  $\hat{\theta}_i$ . Note that if the  $j^{\text{th}}$  node is an anchor,  $\hat{\theta}_j$  simply is the known anchor location. Each unlocalized node examines whether or not its objective value changes over the previous iteration. The  $i^{\text{th}}$  unlocalized node's objective value is defined as

$$\Phi^{\text{ncl}}(\hat{\theta}_i) = \frac{1}{|\mathcal{N}(i)|} \sum_{j \in \mathcal{N}(i)} \left( r_{ij} - \|\hat{\theta}_i - \hat{\theta}_j\| \right)^2, \quad (3.5)$$

where  $\mathcal{N}(i)$  is the set of the  $i^{\text{th}}$  node's neighboring nodes and  $|\cdot|$  denotes cardinality. Note that Equation 3.5 is the same as Equation 2.4 with the anchors replaced by the neighbors of the  $i^{\text{th}}$  node. If its objective value has not changed more than the precision parameter  $\delta$  for  $\kappa$  consecutive iterations, the  $i^{\text{th}}$  node will quit the iterative update step and mark itself as localized. The overall update process terminates after all the nodes are marked as localized. Iterative PPM (IPPM) for collaborative position location is described in detail in Algorithm 4.

In Algorithm 4,  $L_i$  indicates whether the  $i^{\text{th}}$  node has been localized, and  $W_i$  records the number of consecutive iterations that the  $i^{\text{th}}$  node's objective value has not changed more than  $\delta$ . Once  $W_i \geq \kappa$ , we set  $L_i = 1$  and consider the  $i^{\text{th}}$  unlocalized node as localized. Anchor locations  $\hat{\theta}_j$ , for  $j = n+1, n+2, \dots, n+m$ , will remain unchanged during the whole process. Again, as in the case of modified PPM for non-collaborative position location, the final solution of iterative PPM depends on the initial guess.

---

**Algorithm 4 : Iterative PPM**


---

```

1: Obtain initial guess  $[\hat{\theta}_1, \hat{\theta}_2, \dots, \hat{\theta}_n]$ ;  $\hat{\theta}_j \leftarrow \theta_j \forall j > n$   $\triangleright$  Use anchors' actual (known) positions.
2:  $l \leftarrow 0$ ;  $\delta \leftarrow$  a small positive number;  $\kappa \leftarrow$  a positive integer
3:  $L_i \leftarrow 0$  and  $W_i \leftarrow 0$  for  $i = 1, 2, \dots, n$   $\triangleright$  Mark all nodes unlocalized; set counters to zero.
4:  $\Phi_{i,l} \leftarrow \Phi^{\text{ncl}}(\hat{\theta}_i)$ , for  $i = 1, 2, \dots, n$   $\triangleright$  Calculate original objective values for all nodes. (Eqn. 3.5)
5: while  $L_i == 0$  for any  $i$  do  $\triangleright$  while any nodes are unlocalized
6:   for  $i = 1, 2, \dots, n$ ; if  $L_i == 0$  then do  $\triangleright$  for the unlocalized nodes
7:      $\hat{\theta}_i^{\text{new}} \leftarrow (1/|\mathcal{N}(i)|) \sum_{j \in \mathcal{N}(i)} P_{ij}^{\text{col}}(\hat{\theta}_i)$   $\triangleright$  MPPM
8:      $\Phi_{i,l+1} \leftarrow \Phi^{\text{ncl}}(\hat{\theta}_i^{\text{new}})$   $\triangleright$  Calculate objective value for node's new position. (Eqn. 3.5)
9:     if  $|\Phi_{i,l} - \Phi_{i,l+1}| < \delta$  then  $\triangleright$  if the node has not moved by amount  $\delta$ 
10:        $W_i \leftarrow W_i + 1$   $\triangleright$  Increase the node's counter by 1.
11:       if  $W_i \geq \kappa$  then  $L_i \leftarrow 1$   $\triangleright$  Mark node as localized if applicable.
12:     else  $\triangleright$  if the node moved more than amount  $\delta$ 
13:        $W_i \leftarrow 0$   $\triangleright$  Reset node's counter to zero.
14:     end if
15:   end for
16:    $\hat{\Theta} \leftarrow \hat{\Theta}^{\text{new}}$ ;  $l \leftarrow l + 1$   $\triangleright$  After all nodes are moved, update shared location information.
17: end while

```

---

## 3.4 Initialization Techniques

For the purpose of characterizing the collaborative problem, we use two initialization techniques, true initialization and closest anchor initialization. We develop the reflected and flipped initialization techniques in response to the difference in performance between true initialization and closest anchor initialization. The same iterative parallel projection method (IPPM) is used regardless of initialization.

### 3.4.1 Original Initialization Techniques

- True node location initialization:
  - The initialization points  $\hat{\Theta}$  are set as the true node locations. This method provides our baseline of performance and likely provides the solution with minimum RMS error. This may not be the same solution that minimizes  $\Phi^{\text{col}}(\hat{\Theta})$ .

- This initialization is, of course, impossible without knowledge of the nodes' true locations.
- Closest anchor initialization (from [16]):
  - If a node is connected to an anchor, the closest anchor's location is used as the initialization point for that node. If not, the average of all the neighboring nodes' initialization points is used as that node's initialization point. In the absence of any connections, that node is placed at the center of the network. In this case, by the nature of the IPPM, this node's location will remain stationary.
  - Closest anchor initialization provides an easy way to initialize nodes to locations that will provide good results. The ease of computing the closest anchor initialization points is also attractive compared to other initialization techniques [10].

### 3.4.2 Improved Initialization Techniques

The reflected and flipped initialization techniques were developed after analysis of closest anchor initialization performance showed problems that these new initialization techniques could address. The motivation for the reflected and flipped methods is found in Section 3.5.

- Reflected initialization:
  - Analogous to RPPM for the non-collaborative problem. In fully connected networks, an initialization technique such as closest anchor is used, and the minimum found by IPPM with that initialization is stored as  $\hat{\Theta}^1 = \{\hat{\theta}_1^1, \hat{\theta}_2^1, \hat{\theta}_3^1, \dots, \hat{\theta}_N^1\}$ . Next, new initialization points  $\hat{\Theta}^2$  are chosen as the reflections of each node in  $\hat{\Theta}^1$  about the centroid of the anchors. IPPM is run from the new initialization

points  $\hat{\Theta}^2$ , the solution is stored as  $\hat{\Theta}^2$ , and this reflecting process is repeated until  $\hat{\Theta}^i = \hat{\Theta}^j$ ,  $i \neq j$ , or until an iteration limit is reached.

- Flipped initialization:
  - Developed specifically to address the flip ambiguity (as shown in Figure 3.5) and the associated large RMS error found in the collaborative problem. Given a previously-found minimum (from closest anchor or reflected initializations), all nodes are flipped about a linear fit line through the anchors' locations. Then, IPPM is run from this flipped initialization point. This method need only be used when certain criteria are met such as linearity (eccentricity) of anchors being greater than 0.9 or the percentage of nodes in the anchors' convex hull being less than 21%. These criteria are discussed in Section 3.6.

### 3.5 Motivation for the Reflected and Flipped Initialization Techniques

The iterative parallel projection method suffers the same problems as any non-optimal solution method, namely the possibility of failing to find the global minimum. Just as Figure 2.4 shows the possibility of encountering multiple minima in the non-collaborative case, Figure 3.7 shows that multiple minima of  $\Phi^{\text{col}}(\hat{\Theta})$  exist. Therefore, we target the instances when IPPM settles in a non-global minimum. We observed that the IPPM returns a large RMS error value for a small subset of layouts. Our objective is to characterize the performance of the IPPM, to identify the layouts that cause IPPM to return a large RMS error value, and to provide a preliminary solution method.

### 3.5.1 Methodology for Characterization

Knowing that there are some layouts which cause IPPM to fail (as in Figure 3.4), we developed a methodology to characterize the collaborative localization problem and the performance of IPPM. We created 9000 different layouts. Each individual layout has a set of  $K$  anchors where  $K$  is uniformly distributed between 3 and 12. Each layout also has  $N$  nodes where  $N$  is uniformly distributed between 5 and 30. All node and anchor coordinates ( $x$  and  $y$ ) are uniformly distributed between -15 and 15, creating a layout where all nodes and anchors lie inside a  $30 \times 30$  meter square area. Every layout is used seven times, each time with a different noise variance based on  $K_E$ .

Thus, our methodology is to use true initialization and closest anchor initialization for the iterative parallel projection method and compare the results against each other. The layouts which cause high RMS error in closest anchor initialization as compared to true initialization are then the layouts we identify as problematic. Next, we develop a method to identify those problematic layouts using only information available to the localization problem, i.e. *not* the nodes' actual positions. Finally, we propose a method for improving the performance of IPPM, specifically targeting the aforementioned problematic layouts.

### 3.5.2 Comparison of Closest Anchor and True Initializations

Using Jia's closest anchor initialization technique (described in Section 3.4.1), a network with full connectivity (infinite radio range) will sometimes produce large RMS errors. Using the same simulated layouts, the true initialization method provides a baseline for performance. By comparing the two initialization methods' results, we understand how often it is that the closest anchor initialization method finds a non-global minimum and the impact that these wrong minima have on (average) performance.

Figure 3.1 shows the cumulative distribution function of RMS error for all 9000 layouts for both true initialization and closest anchor initialization. For this value of  $K_E$ , the RMS

error of the closest anchor method clearly is more than the true initialization method for nearly 3% of the layouts. Furthermore, when the RMS error is worse than the true-initialized RMS error, the difference is severe. This heavy tail of poor performance is what we want to target and correct.

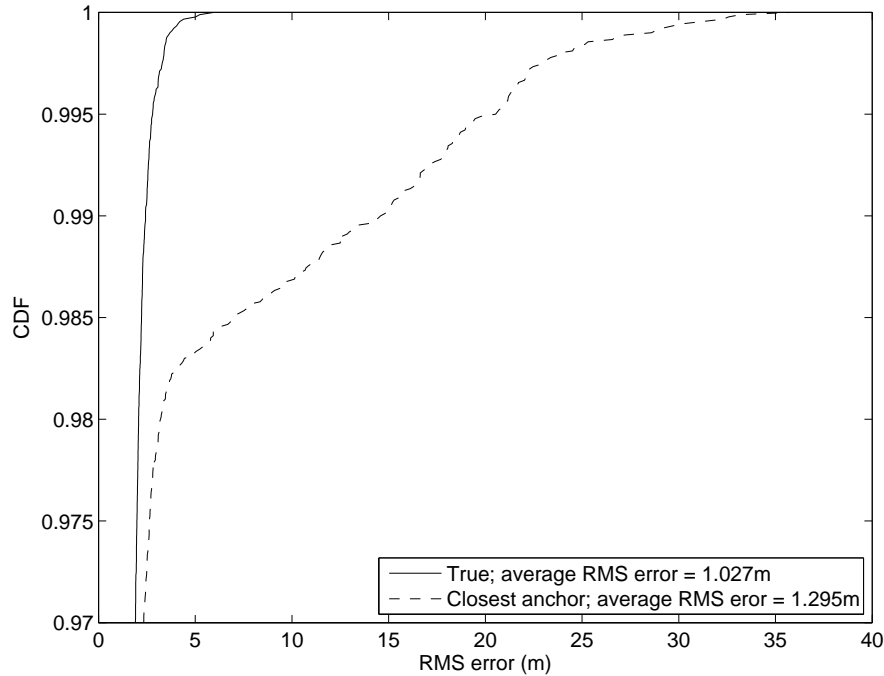


Figure 3.1: CDF of RMS error ( $K_E = 0.0144$ )

Figure 3.2 is a scatter plot of RMS error against objective value for both true and closest anchor initialization techniques for  $K_E = 0.0144$ . This representation clearly shows the instances where closest anchor initialization fails. Specifically, there is a collection of layouts with an objective value similar to the majority of other layouts but with an RMS error an order of magnitude larger.

Figure 3.3 shows the average RMS error gap between true initialization and closest anchor initialization. Figure 3.1 shows that, for  $K_E = 0.0144$ , about 2% or 3% of the layouts are causing the vast majority of the increase in average RMS error. Thus, we want to target those 2% or 3% of layouts that have considerably larger RMS error from closest anchor initialization than from true initialization. For comparison, Figure 3.15 contrasts

Figure 3.3, showing the performance of all initialization techniques.

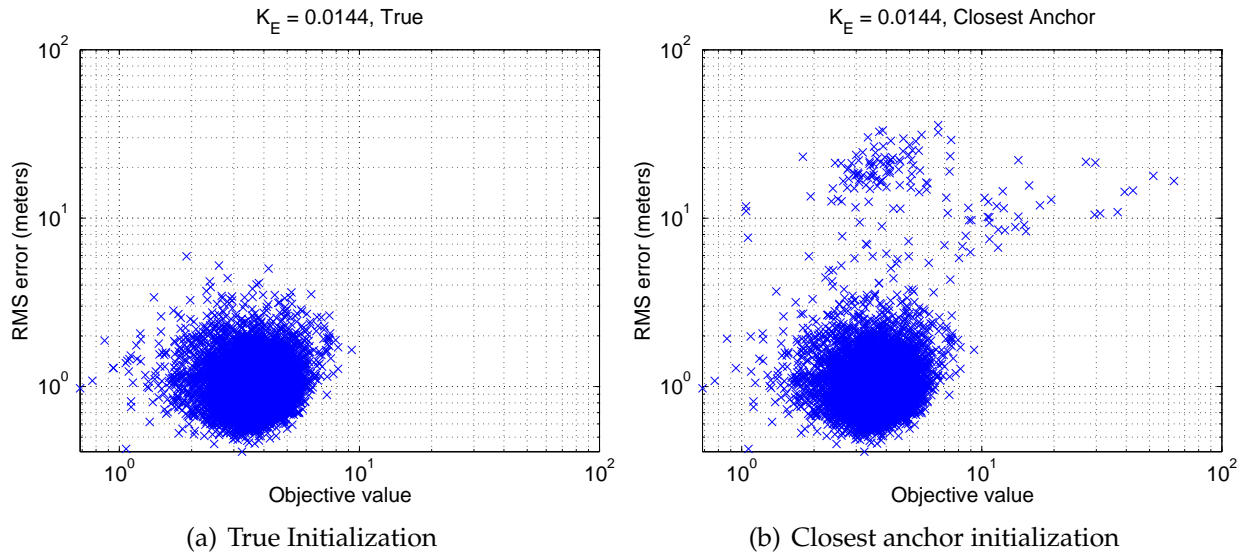


Figure 3.2: RMS error against objective value

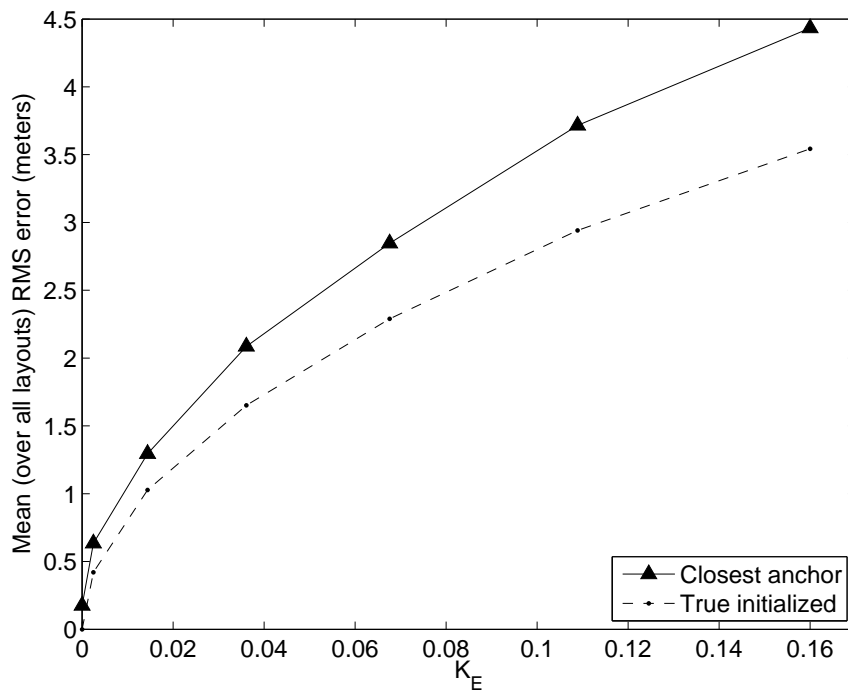


Figure 3.3: Mean RMS error against  $K_E$  for closest anchor and true initializations

Figure 3.4 shows the poor performance of IPPM with closest anchor initialization for a specific layout. The node in the bottom right hand corner is obviously far away from its actual location and is contributing heavily to the RMS error.

Similarly, in Figure 3.5, the closest anchor initialization finds a minimum of  $\Phi^{\text{col}}(\hat{\Theta})$  with a large RMS error  $\Omega = 17.00\text{m}$  while the true initialization method finds a much better minimum. Note here that the two objective values (3.64 for closest anchor and 3.57 for true) are extremely close while the RMS errors are vastly different. The type of whole-network flip ambiguity shown in Figure 3.5 is what the flipped initialization technique is designed to address.

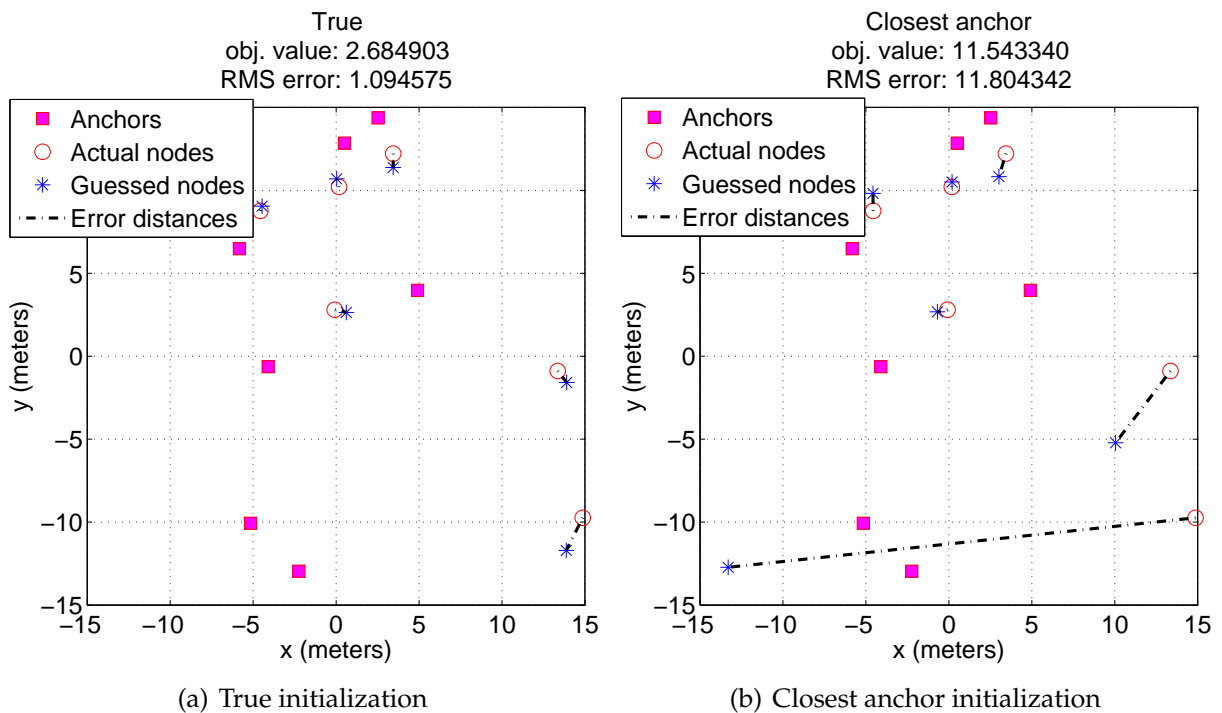


Figure 3.4: Example layout where closest anchor initialization fails ( $K_E = 0.0144$ )

Figure 3.6 shows the likelihood of the closest anchor initialization method settling on the same minimum as the true initialization method. The measure of when a minimum is equal to another is whether all the distances between the gussed node locations are

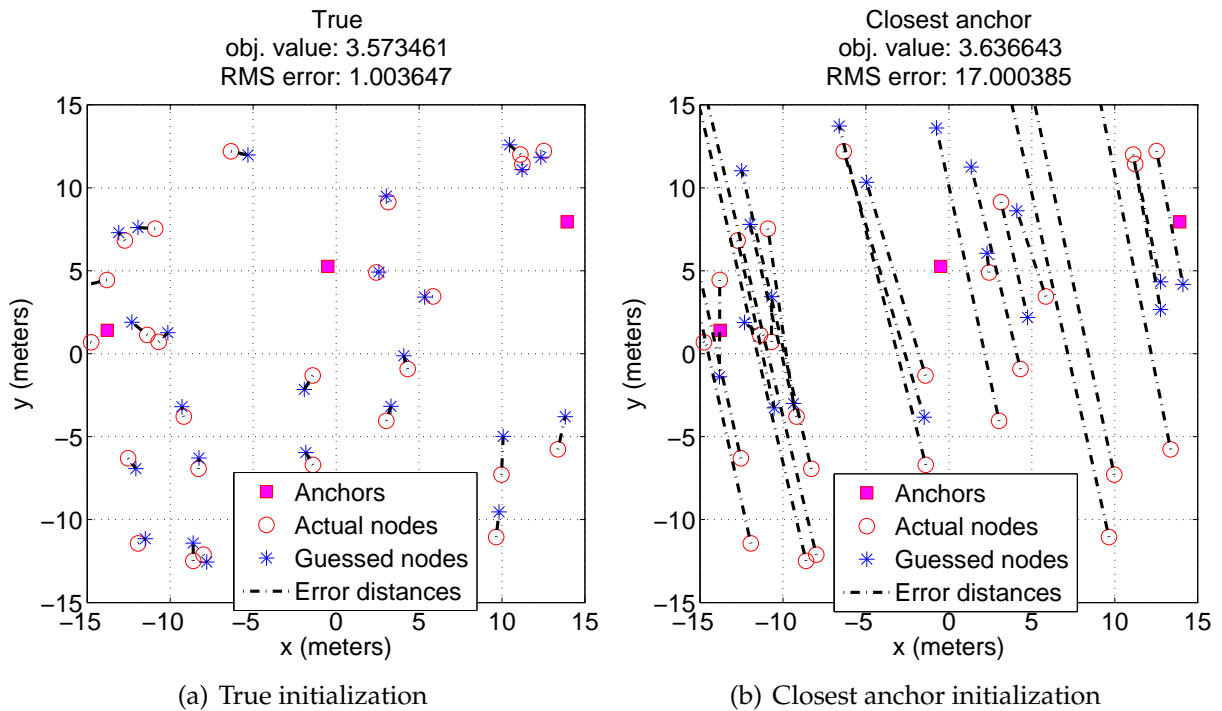


Figure 3.5: Example layout with small objective value and large RMS error ( $K_E = 0.0144$ )

less than 5cm or 10cm. In general, as  $K_E$  increases, the likelihood of the closest anchor initialization method finding the global (true-initialized) minimum becomes slightly less. Depending upon the tolerance level chosen, the likelihood is about 75% or 85% for lower values of  $K_E$ . Focusing on the 5cm tolerance case, we see from Figure 3.1 that only about 3% of the time, the RMS error returned by the closest anchor method is much worse than the true initialization method. However, Figure 3.6 shows that 25% of the time, all nodes are not within 5cm of the true-initialized nodes. Therefore, we conclude that there are instances (about 22% of layouts) when the closest anchor method finds a minimum different than that of the true initialized method but when the RMS error is only slightly increased.

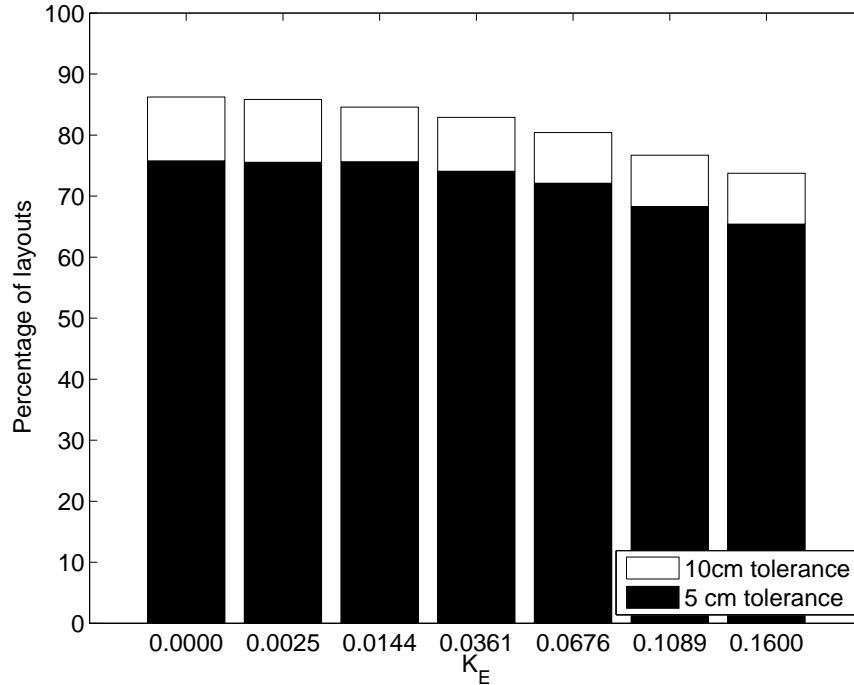


Figure 3.6: Percentage of layouts where closest anchor found same minimum as true

### 3.5.3 Experimental Evaluation of Number of Minima of $\Phi^{\text{col}}(\hat{\Theta})$

As shown in Figures 2.6 and 2.7, the propensity of layouts to produce multiple minima in the non-collaborative problem causes most of the problems when solving  $\Phi^{\text{ncl}}(\hat{\theta})$  with iterative methods. Similarly, multiple minima (solutions) are possible for  $\Phi^{\text{col}}(\hat{\Theta})$ . In Figure 3.7 we plot the number of minima experimentally found for all layouts and  $K_E$  values for 0% NLOS situations. We counted the number of minima by running IPPM with all initialization techniques described in Section 3.4 and then using random initializations until a total of 12 was reached. The solutions found by all initialization techniques were compared against one another. If any particular node (over all solutions) was found to have multiple solution locations, the maximum number of different node locations was returned as the number of minima. Figure 3.7 is indicative of the number of minima likely for collaborative layouts. However, IPPM is not guaranteed to converge to the exact same solution for different initializations, and it is difficult to delineate which solutions are the

same as one another and which are the same. Our method was to count a solution as different from another if any node is more than 10cm away from its counterpart in another solution.

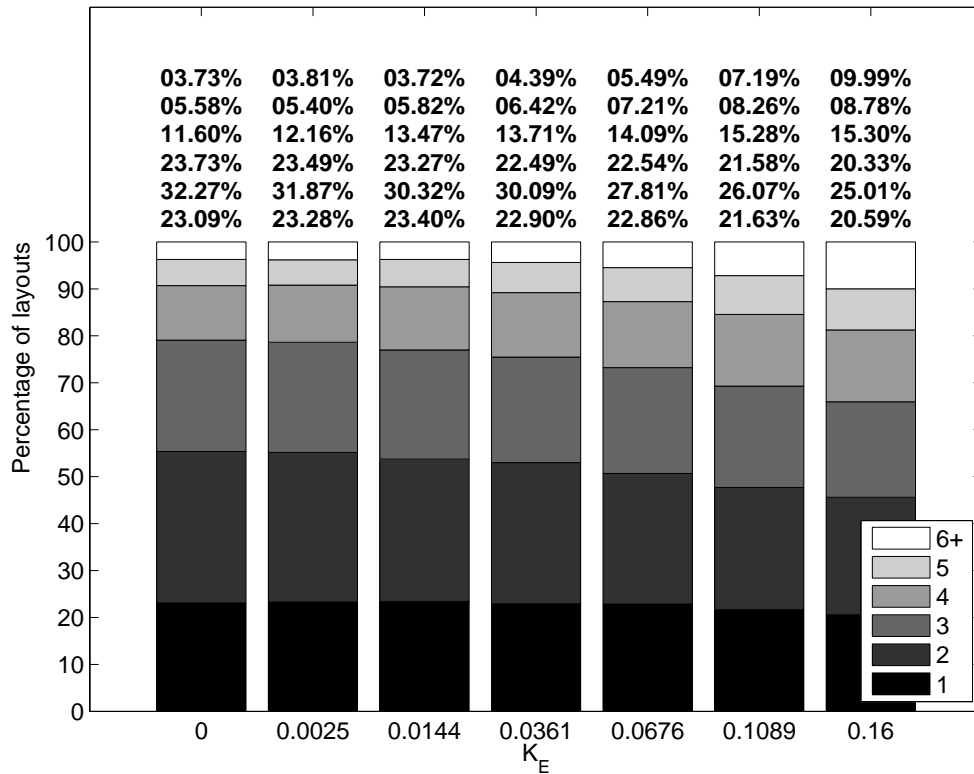


Figure 3.7: Number of minima found experimentally using IPPM

Figure 3.8 shows the same data for  $K_E = 0.0144$  separated by the number of anchors or nodes that appear in each layout. The two left hand bars plot the number of minima found when the number of anchors is  $\leq$  or  $>$  5 while the two right hand bars divide on the number of nodes ( $\leq$  and  $>$  9). Understandably, the probability of a layout having only one minimum increases with more anchors. However, it is interesting to note that layouts with more nodes have a lower probability of having only one minimum than those layouts with fewer nodes. This characteristic is most likely due to the increased possibility of neighbors of nodes moving with the increased number of nodes. This increased variability in the layout probably leads to more minima.

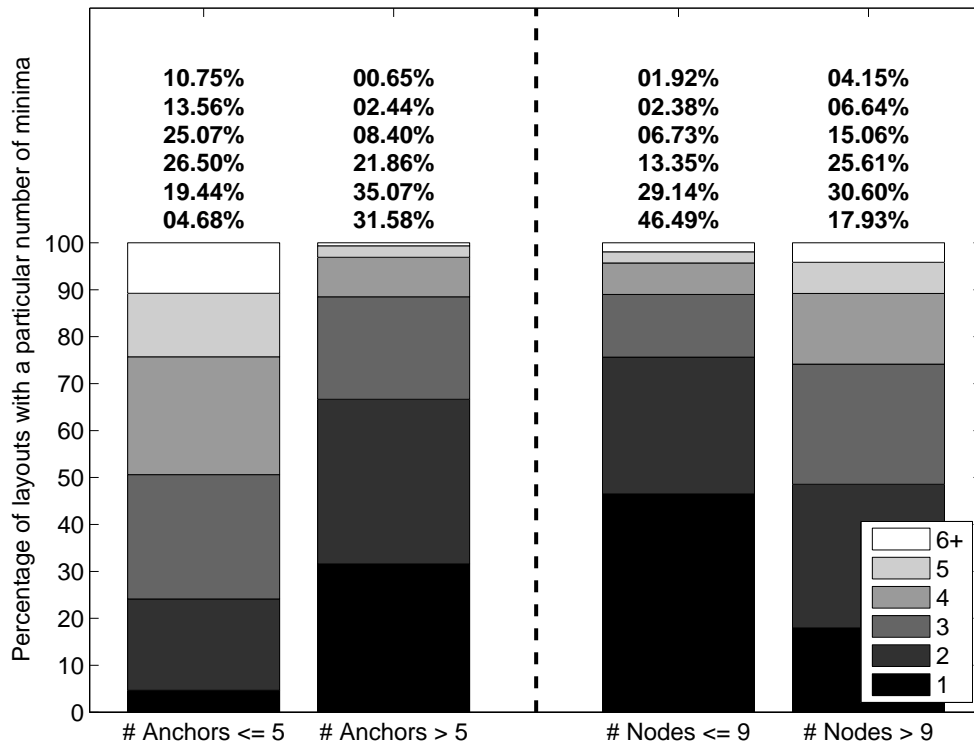


Figure 3.8: Number of minima found experimentally using IPPM, separated by number of anchors/nodes ( $K_E = 0.0144$ )

### 3.5.4 Summary of Motivations

In summary, the motivation for developing new initialization techniques is found in Figures 3.1 - 3.3. These figures show a distinct gap in the RMS error  $\Omega$  returned by the closest anchor initialization and the true initialization. Figures 3.4 and 3.5 show the types of layouts which are causing problems. In Section 3.6, we address the issue of identifying those layouts which are likely to cause large RMS error with only knowledge of the anchors' locations and the node location estimates.

### 3.6 Identification of Problematic Layouts

Figure 3.2 provides the data necessary to target those layouts which are most problematic, the layouts with small objective values but large RMS errors. This figure shows that objective value is not linearly related to RMS error. In other words, it is possible to have a reasonable objective value (about  $1\text{m}^2$ - $10\text{m}^2$ ) like the majority of layouts but an RMS error value of nearly  $40\text{m}$ , far away from the normal range ( $0\text{m}$ - $3\text{m}$ ). To get a better idea of what layouts caused these errors, we plotted each layout with an objective value less than  $10\text{m}^2$  and an RMS error greater than  $10\text{m}$ . An example of these layouts is shown in Figure 3.5. All of those layouts had the same characteristics: high colinearity of the anchors and all or most of the nodes flipped about the anchors. From this observation and from the knowledge gained from characterizing the non-collaborative problem, it proved helpful to plot RMS error against the colinearity of the anchors and against the percentage of nodes inside the convex hull of the anchors.

Figure 3.9 shows the relationship between RMS error, linearity of the anchors, and percentage of nodes inside the convex hull of the anchors. Clearly, layouts with high anchor colinearity and/or low percentage of nodes  $P$  inside the anchors' convex hull are generally the same layouts that cause high RMS error. We use eccentricity, a measure of linearity of a set of points, to measure the colinearity of the anchors. Eccentricity is defined by Stojmenovic in [32] as

$$\text{eccentricity} = \beta = \frac{\sqrt{(\mu_{20} - \mu_{02})^2 + 4\mu_{11}^2}}{\mu_{20} + \mu_{02}}, \quad (3.6)$$

where  $\mu_{pq} = \sum_{i=1}^K (x_i - x_c)^p (y_i - y_c)^q$  are the second order moments of the set of anchors  $A$ . Here,  $K$  is the number of anchors, and  $\{x_c, y_c\}$  are the coordinates of the center of mass of  $A$ . The center of mass is the average of the coordinates of  $A$ . Eccentricity ranges on the interval  $[0, 1]$ , where an eccentricity measure of zero indicates a circle, and an eccentricity

measure of one indicates a line. The author of [32] describes the eccentricity measure (equivalent to rotational correlation) as follows:

If we consider the  $x$  and  $y$  values of points in a space separately and apply correlation, we can directly measure linearity. We first find the center of mass of the set of points along with its orientation. In this algorithm, the curve in question is rotated so that its new orientation is at an angle of  $45^\circ$  from the  $x$  axis. Correlation is then done on the rotated curve. The linearity measure is the absolute value of the measured correlation of points  $(x_i, y_i)$  on the rotated curve.

Using Figure 3.9 as a guide, we can accurately identify the problematic layouts by eccentricity or the percentage of nodes inside the anchors' convex hull. The advantage to using only the eccentricity measure is that it requires minimal effort to obtain. Equation 3.6 shows that, to obtain the eccentricity value, only a few simple averages, sums, and squared terms are required. Conversely, calculating the convex hull of the set of anchors and discovering whether or not a node estimate is inside that convex hull is more complicated. However, using the percentage of nodes inside the convex hull is more tailored to the specific minimum found, while using only the eccentricity of the anchors uses no information about the minimum found. The connection between the two measures is that anchors with high eccentricity are going to cause nodes to fall outside their convex hull with a higher probability than anchors with low eccentricity.

From Figure 3.9, we filtered those layouts that had an eccentricity greater than 0.9 ( $\beta > 0.9$ ) or less than 21% of nodes inside the convex hull of the anchors ( $P < 21$ ). Figure 3.10 shows, in circles, those layouts which meet either of the above criteria. While a large portion of false-positives are also included in this group, nearly all the layouts with high RMS error are identified using this method.

In Section 3.7, we discuss the solution techniques for remedying the layouts' performance

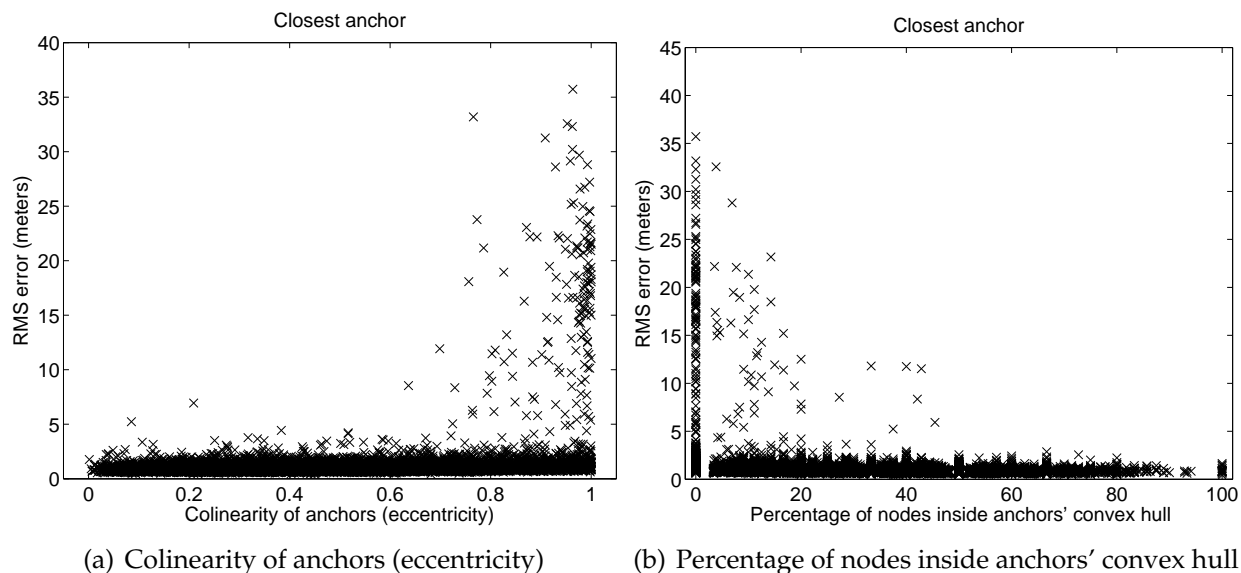


Figure 3.9: RMS error

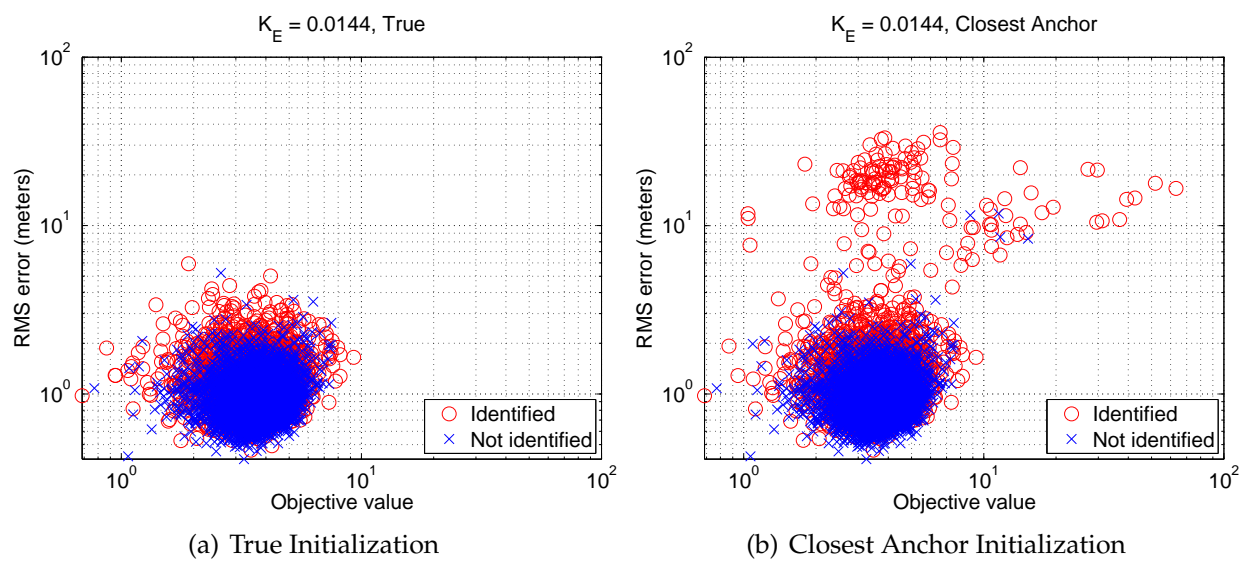


Figure 3.10: RMS error against objective value

with high RMS error  $\Omega$ . Section 3.7.2 discusses performance when using identification techniques described in this section.

## 3.7 Solution Proposition for Problematic Layouts

As with any iterative solution method, the initialization point affects performance. While an increasing number of initialization points usually decreases error, intelligently choosing initialization points saves computation time and power. By observing the layouts causing large RMS errors, we found that flip ambiguities (like those shown in Figure 3.5) cause most of the large RMS errors. Thus, we developed two new initialization techniques, explained in Section 3.4.2. The reflected initialization method creates new initialization points by reflecting nodes about the centroid of the anchors, and the flipped initialization method creates a new initialization point by flipping nodes about a line fit through the anchors' locations. While reflection and flipping are the same operation, we distinguish the two initialization methods by using *reflect* for translating all nodes across the centroid of the anchors and by using *flip* for translating all nodes across a linear fit through the anchors.

### 3.7.1 Improvement from Additional Initialization Techniques

This section compares the performance of all our available initialization techniques. The initialization techniques are described in Section 3.4. The same 9000 layouts were used here, but three different realizations of NLOS noise were tested. Respectively, in the three different cases, there is a 0%, 10%, and 80% chance that a given connection will be non-line of sight (NLOS). For NLOS connections, the added NLOS bias is uniformly distributed between 1m and 10m. Using this data, we show that our improved initialization techniques provide lower RMS error values consistently for 0% and 10% NLOS simulations and nearly always for 80% NLOS.

The nomenclature includes  $\beta$  for eccentricity and  $P$  for the percentage of nodes inside the convex hull of the anchors.

Figures 3.11 - 3.13 show that the additional initialization techniques significantly reduce  $\Omega$  compared to the closest anchor initialization. The dotted line represents the error from true initialization. Solid lines represent reflected initializations while dashed lines represent closest anchor initializations.

The flipped initialization technique is also used. To compare the effect of using the flipped initialization, two different original solutions of  $\min \{ \Phi^{\text{col}}(\hat{\Theta}) \}$  were used as the starting point for flipping, the closest anchor solution and the solution with the lowest objective value from the the reflected initialization technique. In both cases, using the flipped initialization technique provided performance improvement, and using flipped initialization starting with the solution from the reflected method gave the best results.

To highlight the fact that the solution with the lowest objective value does not guarantee the lowest RMS error, plotlines labeled “Best from” denote that the solution with the minimum RMS error  $\Omega$  have been plotted. With our given information, it is impossible to identify which of the two solutions (flipped or non-flipped) gives the minimum  $\Omega$ . However, these “Best from” plotlines show that we have narrowed the solution space to exactly two solutions, one of which is shown on the “Best from” plot. Therefore, if a third party could distinguish the lowest RMS error from only these two solutions, these “Best from” plotlines’ performance could be achieved.

The following two plotlines (square and diamond) display  $\Omega$  when, given the same two minima described above, the one with the lowest objective value is chosen. Clearly, performance degrades when only using the objective value to distinguish between solutions. This underscores our observation that objective value does not fully determine  $\Omega$ . The final two plotlines (asterisk and star) show the RMS error when only reflections or just the closest anchor initializations are used.

Figure 3.13 (with 80% NLOS connections) shows that performance of all initialization techniques degrades as the probability of links being NLOS increases. Not only is  $\Omega$  larger overall, but some initialization techniques which provided better performance than

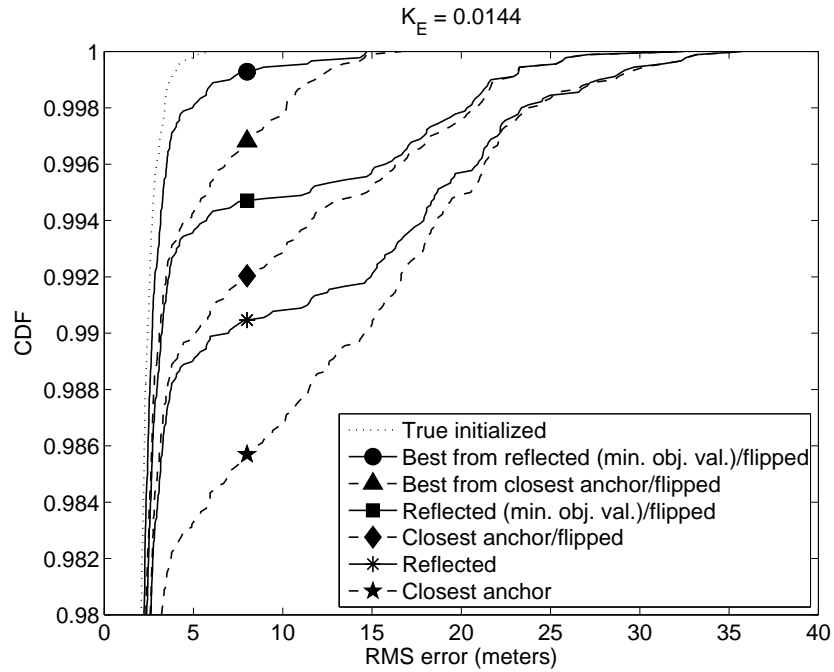


Figure 3.11: CDF of RMS error for additional initialization techniques, 0% NLOS

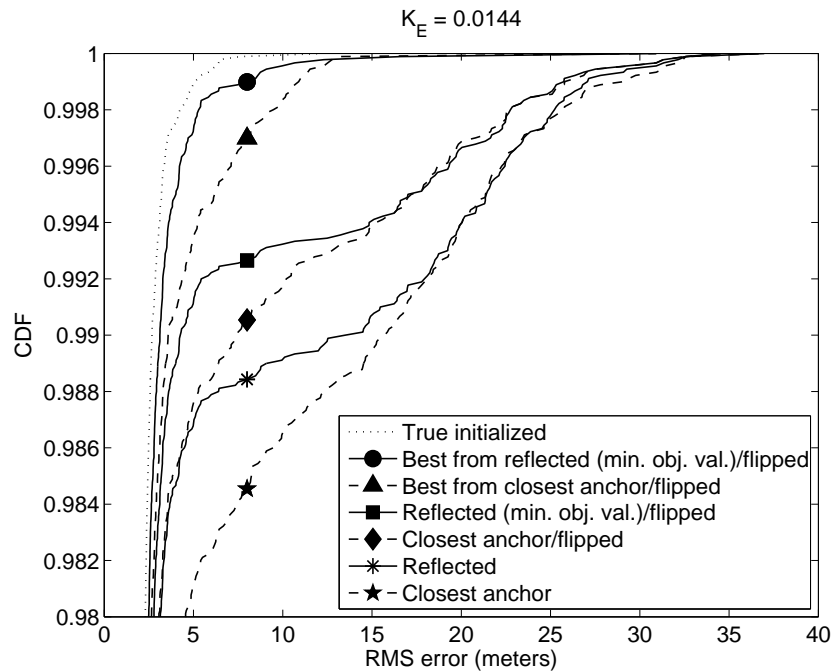


Figure 3.12: CDF of RMS error for additional initialization techniques, 10% NLOS

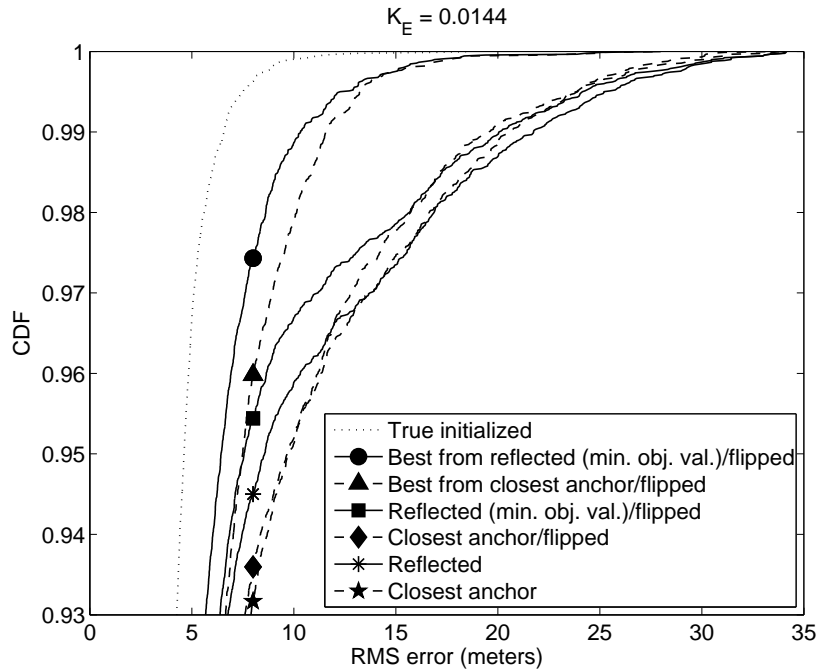


Figure 3.13: CDF of RMS error for additional initialization techniques, 80% NLOS

others in Figures 3.11 and 3.12 no longer are always better. For instance, the closest anchor initialization technique in the 80% NLOS case exceeded performance of the reflected method when  $\Omega > 15\text{m}$ . This is due to the fact that the reflected method finds a solution with a lower objective value than the closest anchor method, but, because of noise, the solution with the minimum objective value does not have the lowest RMS error. Here again, minimum objective value, especially in the presence of high noise, does not always lead to minimum RMS error.

Figure 3.14 shows the same RMS error data as in Figure 3.11. In Figure 3.14, the data is plotted against objective value to give a graphical representation of the improvement gained by each initialization technique for all simulated layouts. The plots are in order (a-f) of decreasing performance (increasing RMS error), with the closest anchor initialization technique at the bottom. Figure 3.14 shows, again, that the reflected method (along with the flipping initialization) performs better than the closest anchor initialization method.

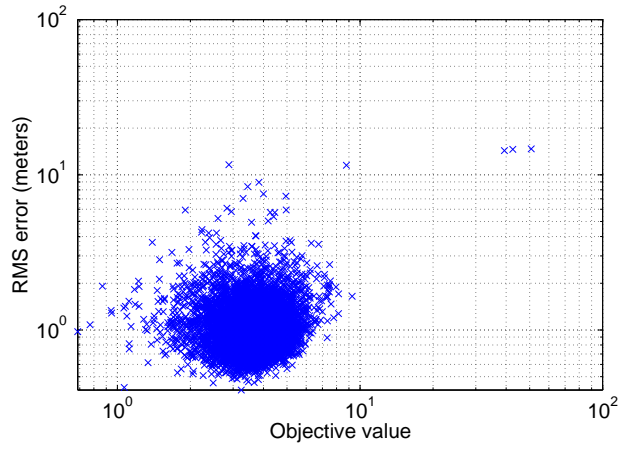
Figures 3.15-3.17 show that the performance of all initialization techniques is consistent across varying values of noise variance (from  $K_E$ ) and different probabilities of NLOS noise.

Figure 3.18 highlights the fact that, across all initialization techniques, the differences between the objective values returned are much less pronounced than the difference between RMS errors (Figure 3.15), again underlining what is shown in Figure 3.14: Solutions with similar objective values may have vastly different RMS errors.

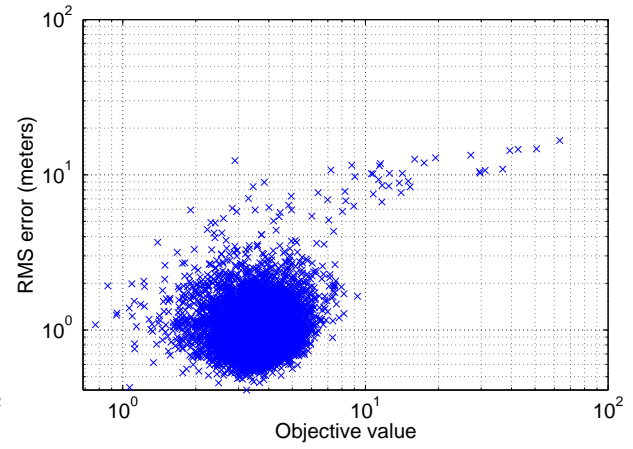
### 3.7.2 Performance Using Identification

To reduce computation requirements, the identification technique described in Section 3.6 is used here, and results of performance when the flipped initialization is used *only* on identified layouts are shown in Figures 3.19 - 3.22.

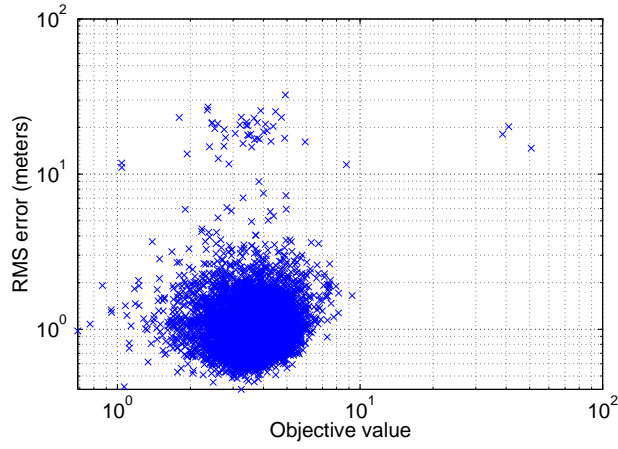
Figures 3.19-3.22 show the performance gained by using the flipped initialization technique. In the first two plots, the comparison of flipping all layouts as opposed to flipping only those identified by  $\beta > 0.9$  is shown. The advantage of only flipping the identified layouts is that only 7% of layouts are identified (as shown in Figure 3.24), and the remaining 93% do not require additional computation. Figures 3.21 and 3.22 show the same trends for identification defined by  $\beta > 0.9 \cup P < 21$ . Here, even though all layouts are not identified, performance of flipping all layouts is nearly indistinguishable from flipping only identified layouts. These plots confirm that the identified layouts are the layouts with the largest RMS errors and that all layouts do not require flipping.



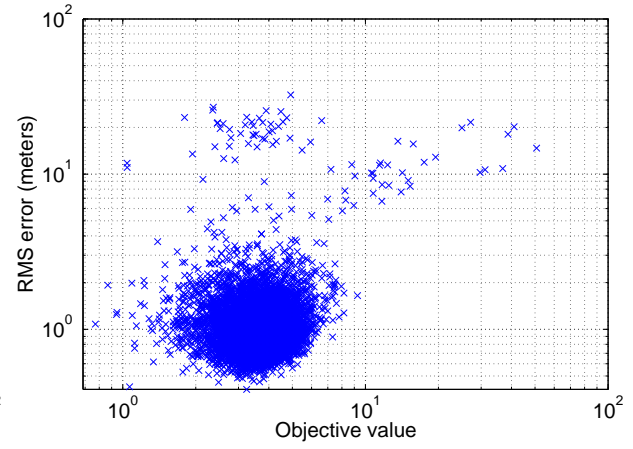
(a) Best of reflected (min. obj. value)/flipped



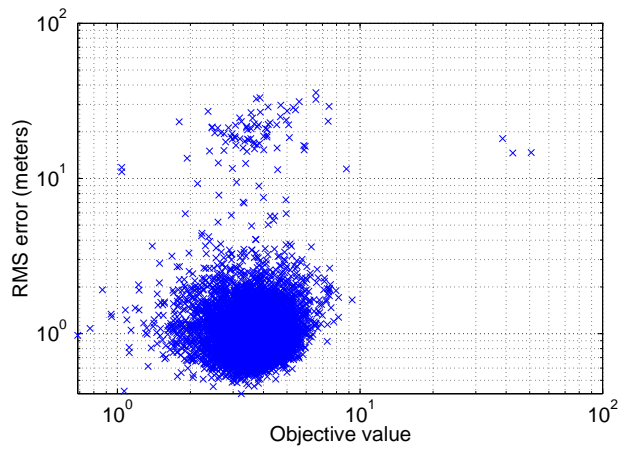
(b) Best of closest anchor/flipped



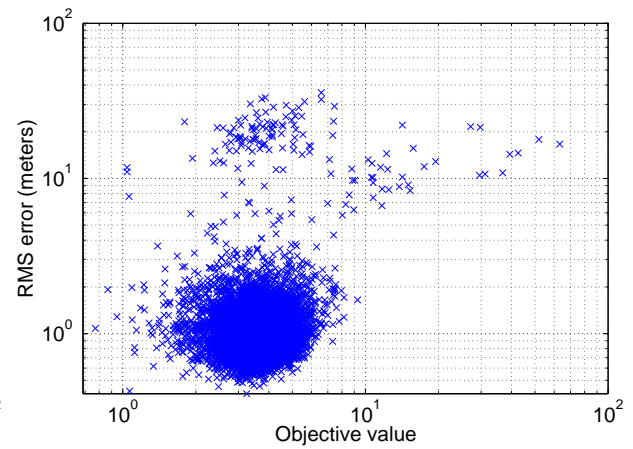
(c) Reflected (min obj. value)/flipped



(d) Closest anchor/flipped



(e) Reflected



(f) Closest anchor

Figure 3.14: RMS error against objective value ( 0% NLOS )

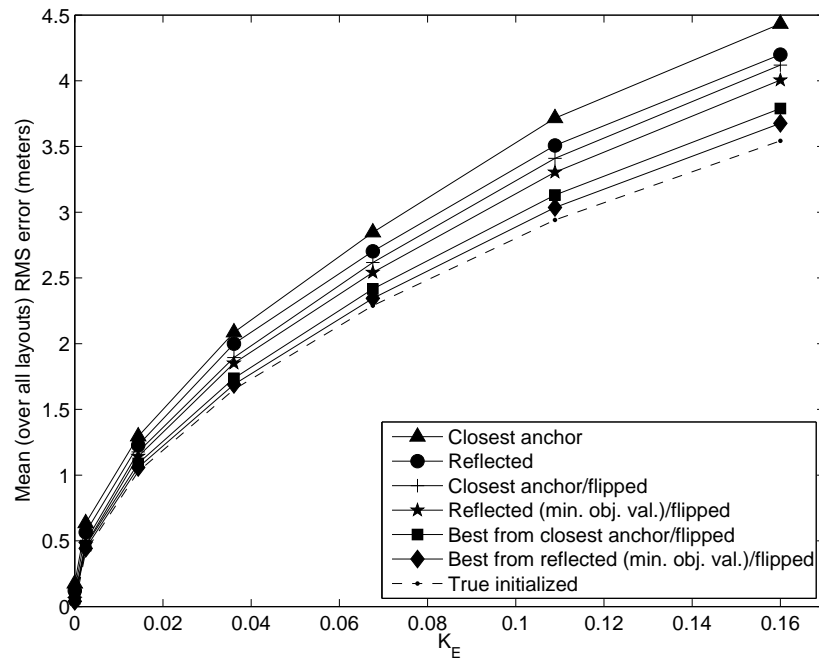


Figure 3.15: Mean RMS error against  $K_E$  for all initialization techniques ( 0% NLOS )

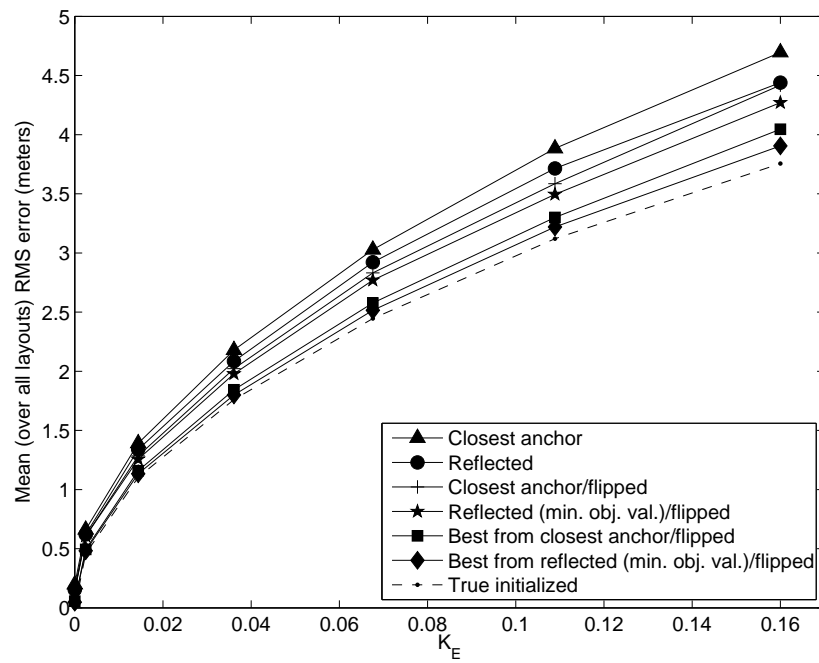


Figure 3.16: Mean RMS error against  $K_E$  for all initialization techniques ( 10% NLOS )

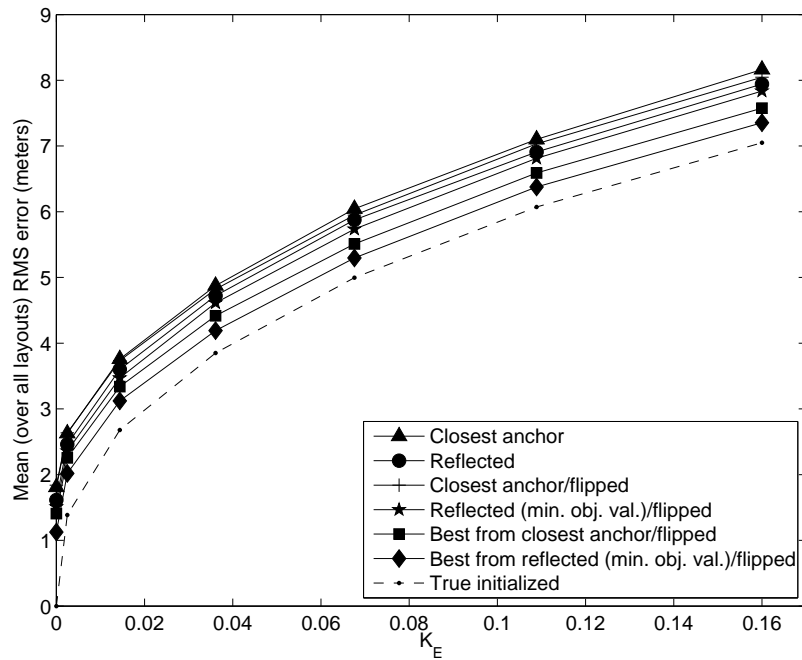


Figure 3.17: Mean RMS error against  $K_E$  for all initialization techniques ( 80% NLOS )

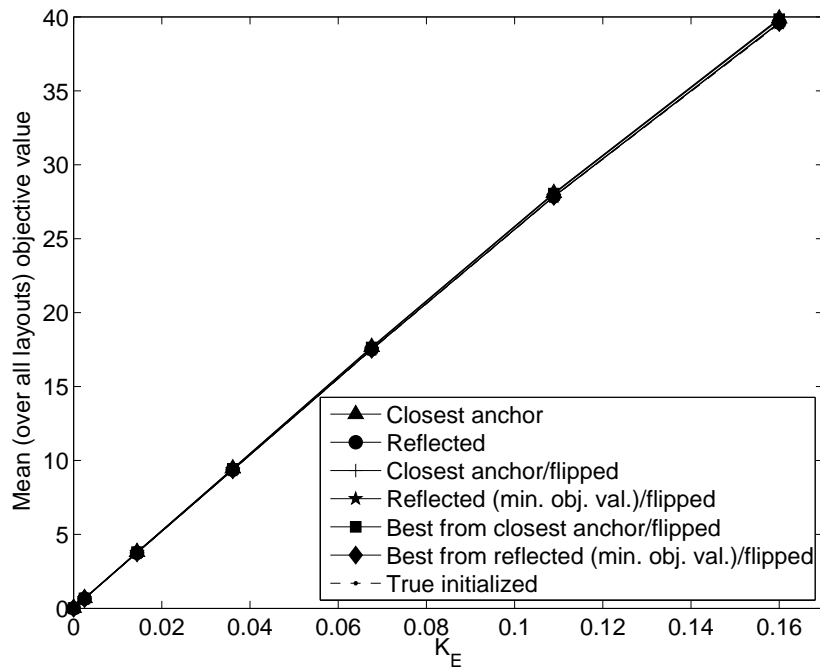


Figure 3.18: Mean  $\Phi^{\text{col}}(\hat{\Theta})$  against  $K_E$  for all initialization techniques ( 0% NLOS )

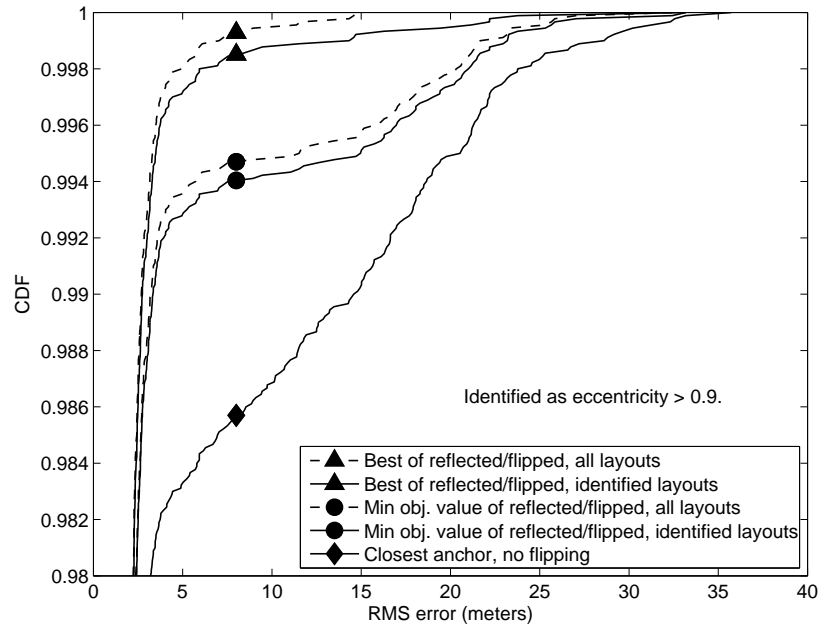


Figure 3.19: Identification improvement (  $\beta > 0.9$ , 0% NLOS )

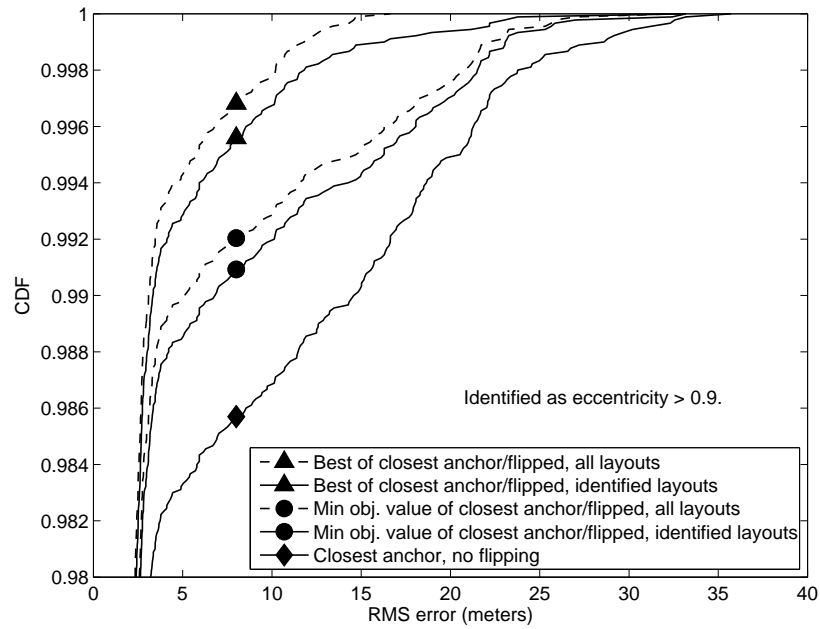


Figure 3.20: Identification improvement (  $\beta > 0.9$ , 0% NLOS )

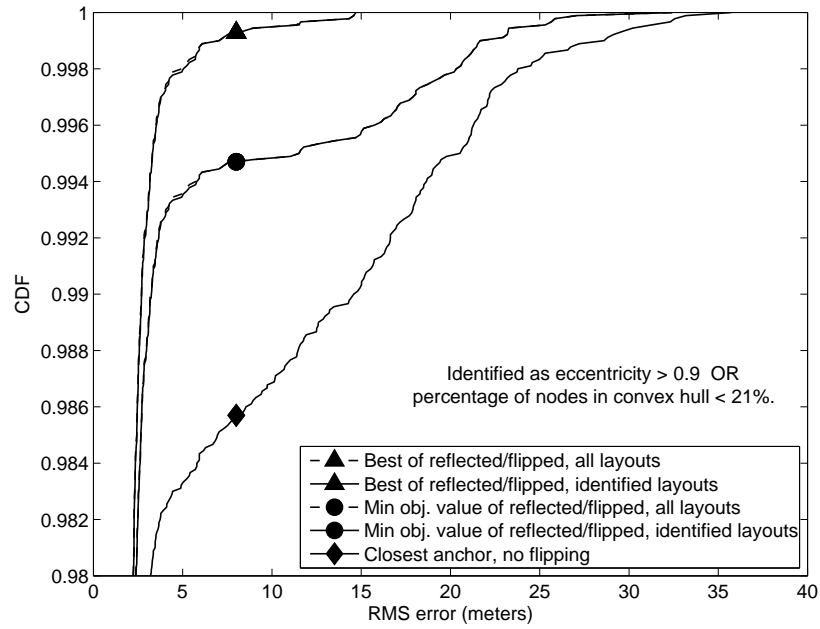


Figure 3.21: Identification improvement ( $\beta > 0.9 \cup P < 21, 0\% \text{ NLOS}$ )

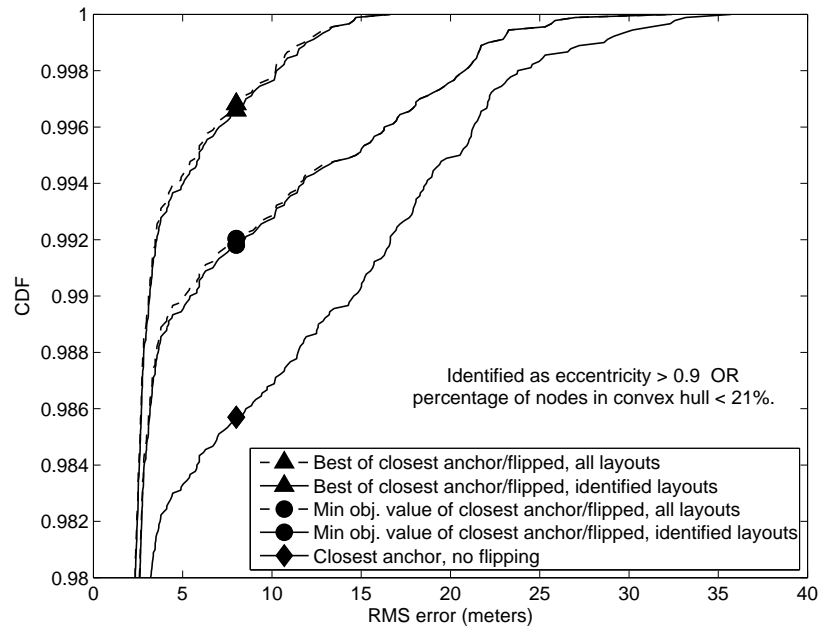


Figure 3.22: Identification improvement ( $\beta > 0.9 \cup P < 21, 0\% \text{ NLOS}$ )

Figure 3.23 shows the CDF of the eccentricity of all layouts. It shows that if the identification criterion is only that eccentricity  $\beta > 0.9$ , only about 7% of the layouts meet this criterion. If we use  $P$ , the percentage of node estimations inside the convex hull, as an additional identification criterion, Figure 3.24 shows the percentage of layouts identified by either criteria.

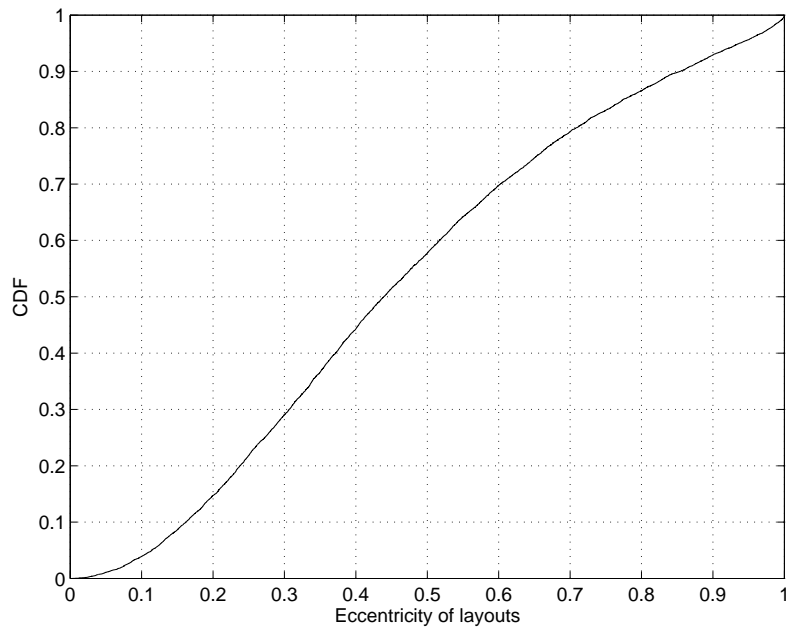


Figure 3.23: CDF of eccentricity of layouts

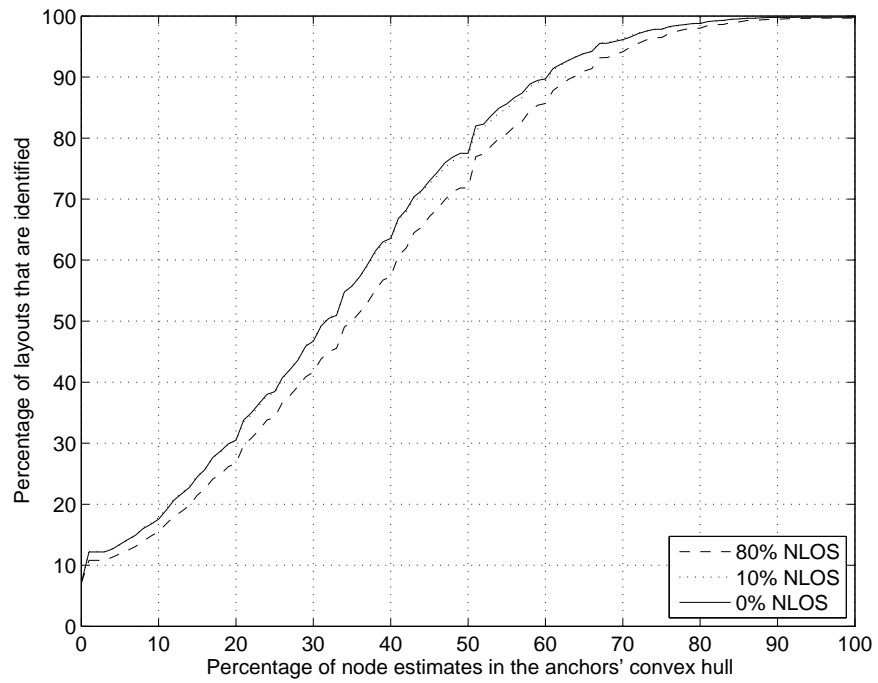


Figure 3.24: Identification of layouts by eccentricity and percentage of node estimations in anchors' convex hull

# Chapter 4

## Measurement Campaign

Throughout our simulations, we have assumed a Gaussian model for LOS noise on range estimates and uniformly distributed NLOS noise. This measurement campaign confirms that, for the particular radios used in measurements, LOS range estimate noise can accurately be modeled as Gaussian. It also shows that NLOS noise, for our test cases, varies inconsistently, and, while being difficult to model, adds importance to techniques robust against NLOS noise. Thus, the results in Figures 3.12 (10% NLOS) and 3.13 (80% NLOS) are notable in that our new initialization methods still provide noticeable reductions in  $\Omega$  above and beyond closest anchor initialization in the presence of our simulated NLOS noise.

### 4.1 Introduction

This chapter describes a measurement campaign executed in the Spring 2011 semester. ENSCO, Inc., provided two prototype radios for range finding. The radios are designed to use 22 MHz of bandwidth at a center frequency of 915 MHz [34] to measure the time-of-flight between the two radios and return a distance. The exact manner in which this

is accomplished is described in articles from ENSCO [35, 34]. In short, coarse timing is accomplished by synchronizing on a special word in the transmission payload. This method achieves an nominal accuracy of 6.8m [34]. Fine timing is achieved by correlating oversampled received and transmitted pseudorandom sequences. This oversampling allows for an estimation of the exact peak of correlation, and this peak gives the radios their fine timing resolution.

### **4.1.1 Format of the Chapter**

This chapter explains the purpose and design of the measurement campaign in Section 4.1. Section 4.2 describes the manner in which calibration was calculated, followed by Sections 4.3 and 4.4, which detail the indoor measurements performed in Durham Hall. Section 4.5 describes the negative effect that multipath components can have on measurements, and overall conclusions are found in Section 4.6. Appendix B shows the raw data collected and the associated empirical probability density functions for each data set.

### **4.1.2 Purpose**

The purpose of our measurement campaign was two-fold:

- to characterize ranging performance so as to better simulate noise (error) in range estimates
- to provide ENSCO with feedback regarding the performance of their radios

### **4.1.3 Data Reported by the Radios**

At a rate of 217 Hz, as long as the radios are able to communicate, the originator records an uncalibrated distance value along with other pieces of data associated with each

distance value. “Coarse count” is a value that records the approximate time-of-flight using number of clock cycles. In keeping with ENSCO’s practices, coarse count values that are less than zero or above 1000 are labeled as erroneous, and the associated distance values are discarded.

#### 4.1.4 Terminology

originator	The ENSCO radio that connects to the computer
transponder	The remote ENSCO radio
location pair	One static location each for the originator and the transponder
scenario	A collection of location pairs in the same vicinity,
data set	A collection of measurements from one location pair
group	A collection of data sets consecutively gathered in one scenario
calibration distance	The positive bias amount on uncalibrated measurements
around the corner dist.	The distance between the radios along a right triangle

#### 4.1.5 Consistent Measurement Practices

Throughout this report, multiple measurement scenarios are described. In all scenarios, the following hold true.

- The longer omni-directional antenna was connected directly to the originator, and the shorter omni-directional antenna was connected directly to the transponder.
- Estimated distance values from one location pair were obtained by
  - filtering measurements from one data set by only keeping data where  $0 \leq \text{coarse count} \leq 1000$ , consistent with ENSCO’s practices.

- taking the mean or median of the filtered data set, with the difference being noted where applicable.
  - subtracting the calibration distance
- All measurements were calibrated using the calibration distance described in Section 4.2.
  - Care was taken to minimize obstructions (other than permanent obstructions) between the radios as the radios are particularly sensitive to them.
  - True distance was measured using a laser range finder and (when needed) a laser T-square (right angle tool). The laser range finder was compared to a tape measure and found to be consistent with the tape measure within 5mm at distances of 3, 6, 9, and 30m. The T-square was not measured for accuracy. The literature about the T-square advertises an accuracy within 1/16in at 20ft (within 0.014921 degrees). To calculate the angle, we find the inverse tangent of  $\frac{1/16\text{in}}{20 \times 12\text{in}}$ , giving us  $260 \times 10^{-6}$  radians =  $14.921 \times 10^{-3}$  degrees.

## 4.2 Calibration

### 4.2.1 Purpose

The ENSCO radios provide a distance value based upon time-of-flight. The measured propagation delay between antennas is what yields the distance estimate; the propagation delay through the radio hardware provides a large positive bias. The purpose of calibration is to account for the time of propagation through both the originator and the transponder's hardware as well as other system delays. Thus, the calibration distance is the amount subtracted from the uncalibrated measurements to yield the calibrated distance.

### 4.2.2 Scenario Setup

To accomplish calibration, the radios were taken to the Drillfield on Virginia Tech's campus, an open, outdoor area. The originator was mounted on top of a stand measuring 0.889m (35in), and the transponder was mounted on top of a stand measuring 0.864m (34in). The originator and transponder both remained stationary for each measurement. For each measurement, the originator was "stopped" and "restarted" using the "stop" and "go" buttons on the originator. Each measurement was taken using a Bosch laser range finder from the front of the originator's casing to the front of the transponder's casing. All measurements were line-of-sight (LOS). Twelve originator/transponder location pairs were used for this calibration. Figure 4.1 shows the approximate locations of the originator and transponder for the calibration scenario.

At least three data sets were taken for each location pair, and for each location pair, each of the three data sets was consistent with the others. Each measurement was obtained from approximately two minutes worth of gathered data. The results of the calibration measurement campaign can be seen in Figures 4.2 and 4.3.

Because the measurements at each location pair are so similar, the plotted circles for each location pair in Figures 4.2 and 4.3 overlap each other. The calibration distance was chosen as the value that minimized the total deviation from true distance of the nine location pairs that are aligned linearly. Measurements taken from location pairs T7, T8, and T9, near 19m and near 38m, noticeably deviate from the majority of other measurements, so data from those location pairs was ignored for calibration purposes. The y-axis of Figures 4.2 and 4.3 shows the distance recorded from the radios *after* adjusting using the calculated calibration distance, 1635.453m.

Figure 4.4 shows the error of all calibration measurements after having been calibrated. This shows an error less than 0.5m for the majority of measurements. Recall that the measurements with nearly 3m of error were ignored when calculating the calibration

distance. The measurements with high error are from location pairs T7, T8, and T9. A possible explanation for these discrepancies is discussed in Section 4.2.3.

Because the radios were used with the same antennas throughout this measurement campaign, it was assumed that this calibration distance was accurate for all measurements.

The small error in the line-of-sight calibration measurements highlights the radios' good performance in an open, LOS environment. Table 4.1 summarizes the results of the calibration scenario and shows that the radios achieved an accuracy of 7cm at a range of 28m and an accuracy of 50cm at a range of 62m. The kurtosis values found in Table 4.1 are explained in Section 4.2.4.

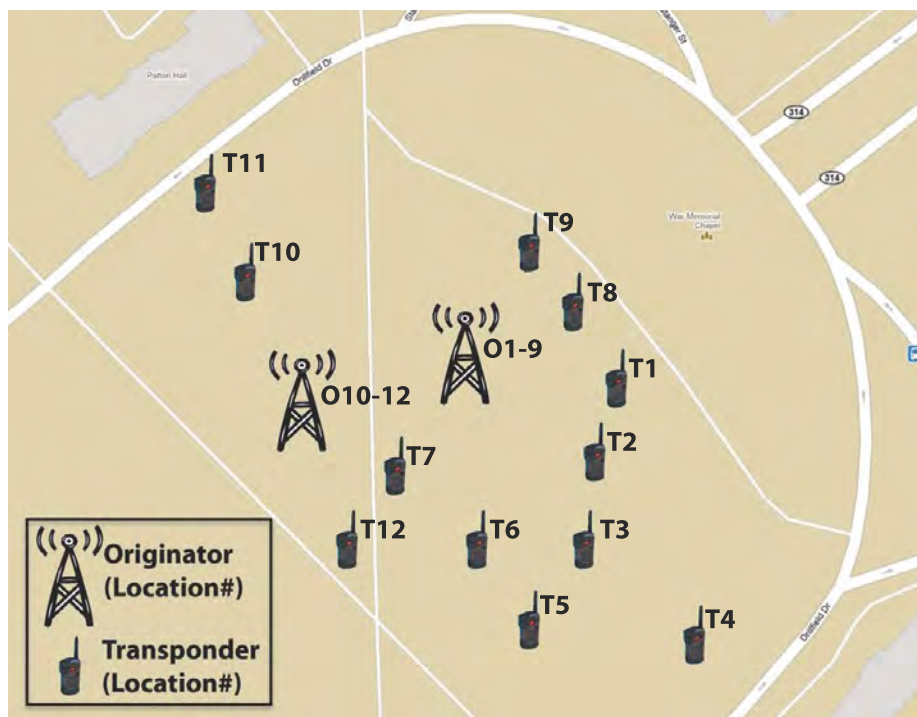


Figure 4.1: Calibration scenario (on the Drillfield)

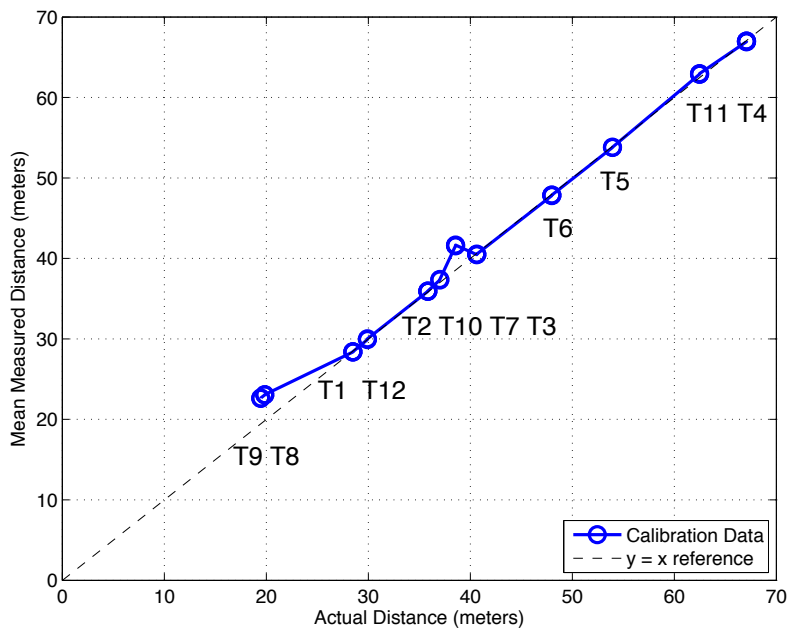


Figure 4.2: Calibration group, mean measurements

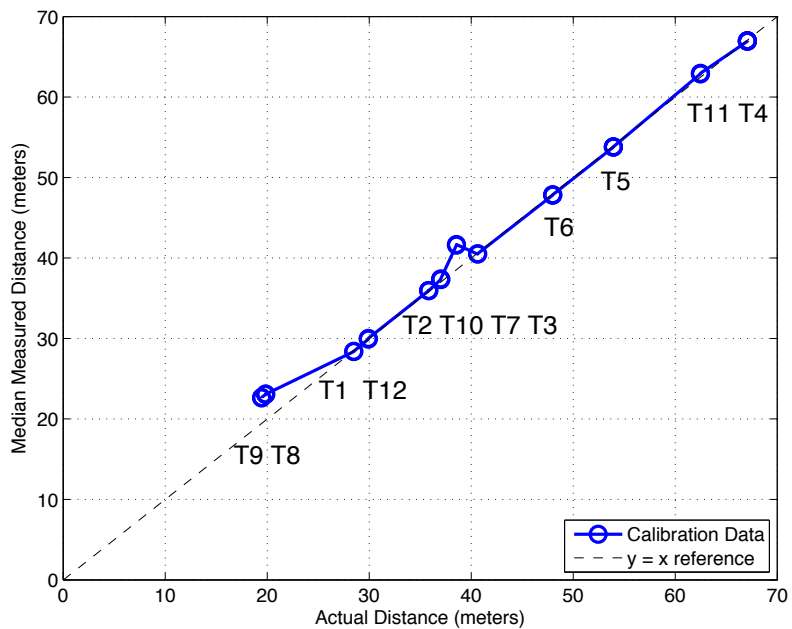


Figure 4.3: Calibration group, median measurements

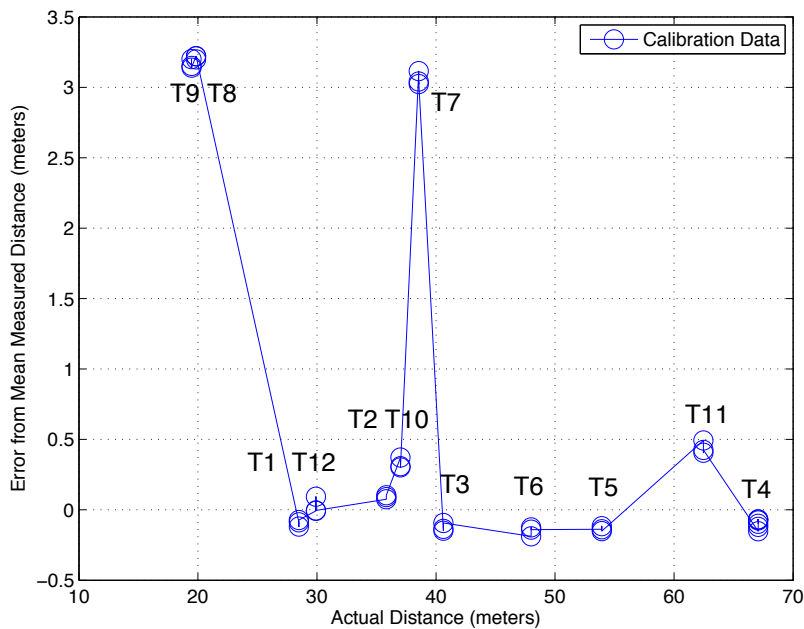


Figure 4.4: Calibration group error (mean)

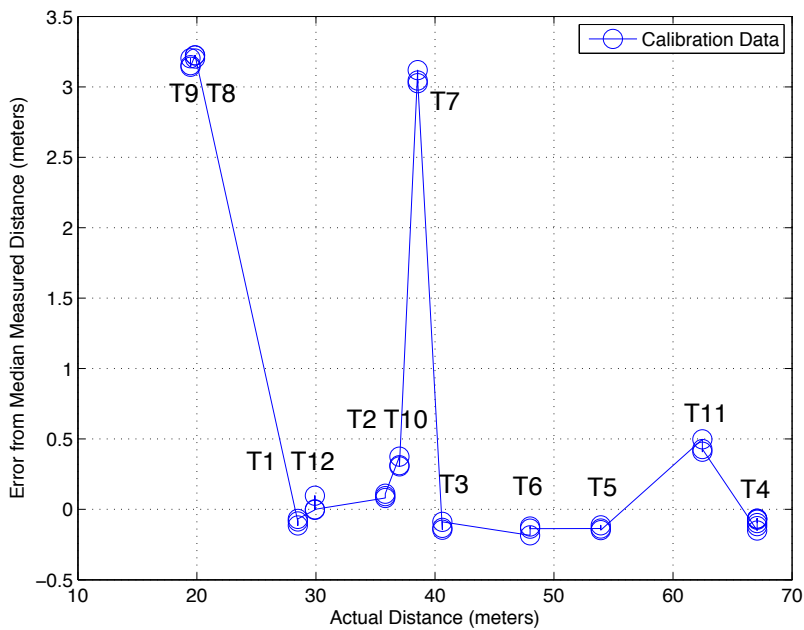


Figure 4.5: Calibration group error (median)

Table 4.1: Calibration Statistics

Label	Kurtosis		Std. Dev.	Distance			Error		
	Pair/Grp.	Unfiltered		Filtered	Mean	Median	Actual	Mean	Median
T1/1		0.5720	—	0.2750	28.3946	28.4081	28.48	-0.09	-0.07
T1/2		0.3239	—	0.2958	28.3659	28.3724	28.48	-0.11	-0.11
T1/3		1.2922	—	0.2869	28.4125	28.4106	28.48	-0.07	-0.07
T2/1		0.3935	—	0.3501	35.9106	35.9399	35.83	0.08	0.11
T2/2		0.3422	—	0.2931	35.9245	35.9631	35.83	0.09	0.13
T2/3		0.2078	—	0.3423	35.9409	35.9488	35.83	0.11	0.12
T3/1		-0.1181	—	0.2638	40.4755	40.4865	40.62	-0.14	-0.13
T3/2		0.0111	—	0.2668	40.4890	40.4913	40.62	-0.13	-0.13
T3/3		0.2060	—	0.2847	40.5311	40.5414	40.62	-0.09	-0.08
T4/1		4.6409	-0.0824	0.2130	66.9202	66.9262	67.07	-0.15	-0.14
T4/2		-0.1215	—	0.1931	66.9510	66.9511	67.07	-0.12	-0.12
T4/3		1.5529	—	0.2167	67.0029	67.0136	67.07	-0.07	-0.06
T4/4		11.7690	0.5682	0.1373	66.9962	66.9971	67.07	-0.07	-0.07
T4/5		410.3820	0.2557	0.1942	67.0042	67.0053	67.07	-0.07	-0.06
T4/6		6.9970	0.3862	0.2202	66.9731	66.9844	67.07	-0.10	-0.09
T5/1		5.9516	0.6934	0.2587	53.7942	53.8000	53.93	-0.14	-0.13
T5/2		0.1734	—	0.2532	53.8166	53.8250	53.93	-0.11	-0.10
T5/3		19.7971	1.5133	0.2523	53.7826	53.7707	53.93	-0.15	-0.16
T6/1		0.0744	—	0.2760	47.8056	47.8050	47.99	-0.18	-0.19
T6/2		0.1566	—	0.2158	47.8681	47.8629	47.99	-0.12	-0.13
T6/3		0.0333	—	0.2981	47.8527	47.8474	47.99	-0.14	-0.14
T7/1		0.1895	—	0.2650	41.6685	41.6806	38.55	3.12	3.13
T7/2		0.1729	—	0.2704	41.5759	41.5866	38.55	3.03	3.04
T7/3		0.9184	—	0.2377	41.5948	41.6021	38.55	3.04	3.05
T8/1		0.4277	—	0.2344	23.0632	23.0810	19.84	3.22	3.24
T8/2		0.1140	—	0.2167	23.0412	23.0497	19.84	3.20	3.21
T8/3		0.7007	—	0.2254	23.0640	23.0726	19.84	3.22	3.23
T9/1		-0.1328	—	0.1932	22.6143	22.6153	19.46	3.15	3.16
T9/2		0.1817	—	0.1949	22.6633	22.6682	19.46	3.20	3.21
T9/3		0.6168	—	0.2167	22.6027	22.6145	19.46	3.14	3.15
T10/1		0.7918	—	0.2283	37.3847	37.4005	37.01	0.37	0.39
T10/2		0.3647	—	0.2565	37.3235	37.3314	37.01	0.31	0.32
T10/3		0.4849	—	0.2273	37.3152	37.3218	37.01	0.31	0.31
T11/1		1.1751	—	0.3893	62.9671	62.9574	62.47	0.50	0.49
T11/2		9.6962	0.1296	0.3189	62.8795	62.8822	62.47	0.41	0.41
T11/3		0.6117	—	0.3109	62.8984	62.9025	62.47	0.43	0.43
T12/1		0.4337	—	0.3344	29.9068	29.9131	29.91	-0.00	0.00
T12/2		0.2584	—	0.3095	30.0068	30.0159	29.91	0.10	0.11
T12/3		0.6608	—	0.3128	29.9100	29.9184	29.91	-0.00	0.01
Average		12.37	0.42	0.26				0.74	0.75
Range		410.51	1.69	0.25				3.41	3.43

### 4.2.3 Possible Cause of Calibration Error: Destructive Interference

The discrepancy between the calibration distances yielded by locations pairs T7, T8, and T9 might have been caused by destructive interference. Because T8 and T9 are almost exactly half the distance of T7 from the originator, we investigate the possibility that T7, T8, and T9 happened to be distances that caused destructive interference due to ground bounce according to the two-ray model.

Here,  $h_1 = 0.889\text{m}$  and  $h_2 = 0.864\text{m}$  are the heights of the stands on which the radios were placed. Because it is not obvious which values of  $h$  to use for the two-ray model, we use the stand heights  $h_1$  and  $h_2$  plus a variable height  $\delta$ . The added height  $\delta$  can also account for the variable elevation of the Drillfield as well as inconsistencies in the ground as a reflecting surface.

$M$  is the LOS distance between the radios as measured with the laser range finder.  $M = \{38.55, 19.84, 19.46\}\text{m}$  for T7, T8, and T9, respectively. The multipath distance  $D = d_1 + d_2$ , as shown in Figure 4.6. The angle of incidence  $\theta$  equals the angle of reflection, and from this, we develop the ratio  $(D - M)/\lambda$ , the ratio between the extra distance traveled by the multipath component (compared to the LOS component) and the wavelength.

Assuming frequency  $f = 2.4\text{GHz}$  and  $c$  as the speed of light, wavelength  $\lambda = c/f = 0.1249135\text{m}$ .

Angle of reflection equals angle of incidence.

$$\cos(\theta) = \frac{l_1}{d_1} = \frac{l_1}{\sqrt{h_1^2 + l_1^2}} \quad \cos(\theta) = \frac{l_2}{d_2} = \frac{L - l_1}{d_2} = \frac{L - l_1}{\sqrt{h_2^2 + (L - l_1)^2}}$$

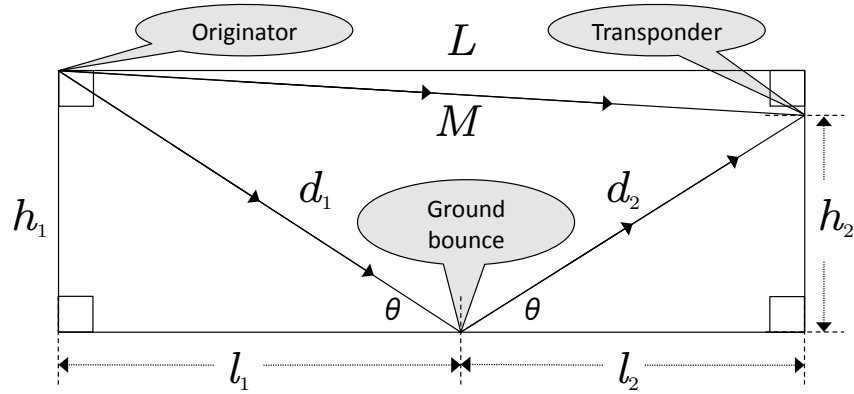


Figure 4.6: Ground bounce diagram

Solving for  $l_1$  and  $l_2$ .

$$\cos(\theta) = \frac{l_1}{\sqrt{h_1^2 + l_1^2}} = \frac{L - l_1}{\sqrt{h_2^2 + (L - l_1)^2}} \quad (4.1)$$

$$l_1^2 (h_2^2 + (L - l_1)^2) = (L - l_1)^2 (h_1^2 + l_1^2) \quad (4.2)$$

$$l_1^2 \left( \frac{h_2^2}{(L - l_1)^2} + 1 \right) = h_1^2 + l_1^2 \quad (4.3)$$

$$\frac{h_2^2 l_1^2}{(L - l_1)^2} = h_1^2 \quad (4.4)$$

$$l_1 h_2 = h_1 L - h_1 l_1 \quad (4.5)$$

$$l_1 (h_2 + h_1) = L h_1 \quad (4.6)$$

$$l_1 = \frac{L h_1}{h_1 + h_2} \quad (4.7)$$

$$l_2 = L - l_1 = L - \frac{L h_1}{h_1 + h_2} = L \left( 1 - \frac{h_1}{h_1 + h_2} \right) = L \left( \frac{h_2}{h_1 + h_2} \right) = \frac{L h_2}{h_1 + h_2} \quad (4.8)$$

Solving for  $d_1$  and  $d_2$  in terms of  $L$ ,  $h_1$ , and  $h_2$ .

$$\begin{aligned} d_1 &= \sqrt{h_1^2 + l_1^2} = \sqrt{h_1^2 + \left(\frac{L h_1}{h_1 + h_2}\right)^2} = \sqrt{\frac{h_1^2 (h_1 + h_2)^2 + h_1^2 L^2}{(h_1 + h_2)^2}} \dots \\ &\dots = \sqrt{\frac{h_1^2}{(h_1 + h_2)^2} ((h_1 + h_2)^2 + L^2)} = \sqrt{L^2 + (h_1 + h_2)^2} \left(\frac{h_1}{h_1 + h_2}\right) \end{aligned} \quad (4.9)$$

$$\begin{aligned} d_2 &= \sqrt{h_2^2 + l_2^2} = \sqrt{h_2^2 + \left(\frac{L h_2}{h_1 + h_2}\right)^2} = \sqrt{\frac{h_2^2 (h_1 + h_2)^2 + h_2^2 L^2}{(h_1 + h_2)^2}} \dots \\ &\dots = \sqrt{\frac{h_2^2}{(h_1 + h_2)^2} ((h_1 + h_2)^2 + L^2)} = \sqrt{L^2 + (h_1 + h_2)^2} \left(\frac{h_2}{h_1 + h_2}\right) \end{aligned} \quad (4.10)$$

Solving for  $D$ , the distance traveled by the multipath wave.

$$\begin{aligned} D = d_1 + d_2 &= \sqrt{L^2 + (h_1 + h_2)^2} \left(\frac{h_1}{h_1 + h_2}\right) + \sqrt{L^2 + (h_1 + h_2)^2} \left(\frac{h_2}{h_1 + h_2}\right) \dots \\ &= \sqrt{L^2 + (h_1 + h_2)^2} \left(\frac{h_1 + h_2}{h_1 + h_2}\right) = \sqrt{L^2 + (h_1 + h_2)^2} \end{aligned} \quad (4.11)$$

Substituting for  $L^2$  in terms of  $M$ , the actual distance between the originator and transponder.

$$L^2 = M^2 - (h_1 - h_2)^2 \quad (4.12)$$

$$\implies D = \sqrt{M^2 - (h_1 - h_2)^2 + (h_1 + h_2)^2} = \sqrt{M^2 + 4 h_1 h_2} \quad (4.13)$$

Adding variable extra height  $\delta$  to  $h_1$  and  $h_2$ .

$$D \Big|_{h_1=h_1+\delta; h_2=h_2+\delta} = \sqrt{M^2 + 4(h_1 + \delta)(h_2 + \delta)} \quad (4.14)$$

The expression for  $D$  in Equation 4.11 is verified in Rappaport's *Wireless Communications: Principles and Practice* [36] in his Section 4.6, but a derivation is not found there.

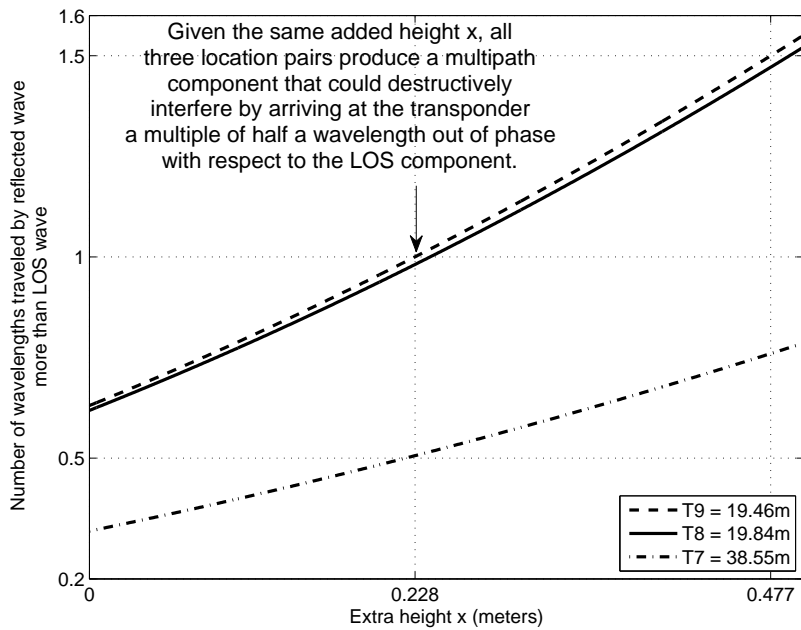


Figure 4.7: Destructive interference

Figure 4.7 plots  $(D - M)/\lambda$ , the number of extra wavelengths that the reflected wave travels with respect to the LOS wave, against  $\delta$  and shows that, with the same additional height  $\delta$  added to both  $h_1$  and  $h_2$ , the ground-bounce wave from location pairs T7, T8, and T9 will arrive a multiple of half a wavelength out of phase with respect to the LOS wave when  $\delta = 0.228\text{m}$ . The wave in T7 arrives at the transponder after having traveled one half wavelength extra while the waves in T8 and T9 both travel one wavelength further than the LOS wave.

Incorporating the assumed perfect reflectivity of the ground into the model, the reflected wave should be  $180^\circ$  out of phase with the incident wave, meaning that a reflected wave traveling an integer number of extra wavelengths would then be exactly out of phase. Accordingly, the wave in T7 traveling one half wavelength extra would have its phase corrected by the reflection and thus arrive in phase with respect to the LOS wave. The obvious discrepancy of the measurements from T7, T8, and T9 with respect to the other calibration location pairs might be explained by destructive interference, but the fact that, according to the simplified ground-bounce model, either T7 waves or T8 and T9 waves would arrive at the transponder out of phase, but not both, makes explaining the outlier calibration measurements difficult.

Other factors besides simple reflection could play a part in explaining the calibration measurements. The method for determining the time instant that the wave arrives, the possibility of reflected waves from the War Memorial Chapel, and the variations in the Drillfield's surface all could affect the accuracy of the calibration measurements from location pairs T7, T8, and T9.

The reason for the discrepancy between T7, T8, and T9 measurements from the rest of the calibration group is not fully known, but destructive interference from ground bounce as explained by the two-ray model is likely. Because of this, those data sets (from location pairs T7, T8, and T9) were ignored when determining the correct calibration distance.

#### **4.2.4 Gaussian Approximation for LOS Noise**

The probability distributions of data sets can help characterize the error expected from a given, one-shot distance measurement with the radios. The cleanest distributions are produced in open, LOS environments such as the Drillfield scenario. The data sets used for calibration of the radios were taken in that type of an environment, and their empirical probability density functions (PDFs) can be accurately modeled as Gaussian distributions.

Each of the measurements in Figure 4.2 was taken as the mean of one data set. The PDF of each of the data sets used in the calibration is plotted in Figure 4.8. The  $x$ -axis represents the error (after calibration), such that the hope would be to have each curve centered at zero (i.e., we hope that the estimator is unbiased). The  $y$ -axis represents the empirical PDF as estimated from a histogram.

Figure 4.8 shows the Gaussian-like curves displayed by the empirical PDFs for the calibration data sets.

Figures B.1 - B.39 show the individual calibration data sets and the associated empirical PDFs along with the kurtosis value for each. The kurtosis is defined as

$$\frac{E \{x - \mu\}^4}{\sigma^4} - 3, \quad (4.15)$$

where  $E \{x\}$  is the expected value of  $x$ , and  $\mu$  and  $\sigma$  are the mean and standard deviation of  $x$ , respectively. The Gaussian distribution has a kurtosis value of zero. More outlier-prone distributions have higher kurtosis values, and less outlier-prone distributions have kurtosis values below zero. Thus, the kurtosis is often used as a measure of the “Gaussianity” of a particular distribution. Figure 4.9 shows the kurtosis values for all calibration data sets. Using unfiltered data, some kurtosis values are extraordinarily high due to obviously incorrect distance measurements. Also plotted are the kurtosis values for the calibration data sets when obviously incorrect outlier measurements are discarded. (In particular, the measurements from location pairs T4-Groups 1, 4, 5, and 6; T5-Groups 1 and 3; T11-Group 2 were filtered. Figures B.10, B.13, B.14, B.15, B.16, B.18, and B.35 show the unfiltered data sets along with the limits used for filtering.) The drastic difference in some kurtosis values shows that, when outliers are discarded, the kurtosis values for open, LOS data sets are quite low. Figure 4.9 shows that kurtosis values for the filtered calibration data sets are very near zero with a range less than 1.8, suggesting the suitability of the Gaussian approximation for LOS noise. Thus, we conclude that the

ranging error of the ENSCO radios in open, LOS scenarios can accurately be modeled as zero-mean Gaussian.

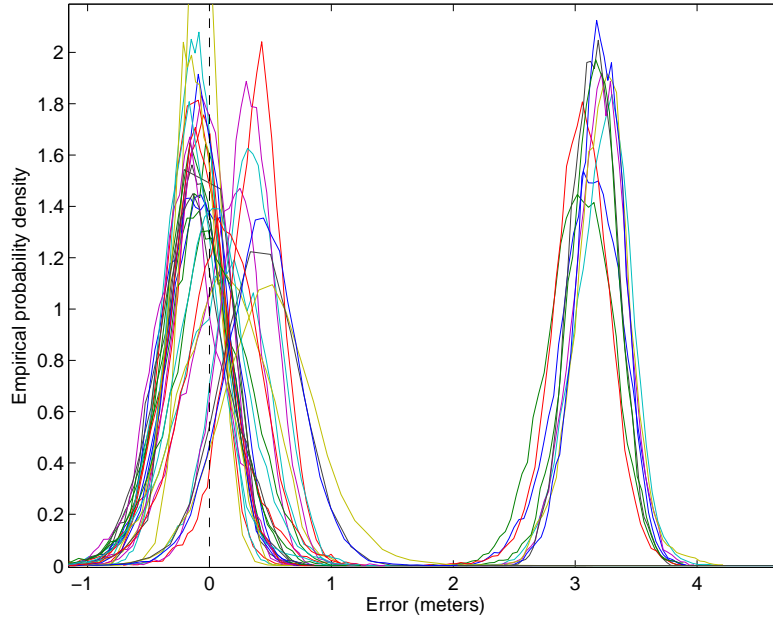


Figure 4.8: PDFs of calibration data sets

#### 4.2.5 Standard Deviations of Data Sets

For modeling LOS noise, we use a variance of noise set by the formula  $K_E d_{ij}^{\beta_{ij}}$ , where  $K_E$  is a noise constant,  $d_{ij}$  is the actual distance between point  $i$  and point  $j$ , and  $\beta_{ij}$  is the path loss exponent (held at 2 for LOS noise). This makes the variance (and the standard deviation) of the noise dependent upon the distance of the measurement, and here, we demonstrate that this model may be inaccurate based on these specific radios' measurements. Figure 4.10 plots the standard deviations of all calibration data sets (filtered to remove outliers as for the filtered kurtosis analysis) against the actual distance at which the measurements were taken. No clear trend exists relating standard deviation to actual distance. In fact, the minimum standard deviation from all these data sets is from the largest actual distance, indicating that these particular radios are fairly equally

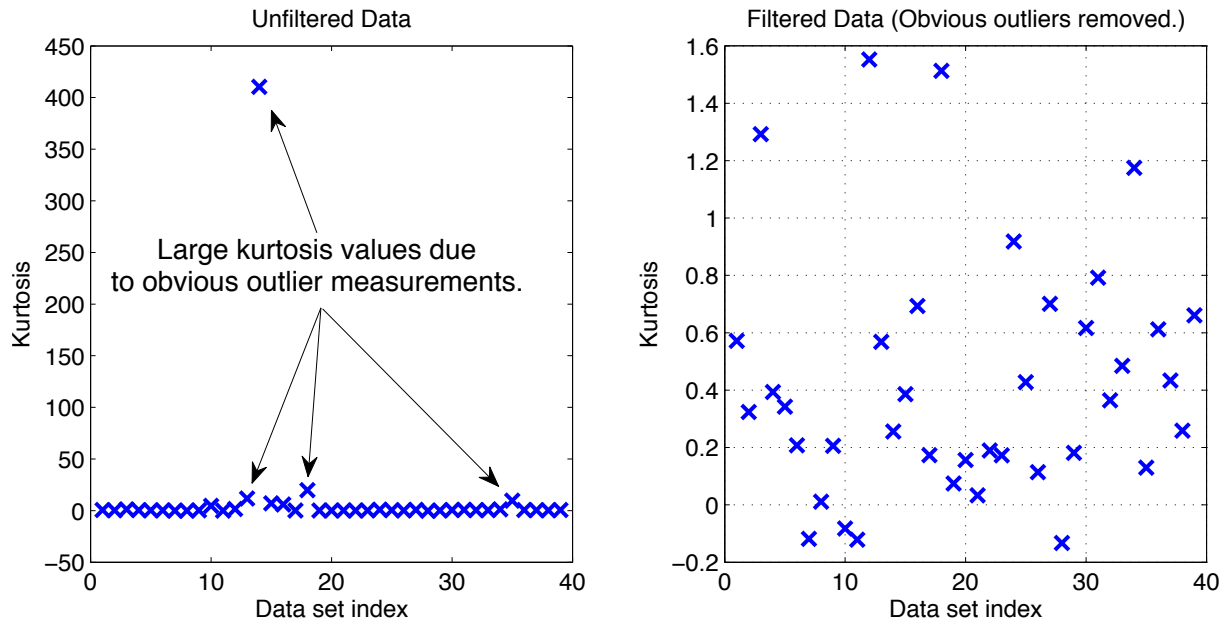


Figure 4.9: Kurtosis values of calibration data sets

accurate at any distance between 20m and 70m.

Thus, our model for LOS noise, which forces noise variance to be directly proportional to actual distance, may be inaccurate. This establishes reason for researching a more accurate noise variance model.

### 4.3 LOS Indoor Scenarios

The calibration measurements serve not only to provide a reasonable calibration distance but to show the radios' good performance in an open, LOS environment. Measurements were also taken indoors, down a long hallway in Durham Hall, to test the radios' performance in an indoor, LOS environment. Two scenarios are described here, one that shows good performance and the other moderate performance. The originator was mounted on a stand measuring 0.889m (35in), and the transponder was mounted on a stand measuring 0.559m (22in). The distance between radios was measured using the

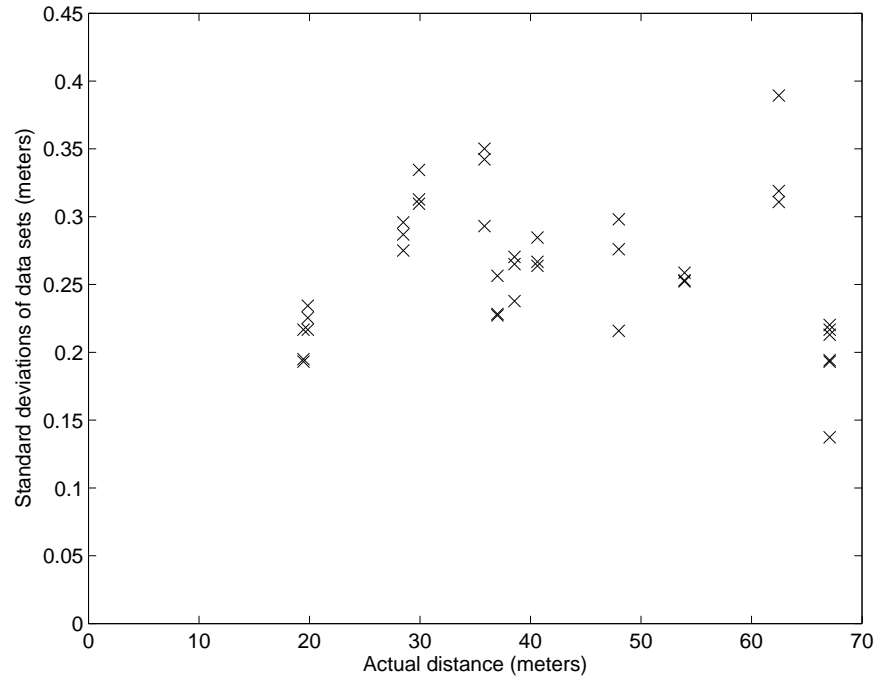


Figure 4.10: Standard deviations of data sets against actual distance

laser range finder from the front of the originator's case to the front of the transponder's case.

### 4.3.1 Durham Hallway, Good LOS Performance Scenario

Figure 4.11 shows the location pairs used to produce the results in Figures 4.12 and 4.13. The results from this indoor, LOS environment are promising, showing an extremely small error. The originator was moved for each different location pair while the transponder remained stationary. Only one data set was collected for each location pair.

While the median of the data provided good results (error under 1m at distances of 20-60m), the standard deviation indoors was much higher than the standard deviation for outdoor LOS measurements. In particular, Tables 4.1 and 4.2 show that all data sets outdoors have a standard deviation below 0.4m while all indoor LOS data sets have a



Table 4.2: Durham Hallway, Good LOS Performance Statistics

			Distance			Error	
Location Pair	Kurtosis	Std. Dev.	Mean	Median	Actual	Mean	Median
T1	-0.2810	1.0808	20.6161	20.5803	19.60	1.02	0.98
T2	38.0238	8.1506	37.0161	35.6323	36.34	0.68	-0.71
T3	33.6032	0.5862	61.4471	61.4340	60.56	0.89	0.87
Average	23.78	3.27				0.86	0.38
Range	38.30	7.56				0.34	1.69

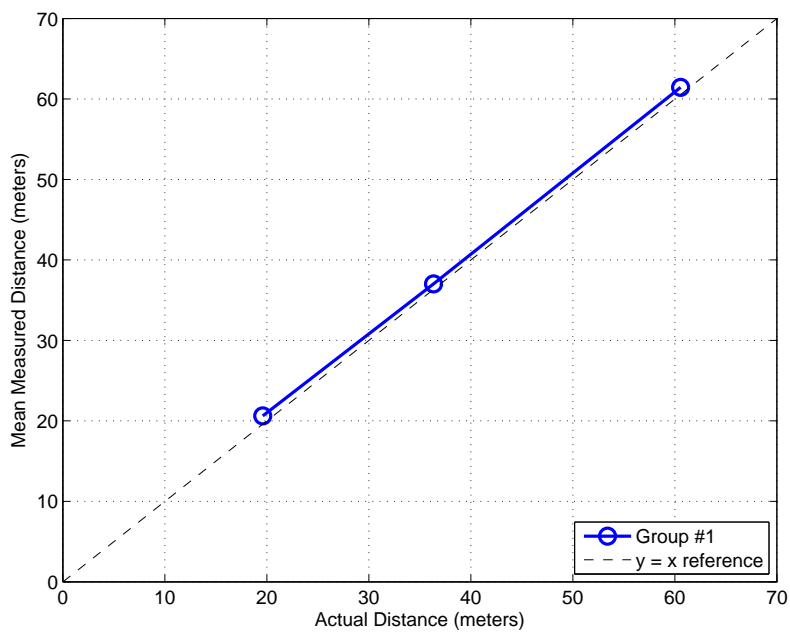


Figure 4.12: Durham hallway, good LOS performance group, mean measurements

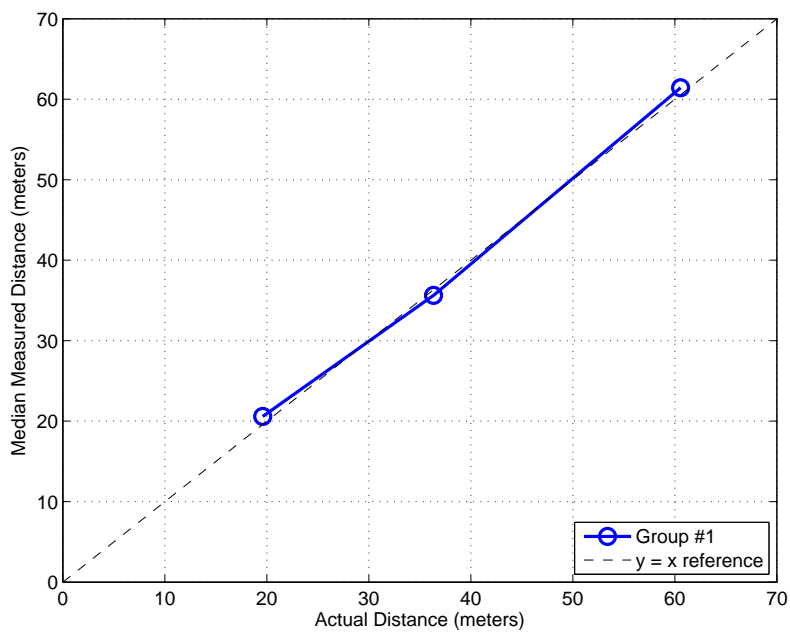


Figure 4.13: Durham hallway, good LOS performance group, median measurements

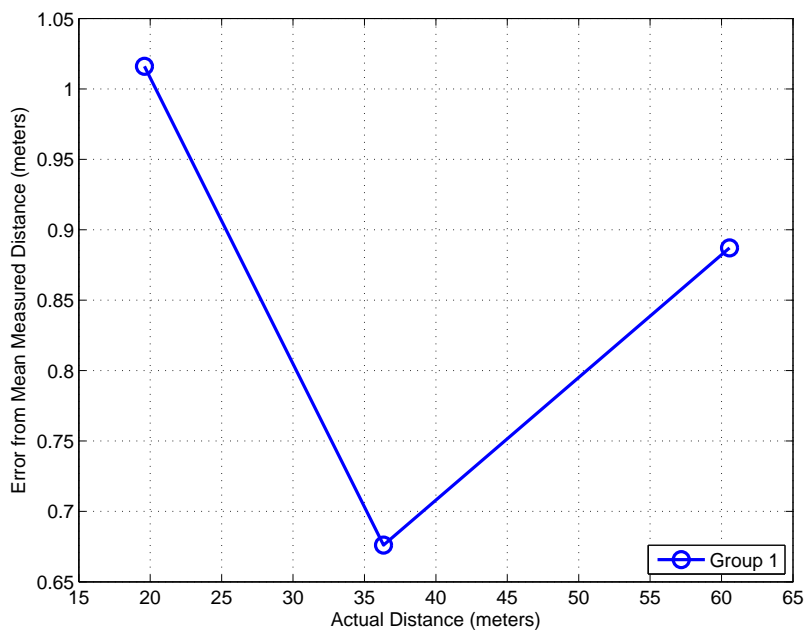


Figure 4.14: Durham hallway, good LOS performance groups, error from mean measurements

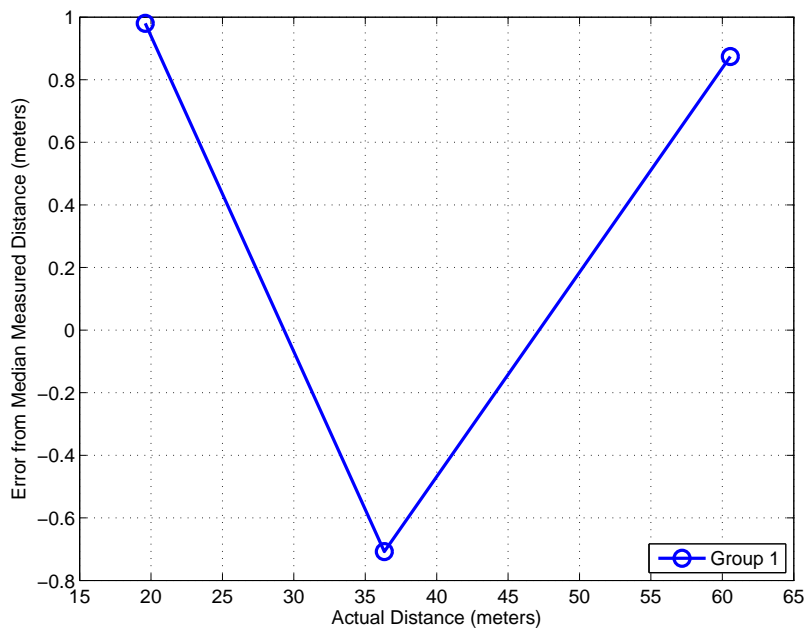


Figure 4.15: Durham hallway, good LOS performance groups, error from median measurements



Table 4.3: Durham Hallway, Moderate LOS Performance Statistics

Label			Distance			Error	
Pair/Group	Kurtosis	Std. Dev.	Mean	Median	Actual	Mean	Median
T1/1	2.4507	0.6425	8.3402	8.4506	9.13	-0.79	-0.68
T1/2	-0.8275	1.1232	7.9247	7.9994	9.13	-1.21	-1.13
T1/3	-0.1475	1.5277	6.2414	6.1954	9.11	-2.87	-2.91
T2/1	0.5605	1.3578	18.9275	19.0926	18.27	0.66	0.82
T2/2	0.4423	2.6007	25.0980	25.3482	18.31	6.79	7.04
T2/3	3.1044	1.6551	25.9048	26.2232	18.30	7.60	7.92
T3/1	3.9286	0.6348	26.2890	26.2209	27.41	-1.12	-1.19
T3/2	1.0727	0.9349	28.1537	28.0374	27.39	0.76	0.65
T3/3	4.6812	0.5229	27.0788	27.1317	27.41	-0.33	-0.28
T4/1	-1.9168	26.5438	69.7185	93.0790	36.56	33.16	56.52
T4/2	1.2914	20.0626	85.3922	94.2441	36.55	48.84	57.69
T4/3	684.9964	2.1282	37.5763	37.4936	36.56	1.02	0.93
T5/1	21.4474	7.4075	82.0747	83.7089	45.71	36.36	38.00
T5/2	-1.0350	16.2047	57.0995	47.6368	45.72	11.38	1.92
T5/3	-1.8736	19.9323	68.4160	84.4949	45.69	22.73	38.80
Average	47.88	6.89				10.87	13.61
Range	686.91	26.02				51.71	60.61

### Explanation for T4 and T5 Errors: Far Wall Reflection

Figures B.52 - B.57 show that the measurements for T4 and T5 were affected by multipath. In most of those data sets, the majority of measurements centered around a much larger distance than the true distance while *some* measurements were very nearly accurate. The

geometry of this scenario suggests that the gross errors were caused by reflections from the back wall of the hallway.

The distance from T4 to the wall and back is  $29.4 \times 2 = 58.8\text{m}$ , and the distance from T5 to the wall and back is  $21.8 \times 2 = 43.6\text{m}$ . Figure 4.20 shows that T4 and T5 have median errors very near the distances suggested by the far wall reflection.

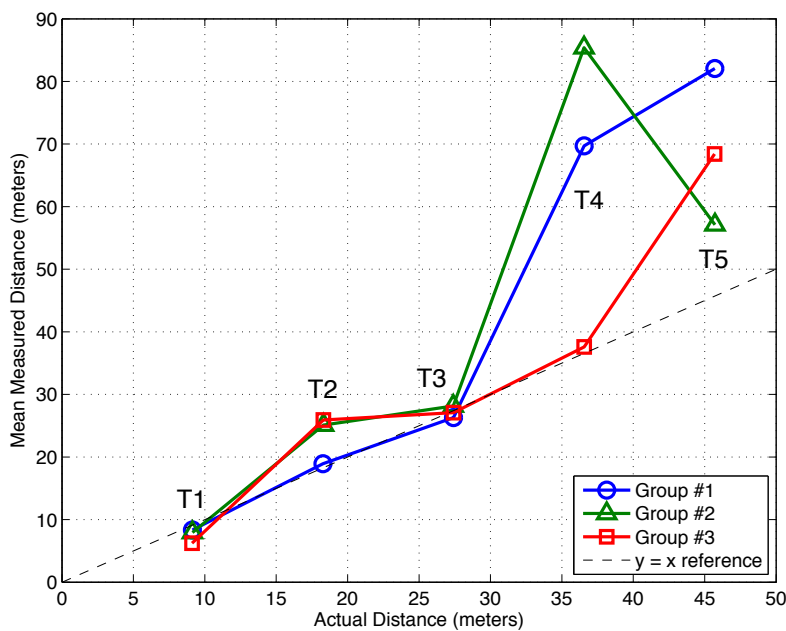


Figure 4.17: Durham hallway, moderate LOS performance groups, mean measurements

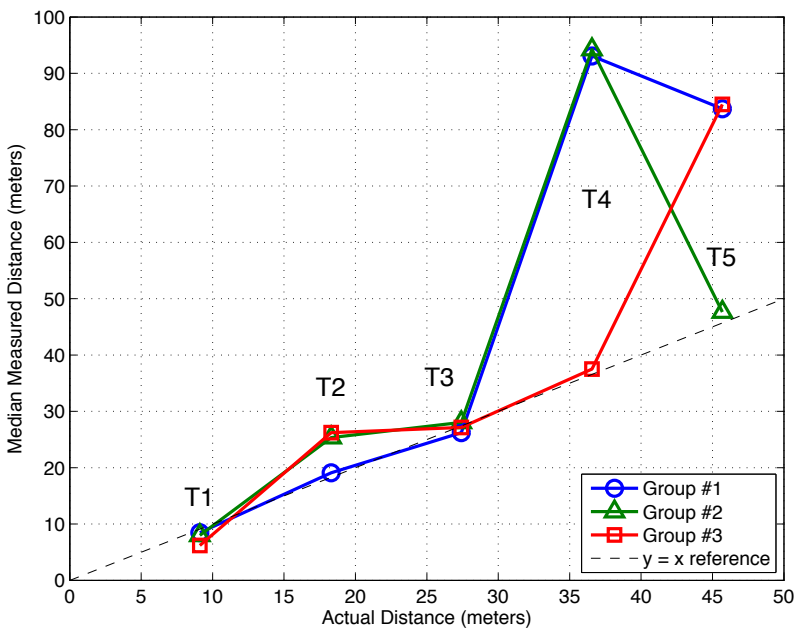


Figure 4.18: Durham hallway, moderate LOS performance groups, median measurements

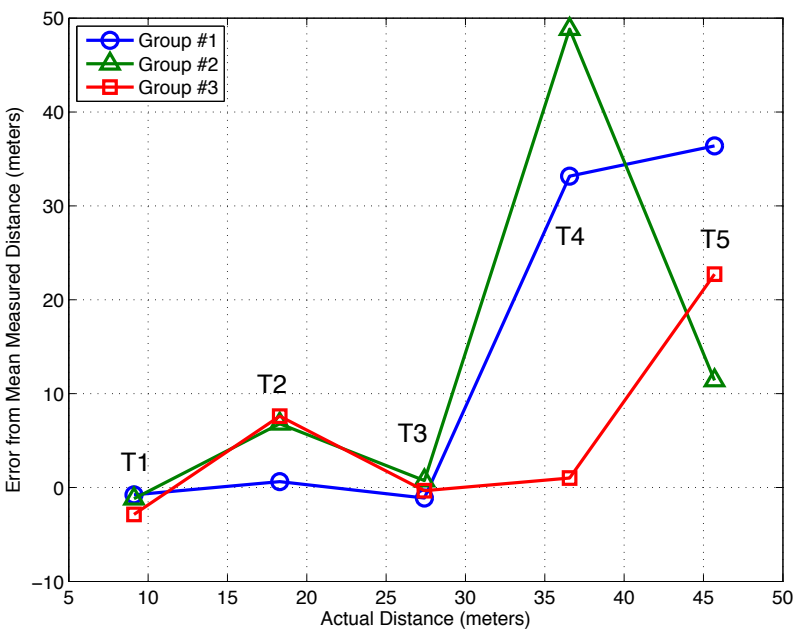


Figure 4.19: Durham hallway, moderate LOS performance groups, error from mean measurements

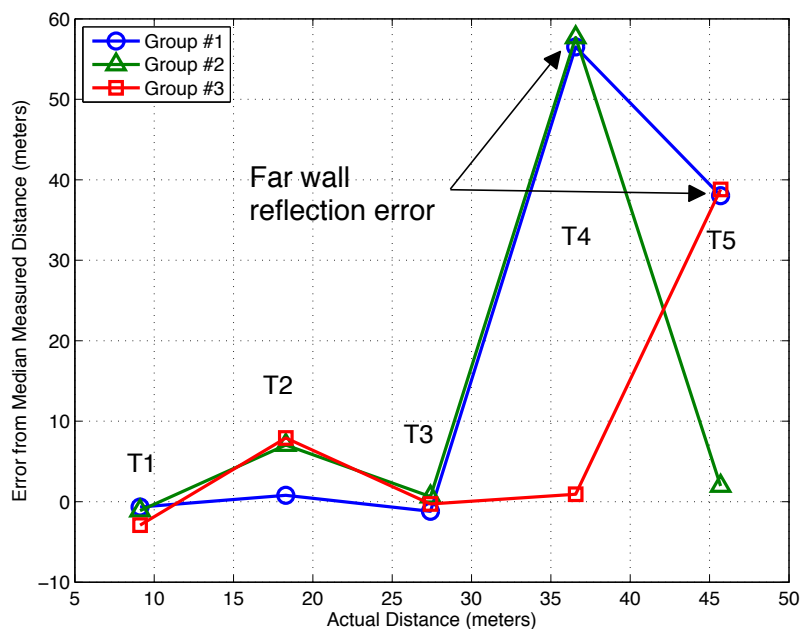


Figure 4.20: Durham hallway, moderate LOS performance groups, error from median measurements

## 4.4 NLOS Indoor Scenarios

Non-line-of-sight (NLOS) measurements were taken inside Durham Hall. True distance was measured using the laser range finder from the front of each radio's casing to the vertex of the right angle as measured with the laser right angle tool. The Pythagorean Theorem was used to calculate the hypotenuse of the right triangle, the true distance between the originator and transponder.

The "around the corner" distance is the summed length of both legs of the triangle, the distance between the radios as walkable down the hallways. Note that the around the corner distance is not the presumed propagation path. Refractions around corners and transmissions through barriers certainly allow a propagation path shorter than that suggested by the around the corner distance. The around the corner distance is simply an

estimate of how far the wave might have traveled down the hallways before reaching its destination. For instance, Figures 4.24 and 4.25 show errors below zero. The reason for this is that the error is measured as the mean/median distance measurement less the  $x$ -axis. In the case of the around the corner distance, this calculation could very well yield a negative result if the wave propagated a shorter distance than the around the corner distance.

NLOS performance of the radios was expectedly poor although the amount of error was somewhat larger than expected. For example, errors of 13-22m were seen at distances under 10m. Without a direct LOS connection between the originator and the transponder, an accurate distance reading is nearly impossible.

#### 4.4.1 MPRG Offices Scenario

For this scenario, care was taken to keep the environment as static as possible. Data sets were discarded and then repeated if disrupted by people moving through the area. Three different groups of measurements were collected from this scenario. Both the originator and the transponder were mounted on top of plastic stands measuring 0.229m (9in). In Figure 4.21, it is shown that all location pairs are NLOS except T9. Walls are constructed with metal studs and drywall; the wall bordering T6-T9 is cinder block. Offices are furnished in the usual manner with desks, computers, and both metal and wood shelving.

Of note is the LOS connection, location pair T9, which is fairly accurate for all three groups. This again reiterates the good performance of the radios in a LOS environment. Figures B.58 - B.84 show the data sets and distributions. The inconsistency between groups in this scenario can most likely be attributed to the difficult RF environment including walls, metal furniture, and moving people.

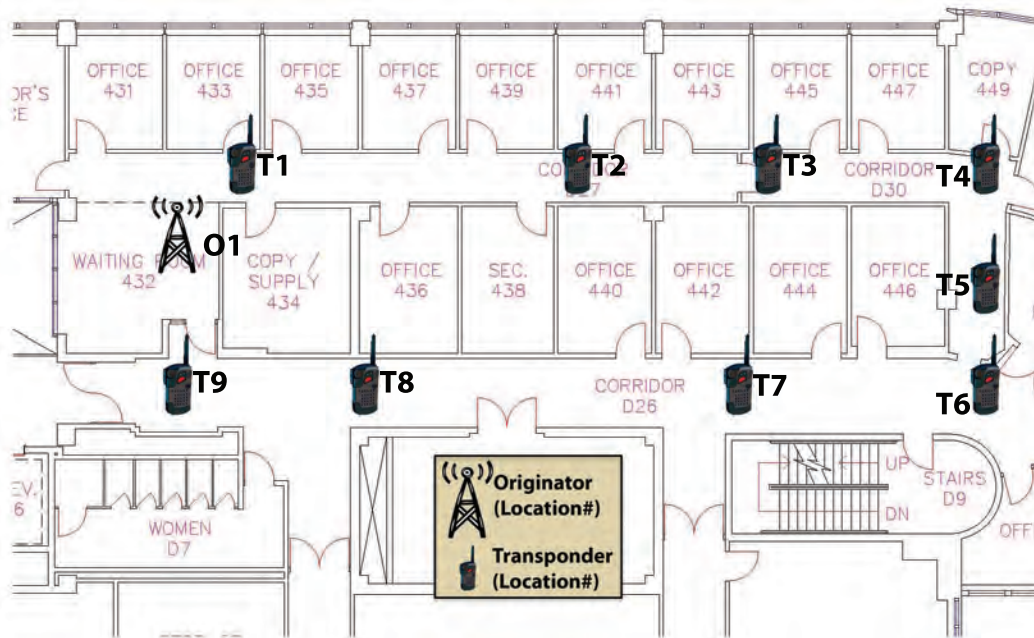


Figure 4.21: MPRG offices scenario

Table 4.4: MPRG Offices Statistics

Label			Distance			Error	
Pair/Group	Kurtosis	Std. Dev.	Mean	Median	Actual	Mean	Median
T1/1	7.6947	0.6070	7.3204	7.2488	5.05	2.27	2.20
T1/2	2.2069	2.5054	8.3098	8.3054	5.05	3.26	3.26
T1/3	5.4545	1.7501	9.7833	9.9787	5.05	4.73	4.93
T2/1	6.9022	0.6871	16.5082	16.2775	10.85	5.66	5.43
T2/2	3.2887	1.2049	20.1241	19.7797	10.85	9.27	8.93
T2/3	4.9756	3.0122	16.8508	16.6370	10.85	6.00	5.79
T3/1	28.7751	1.5306	21.7987	21.7906	16.98	4.82	4.81
T3/2	6.3514	3.3881	24.9485	25.3083	16.98	7.97	8.33
T3/3	7936.5555	2.6010	24.0583	24.1231	16.98	7.08	7.14
T4/1	8.1917	2.3281	36.3800	36.4015	24.02	12.36	12.38
T4/2	0.6944	4.6227	32.0872	32.9000	24.02	8.07	8.88
T4/3	4.9431	2.6690	30.4098	30.3147	24.02	6.39	6.29
T5/1	28.5606	1.7399	40.9747	41.1622	24.01	16.96	17.15
T5/2	28.3827	2.0665	33.8616	33.8635	24.01	9.85	9.85
T5/3	14.8967	3.4757	30.3487	29.4889	24.01	6.34	5.48
T6/1	14.6355	6.6326	39.6747	38.4090	24.68	14.99	13.73
T6/2	2348.5748	18.9786	38.9086	39.5975	24.68	14.23	14.92
T6/3	2.6668	4.4538	40.6765	40.5199	24.68	16.00	15.84
T7/1	2.8395	7.1527	45.9477	48.3617	17.26	28.69	31.10
T7/2	11.0815	2.0843	19.7581	19.7886	17.26	2.50	2.53
T7/3	0.6386	5.7857	31.0514	30.1991	17.26	13.79	12.94
T8/1	7.2354	3.3899	21.1046	20.8909	7.80	13.30	13.09
T8/2	4.4488	4.7895	23.7701	24.4315	7.80	15.97	16.63
T8/3	5.2540	4.6234	29.4445	30.7702	7.80	21.64	22.97
T9/1	4.7538	0.3232	5.9894	5.9774	5.83	0.16	0.15
T9/2	73.9942	0.5003	6.6621	6.6314	5.83	0.83	0.80
T9/3	17.5693	0.9540	7.5969	7.2360	5.83	1.77	1.41
Average	391.91	3.48				9.44	9.52
Range	7935.92	18.66				28.53	30.95

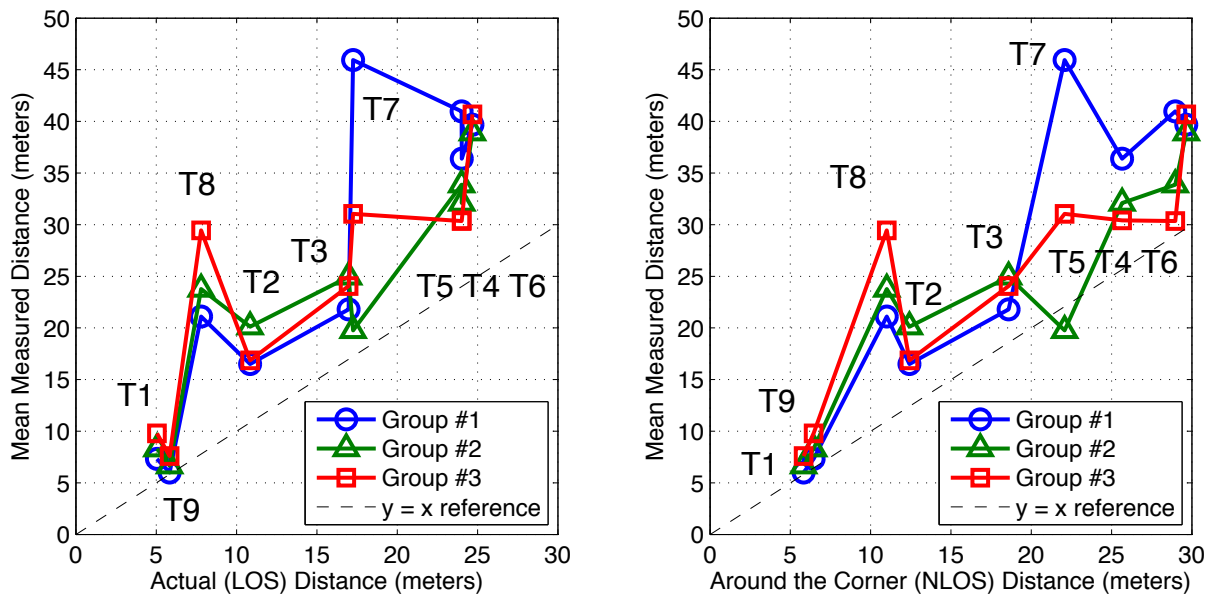


Figure 4.22: MPRG offices groups, mean measurements

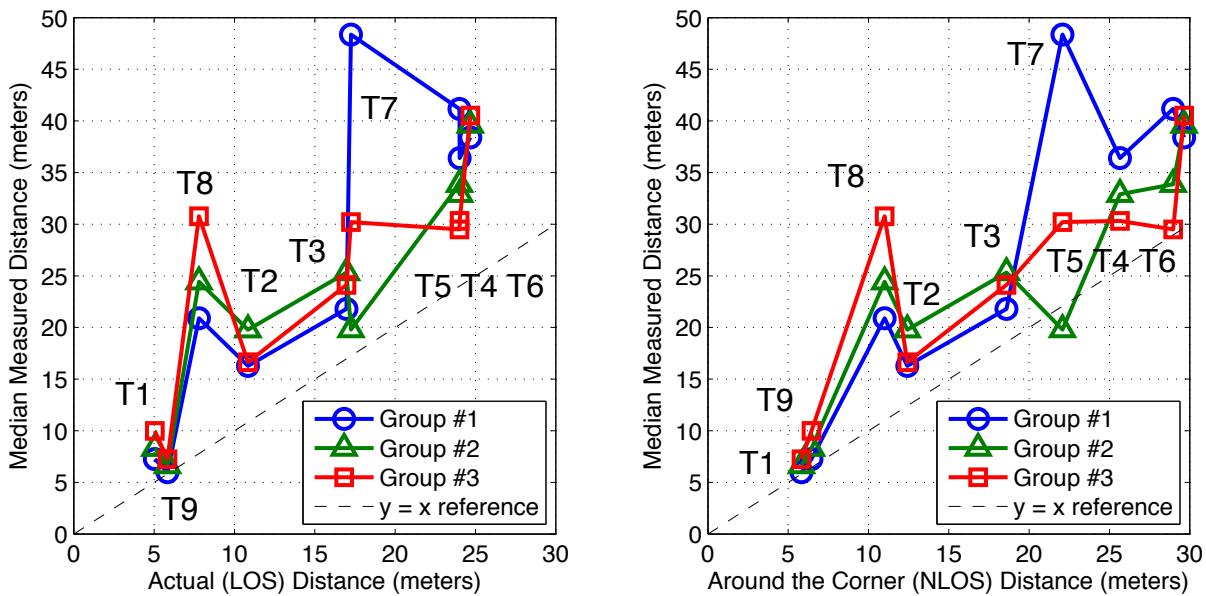


Figure 4.23: MPRG offices groups, median measurements

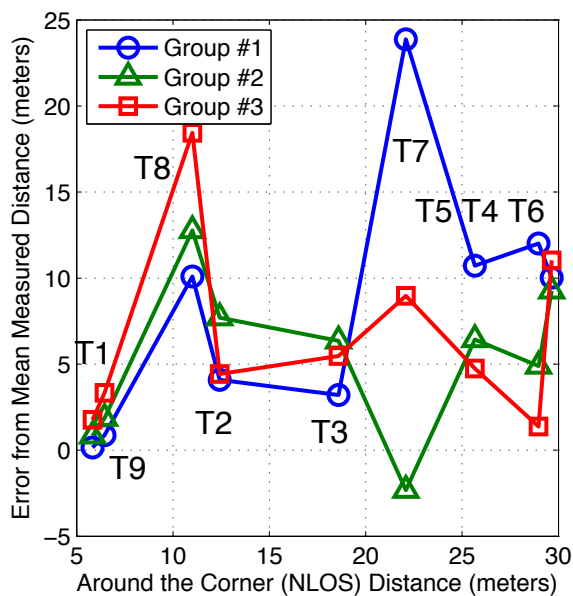
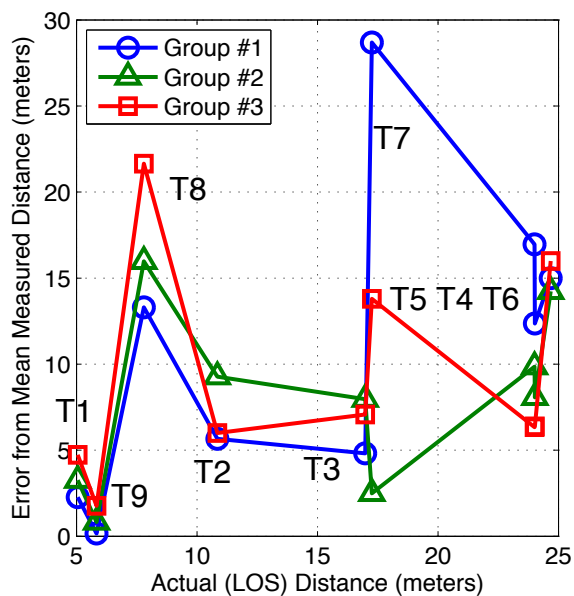


Figure 4.24: MPRG offices, error from mean measurements

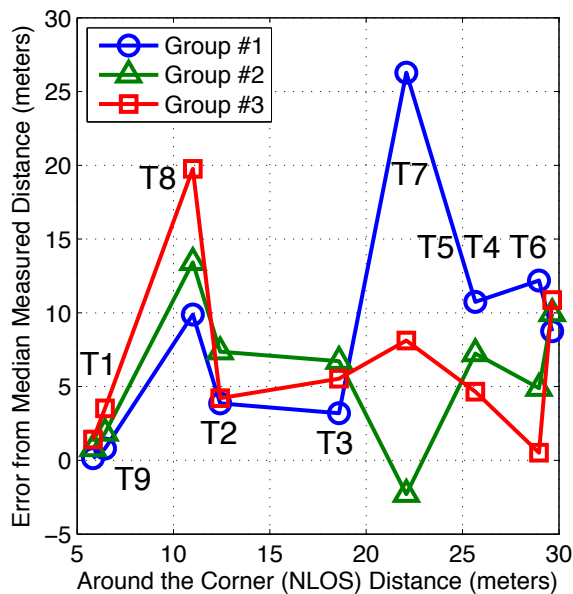
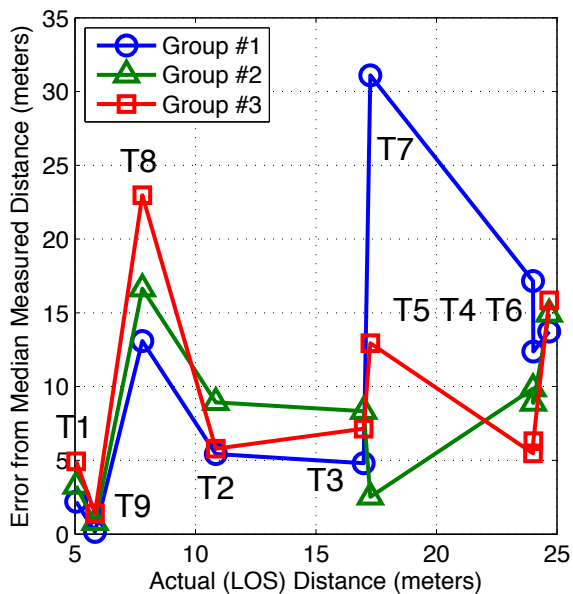


Figure 4.25: MPRG offices, error from median measurements

#### 4.4.2 MPRG Lab Scenario: A Dynamic Environment

Another set of indoor NLOS measurements was taken in the MPRG lab, a large  $15.75 \times 9$ m room with metal-framed, carpet walled cubicles. Data sets were taken during regular working hours, and people moved freely throughout the lab during measurements. Some location pairs (T1, T2, and T6) were LOS connections while the remaining location pairs were NLOS. In a similar manner to the previous NLOS measurements, true distances were measured with right angles and laser range finders, and both the originator and transponder were mounted on top of plastic stands measuring 0.229m (9in). Two sets of data were collected for these location pairs, and the results again show that NLOS connections are far less reliable than LOS connections. Errors as large as 14m appeared for distances of 8m.

Figures B.85 - B.100 show the measurements from these data sets.

In this scenario, the wide variability between the two data sets' NLOS measurements can be attributed to the dynamic environment. As opposed to keeping the environment static as in the previous scenarios, here, measurements were not discarded when people moved through the area. Even in a dynamic environment, though, the radios performed well given LOS connections.

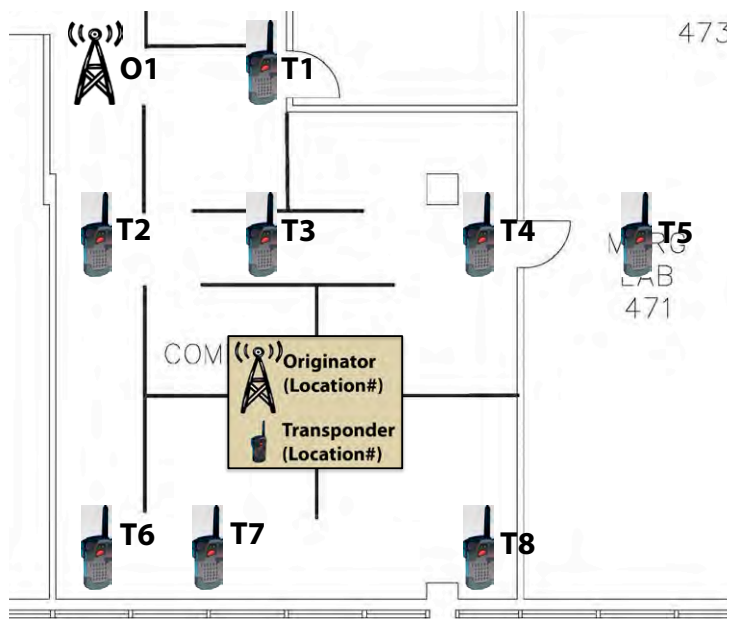


Figure 4.26: MPRG lab scenario

Table 4.5: MPRG Lab Statistics

Label			Distance			Error	
Pair/Group	Kurtosis	Std. Dev.	Mean	Median	Actual	Mean	Median
T1/1	9.6966	1.5928	7.2292	7.1934	4.57	2.66	2.62
T1/2	6.7594	0.4896	6.0439	6.1803	4.57	1.47	1.61
T2/1	1.3483	1.5867	6.3384	6.3374	3.48	2.86	2.86
T2/2	355.0846	3.1104	4.1506	4.4989	3.48	0.67	1.02
T3/1	24.5586	3.2191	10.5231	9.9488	4.58	5.94	5.37
T3/2	91.8545	1.2969	6.1923	6.0384	4.58	1.61	1.46
T4/1	17.4605	1.4652	21.4531	21.5682	11.08	10.37	10.49
T4/2	13.8717	2.3151	25.3571	25.2630	11.08	14.28	14.18
T5/1	6.9358	4.6148	33.2601	34.3239	8.30	24.96	26.02
T5/2	2.9732	1.6263	22.8214	23.0511	8.30	14.52	14.75
T6/1	55.3925	0.2498	9.3161	9.3178	9.40	-0.08	-0.08
T6/2	51.9284	1.5200	10.7162	10.4264	9.40	1.32	1.03
T7/1	1.5012	4.5460	24.9059	24.3740	9.59	15.32	14.78
T7/2	39.7103	2.4879	18.1463	17.3211	9.59	8.56	7.73
T8/1	3.6995	2.6740	17.6825	17.6396	11.13	6.55	6.51
T8/2	11.0628	4.0642	34.4178	34.8378	11.13	23.29	23.71
Average	43.36	2.30				8.39	8.38
Range	353.74	4.37				25.04	26.11

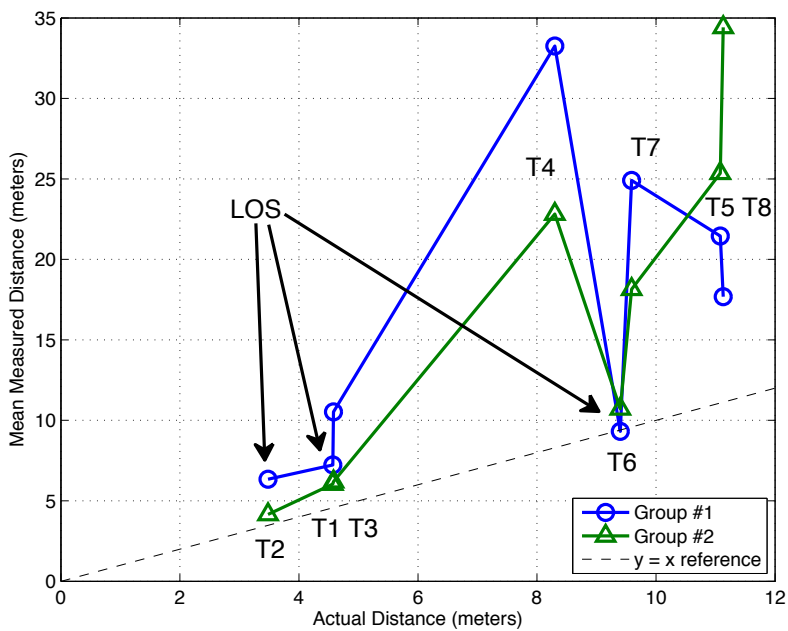


Figure 4.27: MPRG lab groups, mean measurements

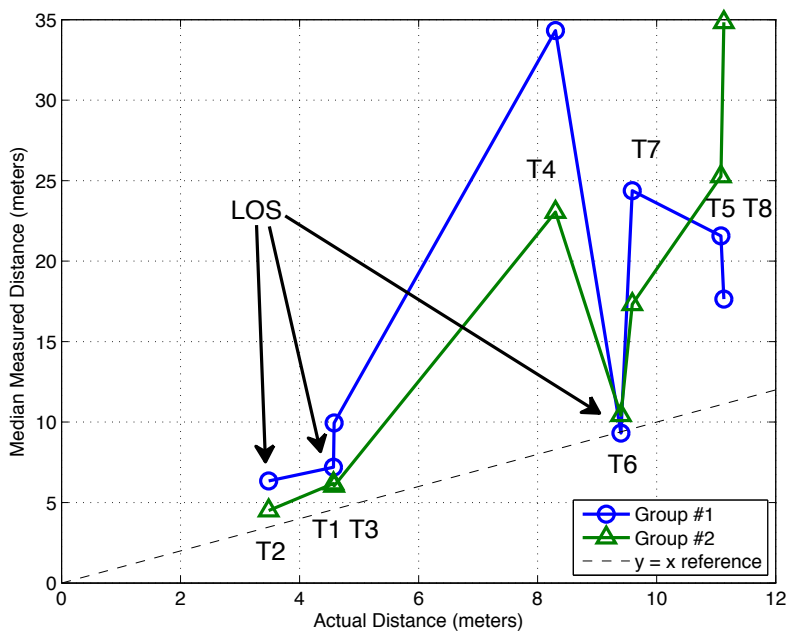


Figure 4.28: MPRG lab groups, median measurements

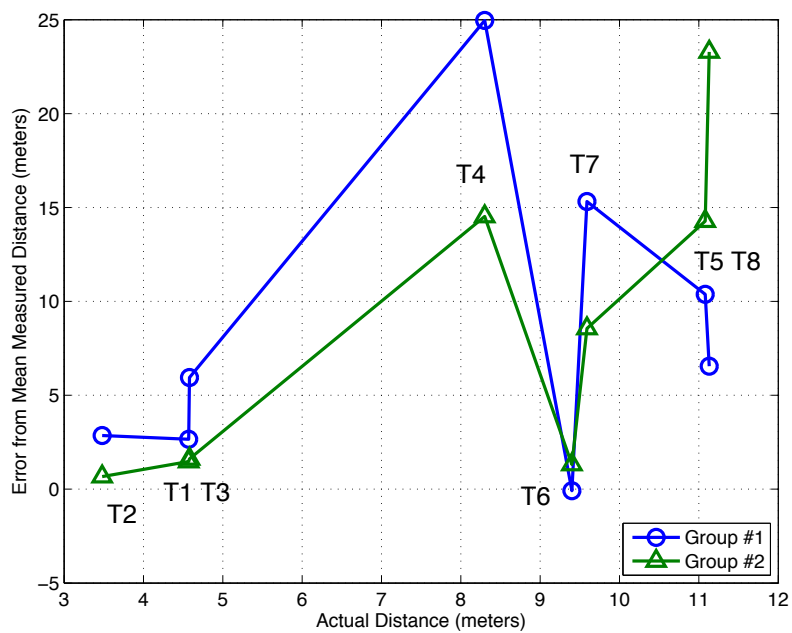


Figure 4.29: MPRG lab, error from mean measurements

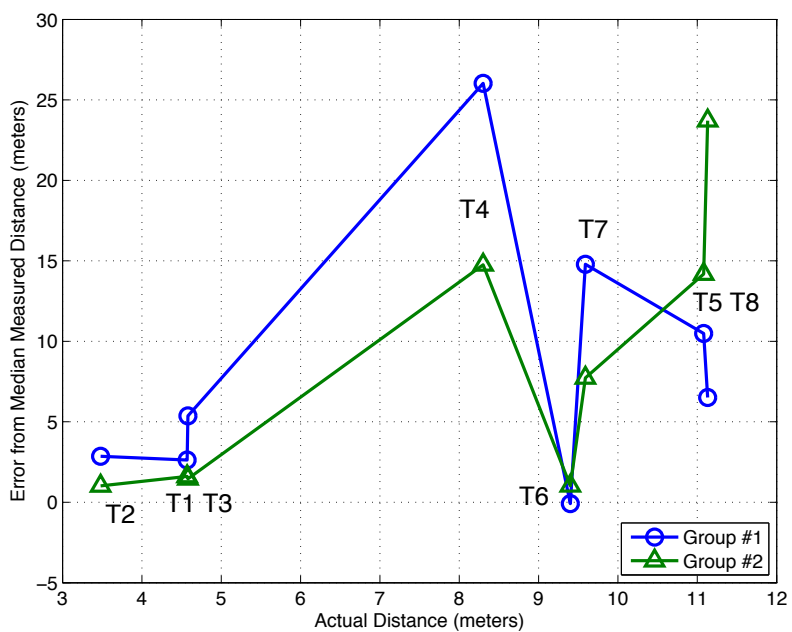


Figure 4.30: MPRG lab, error from median measurements

## 4.5 Apparent Multipath Effects

Figure 4.31 shows measured and calibrated distance data from Figure 4.11, location pair T2. The true distance was 36.34m, and that is reflected in the mean of the data. However, it is easy to see the apparent effect of multipath in the distinct jumps in measured distance up to 91m. Furthermore, the other two location pairs noted in Figure 4.11 do *not* show the same jumps in measured distance, making the case that the erroneous measurements were due to location and, subsequently, location-dependent multipath.

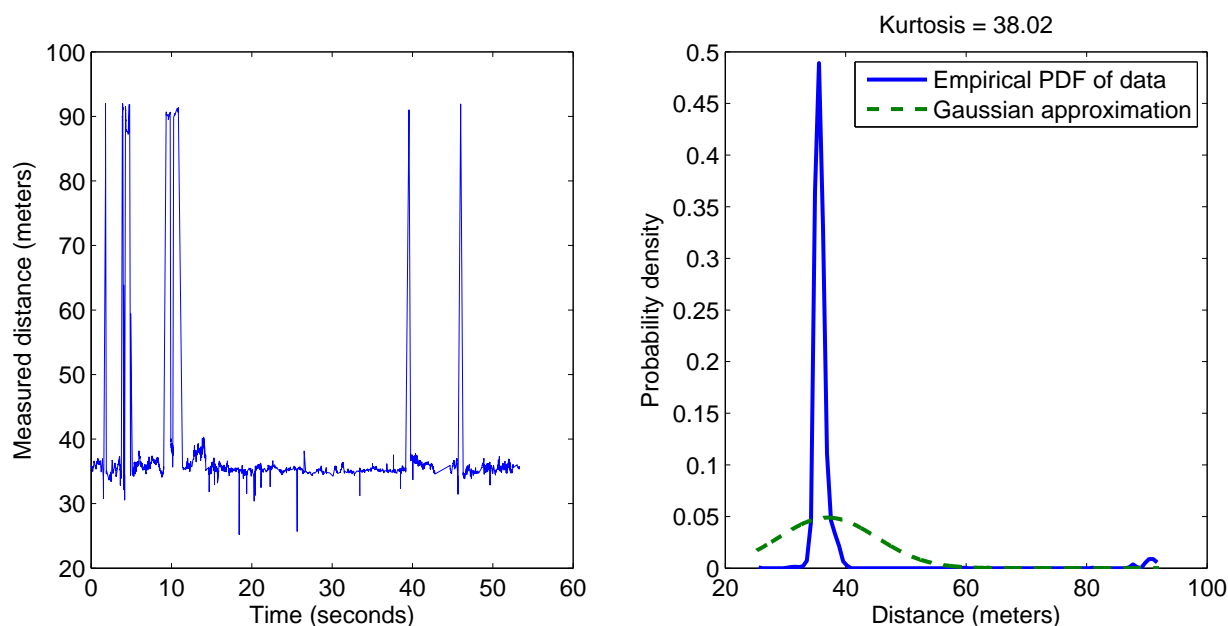


Figure 4.31: Multipath effect corrupts Gaussian approximation

Figure 4.31 shows that the Gaussian approximation to multipath-affected data is poor. This is due to the relatively heavy tail associated with the multipath distance measurements. If the data were filtered to reject the erroneous multipath measurements (in this case, rejecting all measurements above 45m), Figure 4.32 shows that the Gaussian approximation to this data set is much better. The respective kurtosis values for the unfiltered and filtered data sets are 38.02 and 7.73, reiterating the negative effect that

multipath can have on the Gaussian model for LOS noise.

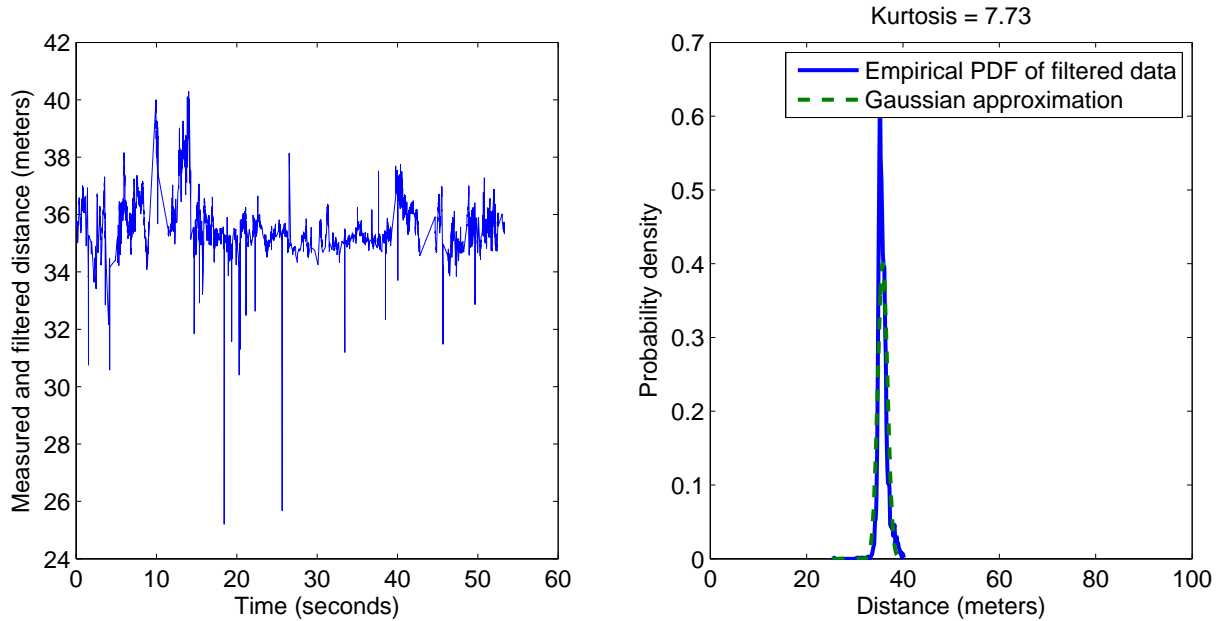


Figure 4.32: Multipath effect nullified

## 4.6 Measurement Campaign Conclusions

Statistics for the conclusions are found in Tables B.1 - B.5.

- The ENSCO radios perform well in open, LOS environments, and noise in open LOS environments can be modeled as zero-mean Gaussian.
  - Distances ranged from 19m to 67m.
  - The average unfiltered and filtered kurtosis values for the calibration data sets are 12.37 and 0.42 respectively, indicating that the open, LOS noise can be modeled as Gaussian.
  - The average standard deviation of the error for these data sets is 0.26m.

- The average error for the calibration data sets is 0.74m, dropping to 0.02m when the outlier data sets from T7, T8, and T9 are excluded.
- The ENSCO radios perform reasonably well in indoor LOS environments. However, multipath effects can add a large positive bias to range estimates. As we refer to “good” and “moderate” performance scenarios, the only difference between the two was the effect of multipath based on specific location in the hallway.
  - Distances ranged from 20m to 60m for the good performance scenario and from 9m to 46m for the moderate performance scenario.
  - The average kurtosis values for indoor LOS (good performance/moderate performance) data sets are 23.78 and 47.88 respectively, indicating that the indoor, LOS noise is less Gaussian than outdoor LOS noise.
  - The average standard deviations of the indoor LOS (good performance/moderate performance) data sets are 3.27m and 6.89m respectively, more than an order of magnitude higher than for the outdoor LOS data sets.
  - The average errors for the indoor LOS (good performance/moderate performance) data sets are 0.86m and 10.87m respectively.
- The ENSCO radios perform poorly in indoor NLOS environments, and this data does not support NLOS data being modeled as zero-mean Gaussian.
  - Distances ranged from 5m to 25m for the MPRG offices scenario and from 5m to 11m for the MPRG lab scenario.
  - The average kurtosis values for indoor NLOS (MPRG offices/MPRG lab) data sets are 391.91 and 43.36 respectively, indicating poor Gaussian statistics for modeling NLOS noise.
  - The average standard deviations of the indoor NLOS (MPRG offices/MPRG lab) data sets are 3.48m and 2.30m respectively, an order of magnitude higher than for the outdoor LOS data sets.

- The average errors for the indoor NLOS (MPRG offices/MPRG lab) data sets are 9.44m and 8.39m respectively.

# Chapter 5

## Conclusions

In this thesis, we present the non-collaborative and collaborative localization problems. We characterize the minima present for a given objective function in each case and propose improved solution algorithms. Also, we describe a measurement campaign that confirms some assumptions about noise modeling in line of sight (LOS) situations while solidifying our assumption that non line of sight (NLOS) noise remains difficult to accurately model.

### Chapter 2: The Non-Collaborative Problem

Chapter 2 introduces the non-collaborative localization problem and the associated least squares formulation. The least squares formulation is used as a way to associate a cost function when range estimates form an inconsistent system of equations. This cost (objective) function  $\Phi^{\text{ncl}}(\hat{\theta})$  has an unknown surface, and we characterize the minima of  $\Phi^{\text{ncl}}(\hat{\theta})$  to better understand how our steepest descent MPPM algorithm will perform.

To accomplish this characterization, we leverage the optimal (global) interval analysis solver, which yields all the minima of  $\Phi^{\text{ncl}}(\hat{\theta})$  in a given area. Thus, we are able to analyze under what conditions multiple minima occur. We confirm that when nodes are outside

the convex hull of the anchors, multiple minima are much more likely.

Using the information gained from characterizing the minima of  $\Phi^{\text{ncl}}(\hat{\theta})$ , we turn our attention to the modified parallel projection method (MPPM), a sub-optimal solver. We prove that MPPM is a steepest descent algorithm, and, as such, is only guaranteed to converge to a stationary point of  $\Phi^{\text{ncl}}(\hat{\theta})$ . Knowledge of where the minima are for each specific layout allowed us to develop an improved initialization technique for MPPM titled the reflected parallel projection method (RPPM).

RPPM uses a reflection of a stationary point of  $\Phi^{\text{ncl}}(\hat{\theta})$  about the anchors as its next starting point and leverages the fact that, most of the time, minima of  $\Phi^{\text{ncl}}(\hat{\theta})$  are separated spatially by the anchors. Thus, initializing across the anchors usually allows RPPM to converge to multiple minima of  $\Phi^{\text{ncl}}(\hat{\theta})$  (if they exist) and therefore increases the probability of finding the global minimum of  $\Phi^{\text{ncl}}(\hat{\theta})$ . We show through comparison that RPPM nearly matches the performance of the optimal interval analysis solver. It is also important to note that, because we can compare all the minima of a given layout found through interval analysis or RPPM, we show that minimizing  $\Phi^{\text{ncl}}(\hat{\theta})$  does not necessarily minimize the RMS error of the network.

### Chapter 3: The Collaborative Problem

Expanding analysis into the collaborative problem, Chapter 3 focuses on the collaborative objective function  $\Phi^{\text{col}}(\hat{\Theta})$ . Hypothesizing that the small number of layouts that show large RMS error in the collaborative case is due to  $\Phi^{\text{col}}(\hat{\Theta})$  having multiple minima (just as in the non-collaborative case), we develop a methodology to estimate the number of minima of  $\Phi^{\text{col}}(\hat{\Theta})$  by initializing the iterative parallel projection method (IPPM) solver multiple times and comparing the solutions returned from all initializations. This revealed a similar phenomenon to what was observed in the non-collaborative problem: multiple minima of  $\Phi^{\text{col}}(\hat{\Theta})$  are more likely to occur when nodes are outside the convex hull of the anchors. Just as in the non-collaborative case, we also show that minimizing

$\Phi^{\text{col}}(\hat{\Theta})$  will not necessarily minimize the RMS error of the network.

Through this characterization, we observed that many large RMS errors were due to entire networks being subject to the “flip ambiguity” where all the nodes were estimated to be opposite (across the anchors from) their actual locations. This particular flip ambiguity problem led us to develop the flipped initialization technique where layouts identified to be likely subject to the flip ambiguity are solved at least twice, once initialized normally and once initialized to the opposite side of the anchors. Results show that this flipped initialization significantly reduced the error due to this problem.

Other errors in the collaborative case can be attributed to a small subset of nodes’ locations being estimated far away from their true locations. We address this issue by employing another initialization technique, the reflected initialization. Results show that using either the reflected or flipped initialization techniques reduces RMS error and using both in tandem further reduces error.

Noting that running IPPM multiple times with additional initializations, we propose techniques that accurately identify which node/anchor layouts are likely to have multiple minima, allowing the user to be selective in which layouts need additional initializations to achieve accurate localization. One identification technique is based solely on the configuration of the anchors and measures the colinearity between them, a simple calculation. Another identification technique analyzes the percentage of node location estimates that are inside the convex hull of the anchors. Either identification technique significantly reduces the set of layouts that should be solved with multiple initializations, and this translates into a time and power saving mechanism.

#### **Chapter 4: The Measurement Campaign**

While Chapters 2 and 3 focus on simulations, Chapter 4 describes a measurement campaign with the purpose of assisting in noise modeling for both LOS and NLOS

situations. Two radios from ENSCO, Inc. ®, recorded the distance between each other using the unlicensed Wi-Fi band. For each location, multiple distance estimates were obtained. By analyzing the measurement distributions, we conclude that, according to these measurements, LOS ranging noise can accurately be modeled as Gaussian. We also conclude that NLOS ranging noise is highly variable depending on the environment but nearly always shows a considerable positive bias. Expectedly, the radios performed poorly when people or substantial walls separated them, and they performed well in open, clean, LOS environments. Additionally, we show that, for these particular radios, the standard deviation of the distributions did not noticeably increase with increased distance (between 20m and 70m).

These measurements confirmed our modeling of LOS noise as Gaussian but did not confirm our noise model based directly on distance. Our model of noise variance  $\sigma^2 = K_E d_{ij}^{\beta_{ij}}$  may be useful, but the direct dependence upon  $d_{ij}$  was not observed. This could be due to the nature of how ENSCO's radios obtain distance estimates or the relatively short range of distances over which we tested the radios. Additional measurement campaigns with different radios and different bandwidths would be necessary to make conclusive statements about the suitability of our noise model.

We appreciate ENSCO's allowing us to use the radios for our research purposes.

# Appendix A

## Derivation of Derivatives

This appendix lists the derivations of the first and second derivatives of  $\Phi^{\text{ncl}}(\hat{\theta})$  and  $\Phi^{\text{col}}(\hat{\Theta})$ . In particular, these derivatives are necessary for the execution of interval analysis and also assist in identifying which stationary points are minima.

For the non-collaborative derivations: Recall that  $K$  is the number of anchors,  $x$  and  $y$  are the coordinates of the node location estimate  $\hat{\theta}$ , and  $r_k$  is the range estimate between the  $k^{\text{th}}$  anchor and the node.

For the collaborative derivations: Recall that  $N$  is the number of nodes,  $\mathcal{N}_p$  is the set of neighbors (nodes and anchors) of the  $p^{\text{th}}$  node,  $C$  is the number of total connections in the network,  $r_{pq}$  is the range estimate between the  $p^{\text{th}}$  node and the  $q^{\text{th}}$  node/anchor, and  $x_p$  and  $y_p$  are the coordinates of estimate of the  $p^{\text{th}}$  node/anchor.

## A.1 Derivatives of $\Phi^{\text{ncl}}(\hat{\theta})$

$$\Phi^{\text{ncl}}(\hat{\theta}) = \frac{1}{K} \sum_{k=1}^K \left( r_k - \sqrt{(x - x_k)^2 + (y - y_k)^2} \right)^2 \quad (\text{A.1})$$

### A.1.1 First Derivatives

$$\frac{\partial \Phi^{\text{ncl}}(\hat{\theta})}{\partial x} = \frac{2}{K} \sum_{k=1}^K \left( \underbrace{r_k - \sqrt{(x - x_k)^2 + (y - y_k)^2}}_A \right) \frac{\partial A}{\partial x} \quad (\text{A.2})$$

$$\frac{\partial A}{\partial x} = \frac{-1}{2} \left[ \underbrace{(x - x_k)^2 + (y - y_k)^2}_B \right]^{-1/2} \frac{\partial B}{\partial x} \quad (\text{A.3})$$

$$\frac{\partial B}{\partial x} = 2(x - x_k) \quad (\text{A.4})$$

$$\Rightarrow \frac{\partial \Phi^{\text{ncl}}(\hat{\theta})}{\partial x} = \frac{-2}{K} \sum_{k=1}^K \left( \frac{r_k - \sqrt{(x - x_k)^2 + (y - y_k)^2}}{\sqrt{(x - x_k)^2 + (y - y_k)^2}} \right) (x - x_k) \quad (\text{A.5})$$

$$= \frac{-2}{K} \sum_{k=1}^K \left( r_k [(x - x_k)^2 + (y - y_k)^2]^{-1/2} - 1 \right) (x - x_k) \quad (\text{A.6})$$

$$\frac{\partial \Phi^{\text{ncl}}(\hat{\theta})}{\partial y} = \frac{-2}{K} \sum_{k=1}^K \left( r_k [(x - x_k)^2 + (y - y_k)^2]^{-1/2} - 1 \right) (y - y_k) \quad (\text{A.7})$$

### A.1.2 Second Derivatives

$$\frac{\partial \Phi^{\text{ncl}}(\hat{\theta})}{\partial x} = \frac{-2}{K} \sum_{k=1}^K \underbrace{\left( r_k [(x - x_k)^2 + (y - y_k)^2]^{-1/2} - 1 \right)}_A \underbrace{(x - x_k)}_B \quad (\text{A.8})$$

$$\frac{\partial^2 \Phi^{\text{ncl}}(\hat{\theta})}{\partial x^2} = \frac{-2}{K} \sum_{k=1}^K \frac{\partial A}{\partial x} B + \frac{\partial B}{\partial x} A \quad (\text{A.9})$$

$$\frac{\partial A}{\partial x} = \frac{-1}{2} r_k [(x - x_k)^2 + (y - y_k)^2]^{-3/2} (2)(x - x_k) \quad (\text{A.10})$$

$$= -r_k [(x - x_k)^2 + (y - y_k)^2]^{-3/2} (x - x_k) \quad (\text{A.11})$$

$$\frac{\partial^2 \Phi^{\text{ncl}}(\hat{\theta})}{\partial x^2} = \frac{-2}{K} \sum_{k=1}^K \left[ \underbrace{\left( \frac{-r_k}{[(x - x_k)^2 + (y - y_k)^2]^{3/2}} \right)}_{\frac{\partial A}{\partial x}} \underbrace{(x - x_k)(x - x_k)}_B \dots \right. \\ \left. + \underbrace{\left( \frac{r_k}{[(x - x_k)^2 + (y - y_k)^2]^{1/2}} - 1 \right)}_A \underbrace{(1)}_{\frac{\partial B}{\partial x}} \right] \quad (\text{A.12})$$

$$= \frac{-2}{K} \sum_{k=1}^K \left[ \frac{-r_k (x - x_k)^2}{[(x - x_k)^2 + (y - y_k)^2]^{3/2}} + \frac{r_k}{[(x - x_k)^2 + (y - y_k)^2]^{1/2}} - 1 \right] \quad (\text{A.13})$$

$$= \frac{-2}{K} \sum_{k=1}^K \left[ \frac{-r_k}{[(x - x_k)^2 + (y - y_k)^2]^{1/2}} \left( \frac{(x - x_k)^2}{(x - x_k)^2 + (y - y_k)^2} - 1 \right) - 1 \right] \quad (\text{A.14})$$

$$= \frac{-2}{K} \sum_{k=1}^K \left[ \frac{-r_k}{[(x-x_k)^2 + (y-y_k)^2]^{1/2}} \left( \frac{-(y-y_k)^2}{(x-x_k)^2 + (y-y_k)^2} \right) - 1 \right] \quad (\text{A.15})$$

$$= \frac{-2}{K} \sum_{k=1}^K \left[ \frac{r_k (y-y_k)^2}{[(x-x_k)^2 + (y-y_k)^2]^{3/2}} - 1 \right] \quad (\text{A.16})$$

$$\frac{\partial^2 \Phi^{\text{ncl}}(\hat{\theta})}{\partial y^2} = \frac{-2}{K} \sum_{k=1}^K \left[ \frac{r_k (x-x_k)^2}{[(x-x_k)^2 + (y-y_k)^2]^{3/2}} - 1 \right] \quad (\text{A.17})$$

$$\frac{\partial \Phi^{\text{ncl}}(\hat{\theta})}{\partial x} = \frac{-2}{K} \sum_{k=1}^K \underbrace{\left( r_k [(x-x_k)^2 + (y-y_k)^2]^{-1/2} - 1 \right)}_A \underbrace{(x-x_k)}_B \quad (\text{A.18})$$

$$\frac{\partial^2 \Phi^{\text{ncl}}(\hat{\theta})}{\partial x \partial y} = \frac{-2}{K} \sum_{k=1}^K \frac{\partial A}{\partial y} B + \frac{\partial B}{\partial y} A \quad (\text{A.19})$$

$$\frac{\partial A}{\partial y} = \frac{-1}{2} r_k [(x-x_k)^2 + (y-y_k)^2]^{-3/2} (2)(y-y_k) \quad (\text{A.20})$$

$$= -r_k [(x-x_k)^2 + (y-y_k)^2]^{-3/2} (y-y_k) \quad (\text{A.21})$$

$$\frac{\partial^2 \Phi^{\text{ncl}}(\hat{\theta})}{\partial x \partial y} = \frac{\partial^2 \Phi^{\text{ncl}}(\hat{\theta})}{\partial y \partial x} = \frac{-2}{K} \sum_{k=1}^K \frac{-r_k (x-x_k) (y-y_k)}{[(x-x_k)^2 + (y-y_k)^2]^{3/2}} \quad (\text{A.22})$$

### A.1.3 Summary of Derivatives of $\Phi^{\text{ncl}}(\hat{\theta})$

$$\Phi^{\text{ncl}}(\hat{\theta}) = \frac{1}{K} \sum_{k=1}^K \left( r_k - \sqrt{(x - x_k)^2 + (y - y_k)^2} \right)^2 \quad (\text{A.23})$$

$$\Phi'^{\text{ncl}}(\hat{\theta}) = \begin{bmatrix} \frac{-2}{K} \sum_{k=1}^K \left( \frac{r_k}{[(x - x_k)^2 + (y - y_k)^2]^{1/2}} - 1 \right) (x - x_k) \\ \frac{-2}{K} \sum_{k=1}^K \left( \frac{r_k}{[(x - x_k)^2 + (y - y_k)^2]^{1/2}} - 1 \right) (y - y_k) \end{bmatrix} \quad (\text{A.24})$$

$$\Phi''^{\text{ncl}}(\hat{\theta}) = \begin{bmatrix} \frac{\partial^2 \Phi^{\text{ncl}}(\hat{\theta})}{\partial x^2} & \frac{\partial^2 \Phi^{\text{ncl}}(\hat{\theta})}{\partial x \partial y} \\ \frac{\partial^2 \Phi^{\text{ncl}}(\hat{\theta})}{\partial y \partial x} & \frac{\partial^2 \Phi^{\text{ncl}}(\hat{\theta})}{\partial y^2} \end{bmatrix} \quad (\text{A.25})$$

$$\frac{\partial^2 \Phi^{\text{ncl}}(\hat{\theta})}{\partial x^2} = \frac{-2}{K} \sum_{k=1}^K \left[ \frac{r_k (y - y_k)^2}{[(x - x_k)^2 + (y - y_k)^2]^{3/2}} - 1 \right] \quad (\text{A.26})$$

$$\frac{\partial^2 \Phi^{\text{ncl}}(\hat{\theta})}{\partial y^2} = \frac{-2}{K} \sum_{k=1}^K \left[ \frac{r_k (x - x_k)^2}{[(x - x_k)^2 + (y - y_k)^2]^{3/2}} - 1 \right] \quad (\text{A.27})$$

$$\frac{\partial^2 \Phi^{\text{ncl}}(\hat{\theta})}{\partial x \partial y} = \frac{\partial^2 \Phi^{\text{ncl}}(\hat{\theta})}{\partial y \partial x} = \frac{-2}{K} \sum_{k=1}^K \frac{-r_k (x - x_k) (y - y_k)}{[(x - x_k)^2 + (y - y_k)^2]^{3/2}} \quad (\text{A.28})$$

## A.2 Derivatives of $\Phi^{\text{col}}(\hat{\Theta})$

### A.2.1 First Derivatives

$$\Phi^{\text{col}}(\hat{\Theta}) = \frac{1}{C} \sum_{i=1}^N \sum_{j=i+1; j \in \mathcal{N}_i}^{N+K} \left( r_{ij} - \sqrt{(x_i - x_j)^2 + (y_i - y_j)^2} \right)^2 \quad (\text{A.29})$$

Finding the derivative of  $\Phi^{\text{col}}(\hat{\Theta})$  with respect to one node's  $x$  or  $y$  coordinate is easier when thinking of what  $\Phi^{\text{col}}(\hat{\Theta})$  actually does.  $\Phi^{\text{col}}(\hat{\Theta})$  simply sums over each connection (node/node and node/anchor) in the network and ensures that each connection contributes to  $\Phi^{\text{col}}(\hat{\Theta})$  exactly once. Thus, when taking the derivative of  $\Phi^{\text{col}}(\hat{\Theta})$  with respect to one node (the  $p^{\text{th}}$  node), we know that the  $p^{\text{th}}$  node and all its connections appear only once in  $\Phi^{\text{col}}(\hat{\Theta})$ . We can think of the  $p^{\text{th}}$  node as the only unlocalized node and all its neighbors as anchors (for the purposes of finding the derivative of  $\Phi^{\text{col}}(\hat{\Theta})$  with respect to just the  $p^{\text{th}}$  node). In this sense, we are in the non-collaborative scenario, and the derivative of  $\Phi^{\text{col}}(\hat{\Theta})$  with respect to the  $p^{\text{th}}$  node is equivalent to the derivative of  $\Phi^{\text{ncl}}(\hat{\theta})$  (Equations A.6-A.7). Recall that  $\mathcal{N}_p$  is the set of neighbors to the  $p^{\text{th}}$  node and that  $C$  is the total number of connections in the network, equal to the number of summed terms in  $\Phi^{\text{col}}(\hat{\Theta})$ .

$$\frac{\partial \Phi^{\text{col}}(\hat{\Theta})}{\partial x_p} = \frac{-2}{C} \sum_{q \in \mathcal{N}_p} \left( \frac{r_{pq}}{[(x_p - x_q)^2 + (y_p - y_q)^2]^{1/2}} - 1 \right) (x_p - x_q) \quad (\text{A.30})$$

$$\frac{\partial \Phi^{\text{col}}(\hat{\Theta})}{\partial y_p} = \frac{-2}{C} \sum_{q \in \mathcal{N}_p} \left( \frac{r_{pq}}{[(x_p - x_q)^2 + (y_p - y_q)^2]^{1/2}} - 1 \right) (y_p - y_q) \quad (\text{A.31})$$

## A.2.2 Second Derivatives

$$\frac{\partial \Phi^{\text{col}}(\hat{\Theta})}{\partial x_p} = \frac{-2}{C} \sum_{q \in \mathcal{N}_p} \underbrace{\left( r_{pq} [(x_p - x_q)^2 + (y_p - y_q)^2]^{-1/2} - 1 \right)}_A \underbrace{(x_p - x_q)}_B \quad (\text{A.32})$$

$$\frac{\partial^2 \Phi^{\text{col}}(\hat{\Theta})}{\partial x_p^2} = \frac{-2}{C} \sum_{q \in \mathcal{N}_p} \frac{\partial A}{\partial x_p} B + \frac{\partial B}{\partial x_p} A \quad (\text{A.33})$$

$$\begin{aligned} \frac{\partial A}{\partial x_p} &= -\frac{1}{2} r_{pq} [(x_p - x_q)^2 + (y_p - y_q)^2]^{-3/2} (2) (x_p - x_q) \\ &= -r_{pq} [(x_p - x_q)^2 + (y_p - y_q)^2]^{-3/2} (x_p - x_q) \end{aligned} \quad (\text{A.34})$$

$$\begin{aligned} \frac{\partial^2 \Phi^{\text{col}}(\hat{\Theta})}{\partial x_p^2} &= \frac{-2}{C} \sum_{q \in \mathcal{N}_p} \left( \underbrace{-r_{pq} [(x_p - x_q)^2 + (y_p - y_q)^2]^{-3/2} (x_p - x_q)}_{\frac{\partial A}{\partial x_p}} \underbrace{(x_p - x_q)}_B \dots \right. \\ &\quad \left. + \underbrace{(1)}_{\frac{\partial B}{\partial x_k}} \underbrace{\left( r_{pq} [(x_p - x_q)^2 + (y_p - y_q)^2]^{-1/2} - 1 \right)}_A \right) \end{aligned} \quad (\text{A.35})$$

$$= \frac{-2}{C} \sum_{q \in \mathcal{N}_p} \left[ \frac{-r_{pq} (x_p - x_q)^2}{[(x_p - x_q)^2 + (y_p - y_q)^2]^{3/2}} + \frac{r_{pq}}{[(x_p - x_q)^2 + (y_p - y_q)^2]^{1/2}} - 1 \right] \quad (\text{A.36})$$

$$= \frac{-2}{C} \sum_{q \in \mathcal{N}_p} \left[ \frac{-r_{pq}}{[(x_p - x_q)^2 + (y_p - y_q)^2]^{1/2}} \left( \frac{(x_p - x_q)^2}{(x_p - x_q)^2 + (y_p - y_q)^2} - 1 \right) - 1 \right] \quad (\text{A.37})$$

$$= \frac{-2}{C} \sum_{q \in \mathcal{N}_p} \left[ \frac{-r_{pq}}{[(x_p - x_q)^2 + (y_p - y_q)^2]^{1/2}} \left( \frac{-(y_p - y_q)^2}{(x_p - x_q)^2 + (y_p - y_q)^2} \right) - 1 \right] \quad (\text{A.38})$$

$$\frac{\partial^2 \Phi^{\text{col}}(\hat{\Theta})}{\partial x_p^2} = \frac{-2}{C} \sum_{q \in \mathcal{N}_p} \left[ \frac{r_{pq} (y_p - y_q)^2}{[(x_p - x_q)^2 + (y_p - y_q)^2]^{3/2}} - 1 \right] \quad (\text{A.39})$$

$$\frac{\partial^2 \Phi^{\text{col}}(\hat{\Theta})}{\partial x_p^2} = \frac{-2}{C} \sum_{q \in \mathcal{N}_p} \left[ \frac{r_{pq} (y_p - y_q)^2}{[(x_p - x_q)^2 + (y_p - y_q)^2]^{3/2}} - 1 \right] \quad (\text{A.40})$$

$$\frac{\partial^2 \Phi^{\text{col}}(\hat{\Theta})}{\partial y_p^2} = \frac{-2}{C} \sum_{q \in \mathcal{N}_p} \left[ \frac{r_{pq} (x_p - x_q)^2}{[(x_p - x_q)^2 + (y_p - y_q)^2]^{3/2}} - 1 \right] \quad (\text{A.41})$$

$$\frac{\partial \Phi^{\text{col}}(\hat{\Theta})}{\partial x_p} = \frac{-2}{C} \sum_{q \in \mathcal{N}_p} \underbrace{\left( r_{pq} [(x_p - x_q)^2 + (y_p - y_q)^2]^{-1/2} - 1 \right)}_A \underbrace{(x_p - x_q)}_B \quad (\text{A.42})$$

$$\frac{\partial^2 \Phi^{\text{col}}(\hat{\Theta})}{\partial x_p \partial x_q} = \frac{-2}{C} \left( \frac{\partial A}{\partial x_q} B + \frac{\partial B}{\partial x_q} A \right) \quad (\text{A.43})$$

$$\begin{aligned} \frac{\partial A}{\partial x_q} &= -\frac{1}{2} r_{pq} [(x_p - x_q)^2 + (y_p - y_q)^2]^{-3/2} (2) (x_p - x_q) (-1) \\ &= r_{pq} [(x_p - x_q)^2 + (y_p - y_q)^2]^{-3/2} (x_p - x_q) \end{aligned} \quad (\text{A.44})$$

$$\begin{aligned} \frac{\partial^2 \Phi^{\text{col}}(\hat{\Theta})}{\partial x_p \partial x_q} &= \frac{-2}{C} \left( \underbrace{r_{pq} [(x_p - x_q)^2 + (y_p - y_q)^2]^{-3/2} (x_p - x_q)}_{\frac{\partial A}{\partial x_q}} \underbrace{(x_p - x_q)}_B \dots \right. \\ &\quad \left. + \underbrace{(-1)}_{\frac{\partial B}{\partial x_q}} \underbrace{\left( r_{pq} [(x_p - x_q)^2 + (y_p - y_q)^2]^{-1/2} - 1 \right)}_A \right) \end{aligned} \quad (\text{A.45})$$

Notice the similarity to Equation A.35. (Negation of the argument of the summation.)

$$\frac{\partial^2 \Phi^{\text{col}}(\hat{\Theta})}{\partial x_p \partial x_q} = \frac{-2}{C} \left( \frac{-r_{pq} (y_p - y_q)^2}{[(x_p - x_q)^2 + (y_p - y_q)^2]^{3/2}} + 1 \right) \quad (\text{A.46})$$

$$\frac{\partial \Phi^{\text{col}}(\hat{\Theta})}{\partial x_p} = \frac{-2}{C} \sum_{q \in \mathcal{N}_p} \underbrace{\left( r_{pq} [(x_p - x_q)^2 + (y_p - y_q)^2]^{-1/2} - 1 \right)}_A \underbrace{(x_p - x_q)}_B \quad (\text{A.47})$$

$$\frac{\partial^2 \Phi^{\text{col}}(\hat{\Theta})}{\partial x_p \partial y_q} = \frac{-2}{C} \left( \frac{\partial A}{\partial y_q} B + \cancel{\frac{\partial B}{\partial y_q} A}^0 \right) \quad (\text{A.48})$$

$$\begin{aligned} \frac{\partial A}{\partial y_i} &= -\frac{1}{2} r_{pq} [(x_p - x_q)^2 + (y_p - y_q)^2]^{-3/2} (2) (y_p - y_q) (-1) \\ &= r_{pq} [(x_p - x_q)^2 + (y_p - y_q)^2]^{-3/2} (y_p - y_q) \end{aligned} \quad (\text{A.49})$$

$$\frac{\partial^2 \Phi^{\text{col}}(\hat{\Theta})}{\partial x_p \partial y_q} = \frac{-2}{C} \left( \frac{r_{pq} (y_p - y_q)}{\underbrace{[(x_p - x_q)^2 + (y_p - y_q)^2]^{3/2}}_{\frac{\partial A}{\partial y_q}}} \underbrace{(x_p - x_q)}_B \right) \quad (\text{A.50})$$

$$\frac{\partial \Phi^{\text{col}}(\hat{\Theta})}{\partial x_p} = \frac{-2}{C} \sum_{q \in \mathcal{N}_p} \underbrace{\left( r_{pq} [(x_p - x_q)^2 + (y_p - y_q)^2]^{-1/2} - 1 \right)}_A \underbrace{(x_p - x_q)}_B \quad (\text{A.51})$$

$$\frac{\partial^2 \Phi^{\text{col}}(\hat{\Theta})}{\partial x_p \partial y_p} = \frac{-2}{C} \sum_{q \in \mathcal{N}_p} \frac{\partial A}{\partial y_p} B + \frac{\partial B}{\partial y_p} A \quad (\text{A.52})$$

$$\begin{aligned} \frac{\partial A}{\partial y_p} &= -\frac{1}{2} r_{pq} [(x_p - x_q)^2 + (y_p - y_q)^2]^{-3/2} (2) (y_p - y_q) \\ &= -r_{pq} [(x_p - x_q)^2 + (y_p - y_q)^2]^{-3/2} (y_p - y_q) \end{aligned} \quad (\text{A.53})$$

$$\frac{\partial^2 \Phi^{\text{col}}(\hat{\Theta})}{\partial x_p \partial y_p} = \frac{-2}{C} \sum_{q \in \mathcal{N}_p} \underbrace{\frac{-r_{pq} (y_p - y_q)}{[(x_p - x_q)^2 + (y_p - y_q)^2]^{3/2}}}_{\frac{\partial A}{\partial y_p}} \underbrace{(x_p - x_q)}_B \quad (\text{A.54})$$

### A.2.3 Summary of Derivatives of $\Phi^{\text{col}}(\hat{\Theta})$

$$\Phi^{\text{col}}(\hat{\Theta}) = \frac{1}{C} \sum_{i=1}^N \sum_{j=i+1; j \in \mathcal{N}_i}^{N+K} \left( r_{ij} - \sqrt{(x_i - x_j)^2 + (y_i - y_j)^2} \right)^2 \quad (\text{A.55})$$

$$\frac{\partial \Phi^{\text{col}}(\hat{\Theta})}{\partial x_p} = \frac{-2}{C} \sum_{q \in \mathcal{N}_p} \left( \frac{r_{pq}}{[(x_p - x_q)^2 + (y_p - y_q)^2]^{1/2}} - 1 \right) (x_p - x_q) \quad (\text{A.56})$$

$$\frac{\partial \Phi^{\text{col}}(\hat{\Theta})}{\partial y_p} = \frac{-2}{C} \sum_{q \in \mathcal{N}_p} \left( \frac{r_{pq}}{[(x_p - x_q)^2 + (y_p - y_q)^2]^{1/2}} - 1 \right) (y_p - y_q) \quad (\text{A.57})$$

$$\frac{\partial^2 \Phi^{\text{col}}(\hat{\Theta})}{\partial x_p^2} = \frac{-2}{C} \sum_{q \in \mathcal{N}_p} \left[ \frac{r_{pq} (y_p - y_q)^2}{[(x_p - x_q)^2 + (y_p - y_q)^2]^{3/2}} - 1 \right] \quad (\text{A.58})$$

$$\frac{\partial^2 \Phi^{\text{col}}(\hat{\Theta})}{\partial y_p^2} = \frac{-2}{C} \sum_{q \in \mathcal{N}_p} \left[ \frac{r_{pq} (x_p - x_q)^2}{[(x_p - x_q)^2 + (y_p - y_q)^2]^{3/2}} - 1 \right] \quad (\text{A.59})$$

$$\frac{\partial^2 \Phi^{\text{col}}(\hat{\Theta})}{\partial x_p \partial x_q} = \frac{-2}{C} \left( \frac{-r_{pq} (y_p - y_q)^2}{[(x_p - x_q)^2 + (y_p - y_q)^2]^{3/2}} + 1 \right) \quad (\text{A.60})$$

$$\frac{\partial^2 \Phi^{\text{col}}(\hat{\Theta})}{\partial y_p \partial y_q} = \frac{-2}{C} \left( \frac{-r_{pq} (x_p - x_q)^2}{[(x_p - x_q)^2 + (y_p - y_q)^2]^{3/2}} + 1 \right) \quad (\text{A.61})$$

$$\frac{\partial^2 \Phi^{\text{col}}(\hat{\Theta})}{\partial x_p \partial y_q} = \frac{-2}{C} \left( \frac{r_{pq} (y_p - y_q) (x_p - x_q)}{[(x_p - x_q)^2 + (y_p - y_q)^2]^{3/2}} \right) \quad (\text{A.62})$$

$$\frac{\partial^2 \Phi^{\text{col}}(\hat{\Theta})}{\partial x_p \partial y_p} = \frac{-2}{C} \sum_{q \in \mathcal{N}_p} \frac{-r_{pq} (y_p - y_q) (x_p - x_q)}{[(x_p - x_q)^2 + (y_p - y_q)^2]^{3/2}} \quad (\text{A.63})$$

# Appendix B

## Measurement Campaign Data

Each data set is plotted in an appendix. Each individual distance measurement is plotted against the measurement index on the left, and the right hand plots are empirical probability density functions of the error. Dashed lines on the left mark the actual distances that were being measured, and if the measurement is NLOS, a smaller dashed line represents the “around the corner” distance. For plots of calibration data sets, solid horizontal lines denote the limits where the data was filtered to achieve the low kurtosis values shown in Table B.1 by rejecting obviously erroneous measurements.

Tables 4.1 - 4.5 that are already printed in the body of the report appear in the appendices, also, for convenience in Tables B.1 - B.5.

### B.1 Calibration Scenario

Table B.1 and Figures B.1 - B.39 (below) summarize the results from data sets in the calibration scenario.

Table B.1: Calibration Statistics

Label	Kurtosis		Std. Dev.	Distance			Error		
	Pair/Grp.	Unfiltered		Filtered	Mean	Median	Actual	Mean	Median
T1/1		0.5720	—	0.2750	28.3946	28.4081	28.48	-0.09	-0.07
T1/2		0.3239	—	0.2958	28.3659	28.3724	28.48	-0.11	-0.11
T1/3		1.2922	—	0.2869	28.4125	28.4106	28.48	-0.07	-0.07
T2/1		0.3935	—	0.3501	35.9106	35.9399	35.83	0.08	0.11
T2/2		0.3422	—	0.2931	35.9245	35.9631	35.83	0.09	0.13
T2/3		0.2078	—	0.3423	35.9409	35.9488	35.83	0.11	0.12
T3/1		-0.1181	—	0.2638	40.4755	40.4865	40.62	-0.14	-0.13
T3/2		0.0111	—	0.2668	40.4890	40.4913	40.62	-0.13	-0.13
T3/3		0.2060	—	0.2847	40.5311	40.5414	40.62	-0.09	-0.08
T4/1		4.6409	-0.0824	0.2130	66.9202	66.9262	67.07	-0.15	-0.14
T4/2		-0.1215	—	0.1931	66.9510	66.9511	67.07	-0.12	-0.12
T4/3		1.5529	—	0.2167	67.0029	67.0136	67.07	-0.07	-0.06
T4/4		11.7690	0.5682	0.1373	66.9962	66.9971	67.07	-0.07	-0.07
T4/5		410.3820	0.2557	0.1942	67.0042	67.0053	67.07	-0.07	-0.06
T4/6		6.9970	0.3862	0.2202	66.9731	66.9844	67.07	-0.10	-0.09
T5/1		5.9516	0.6934	0.2587	53.7942	53.8000	53.93	-0.14	-0.13
T5/2		0.1734	—	0.2532	53.8166	53.8250	53.93	-0.11	-0.10
T5/3		19.7971	1.5133	0.2523	53.7826	53.7707	53.93	-0.15	-0.16
T6/1		0.0744	—	0.2760	47.8056	47.8050	47.99	-0.18	-0.19
T6/2		0.1566	—	0.2158	47.8681	47.8629	47.99	-0.12	-0.13
T6/3		0.0333	—	0.2981	47.8527	47.8474	47.99	-0.14	-0.14
T7/1		0.1895	—	0.2650	41.6685	41.6806	38.55	3.12	3.13
T7/2		0.1729	—	0.2704	41.5759	41.5866	38.55	3.03	3.04
T7/3		0.9184	—	0.2377	41.5948	41.6021	38.55	3.04	3.05
T8/1		0.4277	—	0.2344	23.0632	23.0810	19.84	3.22	3.24
T8/2		0.1140	—	0.2167	23.0412	23.0497	19.84	3.20	3.21
T8/3		0.7007	—	0.2254	23.0640	23.0726	19.84	3.22	3.23
T9/1		-0.1328	—	0.1932	22.6143	22.6153	19.46	3.15	3.16
T9/2		0.1817	—	0.1949	22.6633	22.6682	19.46	3.20	3.21
T9/3		0.6168	—	0.2167	22.6027	22.6145	19.46	3.14	3.15
T10/1		0.7918	—	0.2283	37.3847	37.4005	37.01	0.37	0.39
T10/2		0.3647	—	0.2565	37.3235	37.3314	37.01	0.31	0.32
T10/3		0.4849	—	0.2273	37.3152	37.3218	37.01	0.31	0.31
T11/1		1.1751	—	0.3893	62.9671	62.9574	62.47	0.50	0.49
T11/2		9.6962	0.1296	0.3189	62.8795	62.8822	62.47	0.41	0.41
T11/3		0.6117	—	0.3109	62.8984	62.9025	62.47	0.43	0.43
T12/1		0.4337	—	0.3344	29.9068	29.9131	29.91	-0.00	0.00
T12/2		0.2584	—	0.3095	30.0068	30.0159	29.91	0.10	0.11
T12/3		0.6608	—	0.3128	29.9100	29.9184	29.91	-0.00	0.01
Average		12.37	0.42	0.26				0.74	0.75
Range		410.51	1.69	0.25				3.41	3.43

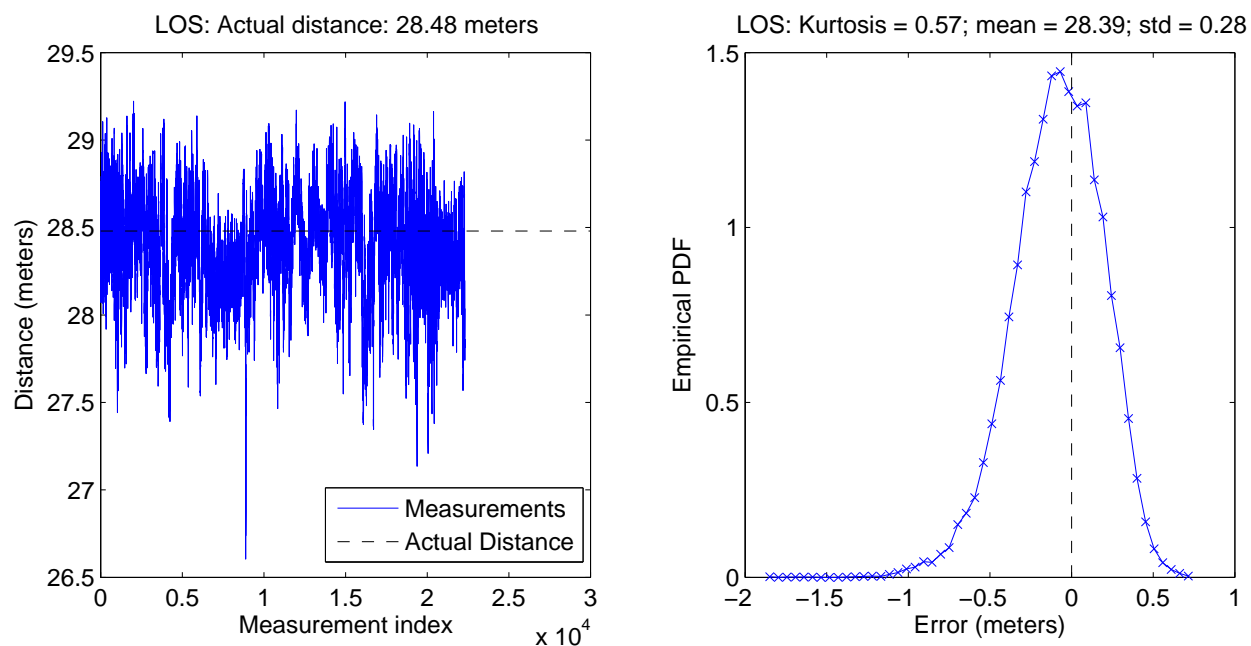


Figure B.1: Calibration, location pair T1, set # 1

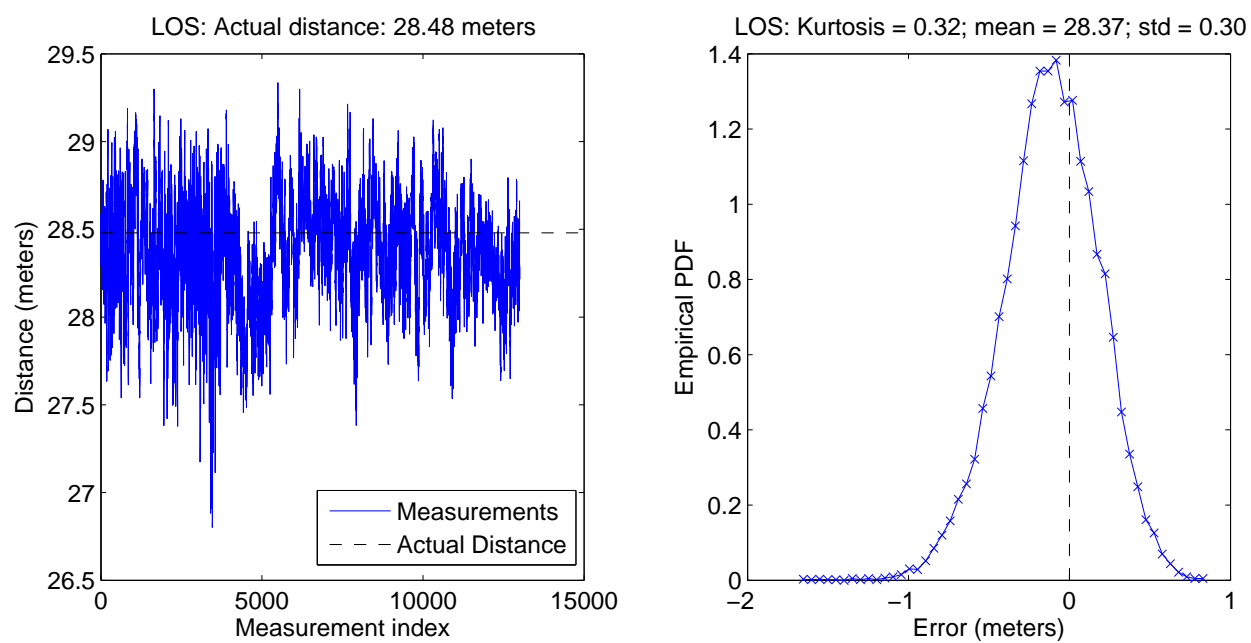


Figure B.2: Calibration, location pair T1, set # 2

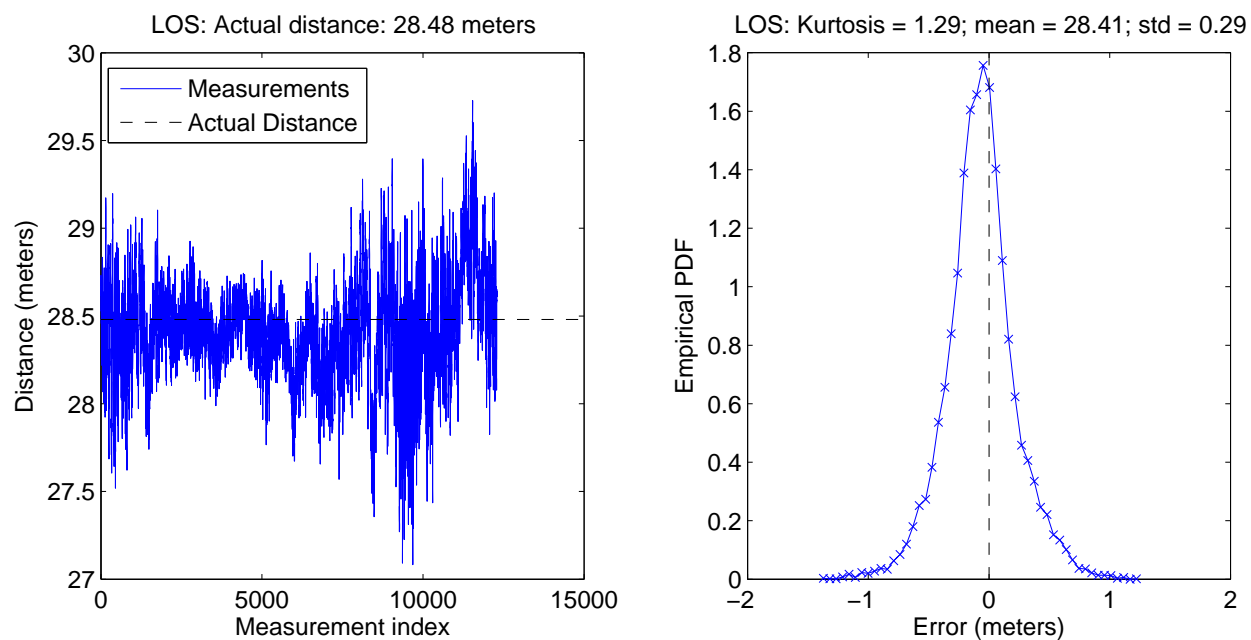


Figure B.3: Calibration, location pair T1, set # 3

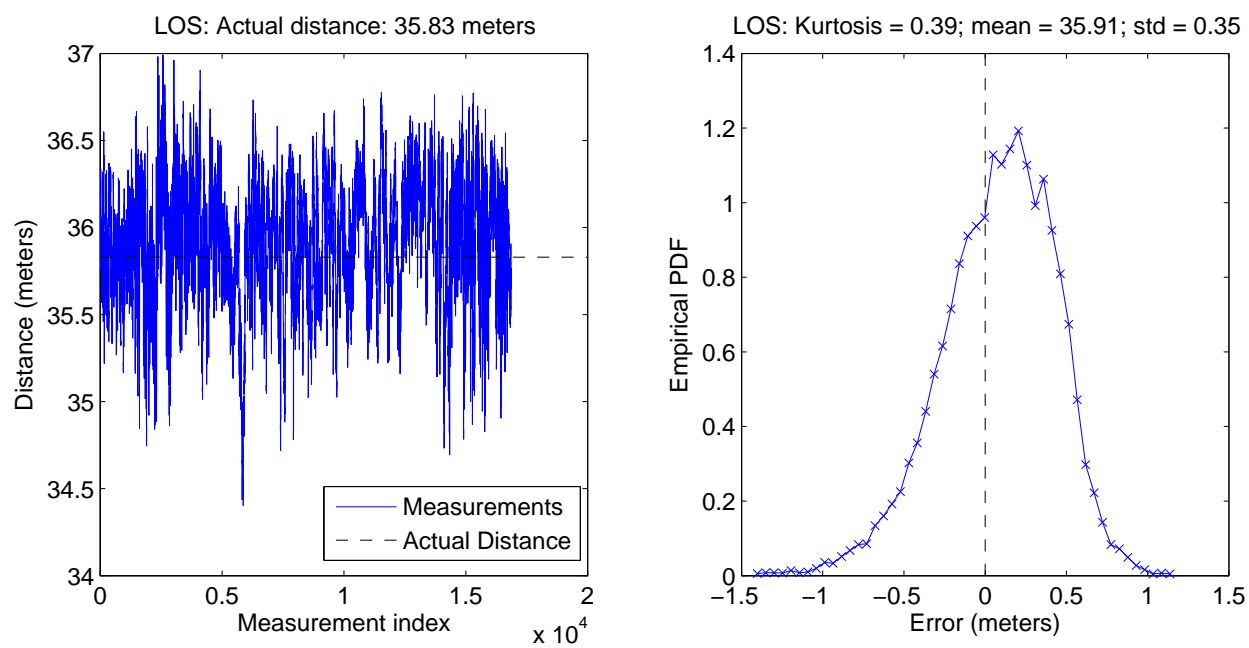


Figure B.4: Calibration, location pair T2, set # 1

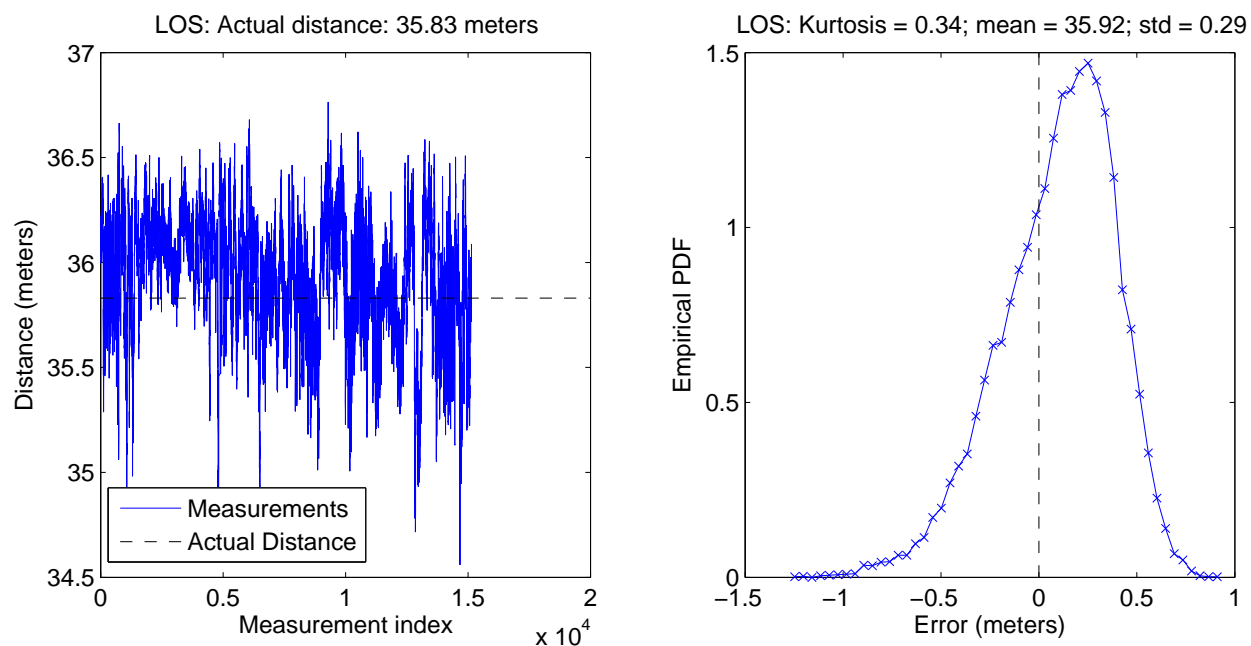


Figure B.5: Calibration, location pair T2, set # 2

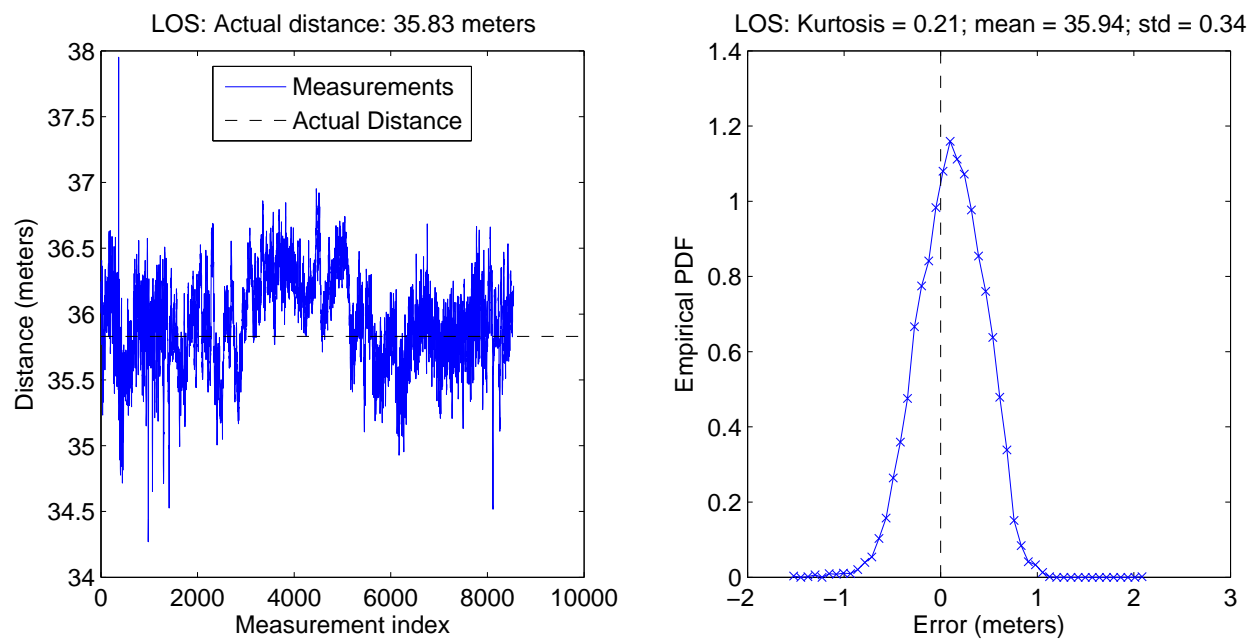


Figure B.6: Calibration, location pair T2, set # 3

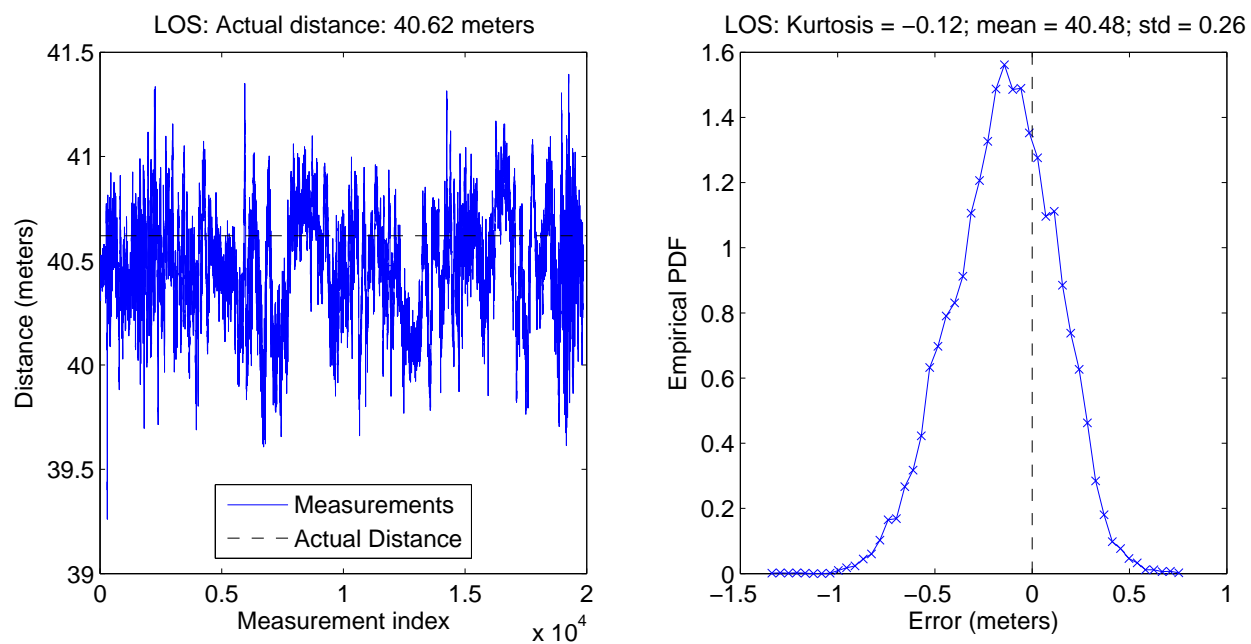


Figure B.7: Calibration, location pair T3, set # 1

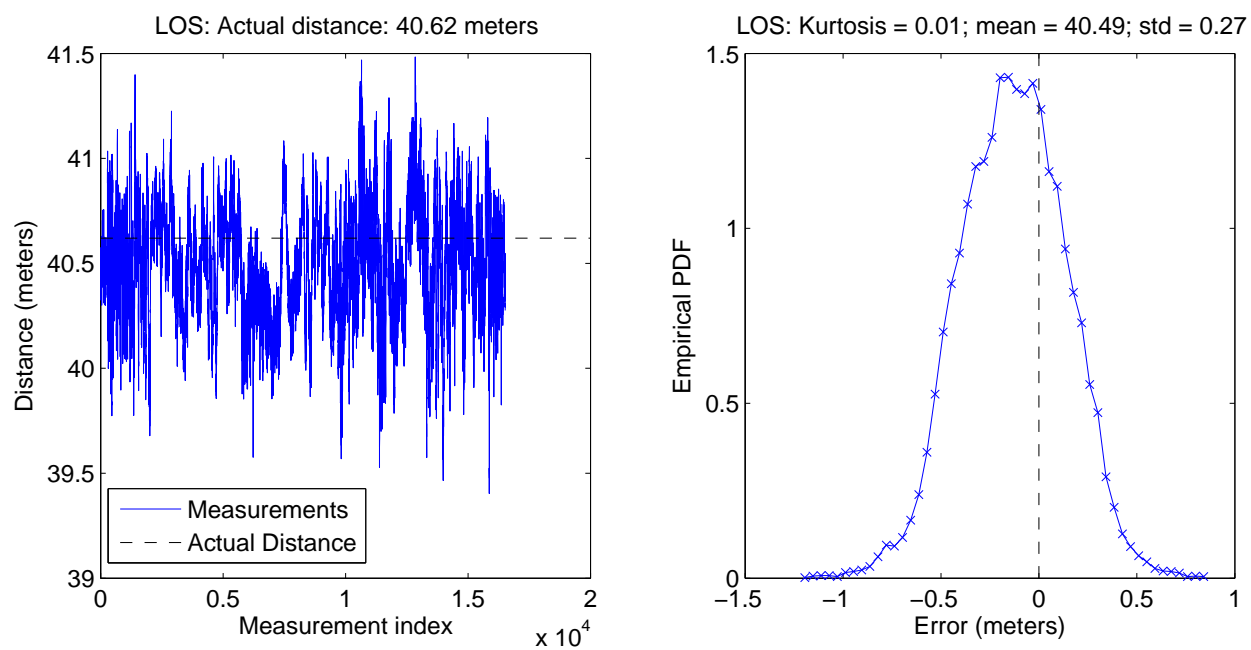


Figure B.8: Calibration, location pair T3, set # 2

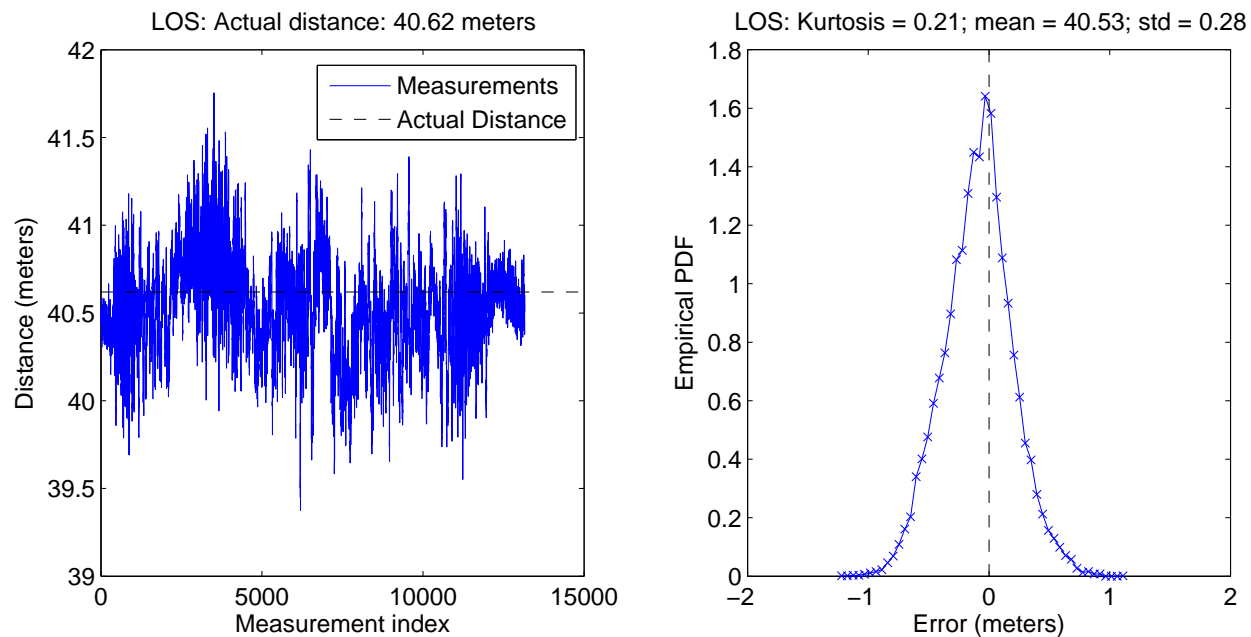


Figure B.9: Calibration, location pair T3, set # 3

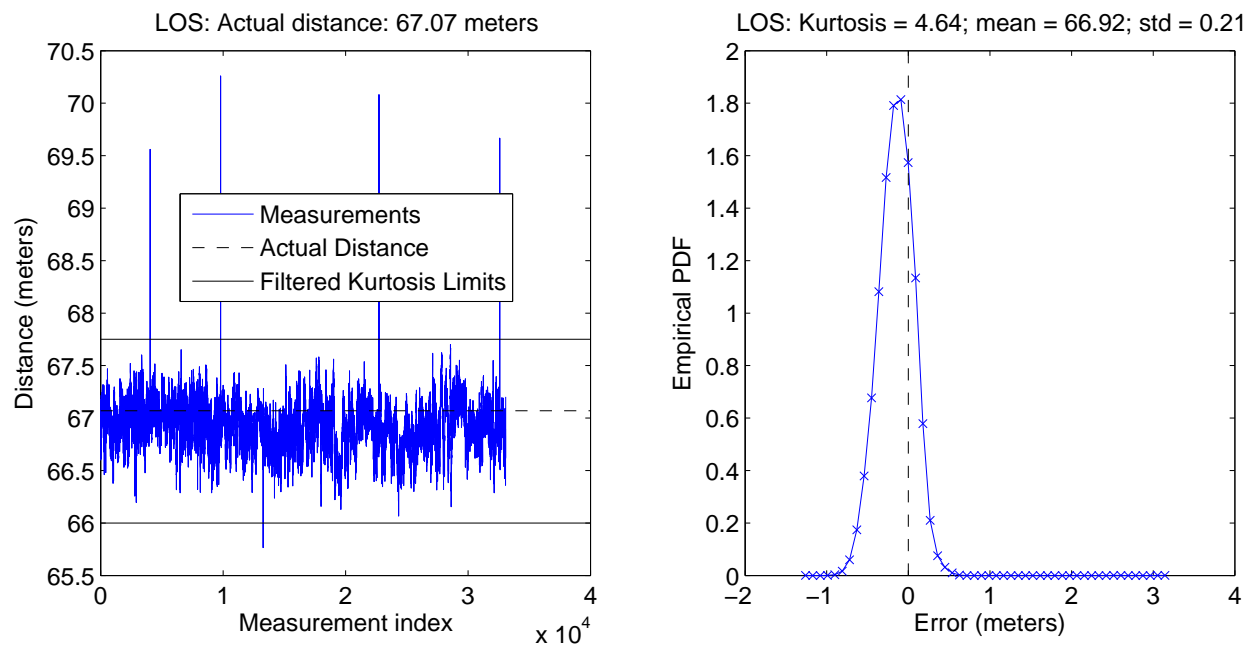


Figure B.10: Calibration, location pair T4, set # 1

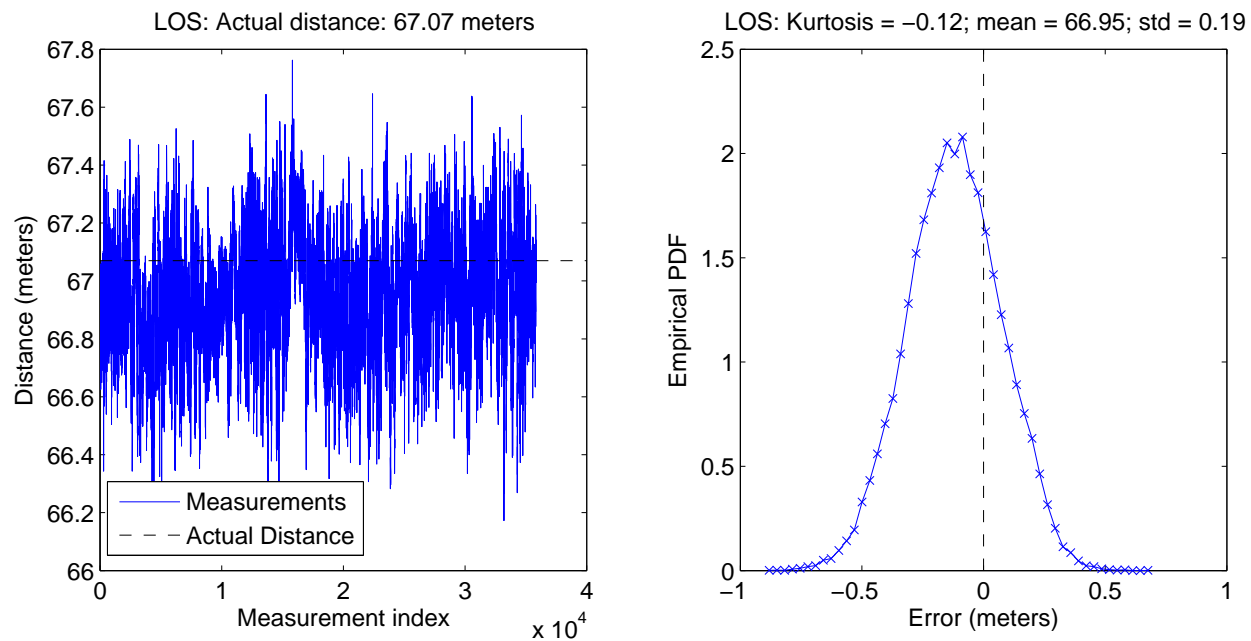


Figure B.11: Calibration, location pair T4, set # 2

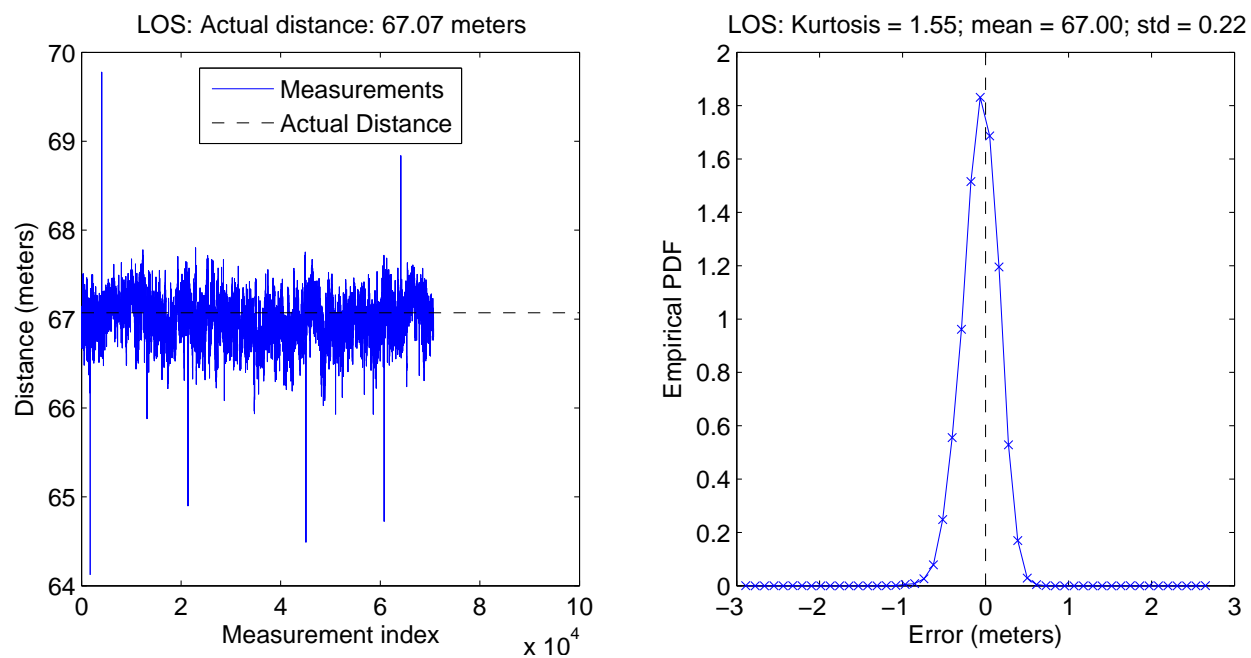


Figure B.12: Calibration, location pair T4, set # 3

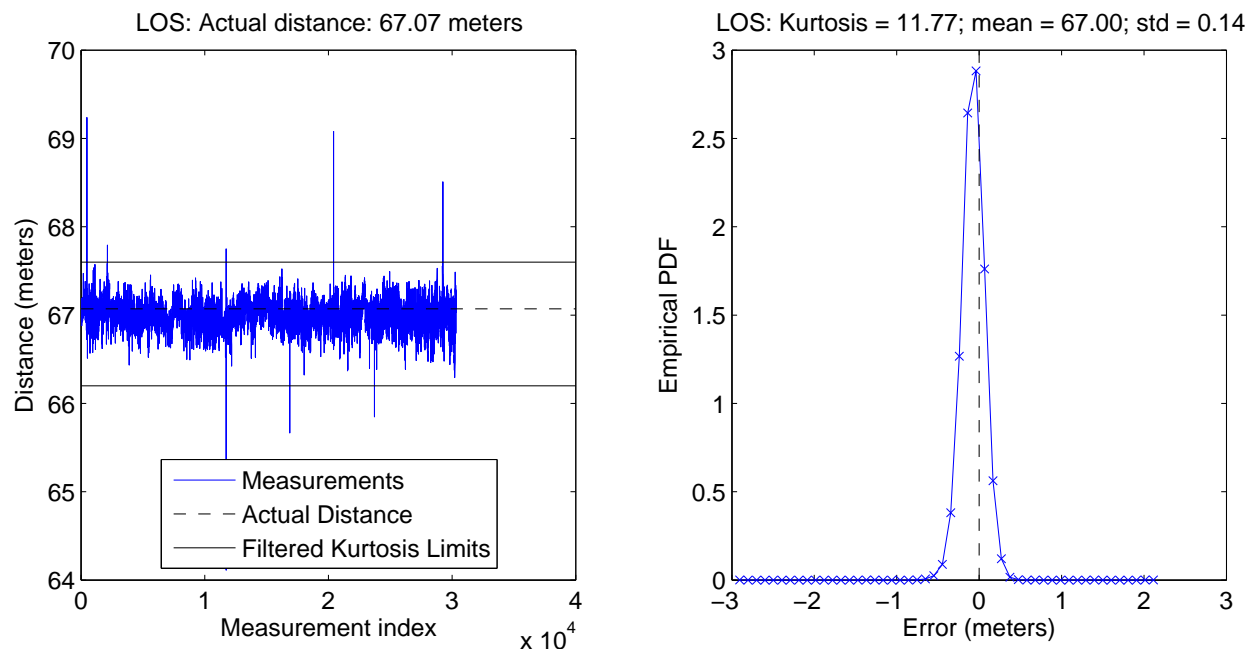


Figure B.13: Calibration, location pair T4, set # 4

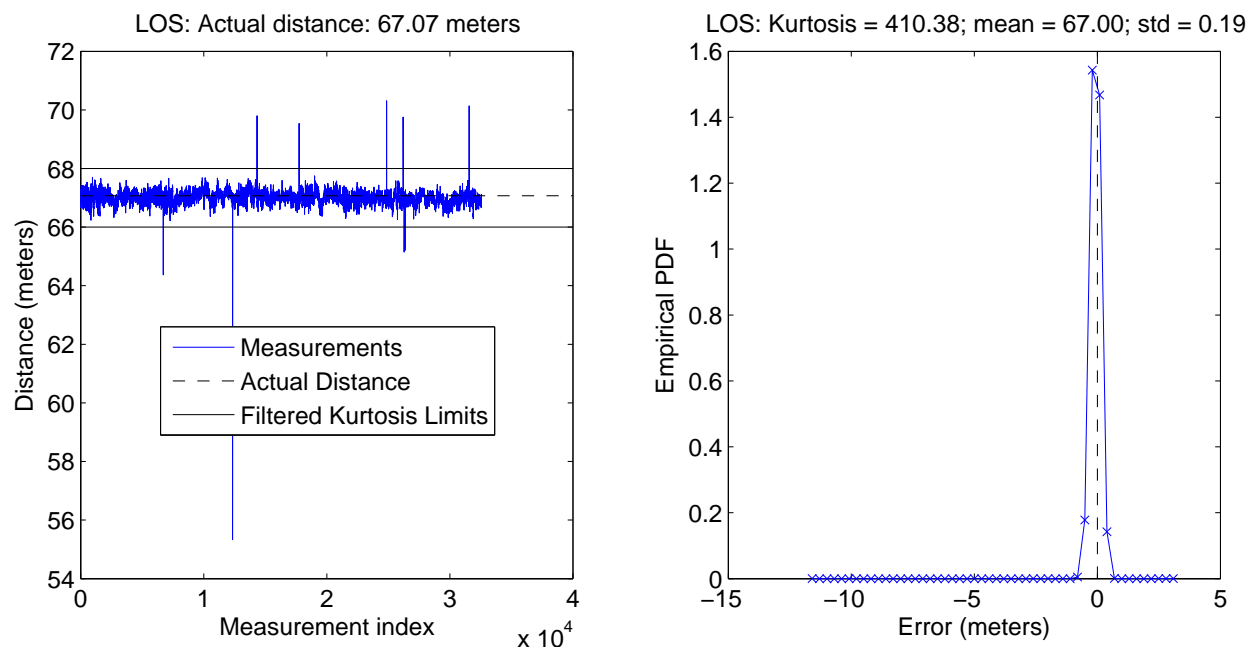


Figure B.14: Calibration, location pair T4, set # 5

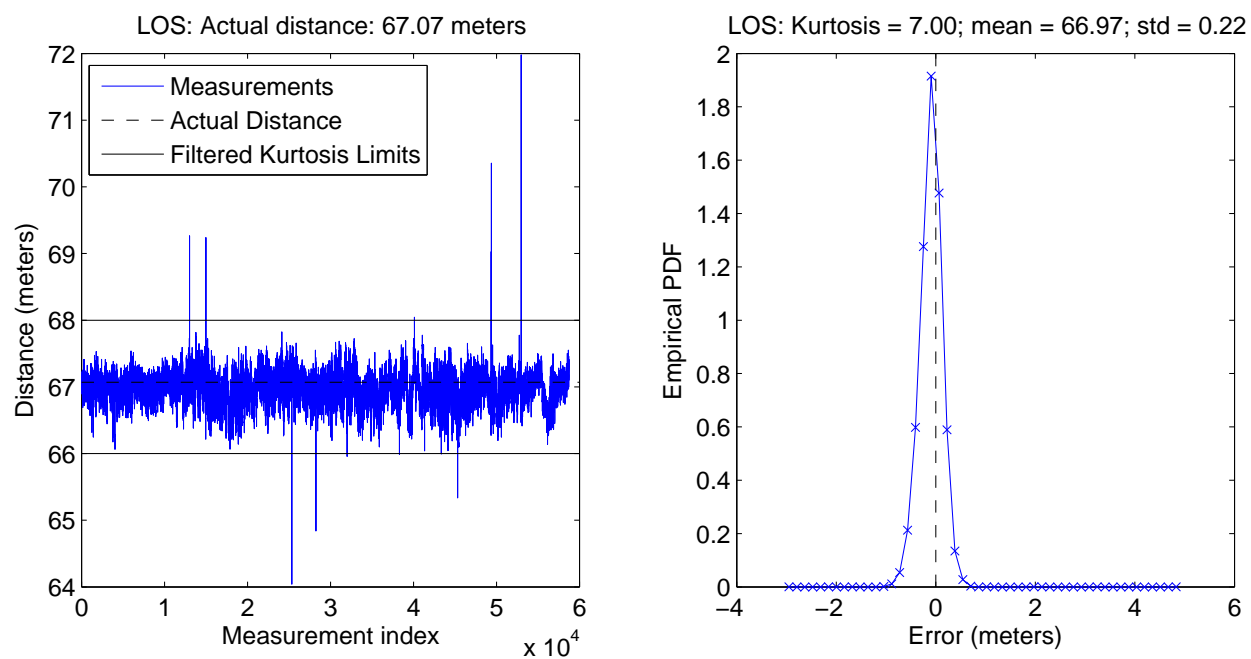


Figure B.15: Calibration, location pair T4, set # 6

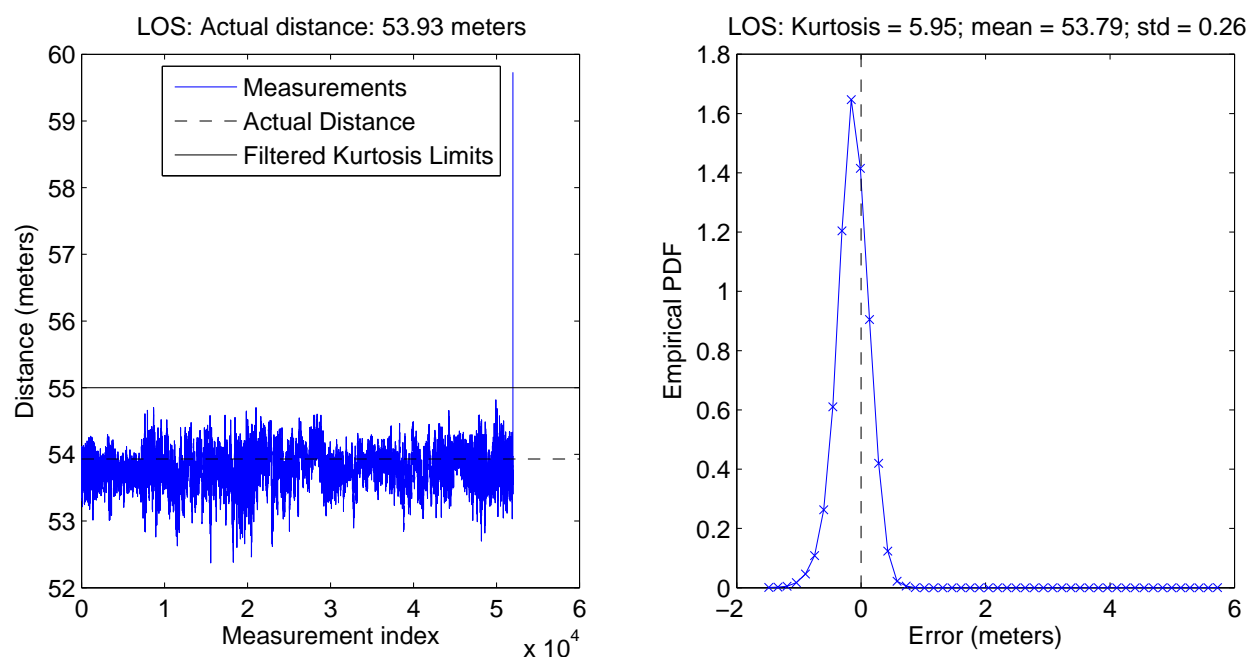


Figure B.16: Calibration, location pair T5, set # 1

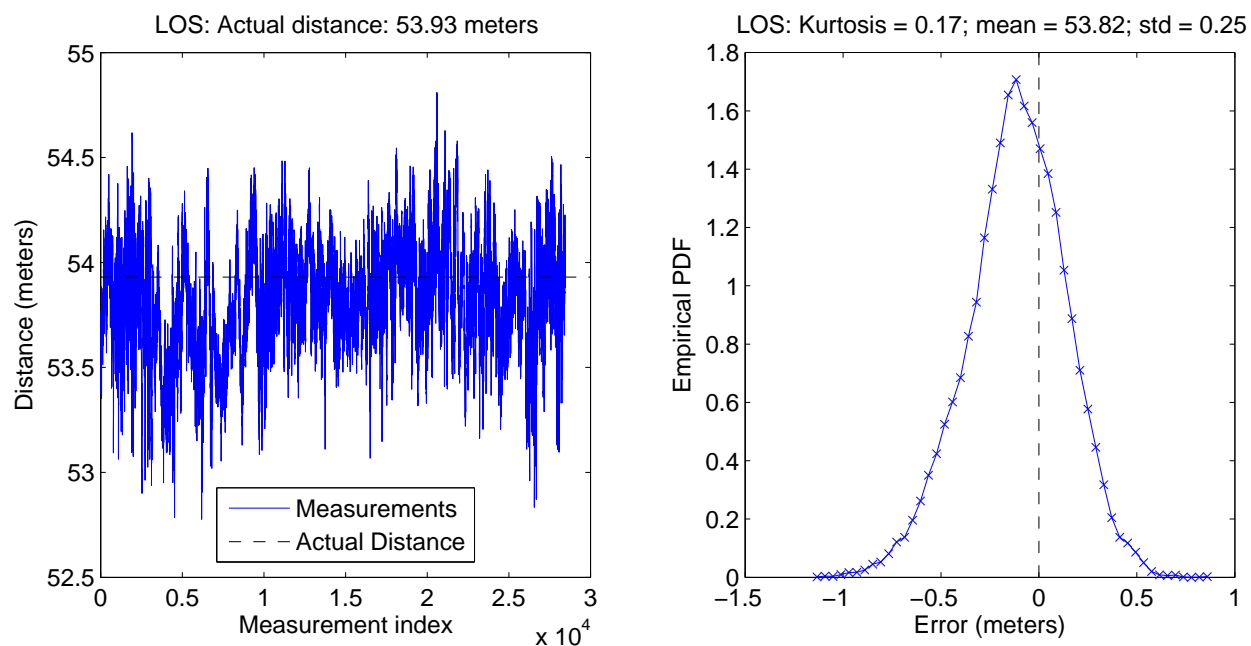


Figure B.17: Calibration, location pair T5, set # 2

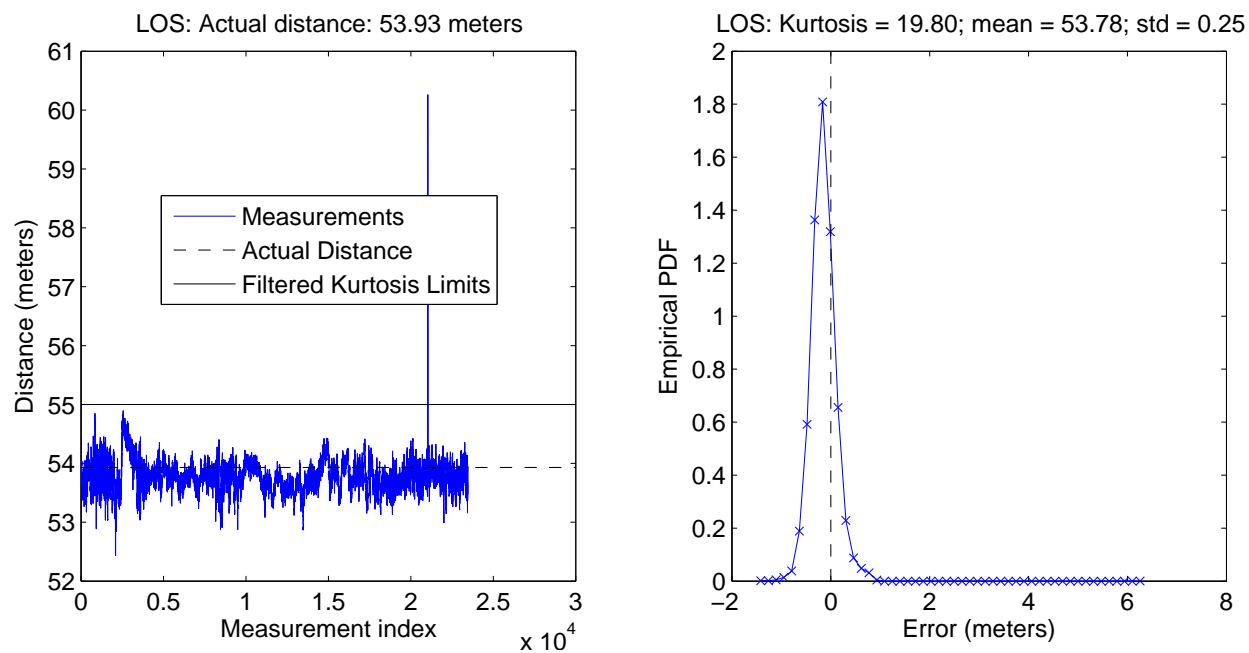


Figure B.18: Calibration, location pair T5, set # 3

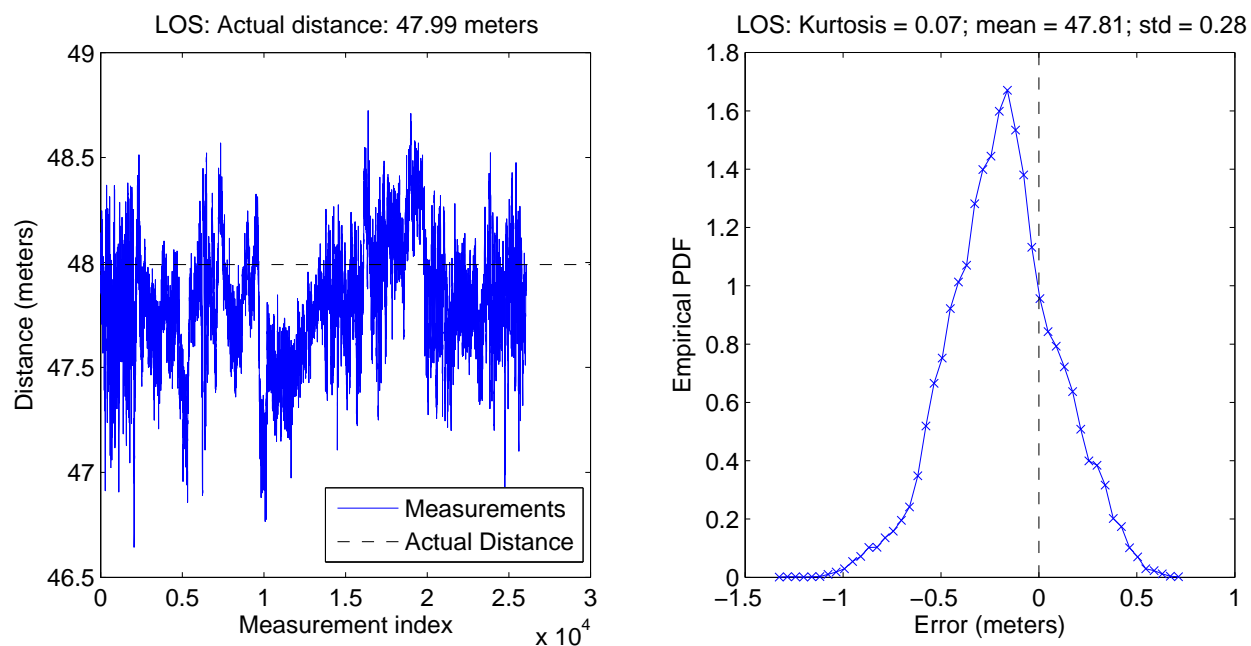


Figure B.19: Calibration, location pair T6, set # 1

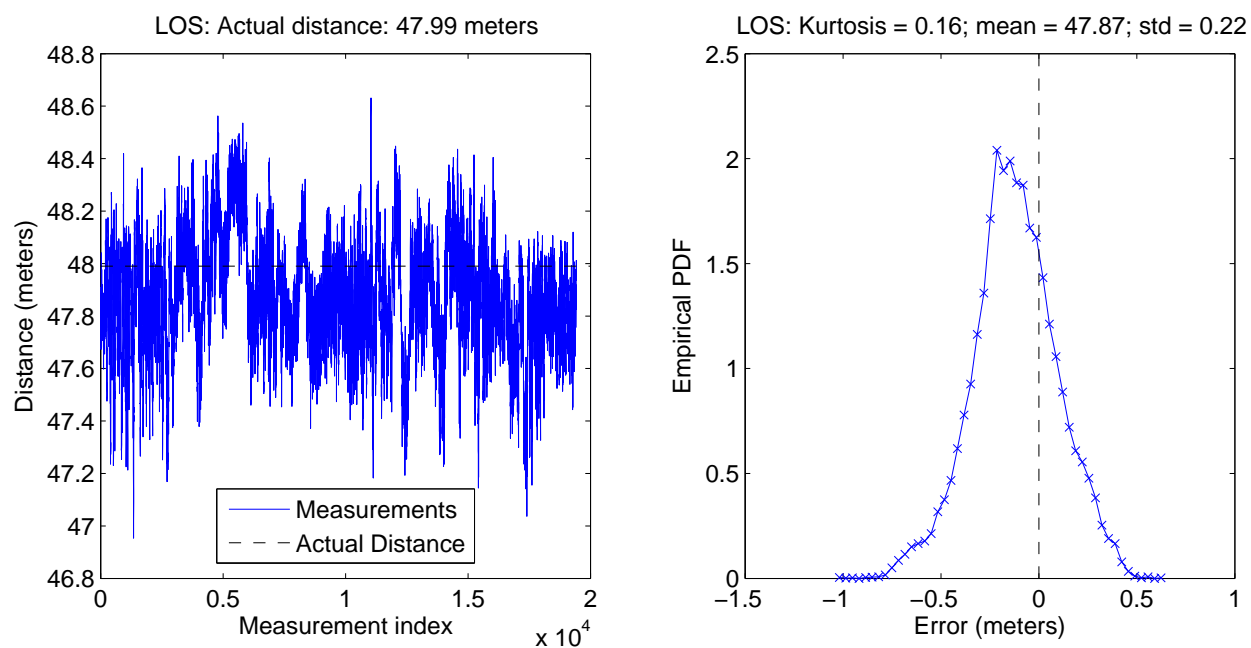


Figure B.20: Calibration, location pair T6, set # 2

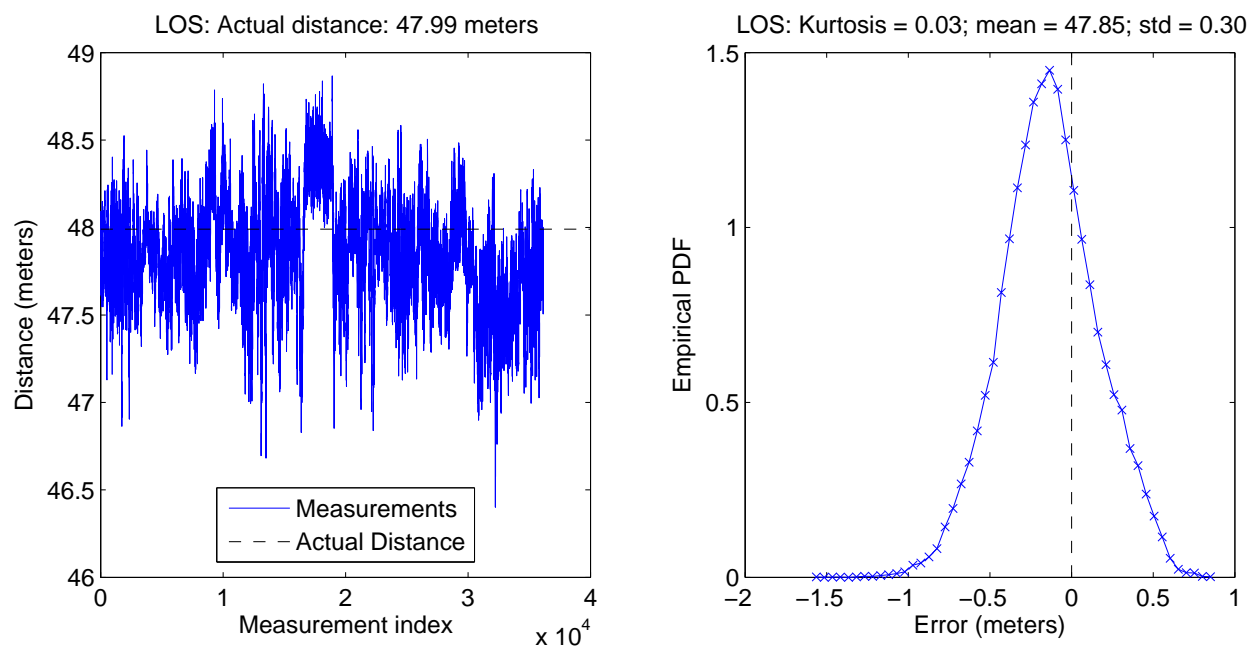


Figure B.21: Calibration, location pair T6, set # 3

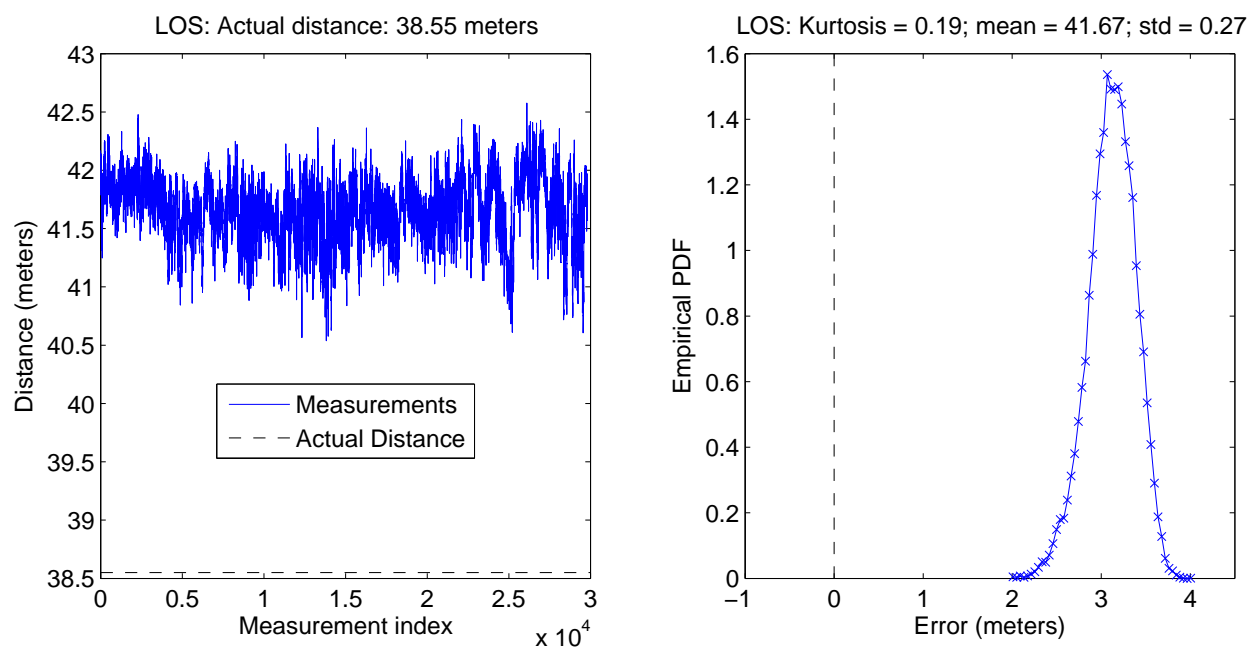


Figure B.22: Calibration, location pair T7, set # 1

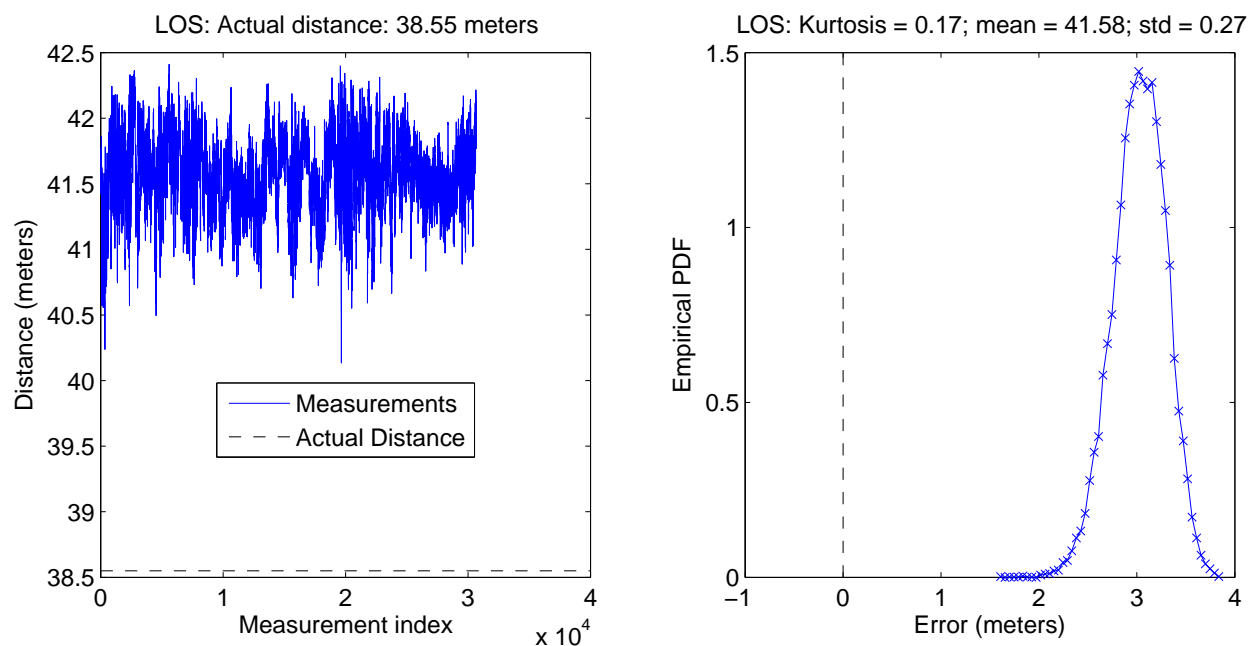


Figure B.23: Calibration, location pair T7, set # 2

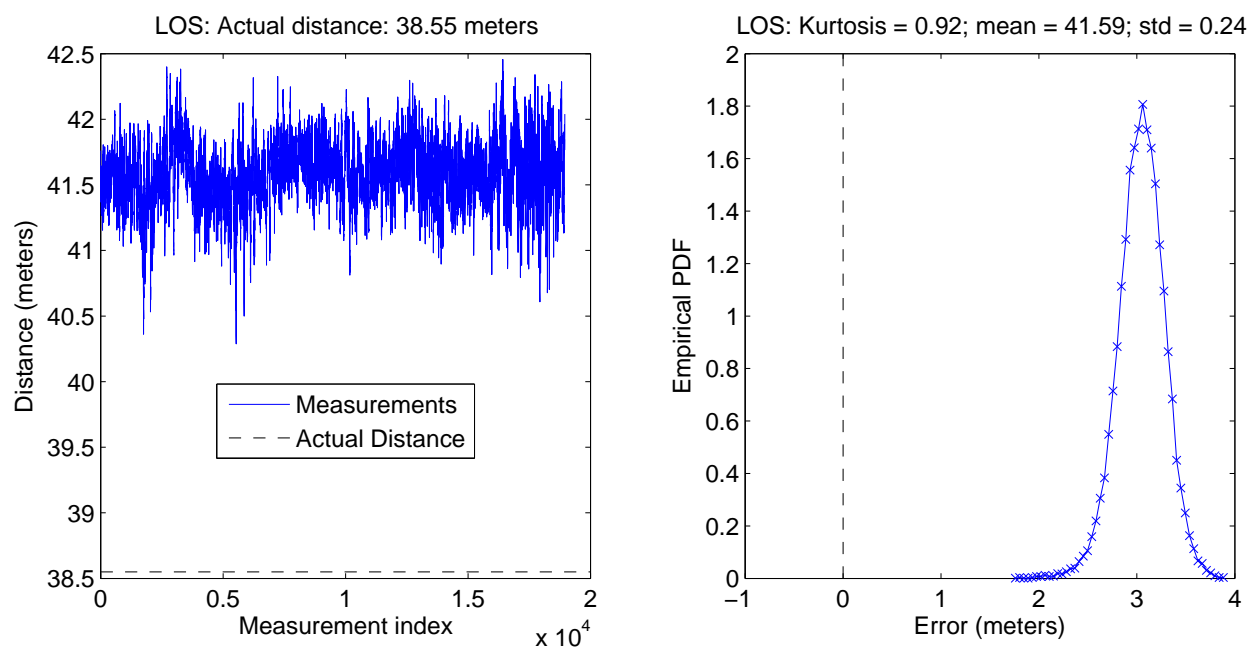


Figure B.24: Calibration, location pair T7, set # 3

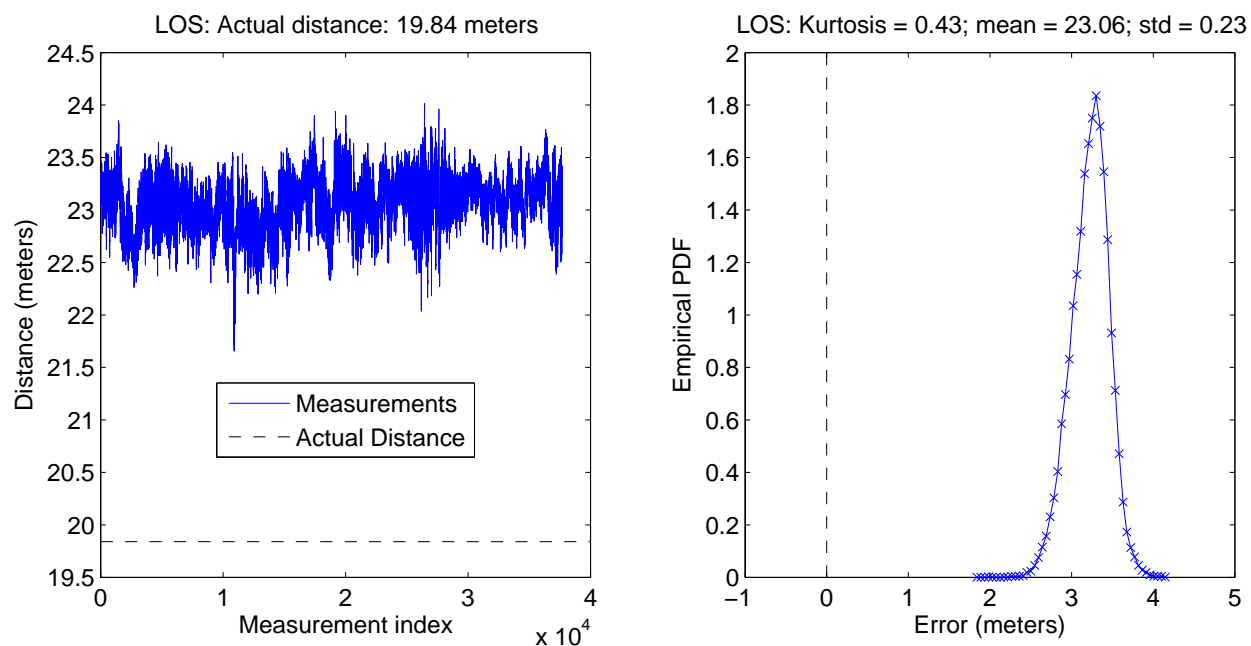


Figure B.25: Calibration, location pair T8, set # 1

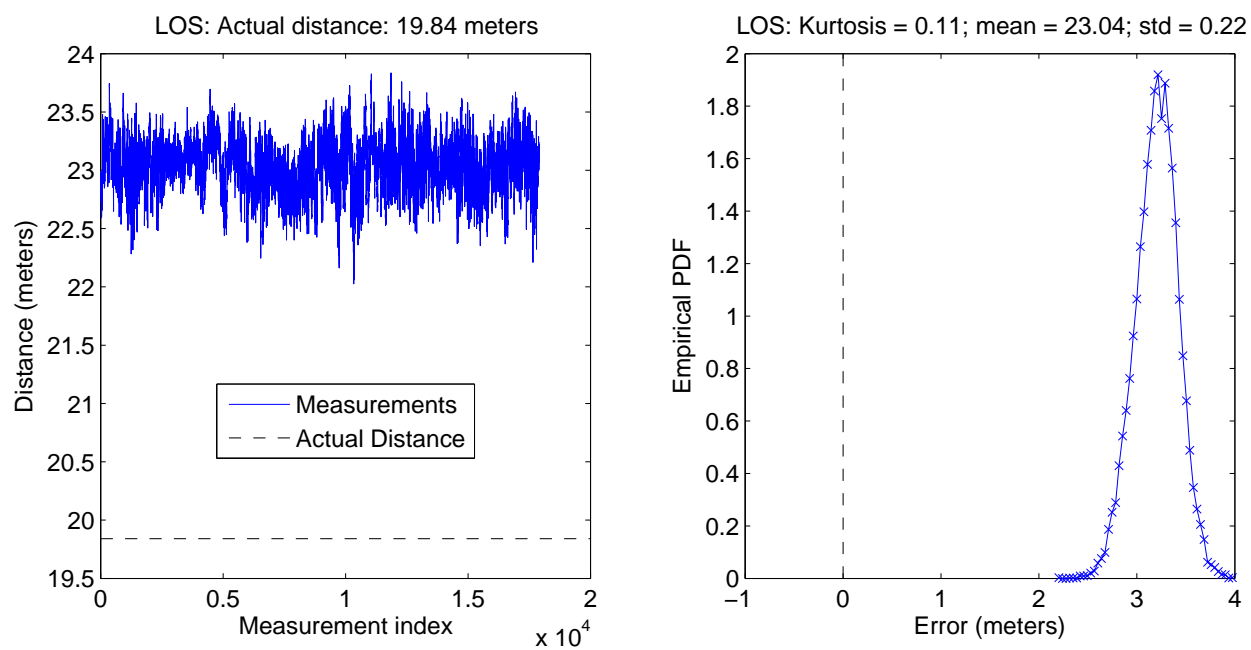


Figure B.26: Calibration, location pair T8, set # 2

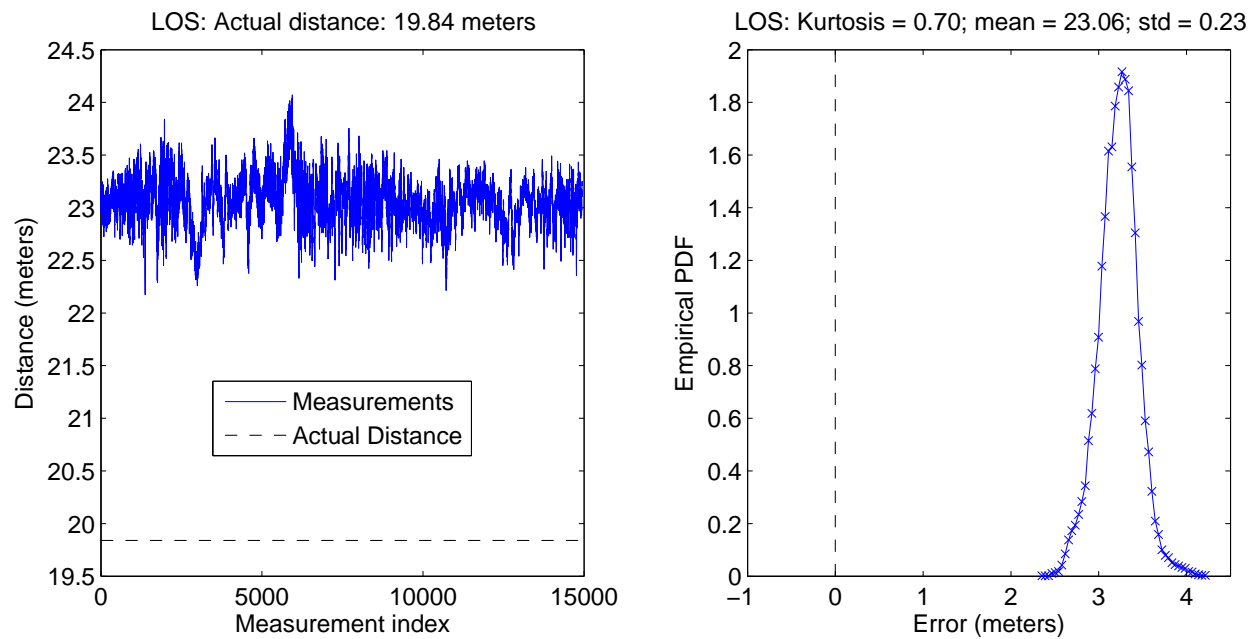


Figure B.27: Calibration, location pair T8, set # 3

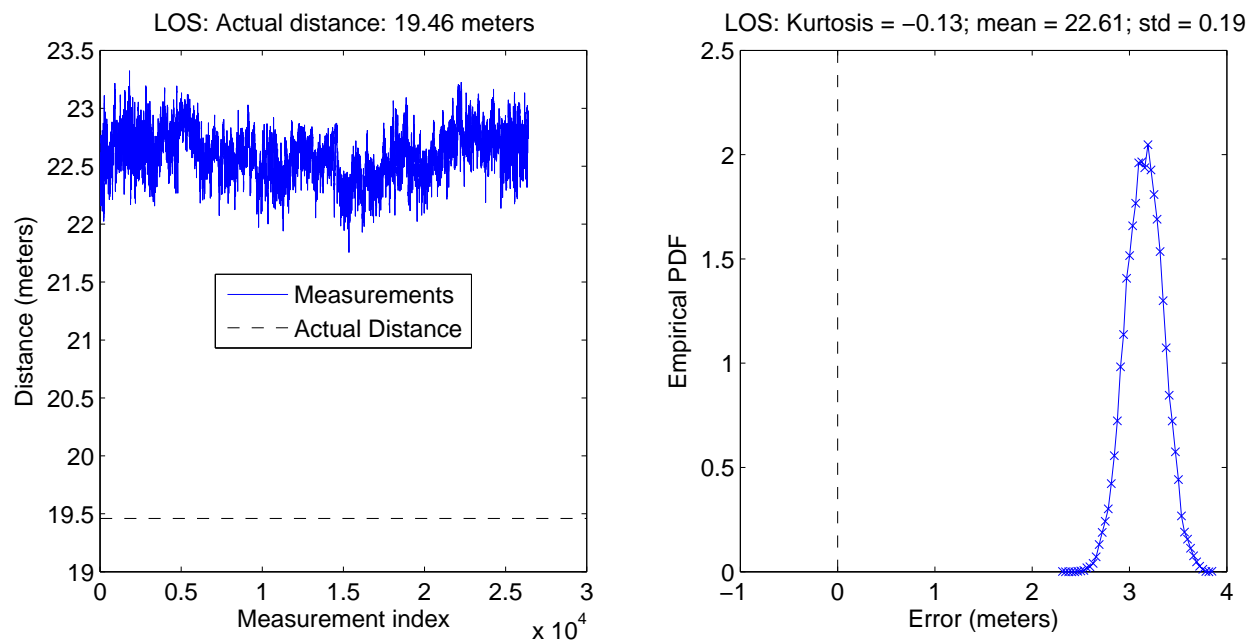


Figure B.28: Calibration, location pair T9, set # 1

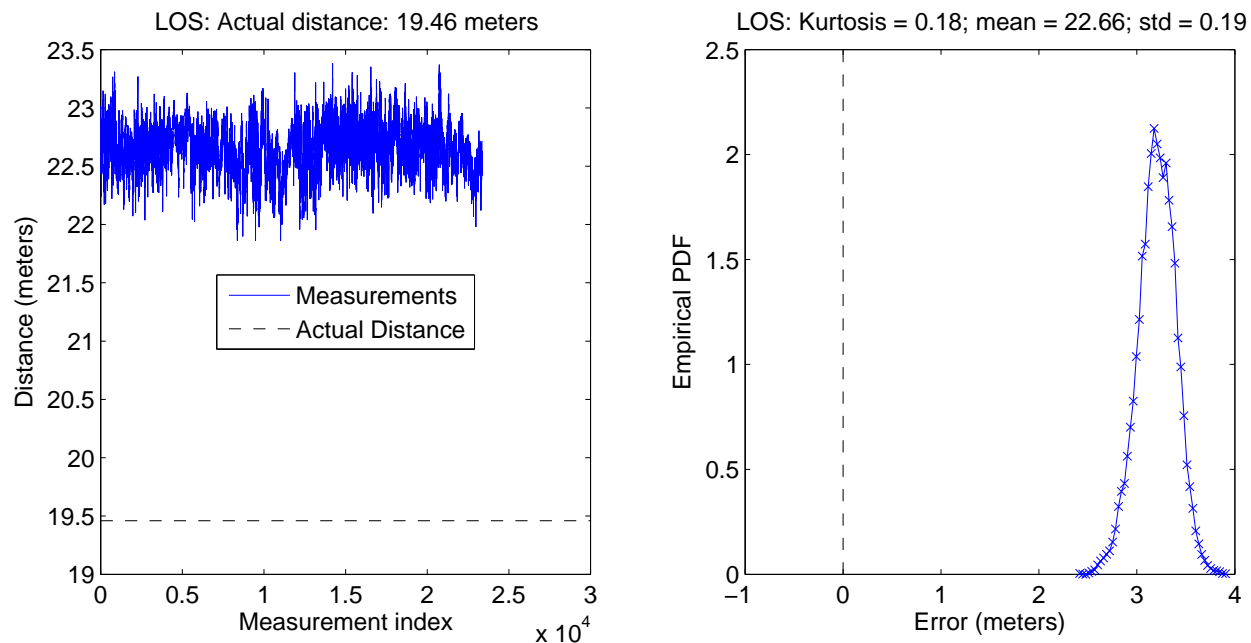


Figure B.29: Calibration, location pair T9, set # 2

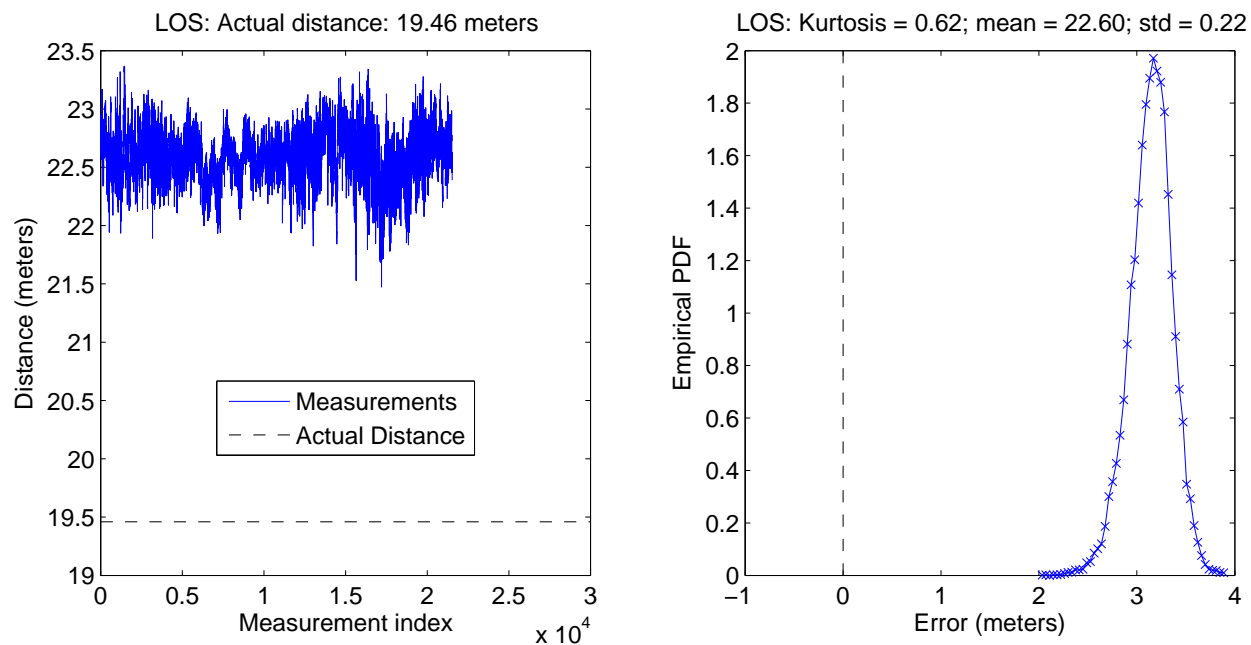


Figure B.30: Calibration, location pair T9, set # 3

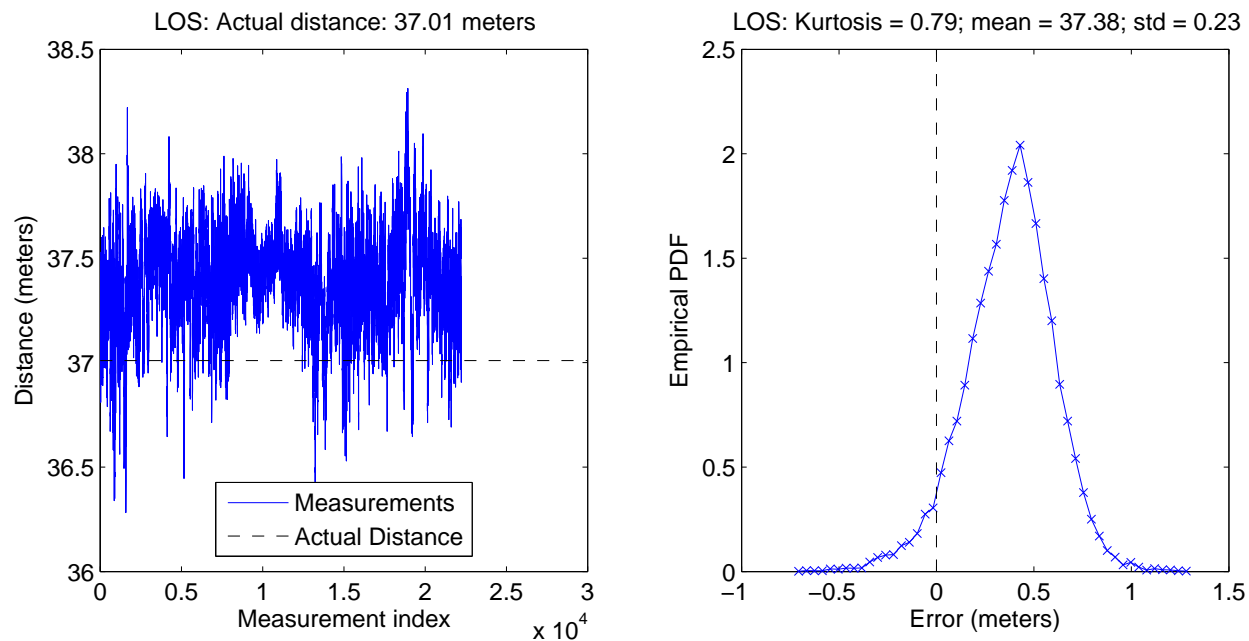


Figure B.31: Calibration, location pair T10, set # 1

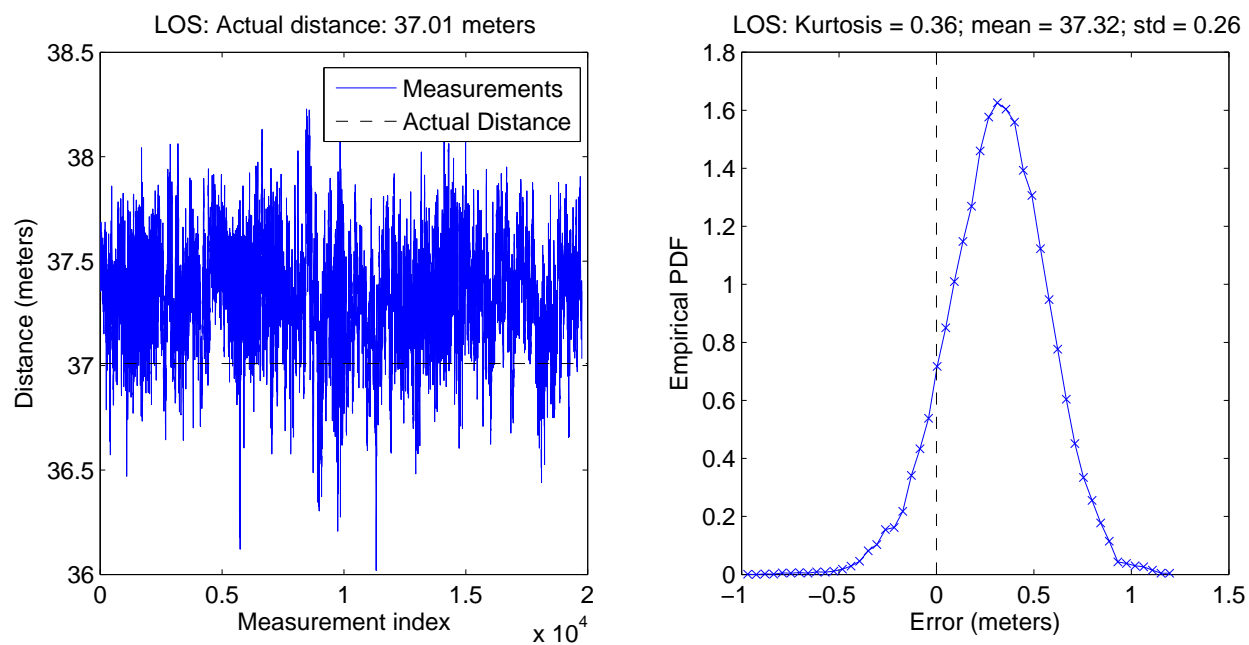


Figure B.32: Calibration, location pair T10, set # 2

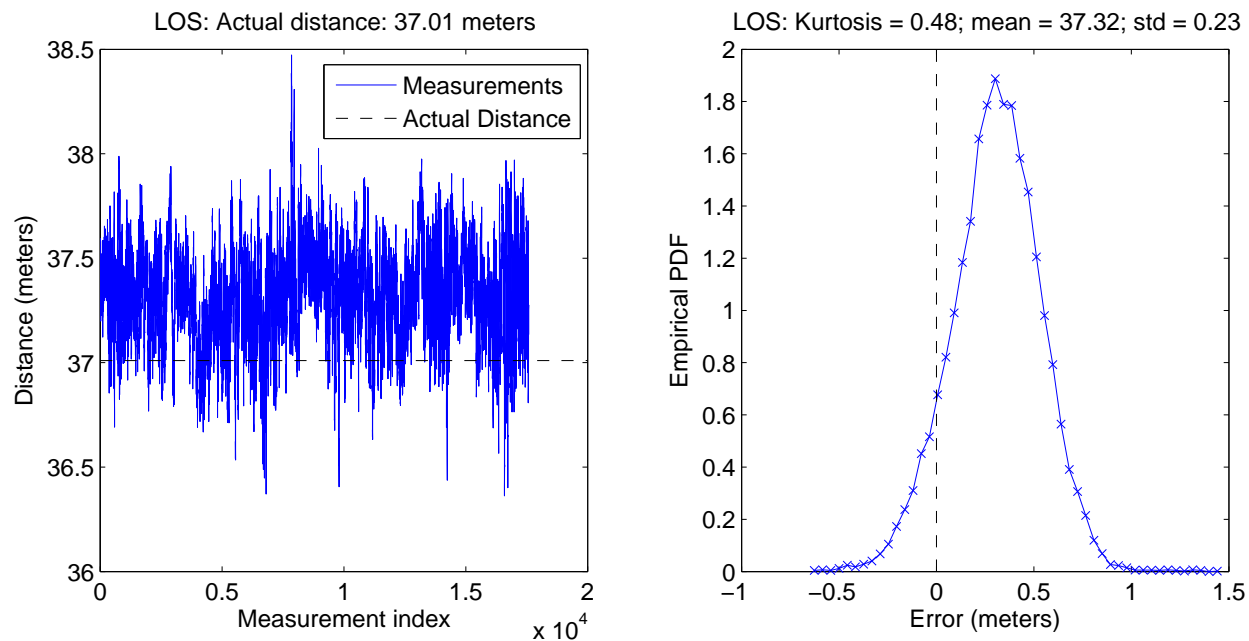


Figure B.33: Calibration, location pair T10, set # 3

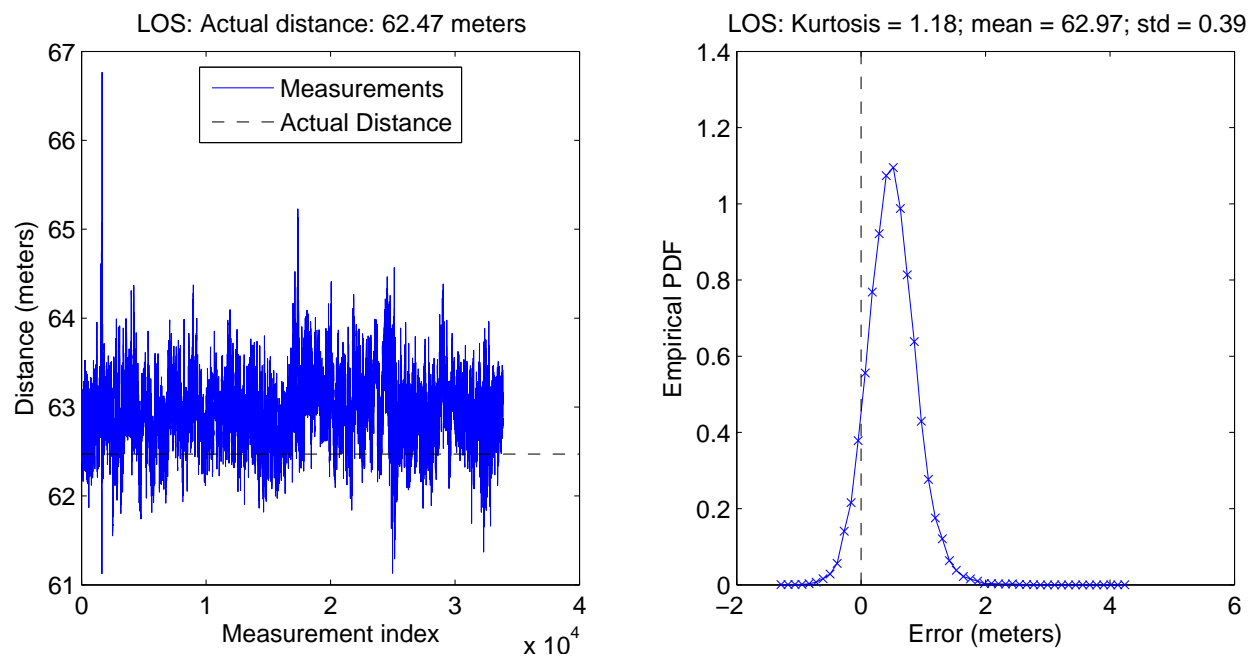


Figure B.34: Calibration, location pair T11, set # 1

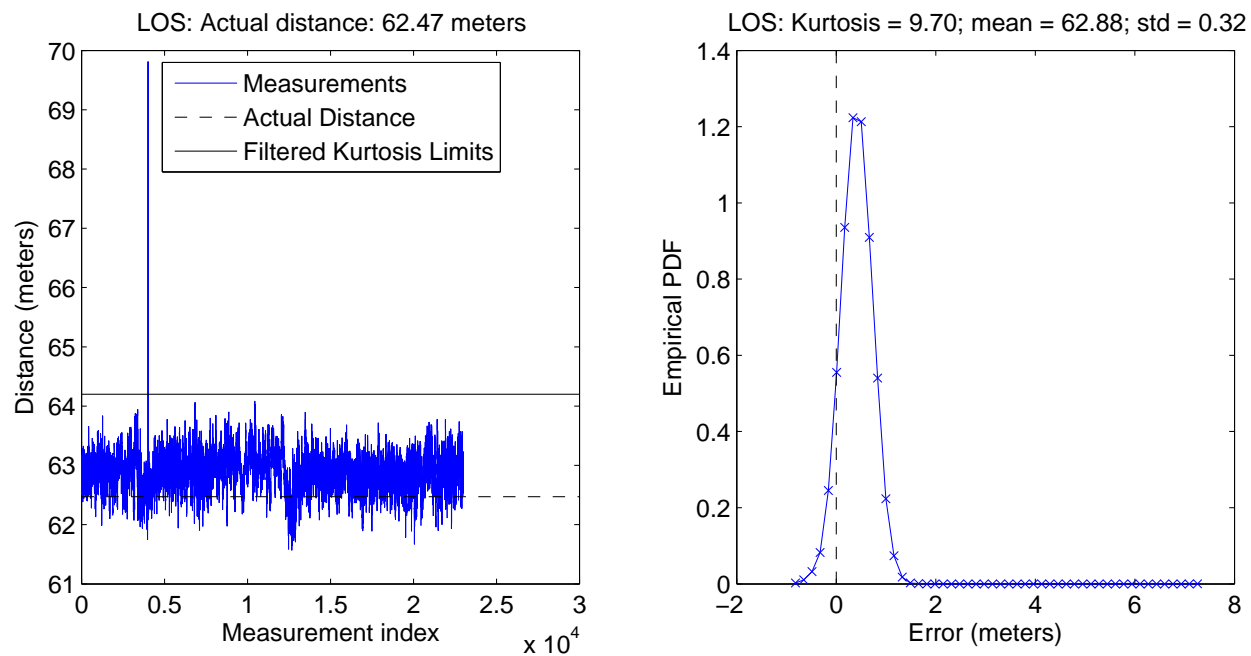


Figure B.35: Calibration, location pair T11, set # 2

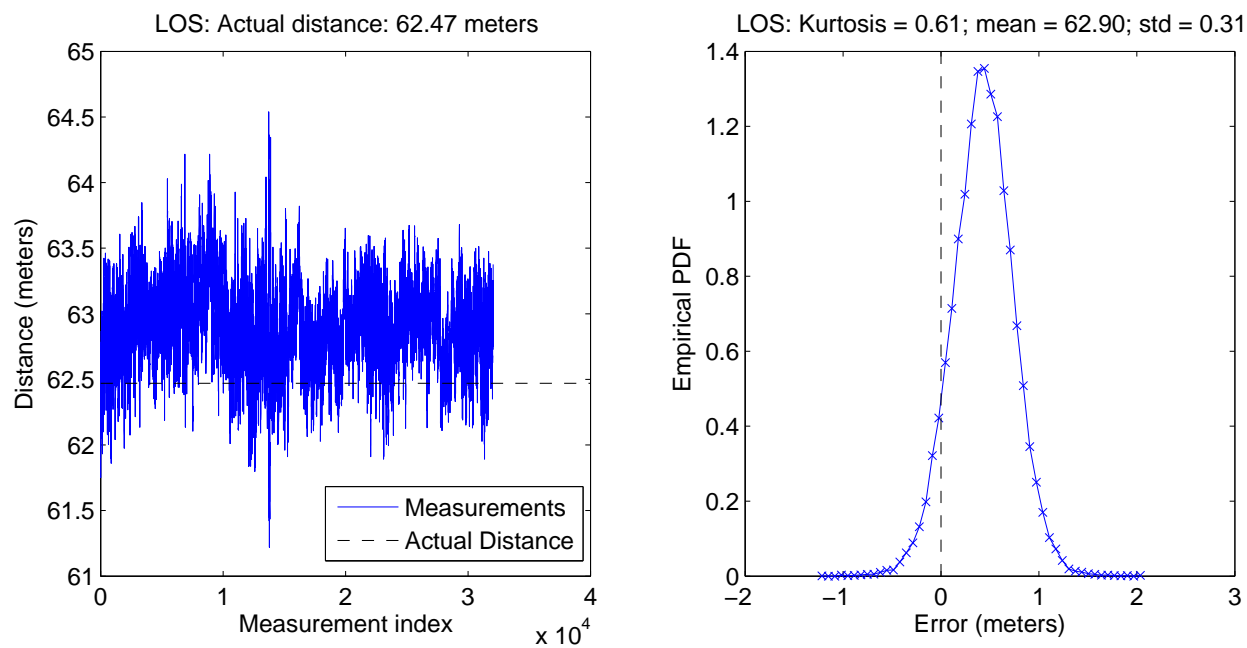


Figure B.36: Calibration, location pair T11, set # 3

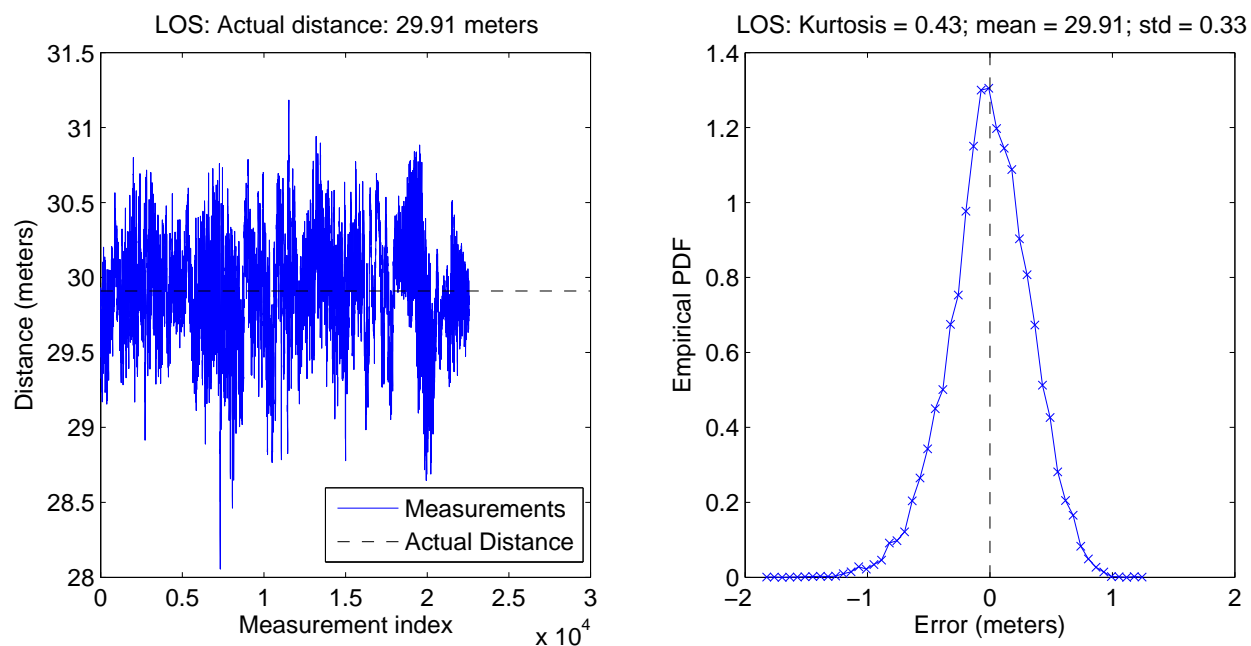


Figure B.37: Calibration, location pair T12, set # 1

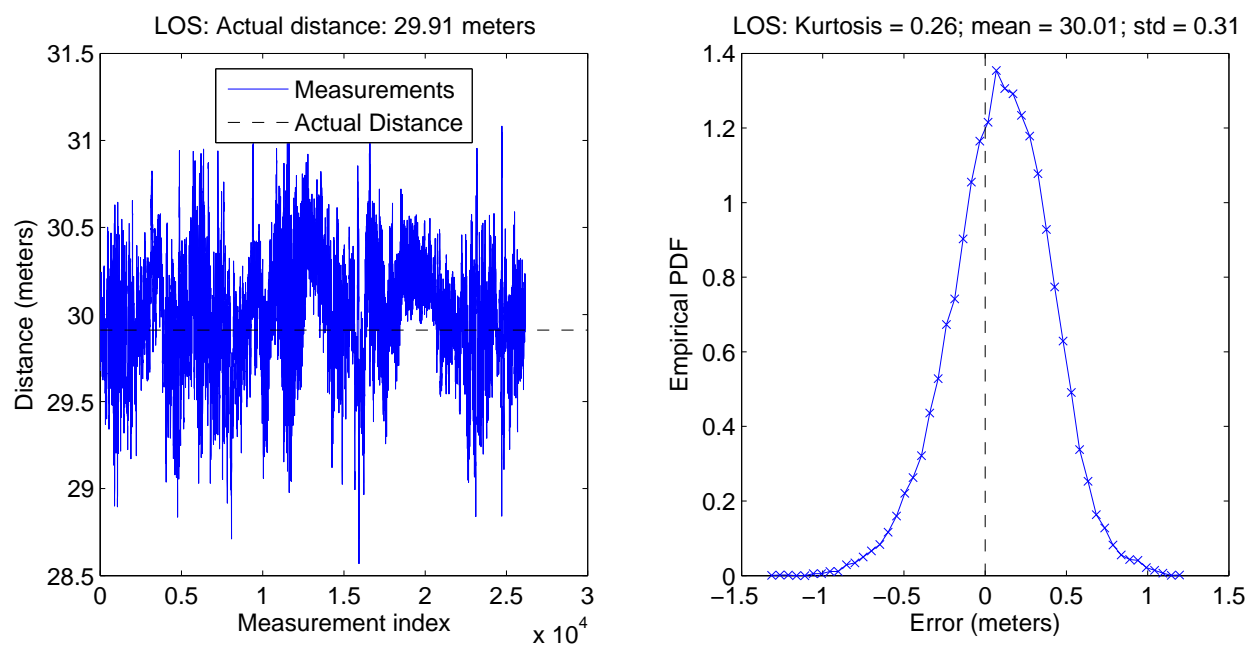


Figure B.38: Calibration, location pair T12, set # 2

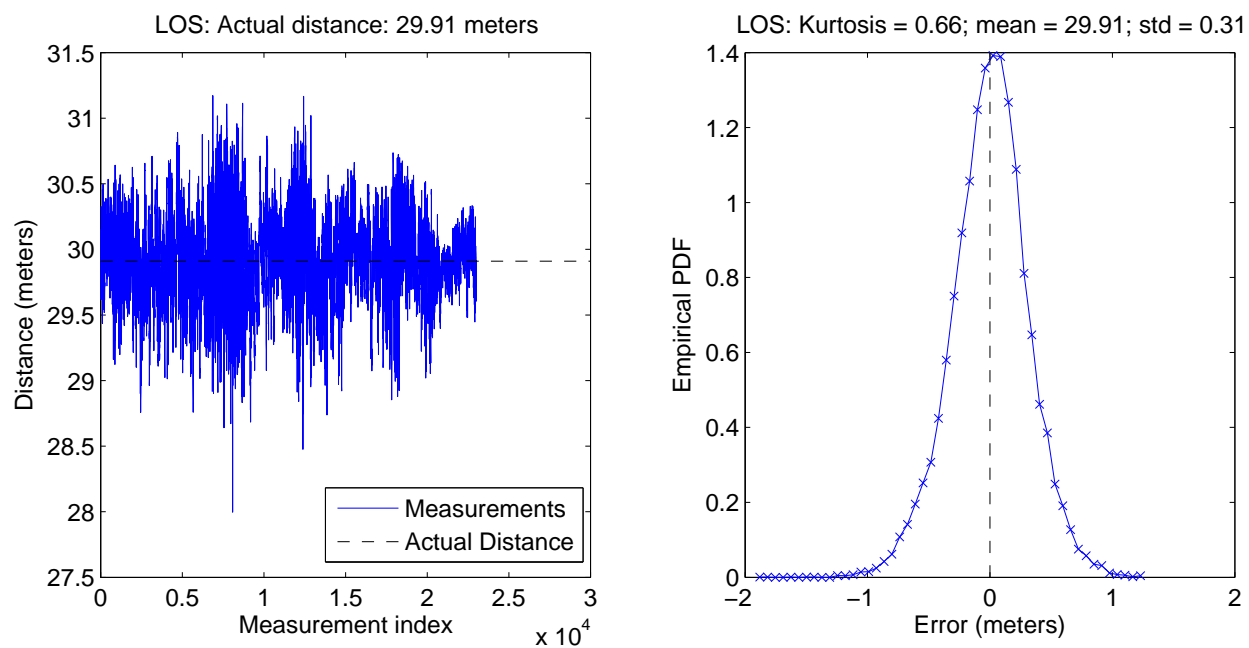


Figure B.39: Calibration, location pair T12, set # 3

## B.2 Durham Hallway, Good LOS Performance Scenario

Table B.2 and Figures B.40 - B.42 (below) summarize the results from data sets in the the Durham hallway, good LOS performance scenario.

Table B.2: Durham Hallway, Good LOS Performance Statistics

Location Pair	Kurtosis	Std. Dev.	Distance			Error	
			Mean	Median	Actual	Mean	Median
T1	-0.2810	1.0808	20.6161	20.5803	19.60	1.02	0.98
T2	38.0238	8.1506	37.0161	35.6323	36.34	0.68	-0.71
T3	33.6032	0.5862	61.4471	61.4340	60.56	0.89	0.87
Average	23.78	3.27				0.86	0.38
Range	38.30	7.56				0.34	1.69

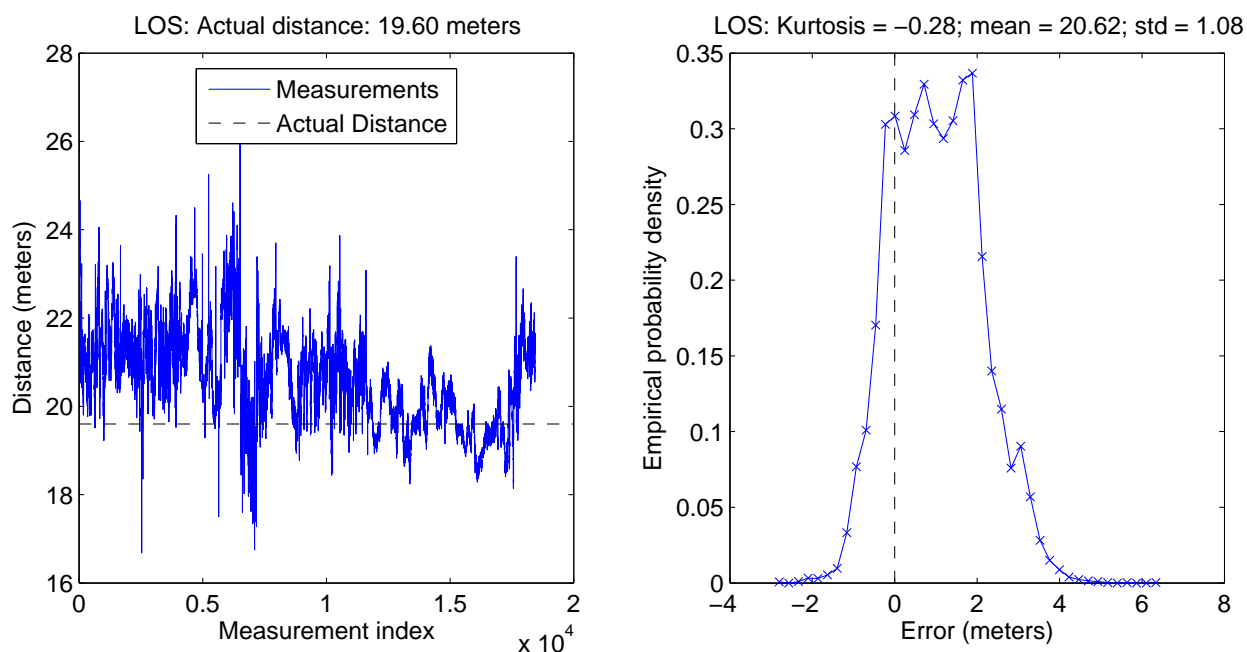


Figure B.40: Durham hallway, good LOS performance, location pair T1

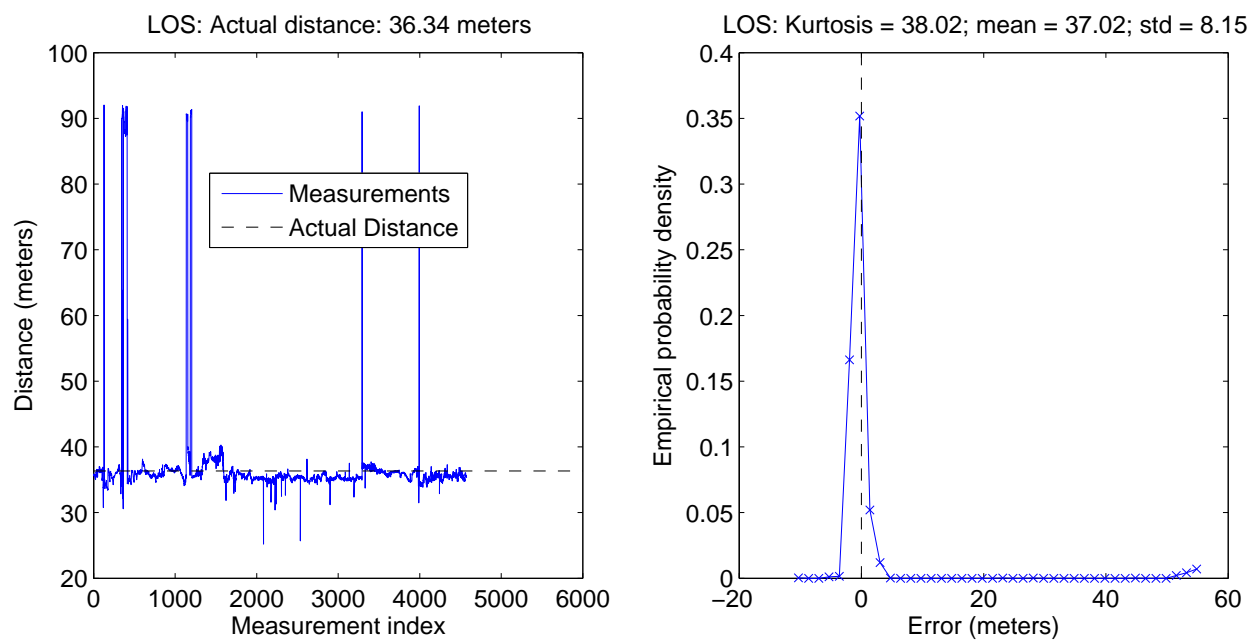


Figure B.41: Durham hallway, good LOS performance, location pair T2

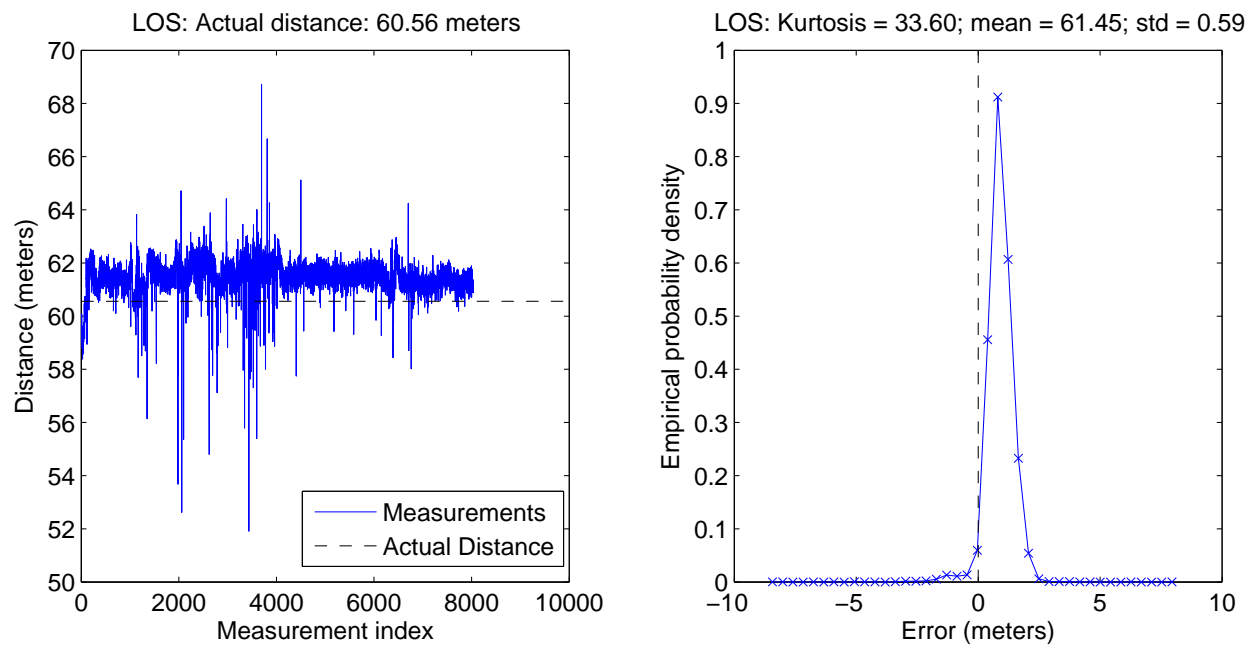


Figure B.42: Durham hallway, good LOS performance, location pair T3

### B.3 Durham Hallway, Moderate LOS Performance Scenario

Table B.3 and Figures B.43 - B.57 (below) summarize the results from data sets in the the Durham hallway, moderate LOS performance scenario.

Table B.3: Durham Hallway, Moderate LOS Performance Statistics

Label			Distance			Error	
Pair/Group	Kurtosis	Std. Dev.	Mean	Median	Actual	Mean	Median
T1/1	2.4507	0.6425	8.3402	8.4506	9.13	-0.79	-0.68
T1/2	-0.8275	1.1232	7.9247	7.9994	9.13	-1.21	-1.13
T1/3	-0.1475	1.5277	6.2414	6.1954	9.11	-2.87	-2.91
T2/1	0.5605	1.3578	18.9275	19.0926	18.27	0.66	0.82
T2/2	0.4423	2.6007	25.0980	25.3482	18.31	6.79	7.04
T2/3	3.1044	1.6551	25.9048	26.2232	18.30	7.60	7.92
T3/1	3.9286	0.6348	26.2890	26.2209	27.41	-1.12	-1.19
T3/2	1.0727	0.9349	28.1537	28.0374	27.39	0.76	0.65
T3/3	4.6812	0.5229	27.0788	27.1317	27.41	-0.33	-0.28
T4/1	-1.9168	26.5438	69.7185	93.0790	36.56	33.16	56.52
T4/2	1.2914	20.0626	85.3922	94.2441	36.55	48.84	57.69
T4/3	684.9964	2.1282	37.5763	37.4936	36.56	1.02	0.93
T5/1	21.4474	7.4075	82.0747	83.7089	45.71	36.36	38.00
T5/2	-1.0350	16.2047	57.0995	47.6368	45.72	11.38	1.92
T5/3	-1.8736	19.9323	68.4160	84.4949	45.69	22.73	38.80
Average	47.88	6.89				10.87	13.61
Range	686.91	26.02				51.71	60.61

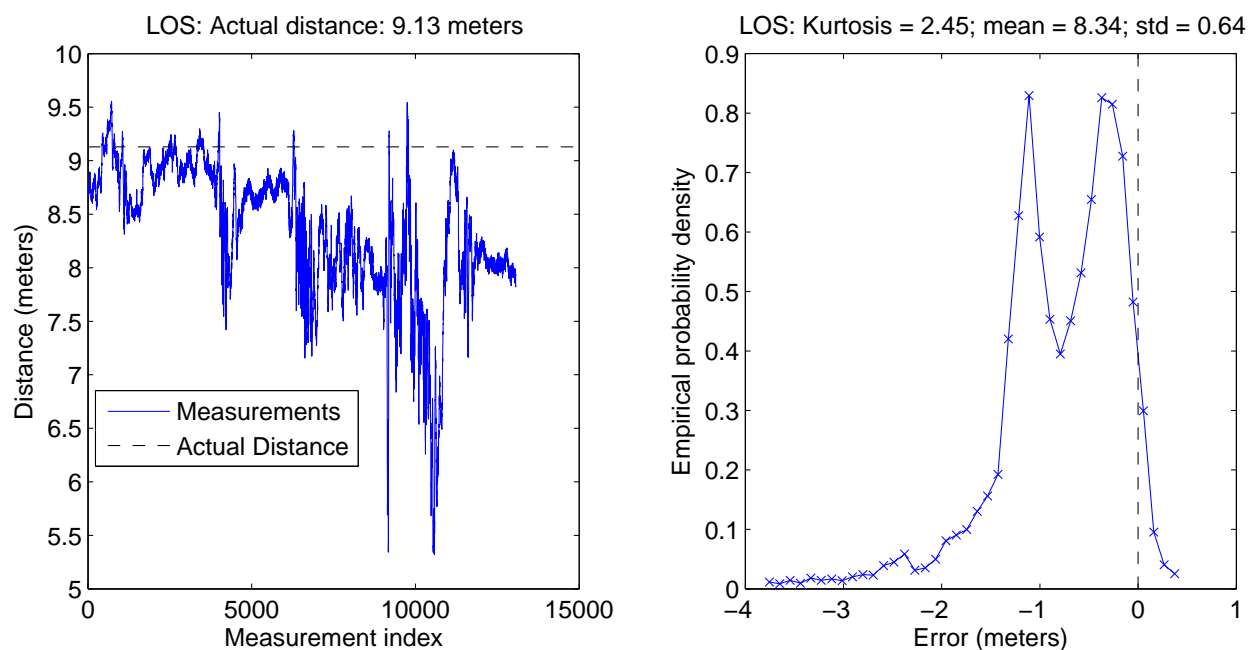


Figure B.43: Durham hallway, moderate LOS performance, location pair T1, group # 1

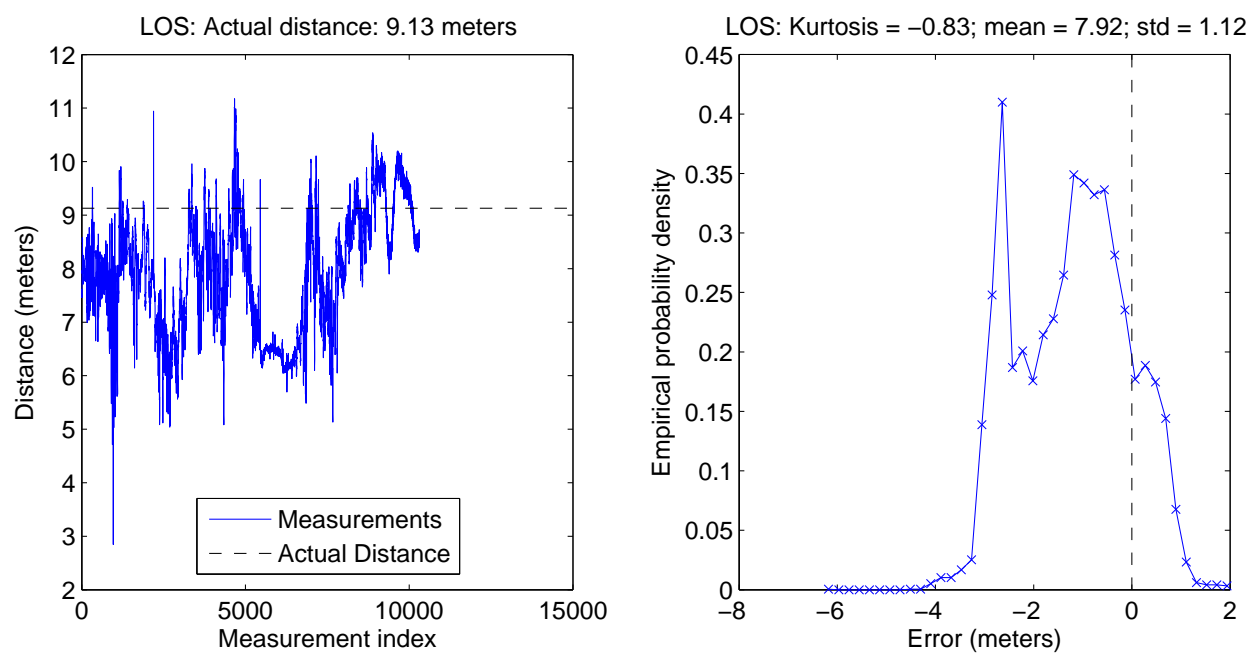


Figure B.44: Durham hallway, moderate LOS performance, location pair T1, group # 2

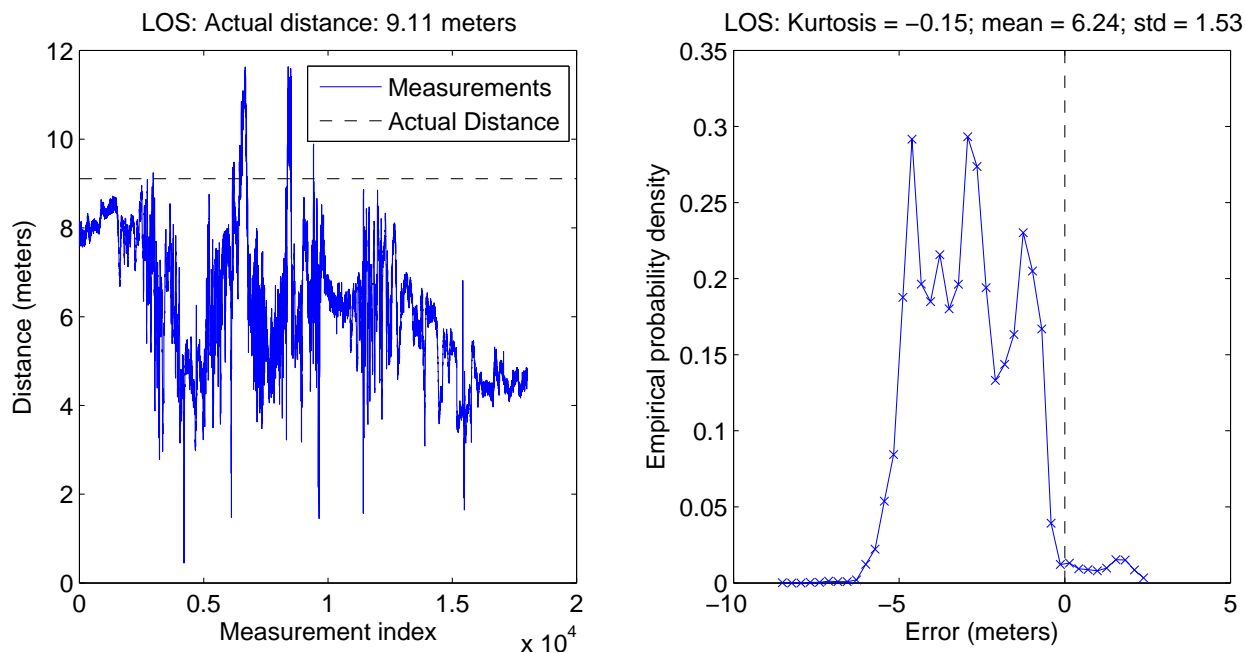


Figure B.45: Durham hallway, moderate LOS performance, location pair T1, group # 3

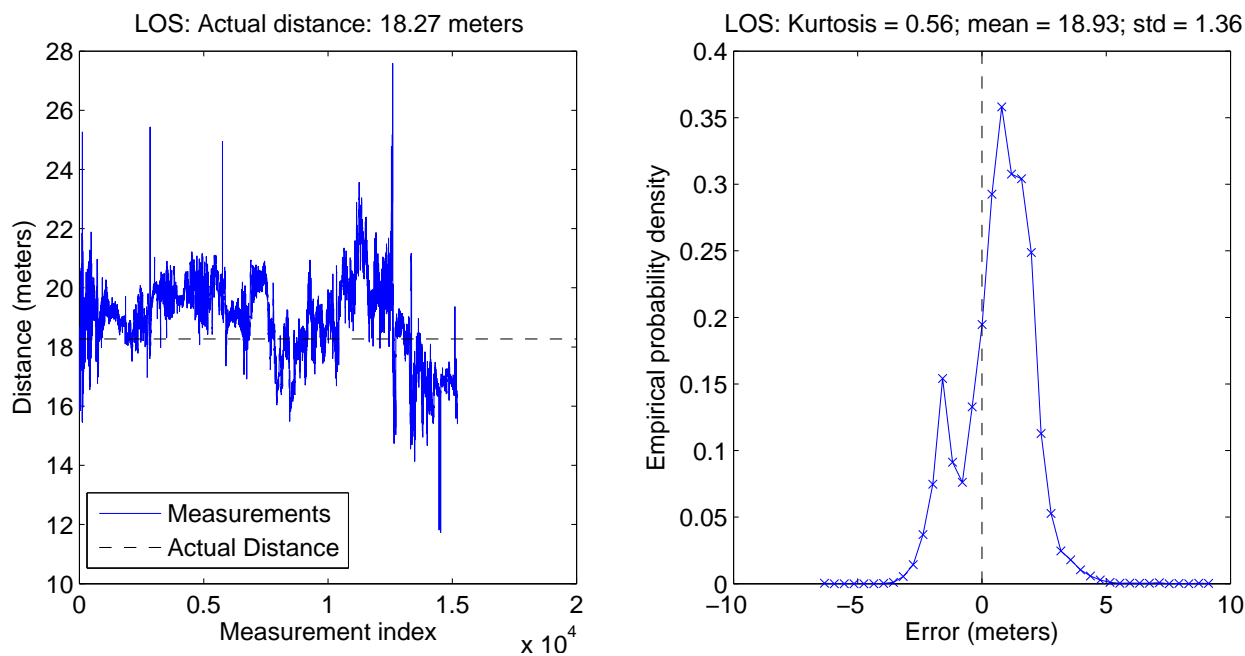


Figure B.46: Durham hallway, moderate LOS performance, location pair T2, group # 1

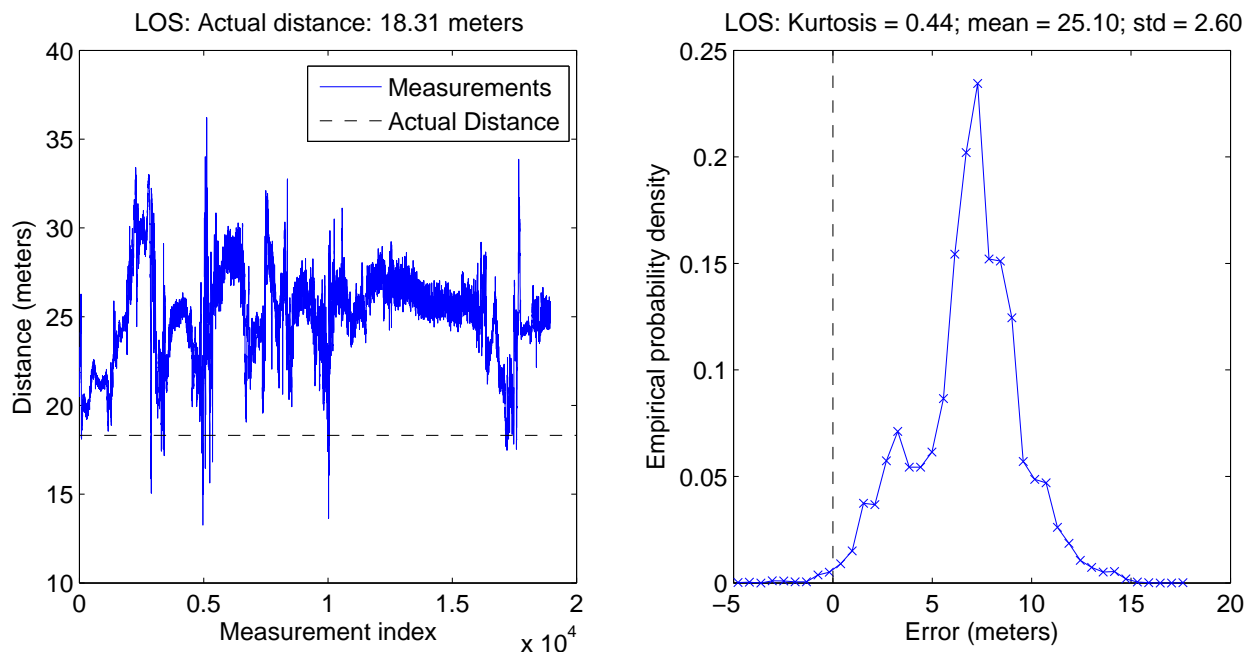


Figure B.47: Durham hallway, moderate LOS performance, location pair T2, group # 2

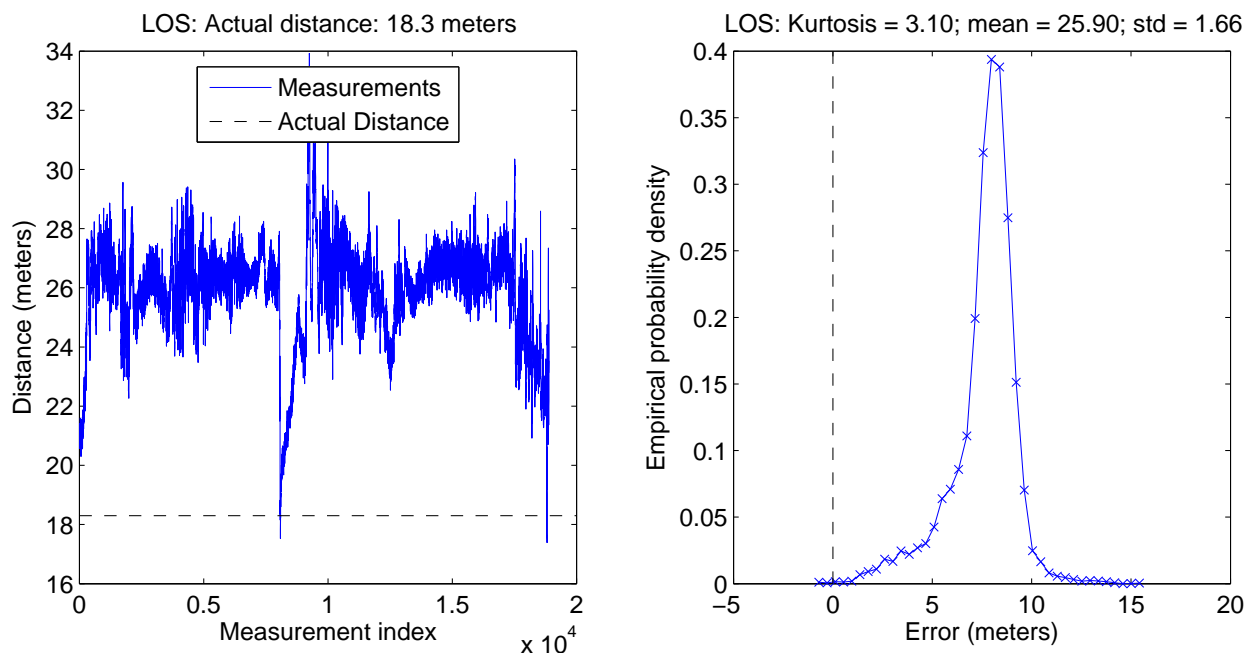


Figure B.48: Durham hallway, moderate LOS performance, location pair T2, group # 3

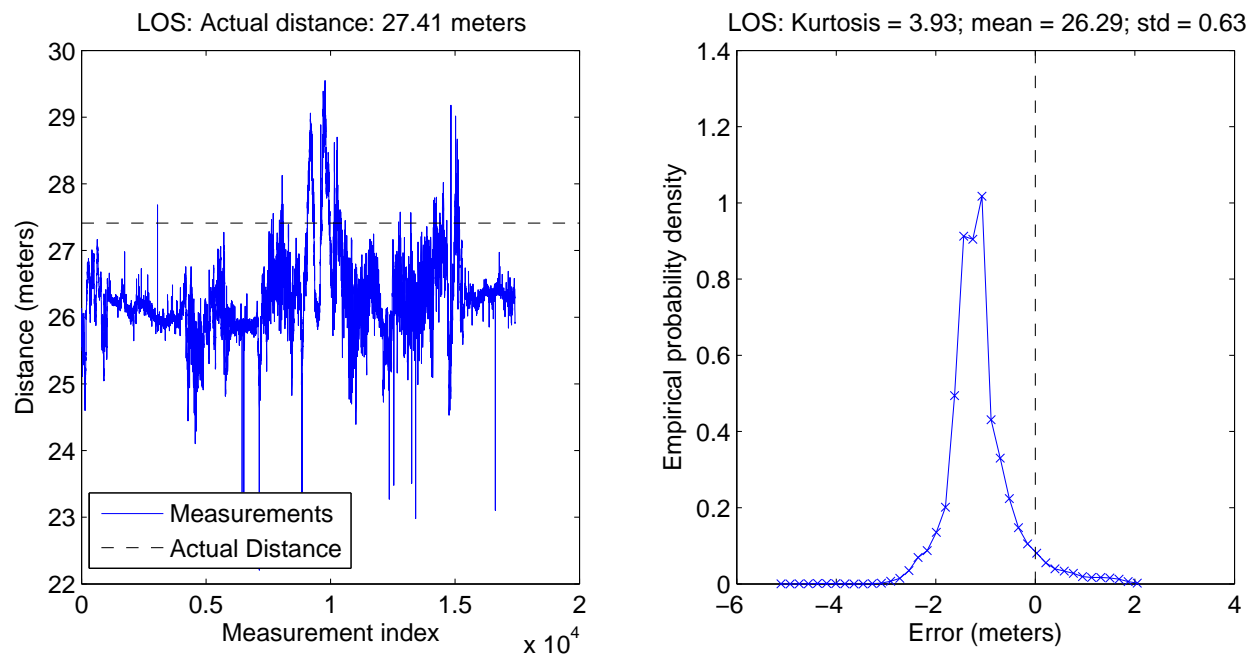


Figure B.49: Durham hallway, moderate LOS performance, location pair T3, group # 1

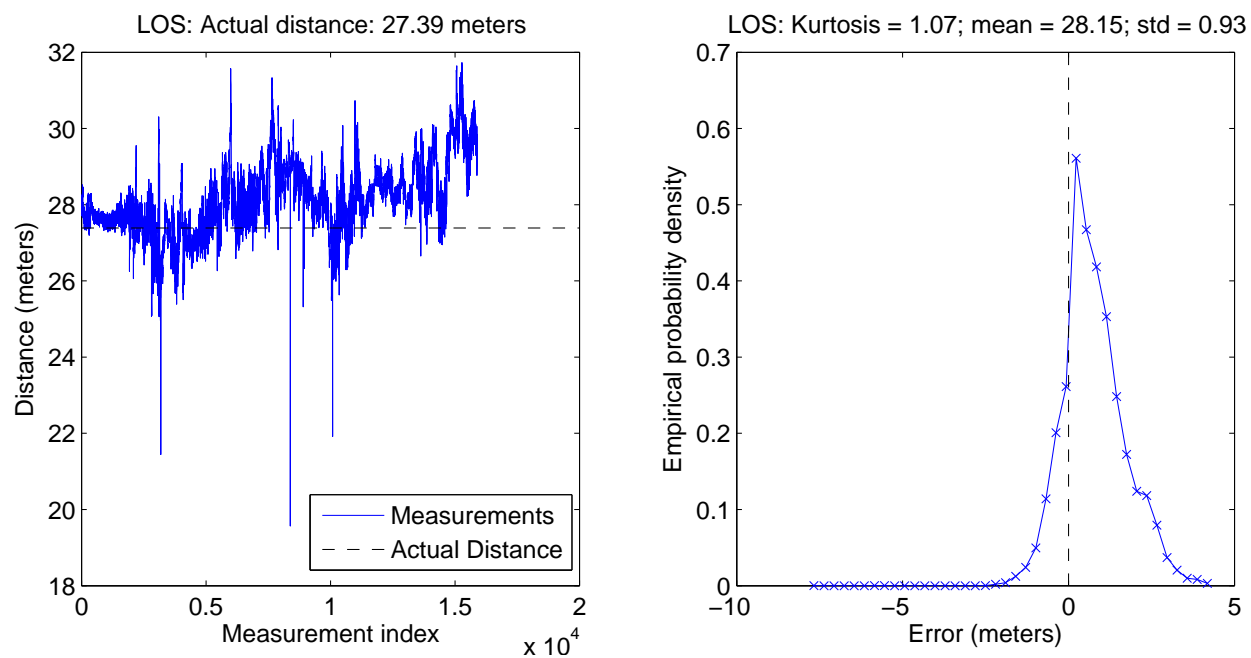


Figure B.50: Durham hallway, moderate LOS performance, location pair T3, group # 2

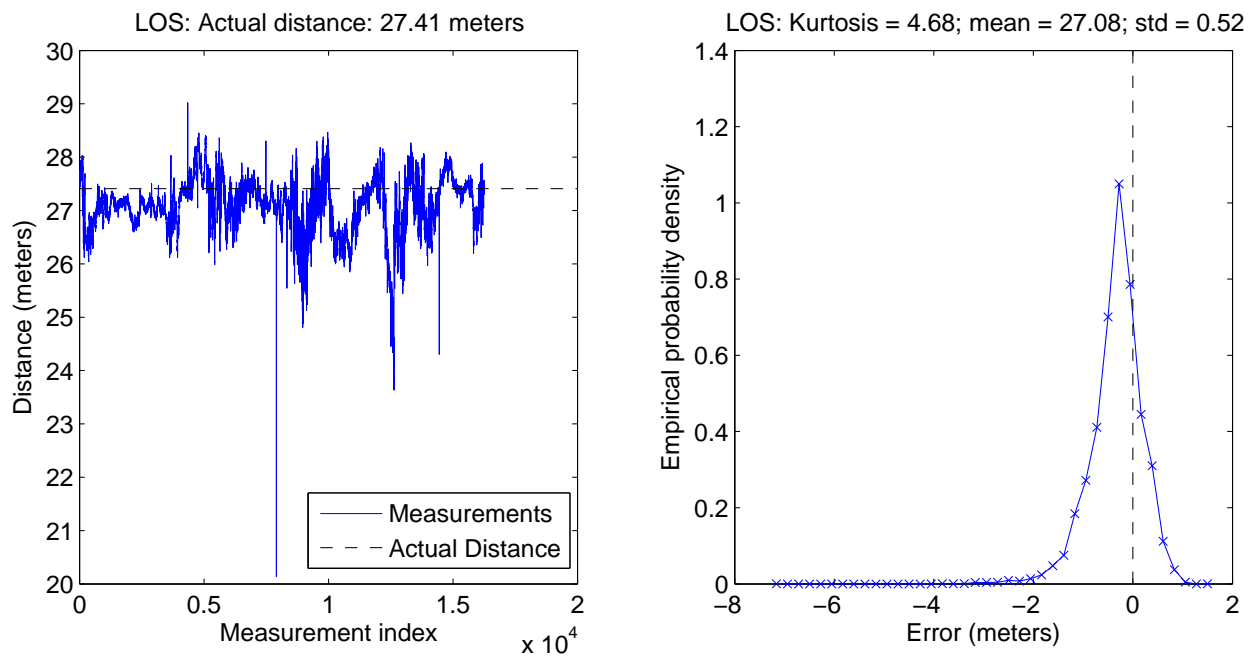


Figure B.51: Durham hallway, moderate LOS performance, location pair T3, group # 3

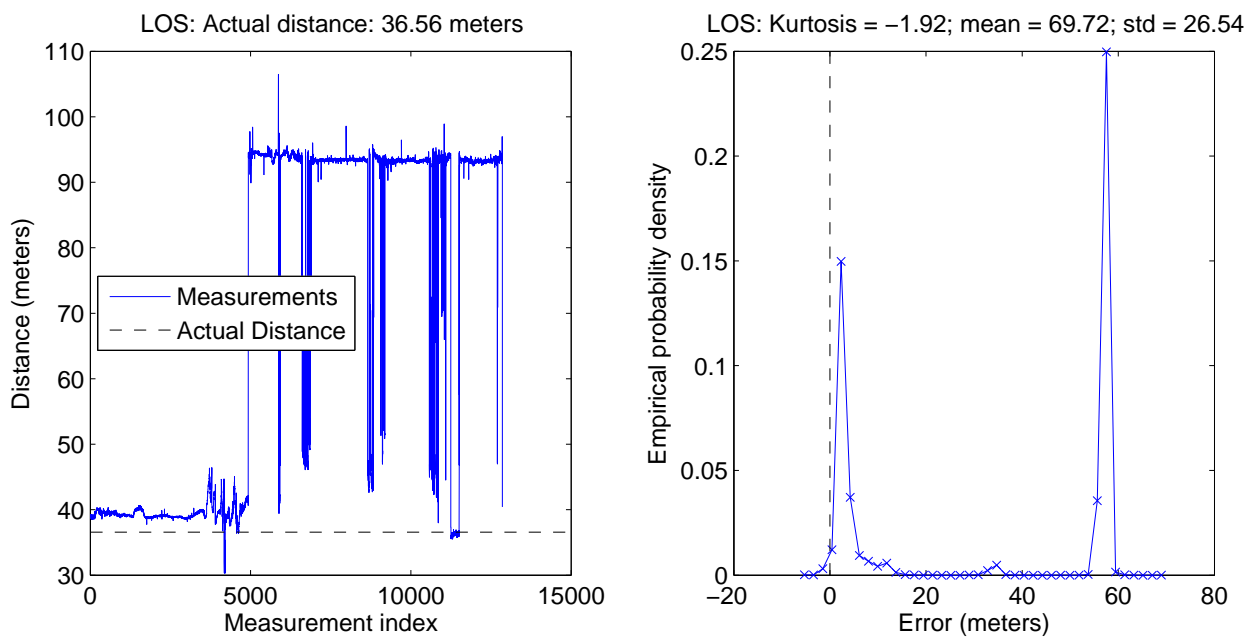


Figure B.52: Durham hallway, moderate LOS performance, location pair T4, group # 1

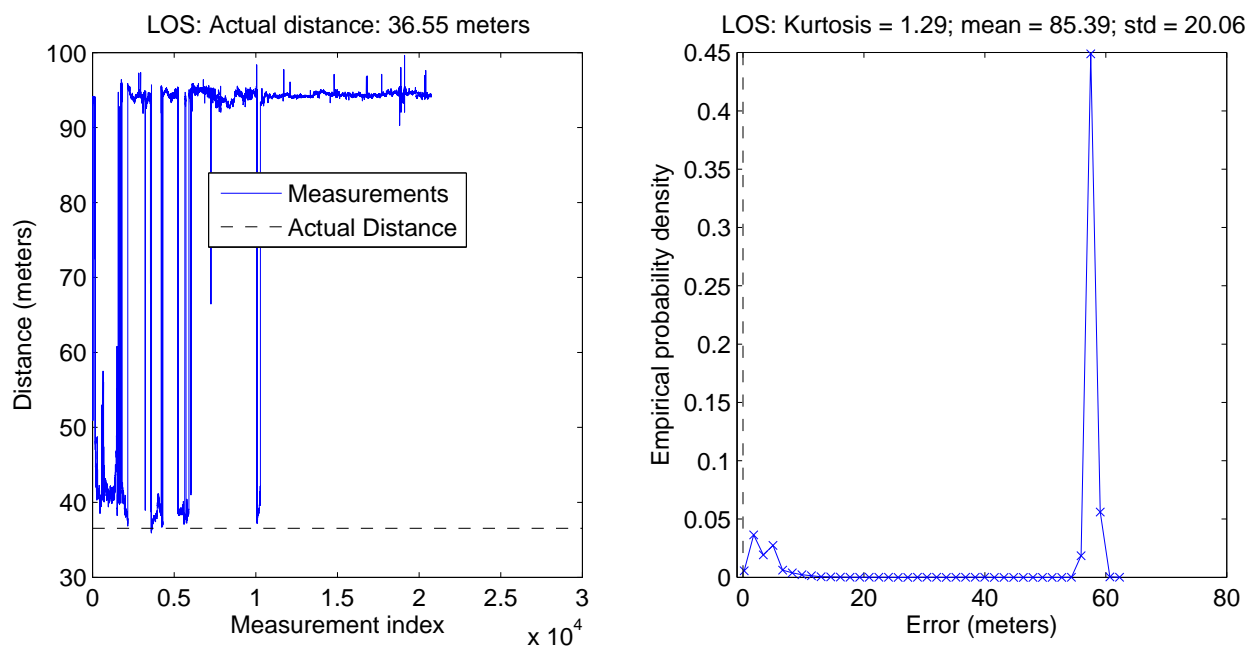


Figure B.53: Durham hallway, moderate LOS performance, location pair T4, group # 2

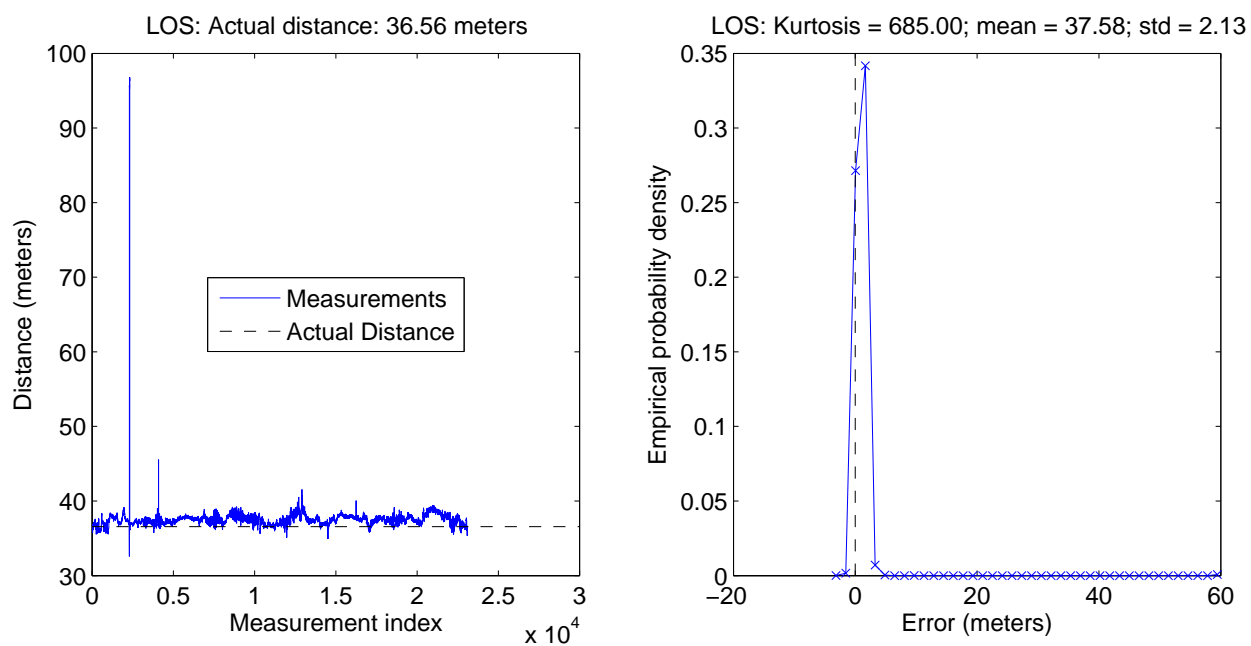


Figure B.54: Durham hallway, moderate LOS performance, location pair T4, group # 3

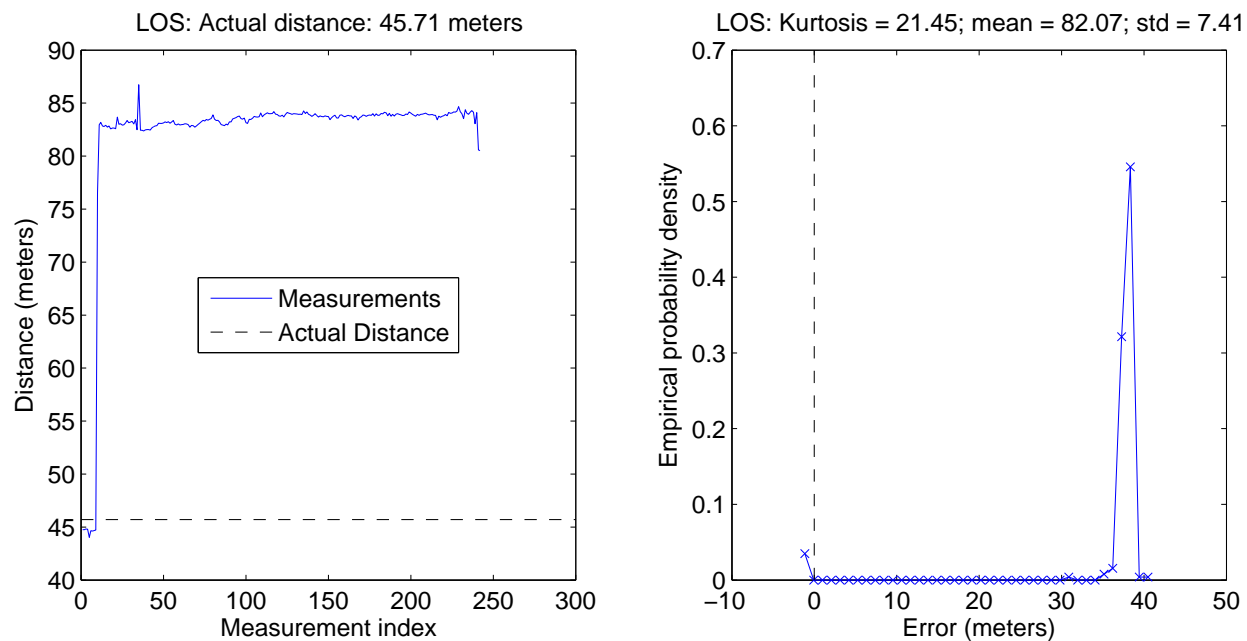


Figure B.55: Durham hallway, moderate LOS performance, location pair T5, group # 1

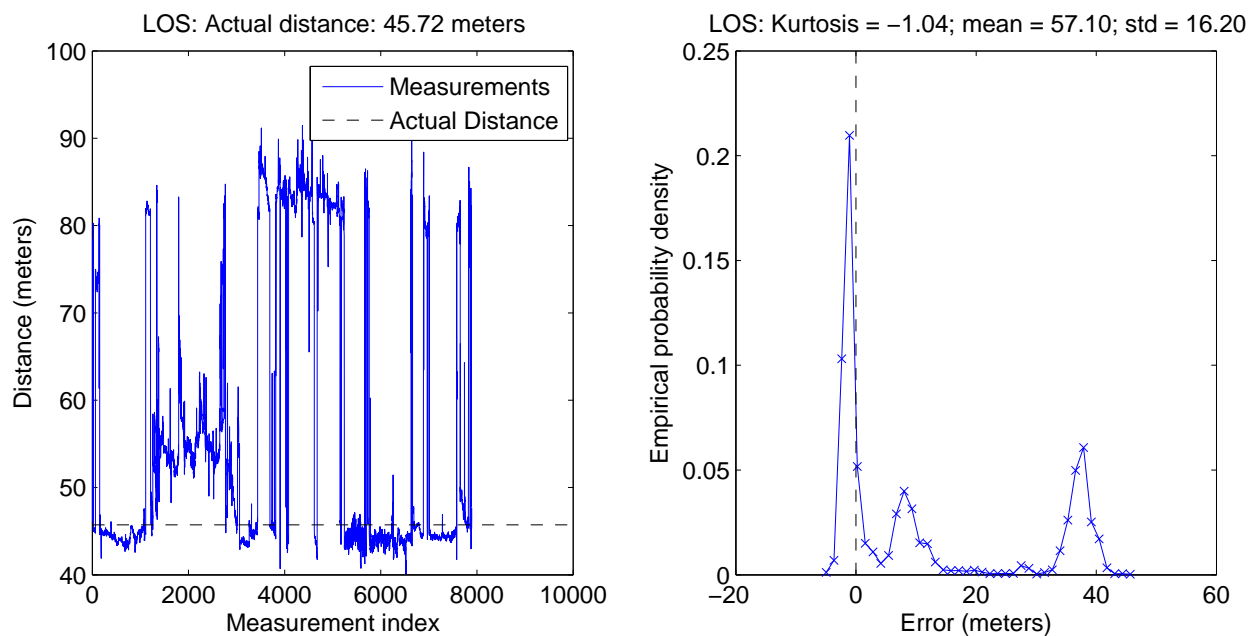


Figure B.56: Durham hallway, moderate LOS performance, location pair T5, group # 2

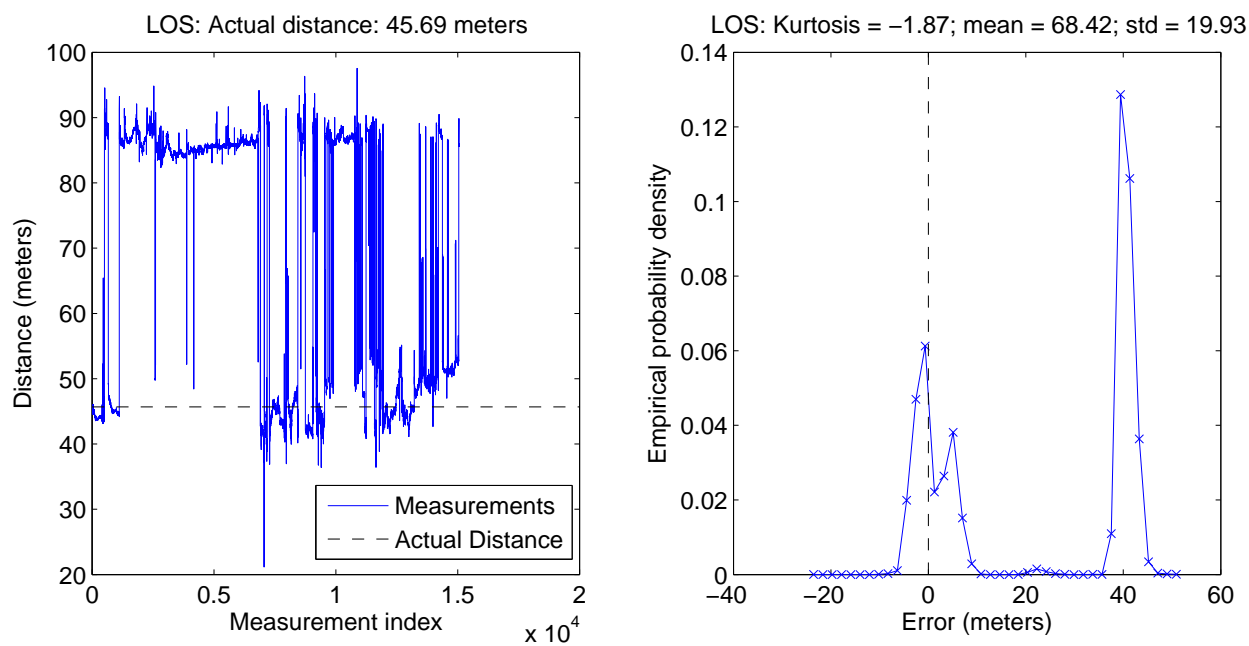


Figure B.57: Durham hallway, moderate LOS performance, location pair T5, group # 3

## **B.4 MPRG Offices Scenario**

Table B.4 and Figures B.58 - B.84 (below) summarize the results from data sets in the the MPRG offices scenario.

Table B.4: MPRG Offices Statistics

Label			Distance			Error	
Pair/Group	Kurtosis	Std. Dev.	Mean	Median	Actual	Mean	Median
T1/1	7.6947	0.6070	7.3204	7.2488	5.05	2.27	2.20
T1/2	2.2069	2.5054	8.3098	8.3054	5.05	3.26	3.26
T1/3	5.4545	1.7501	9.7833	9.9787	5.05	4.73	4.93
T2/1	6.9022	0.6871	16.5082	16.2775	10.85	5.66	5.43
T2/2	3.2887	1.2049	20.1241	19.7797	10.85	9.27	8.93
T2/3	4.9756	3.0122	16.8508	16.6370	10.85	6.00	5.79
T3/1	28.7751	1.5306	21.7987	21.7906	16.98	4.82	4.81
T3/2	6.3514	3.3881	24.9485	25.3083	16.98	7.97	8.33
T3/3	7936.5555	2.6010	24.0583	24.1231	16.98	7.08	7.14
T4/1	8.1917	2.3281	36.3800	36.4015	24.02	12.36	12.38
T4/2	0.6944	4.6227	32.0872	32.9000	24.02	8.07	8.88
T4/3	4.9431	2.6690	30.4098	30.3147	24.02	6.39	6.29
T5/1	28.5606	1.7399	40.9747	41.1622	24.01	16.96	17.15
T5/2	28.3827	2.0665	33.8616	33.8635	24.01	9.85	9.85
T5/3	14.8967	3.4757	30.3487	29.4889	24.01	6.34	5.48
T6/1	14.6355	6.6326	39.6747	38.4090	24.68	14.99	13.73
T6/2	2348.5748	18.9786	38.9086	39.5975	24.68	14.23	14.92
T6/3	2.6668	4.4538	40.6765	40.5199	24.68	16.00	15.84
T7/1	2.8395	7.1527	45.9477	48.3617	17.26	28.69	31.10
T7/2	11.0815	2.0843	19.7581	19.7886	17.26	2.50	2.53
T7/3	0.6386	5.7857	31.0514	30.1991	17.26	13.79	12.94
T8/1	7.2354	3.3899	21.1046	20.8909	7.80	13.30	13.09
T8/2	4.4488	4.7895	23.7701	24.4315	7.80	15.97	16.63
T8/3	5.2540	4.6234	29.4445	30.7702	7.80	21.64	22.97
T9/1	4.7538	0.3232	5.9894	5.9774	5.83	0.16	0.15
T9/2	73.9942	0.5003	6.6621	6.6314	5.83	0.83	0.80
T9/3	17.5693	0.9540	7.5969	7.2360	5.83	1.77	1.41
Average	391.91	3.48				9.44	9.52
Range	7935.92	18.66				28.53	30.95

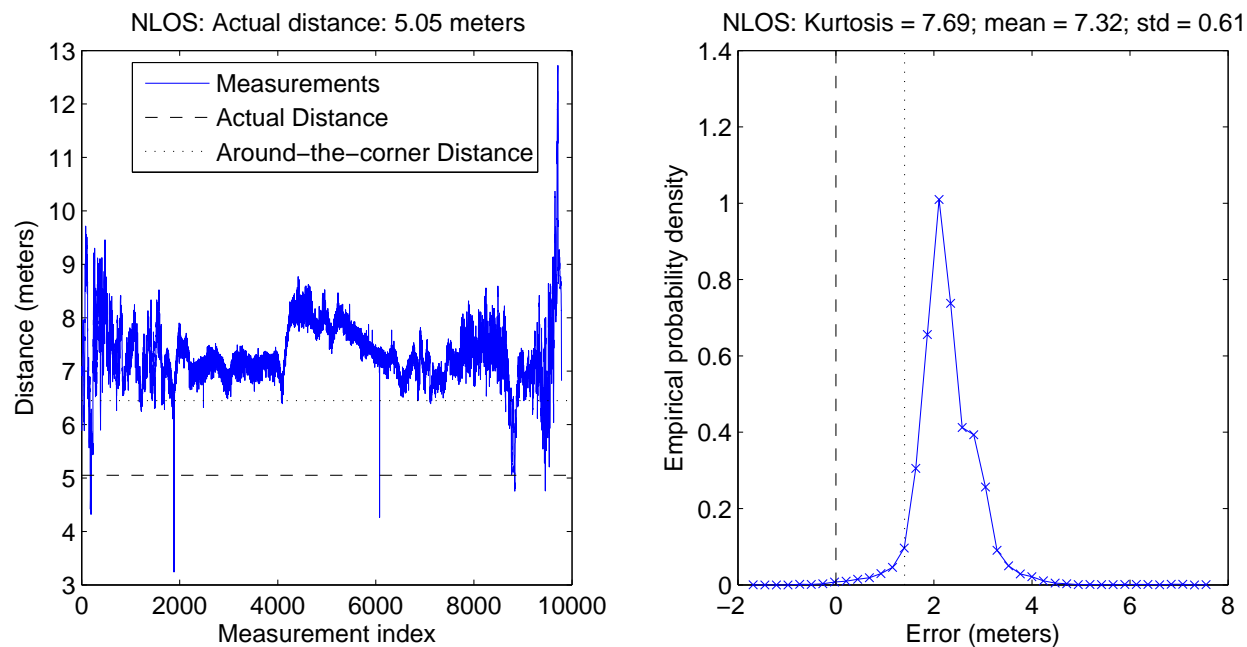


Figure B.58: MPRG offices, location pair T1, group # 1

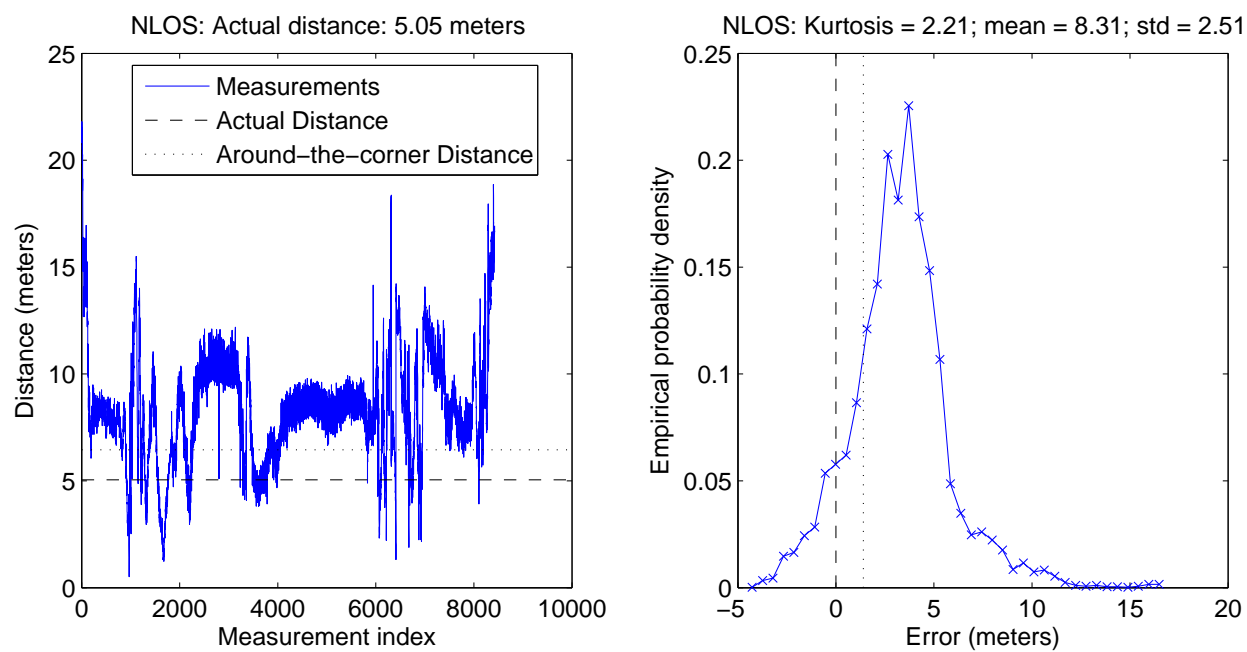


Figure B.59: MPRG offices, location pair T1, group # 2

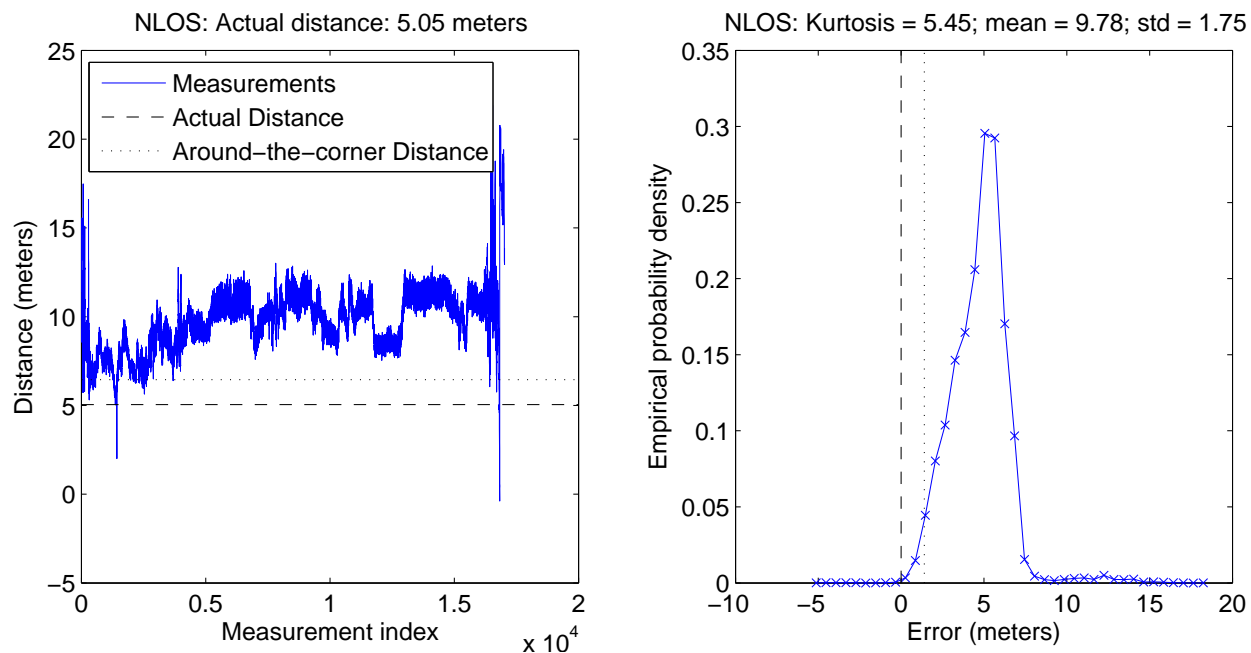


Figure B.60: MPRG offices, location pair T1, group # 3

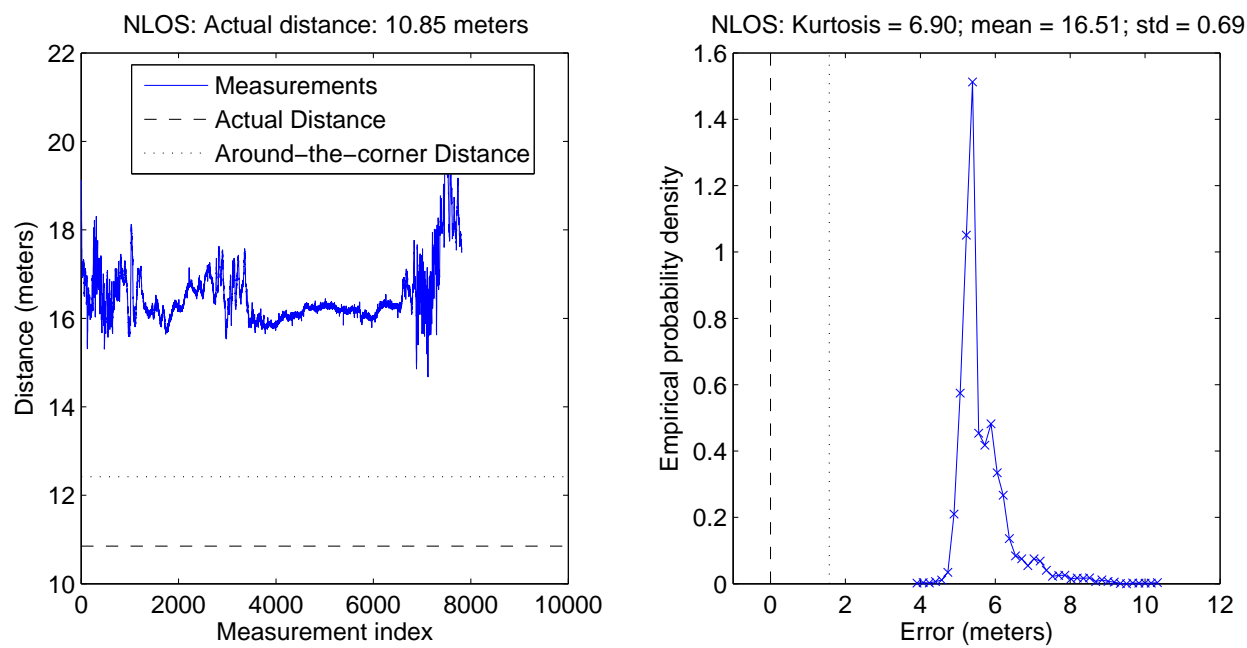


Figure B.61: MPRG offices, location pair T2, group # 1

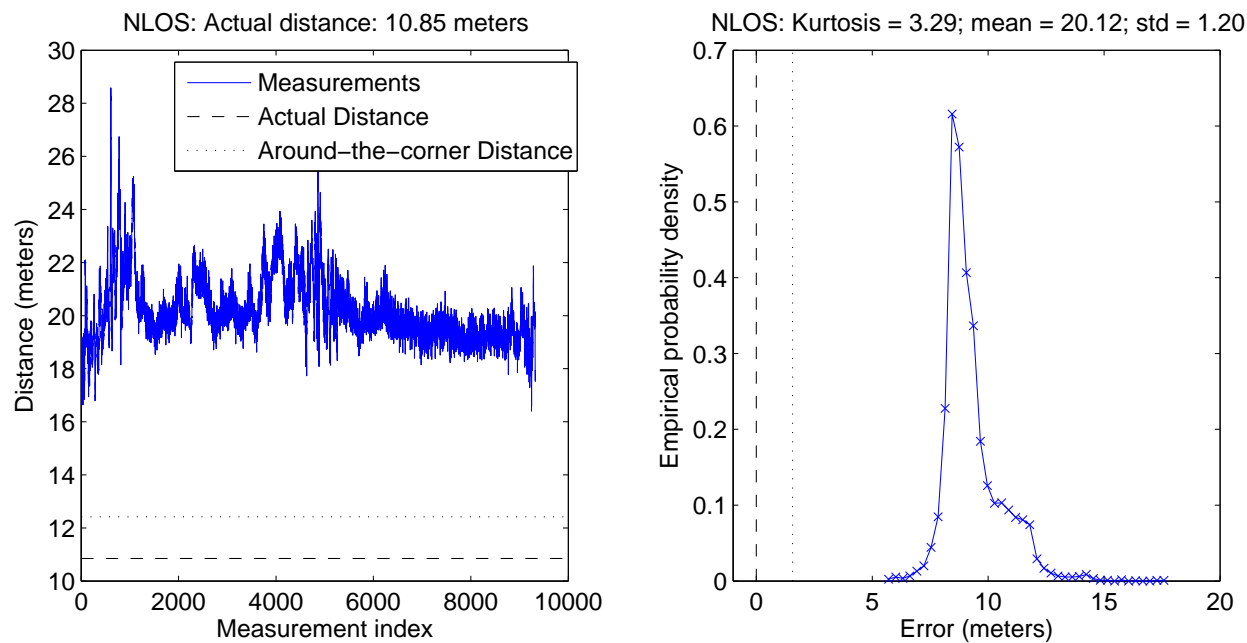


Figure B.62: MPRG offices, location pair T2, group # 2

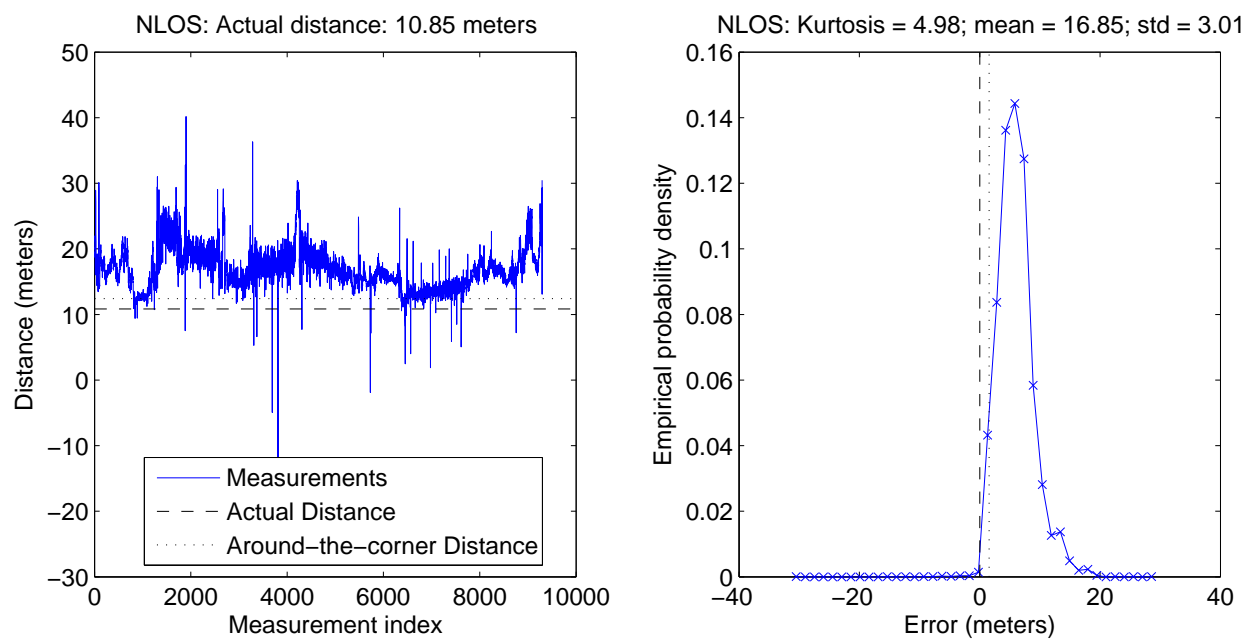


Figure B.63: MPRG offices, location pair T2, group # 3

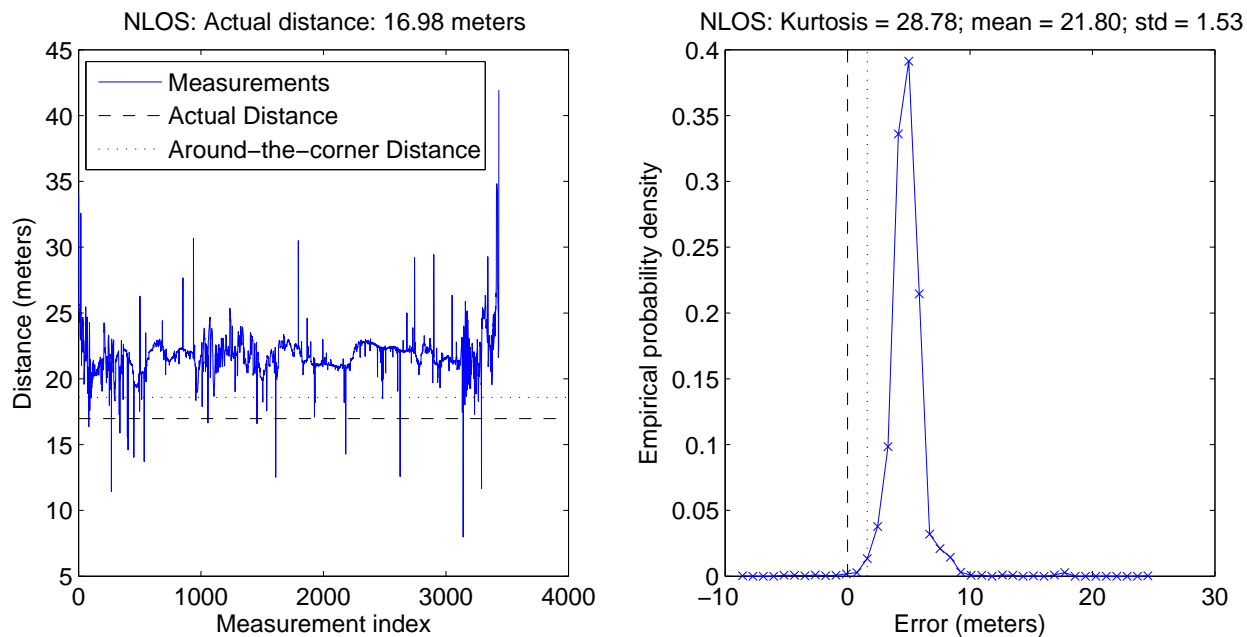


Figure B.64: MPRG offices, location pair T3, group # 1

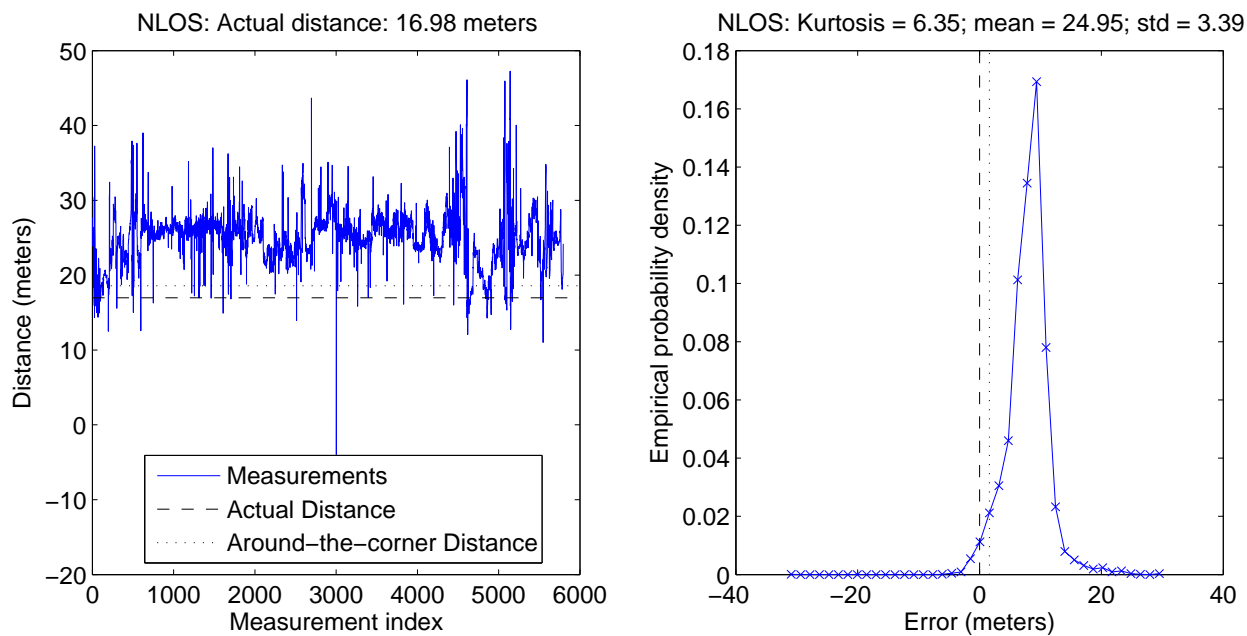


Figure B.65: MPRG offices, location pair T3, group # 2

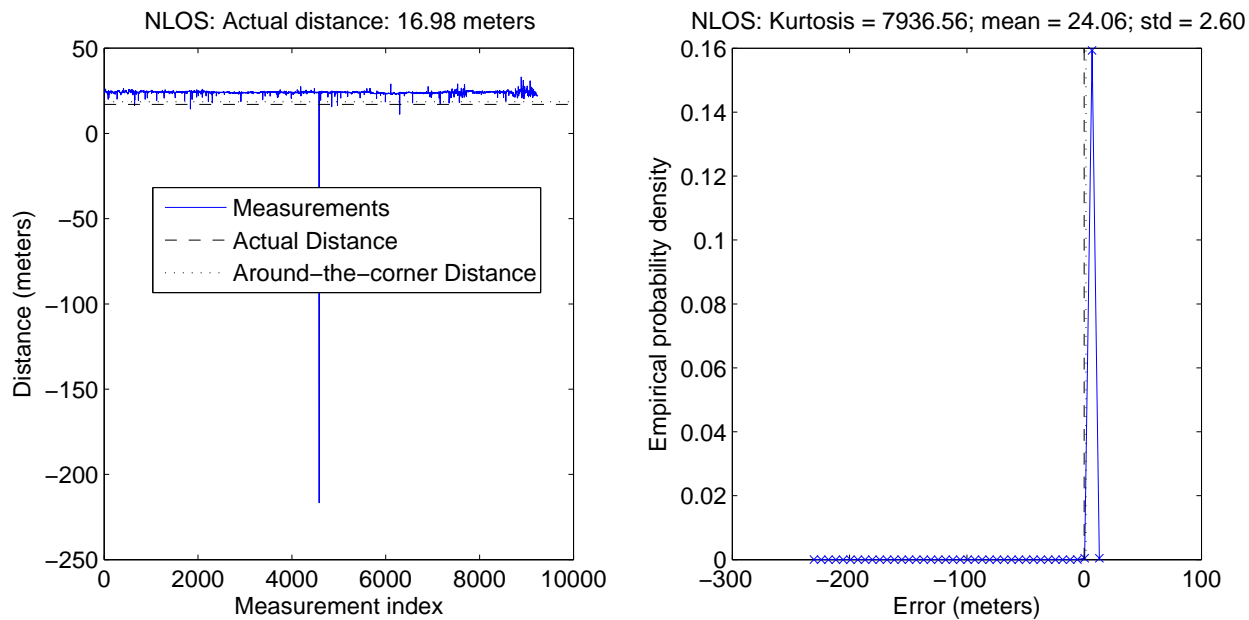


Figure B.66: MPRG offices, location pair T3, group # 3

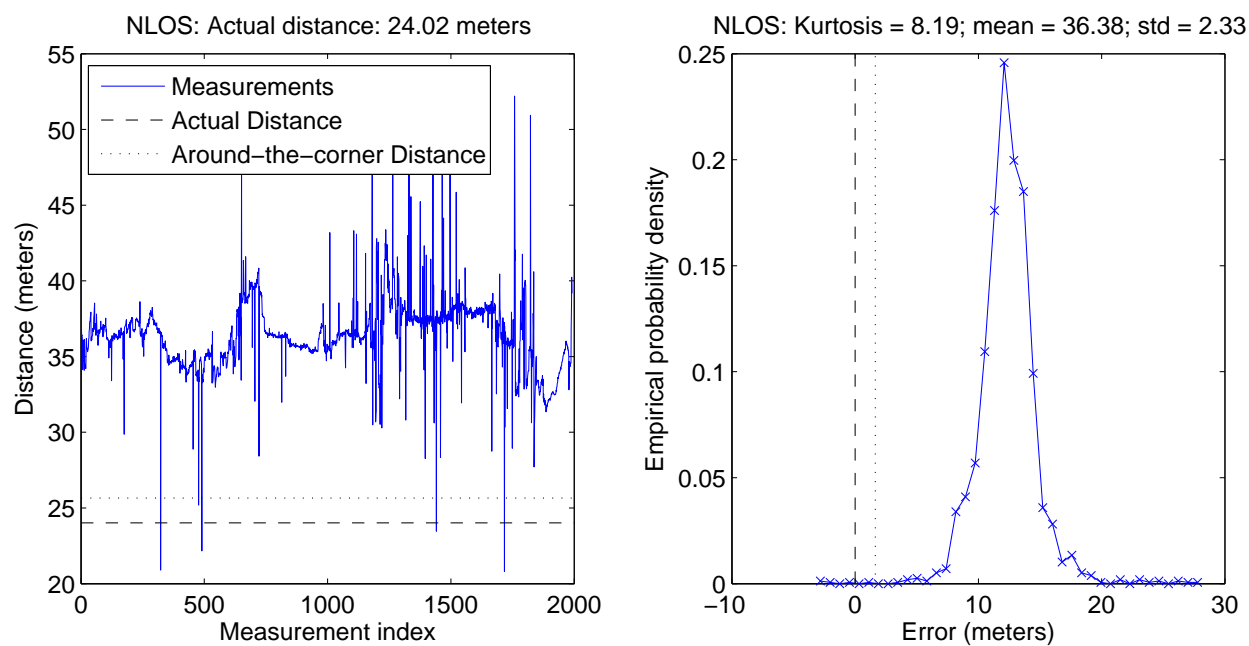


Figure B.67: MPRG offices, location pair T4, group # 1

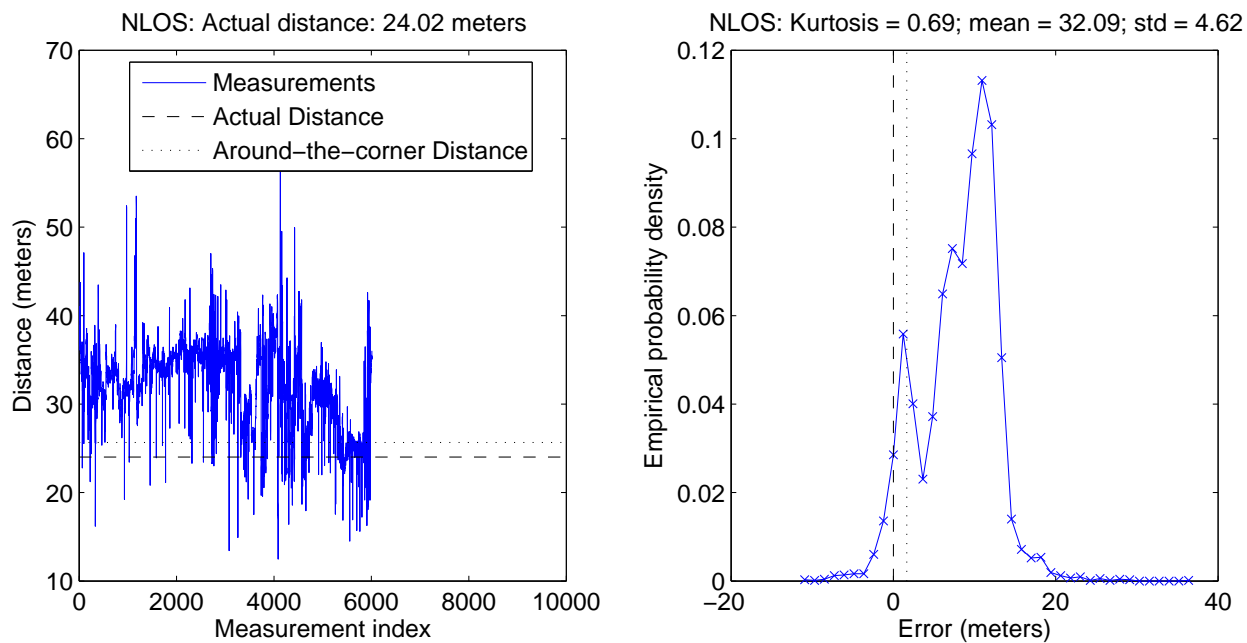


Figure B.68: MPRG offices, location pair T4, group # 2

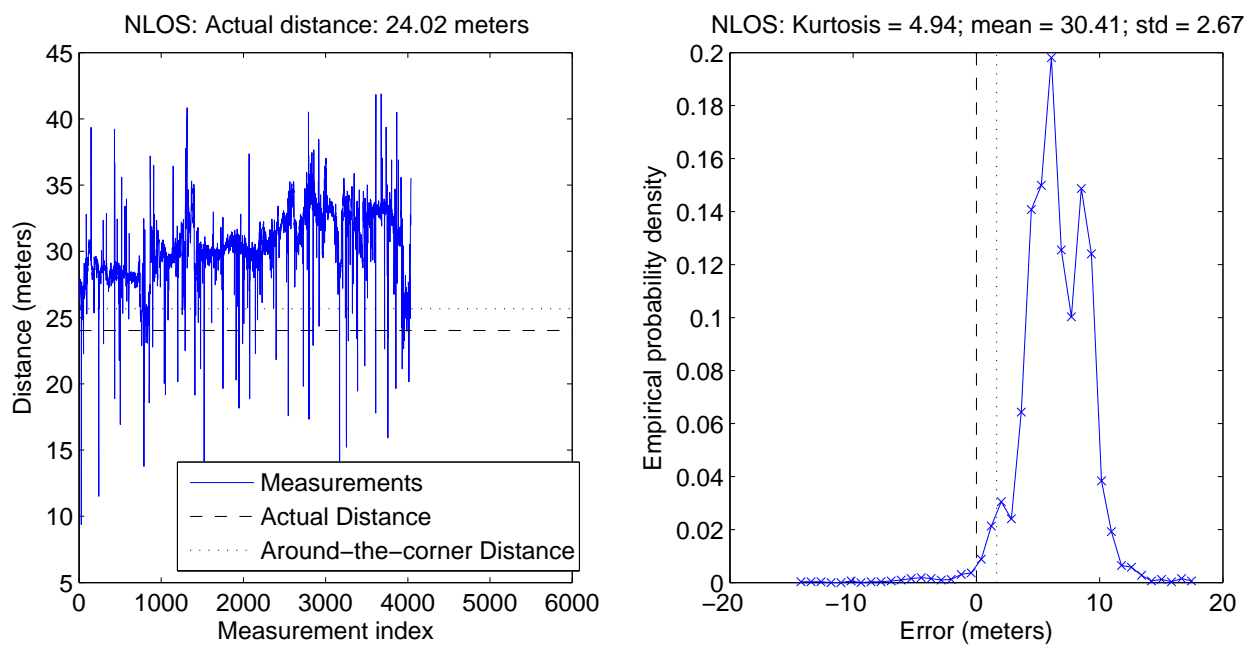


Figure B.69: MPRG offices, location pair T4, group # 3

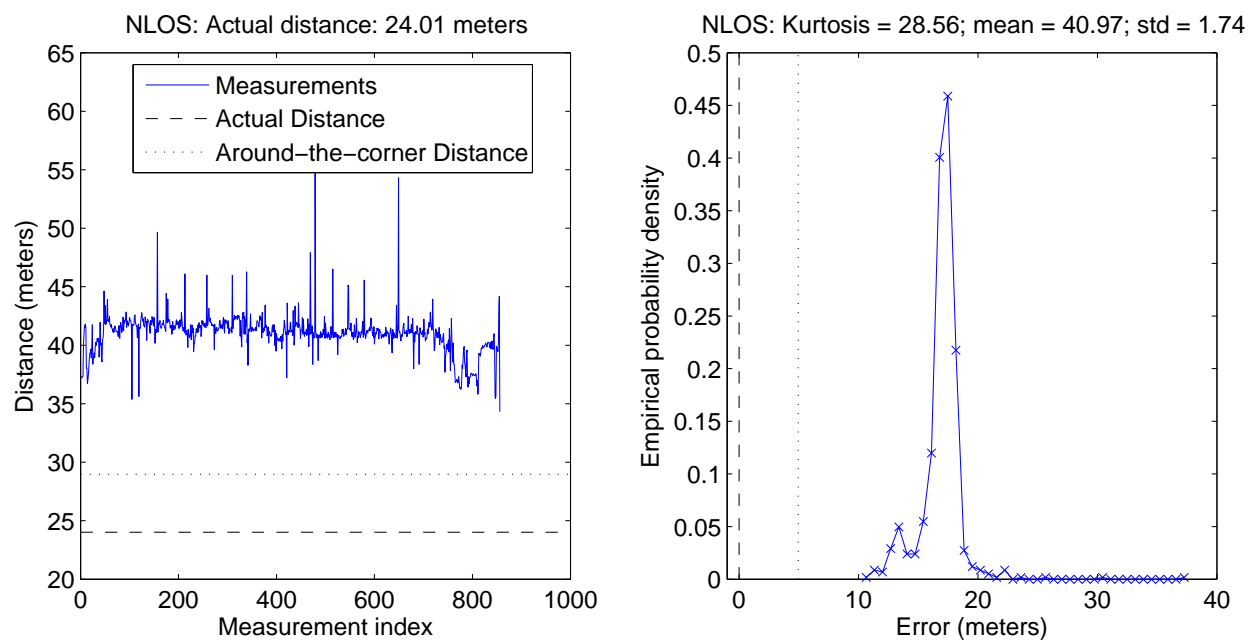


Figure B.70: MPRG offices, location pair T5, group # 1

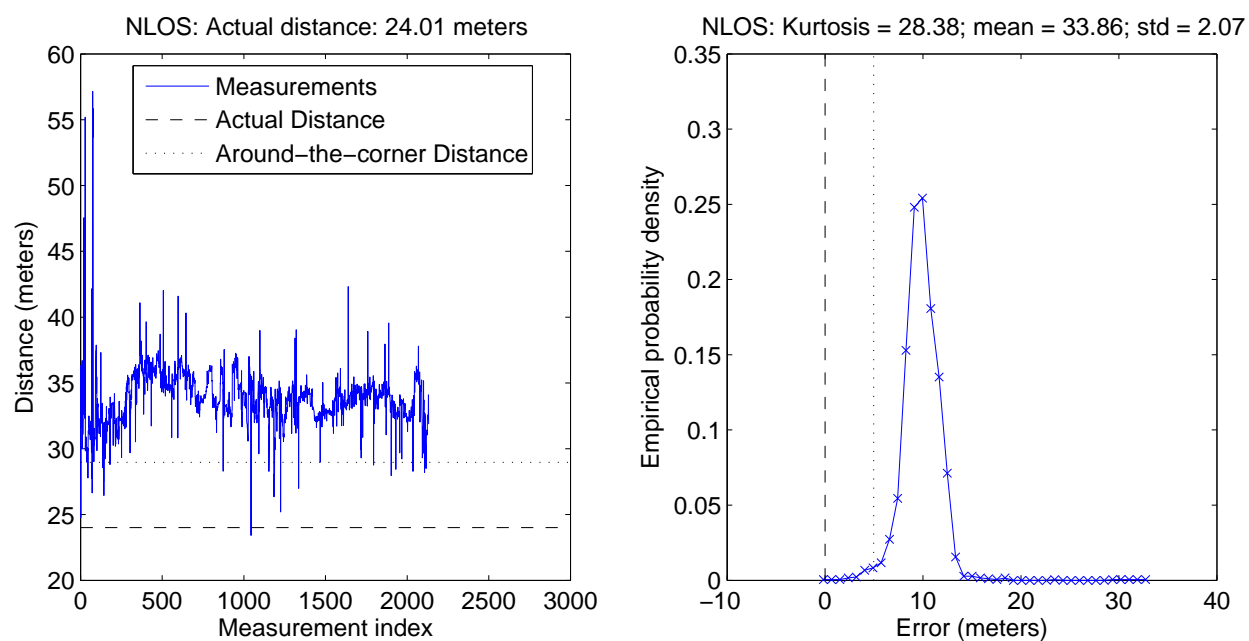


Figure B.71: MPRG offices, location pair T5, group # 2

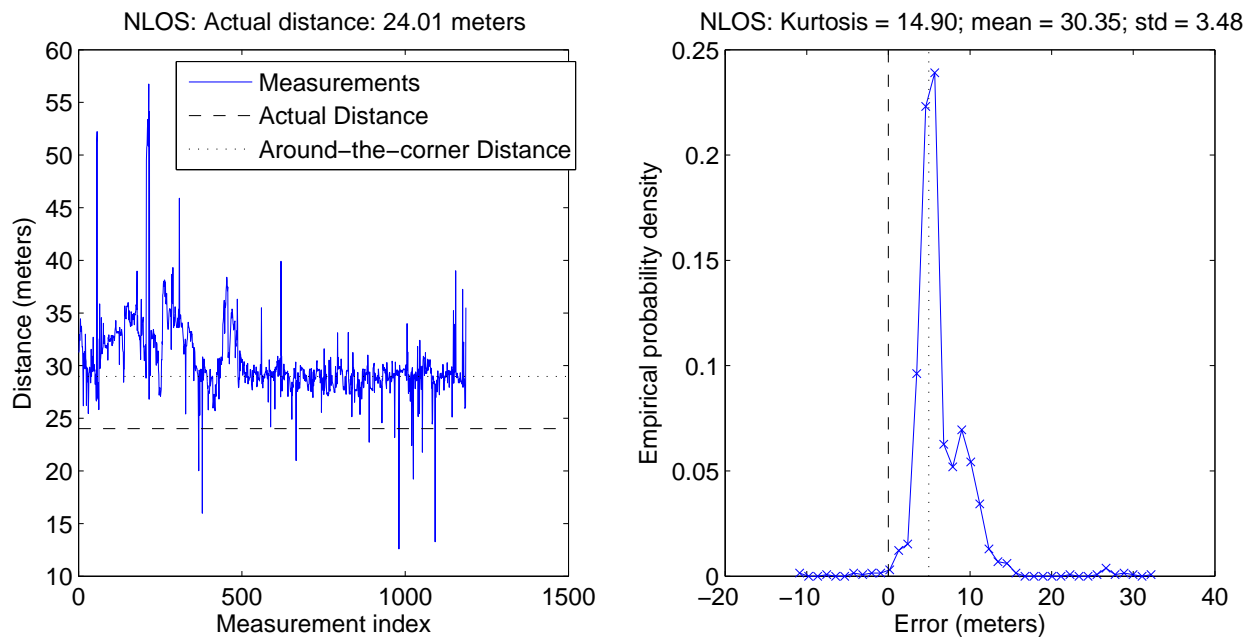


Figure B.72: MPRG offices, location pair T5, group # 3

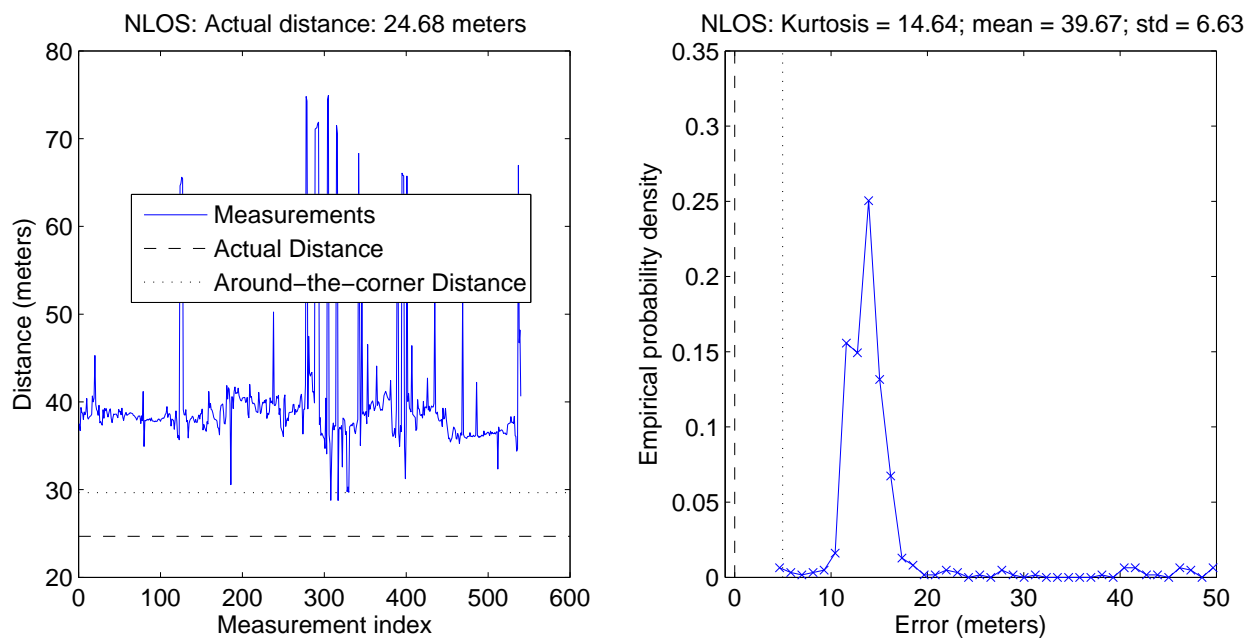


Figure B.73: MPRG offices, location pair T6, group # 1

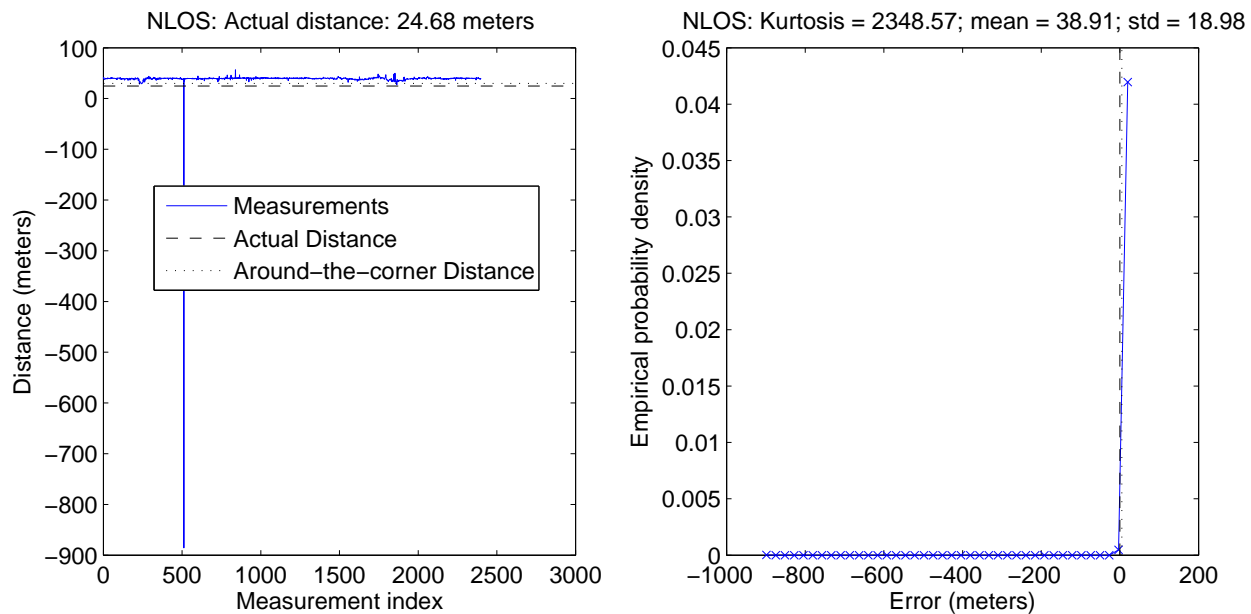


Figure B.74: MPRG offices, location pair T6, group # 2

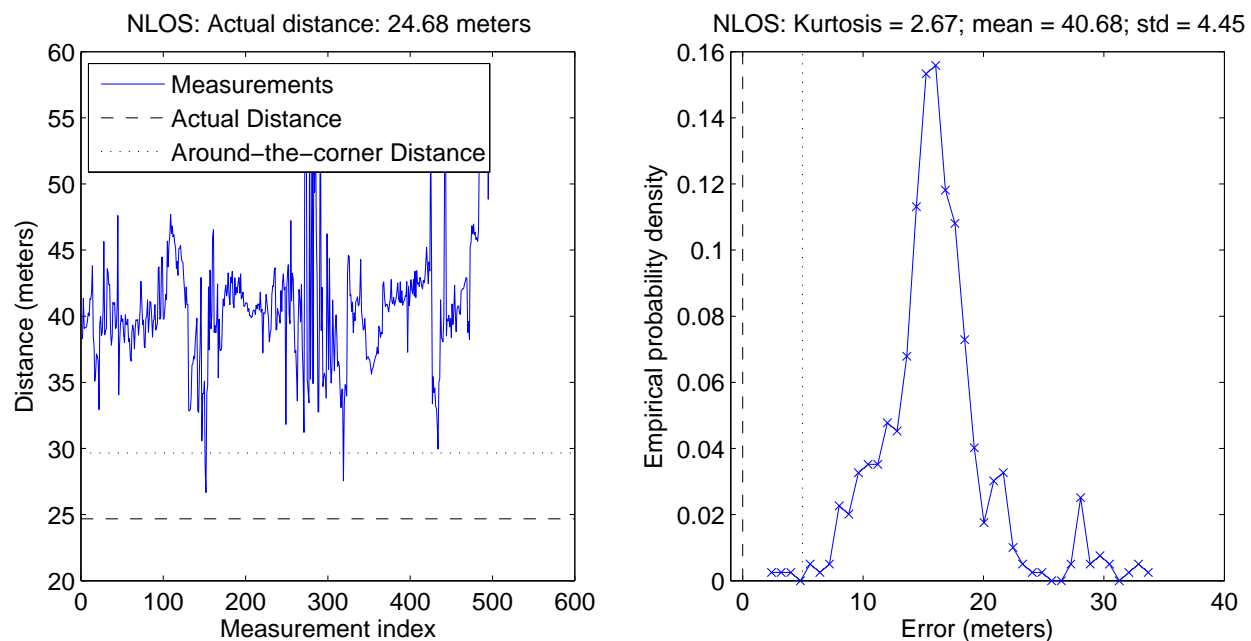


Figure B.75: MPRG offices, location pair T6, group # 3

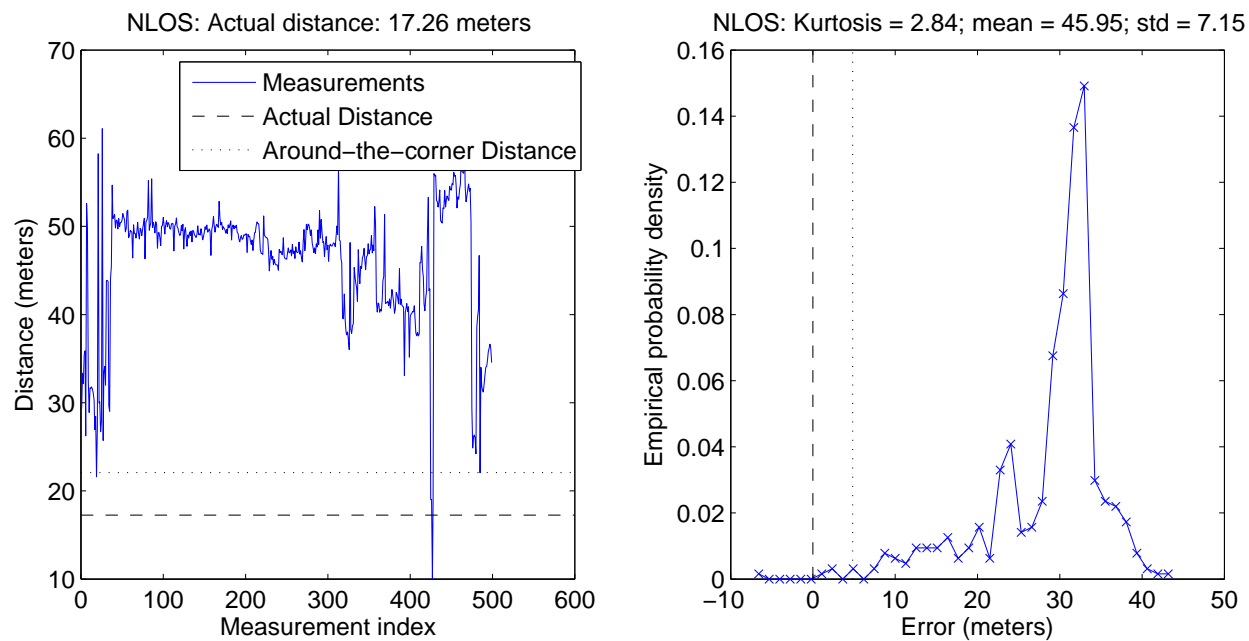


Figure B.76: MPRG offices, location pair T7, group # 1

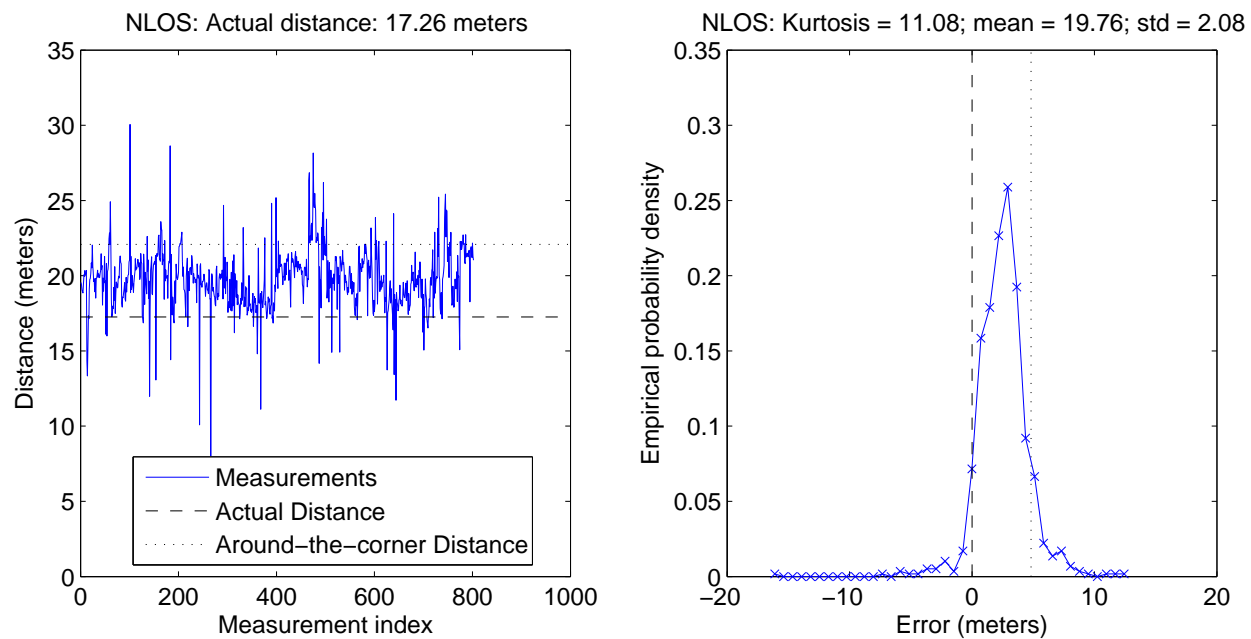


Figure B.77: MPRG offices, location pair T7, group # 2

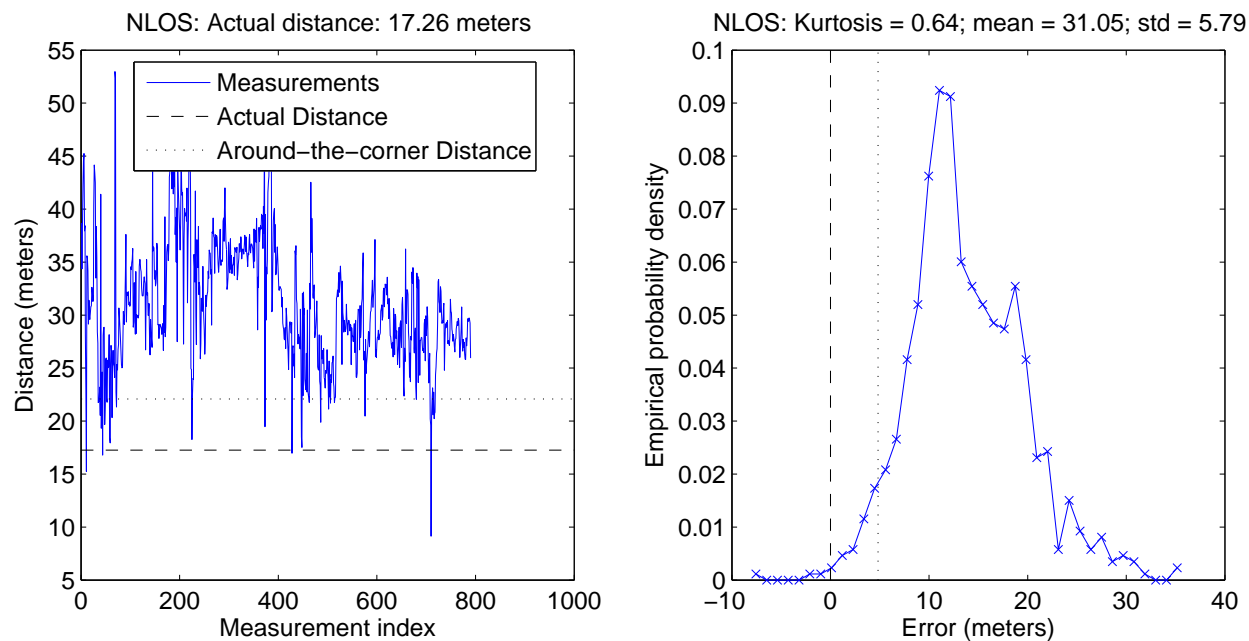


Figure B.78: MPRG offices, location pair T7, group # 3

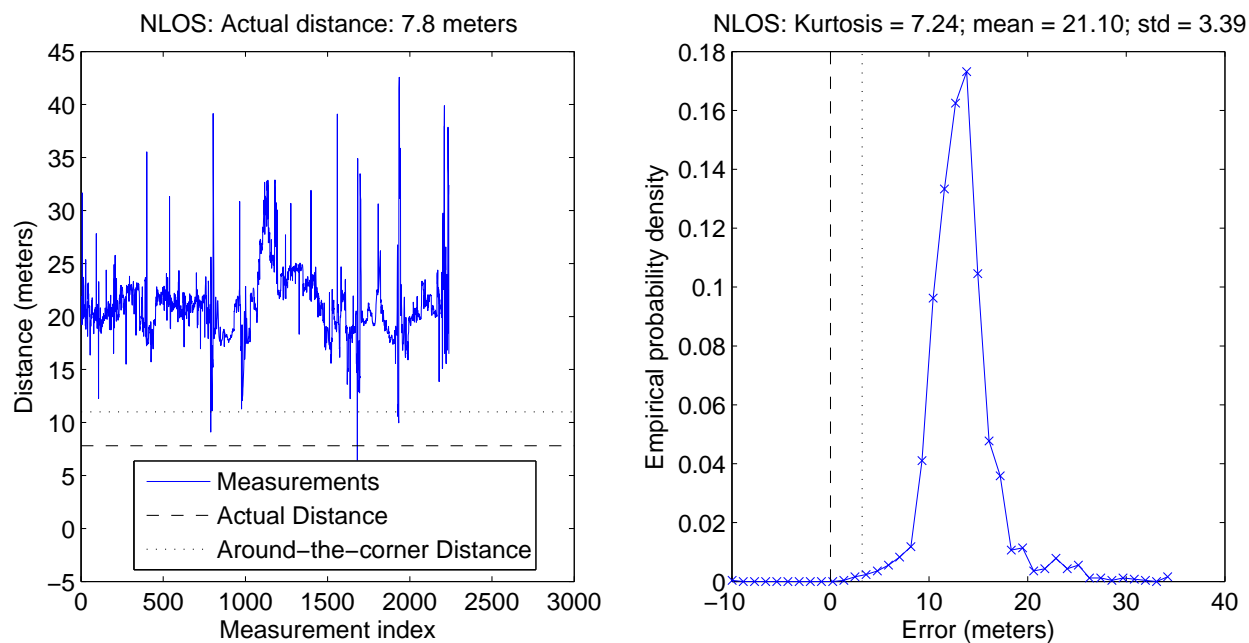


Figure B.79: MPRG offices, location pair T8, group # 1

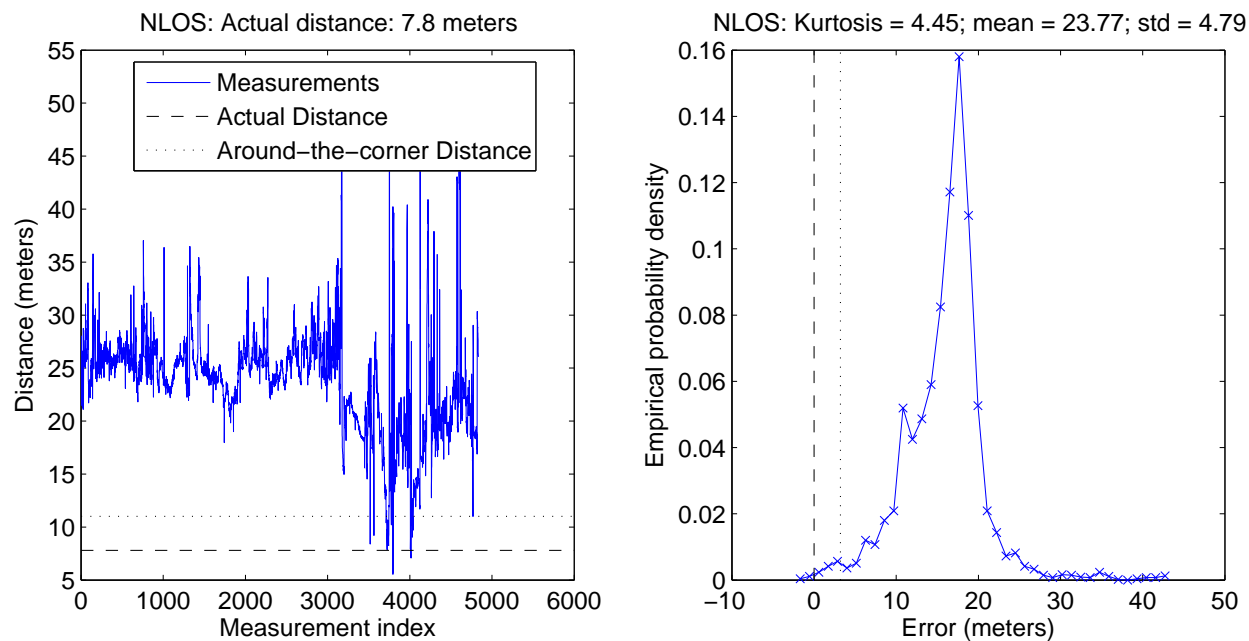


Figure B.80: MPRG offices, location pair T8, group # 2

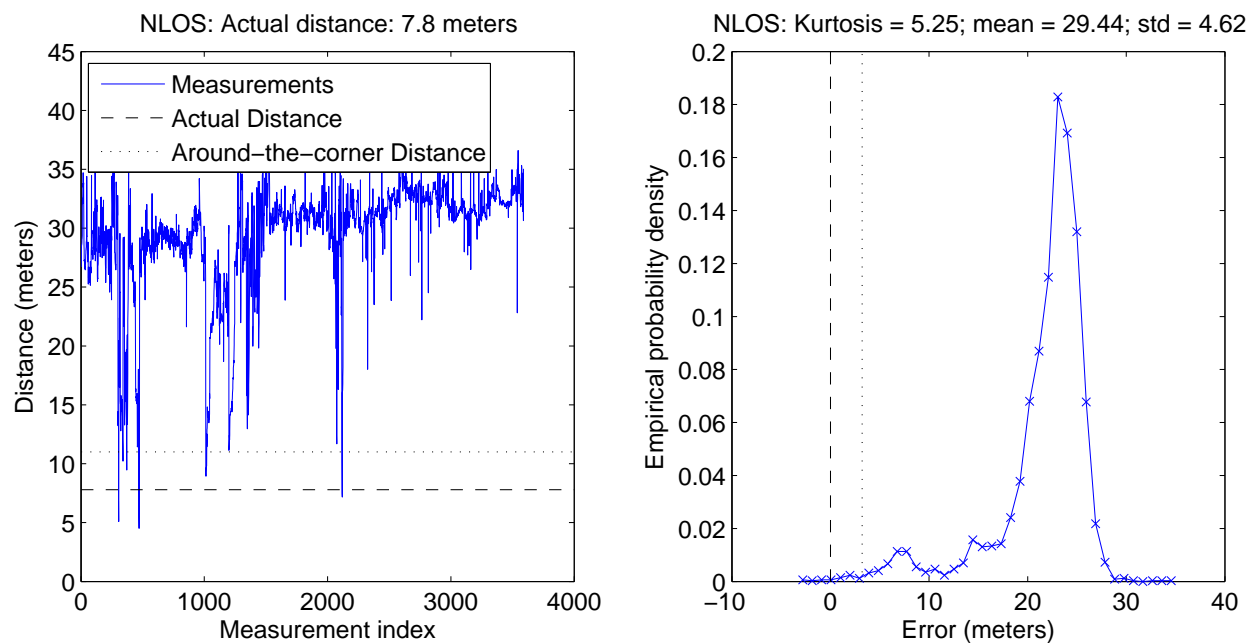


Figure B.81: MPRG offices, location pair T8, group # 3

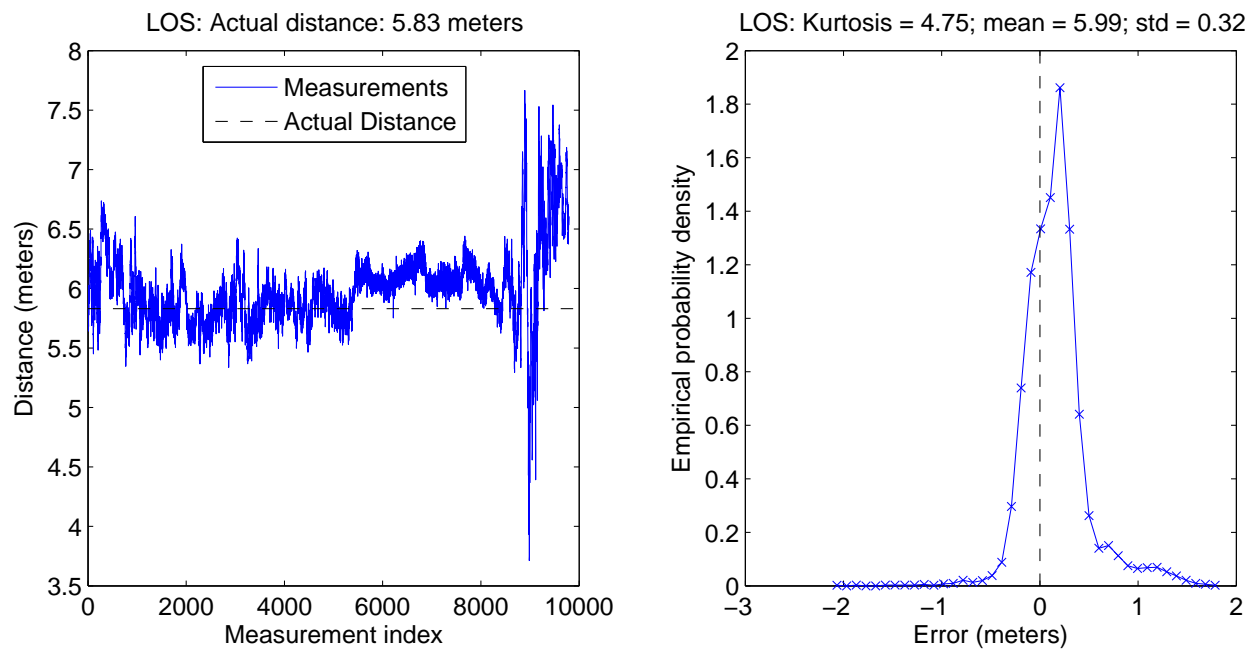


Figure B.82: MPRG offices, location pair T9, group # 1

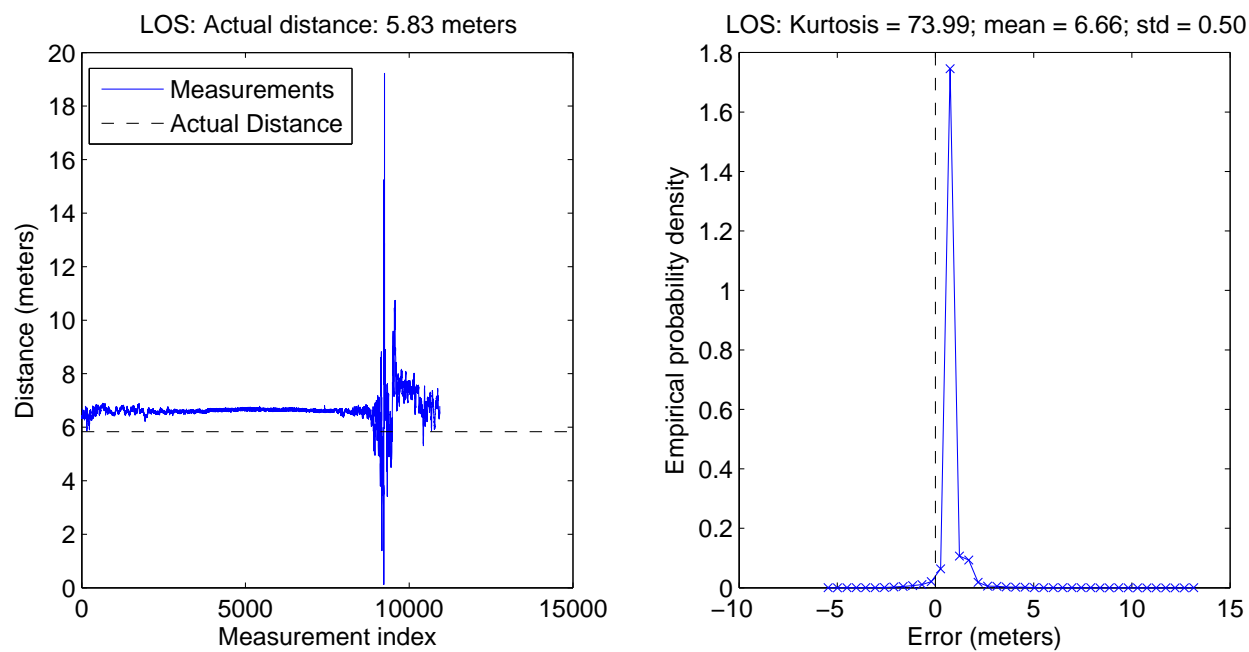


Figure B.83: MPRG offices, location pair T9, group # 2

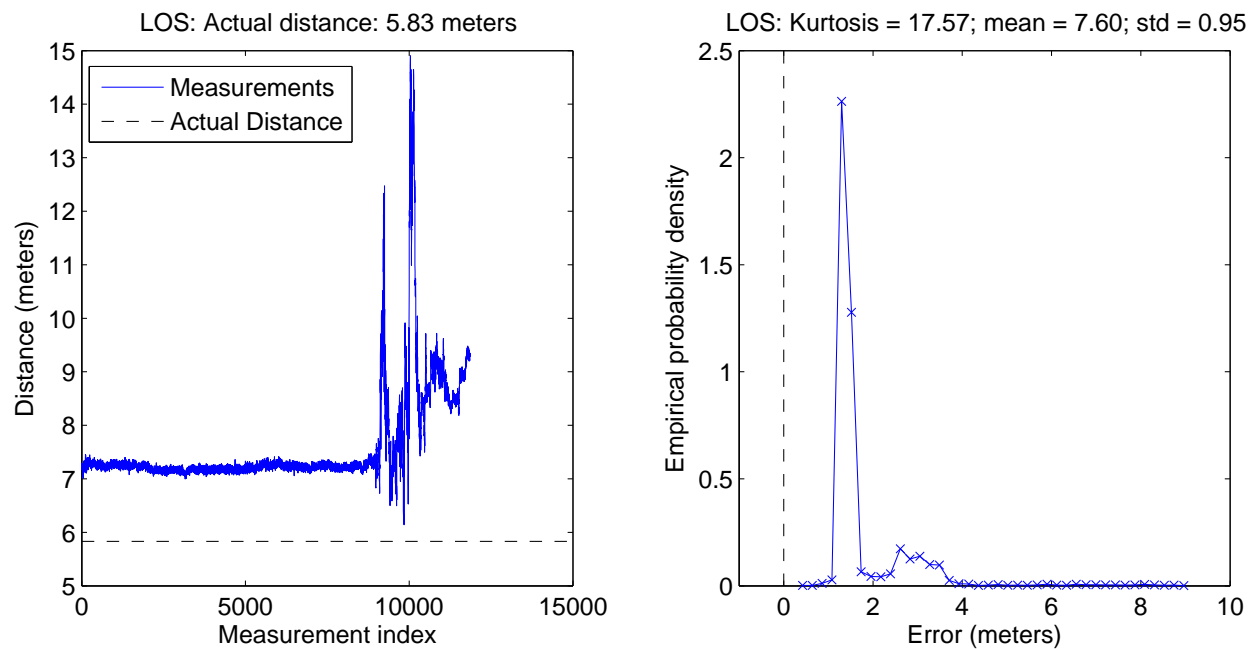


Figure B.84: MPRG offices, location pair T9, group # 3

## B.5 MPRG Lab Scenario

Table B.5 and Figures B.85 - B.100 (below) summarize the results from data sets in the the MPRG lab scenario.

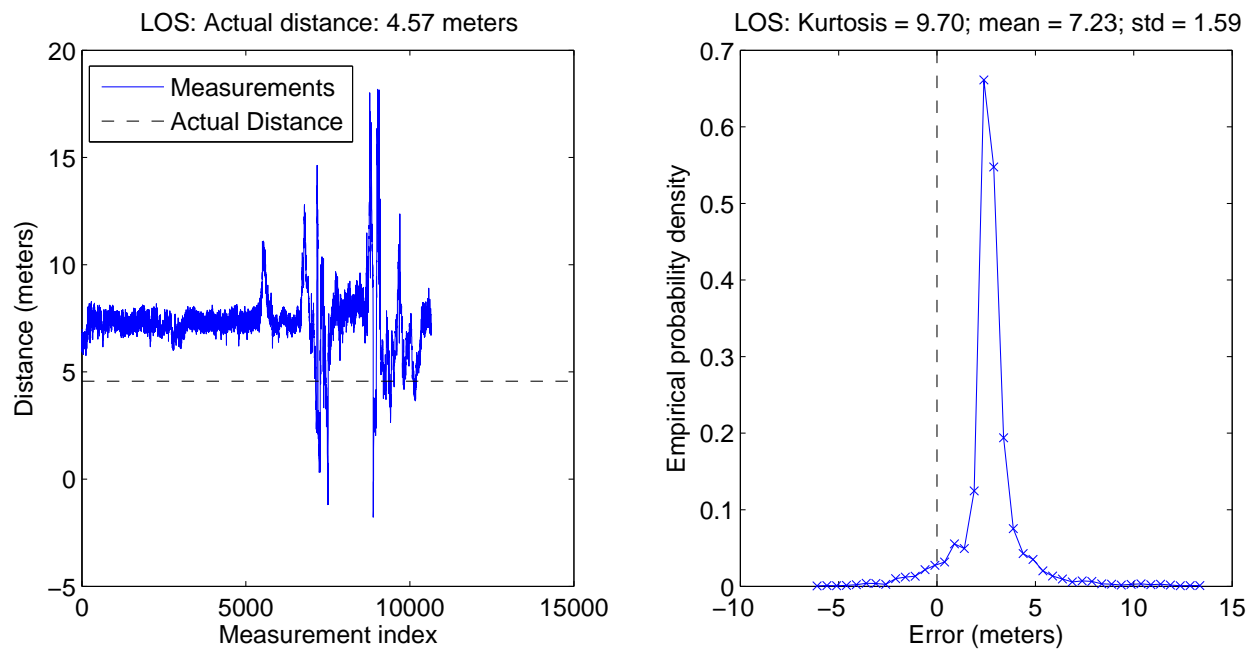


Figure B.85: MPRG lab, location pair T1, group # 1

Table B.5: MPRG Lab Statistics

Label			Distance			Error	
Pair/Group	Kurtosis	Std. Dev.	Mean	Median	Actual	Mean	Median
T1/1	9.6966	1.5928	7.2292	7.1934	4.57	2.66	2.62
T1/2	6.7594	0.4896	6.0439	6.1803	4.57	1.47	1.61
T2/1	1.3483	1.5867	6.3384	6.3374	3.48	2.86	2.86
T2/2	355.0846	3.1104	4.1506	4.4989	3.48	0.67	1.02
T3/1	24.5586	3.2191	10.5231	9.9488	4.58	5.94	5.37
T3/2	91.8545	1.2969	6.1923	6.0384	4.58	1.61	1.46
T4/1	17.4605	1.4652	21.4531	21.5682	11.08	10.37	10.49
T4/2	13.8717	2.3151	25.3571	25.2630	11.08	14.28	14.18
T5/1	6.9358	4.6148	33.2601	34.3239	8.30	24.96	26.02
T5/2	2.9732	1.6263	22.8214	23.0511	8.30	14.52	14.75
T6/1	55.3925	0.2498	9.3161	9.3178	9.40	-0.08	-0.08
T6/2	51.9284	1.5200	10.7162	10.4264	9.40	1.32	1.03
T7/1	1.5012	4.5460	24.9059	24.3740	9.59	15.32	14.78
T7/2	39.7103	2.4879	18.1463	17.3211	9.59	8.56	7.73
T8/1	3.6995	2.6740	17.6825	17.6396	11.13	6.55	6.51
T8/2	11.0628	4.0642	34.4178	34.8378	11.13	23.29	23.71
Average	43.36	2.30				8.39	8.38
Range	353.74	4.37				25.04	26.11

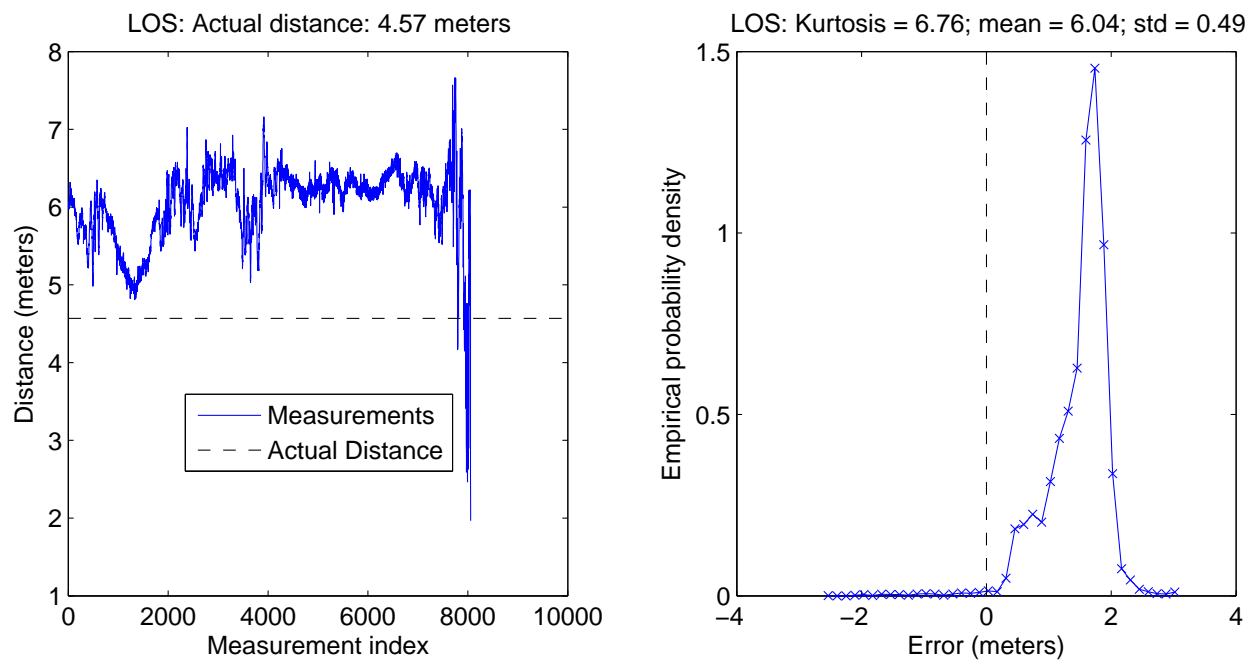


Figure B.86: MPRG lab, location pair T1, group # 2

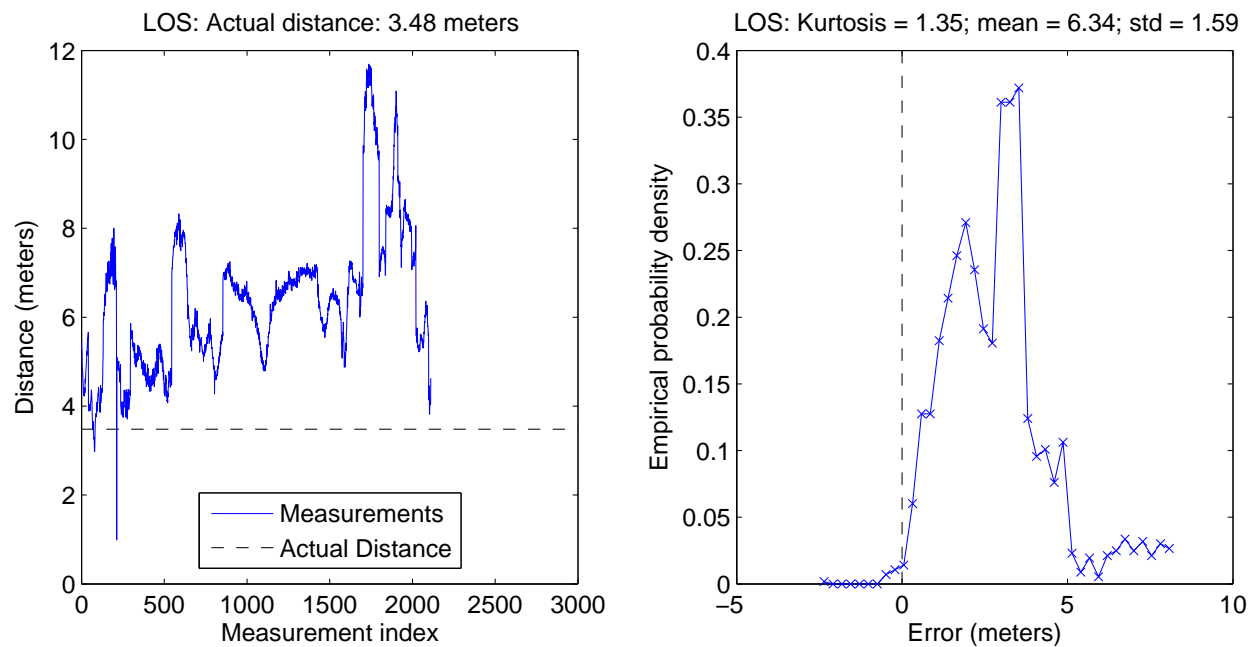


Figure B.87: MPRG lab, location pair T2, group # 1

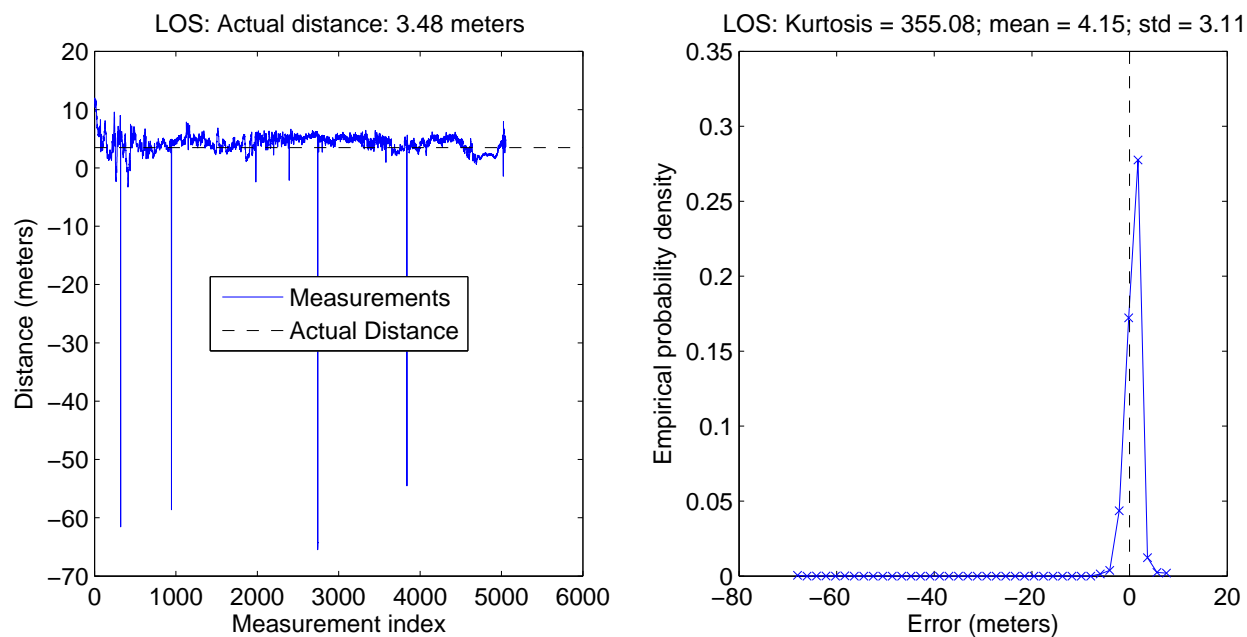


Figure B.88: MPRG lab, location pair T2, group # 2

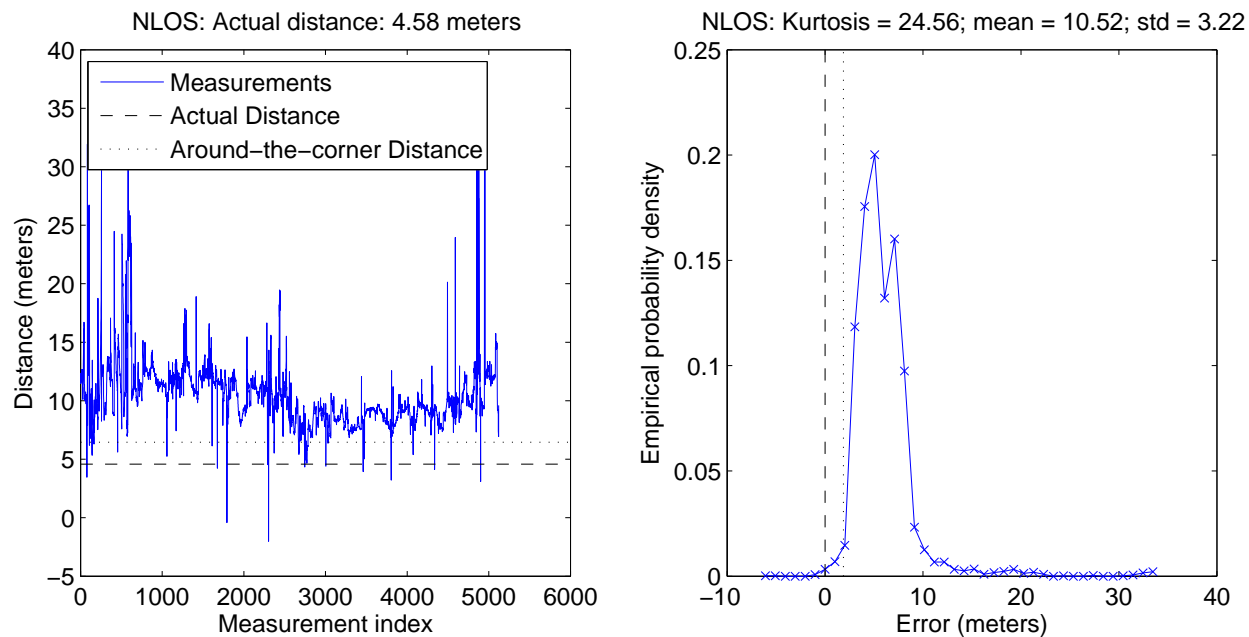


Figure B.89: MPRG lab, location pair T3, group # 1

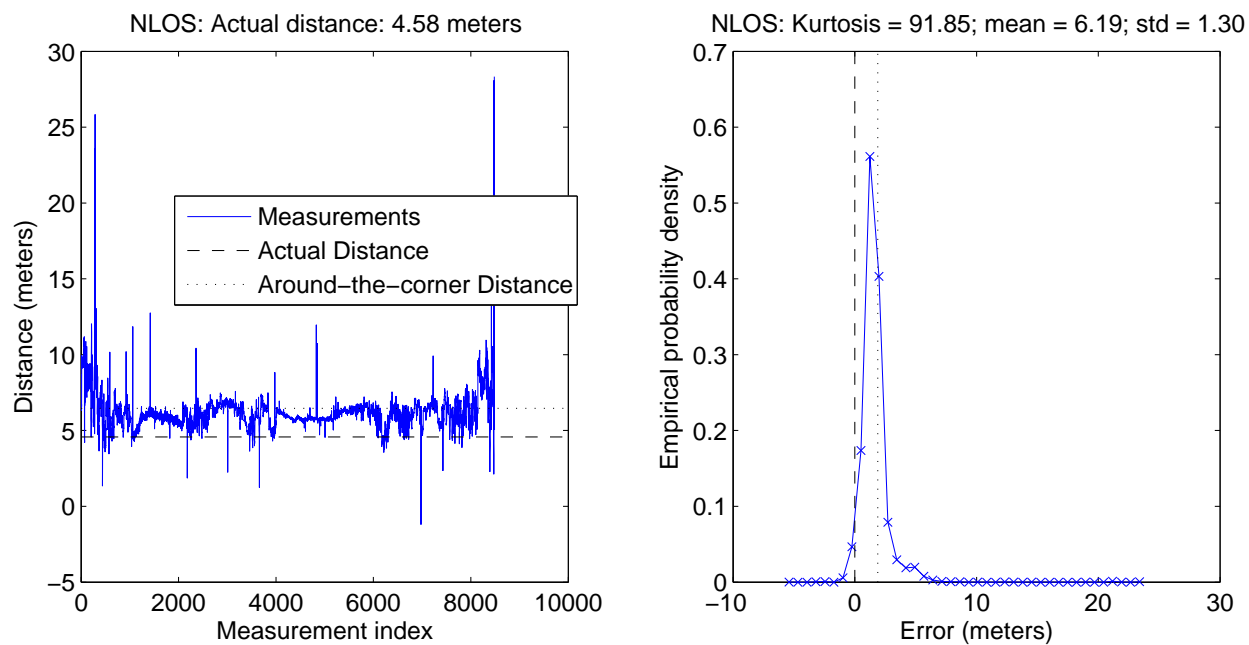


Figure B.90: MPRG lab, location pair T3, group # 2

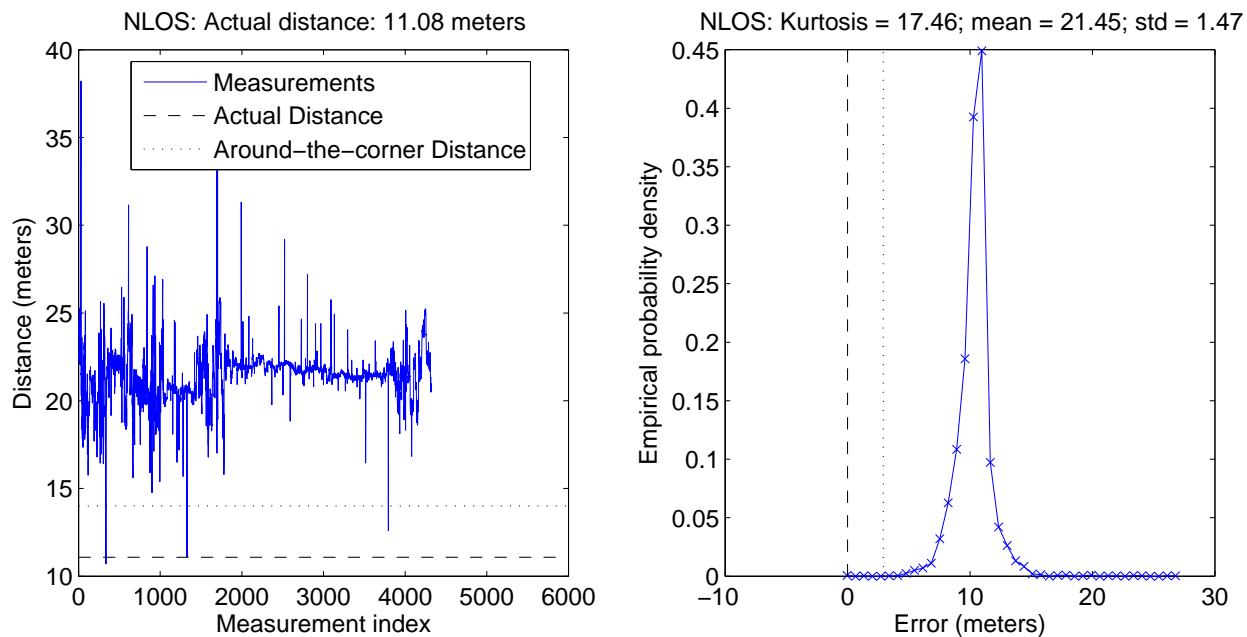


Figure B.91: MPRG lab, location pair T4, group # 1

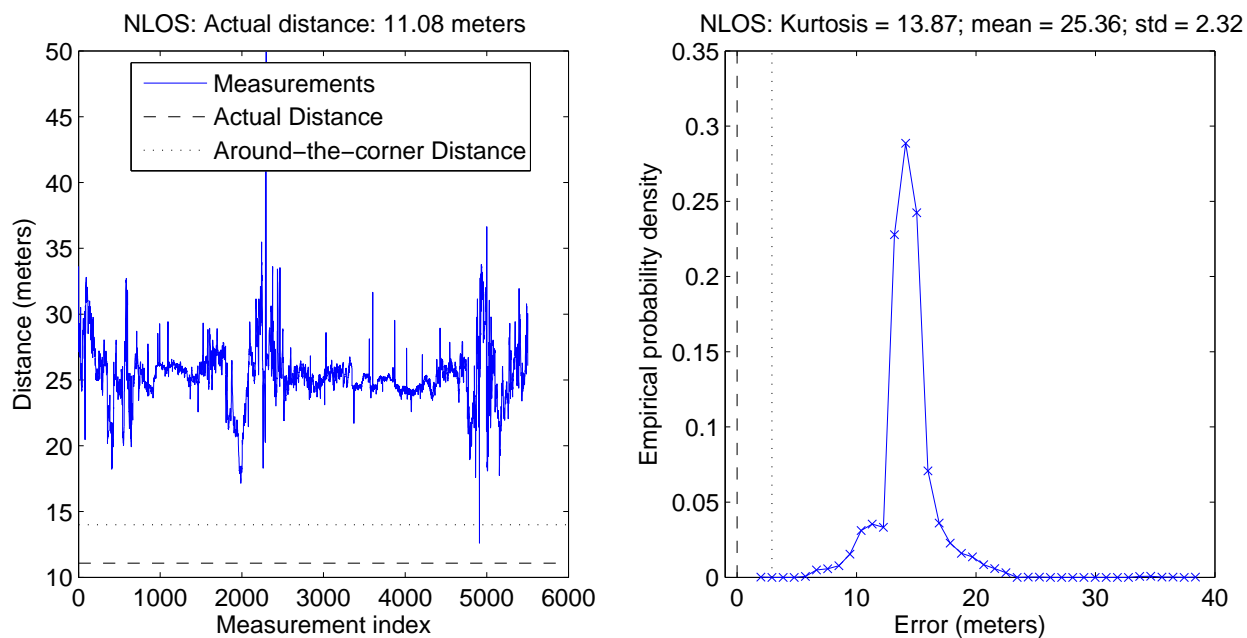


Figure B.92: MPRG lab, location pair T4, group # 2

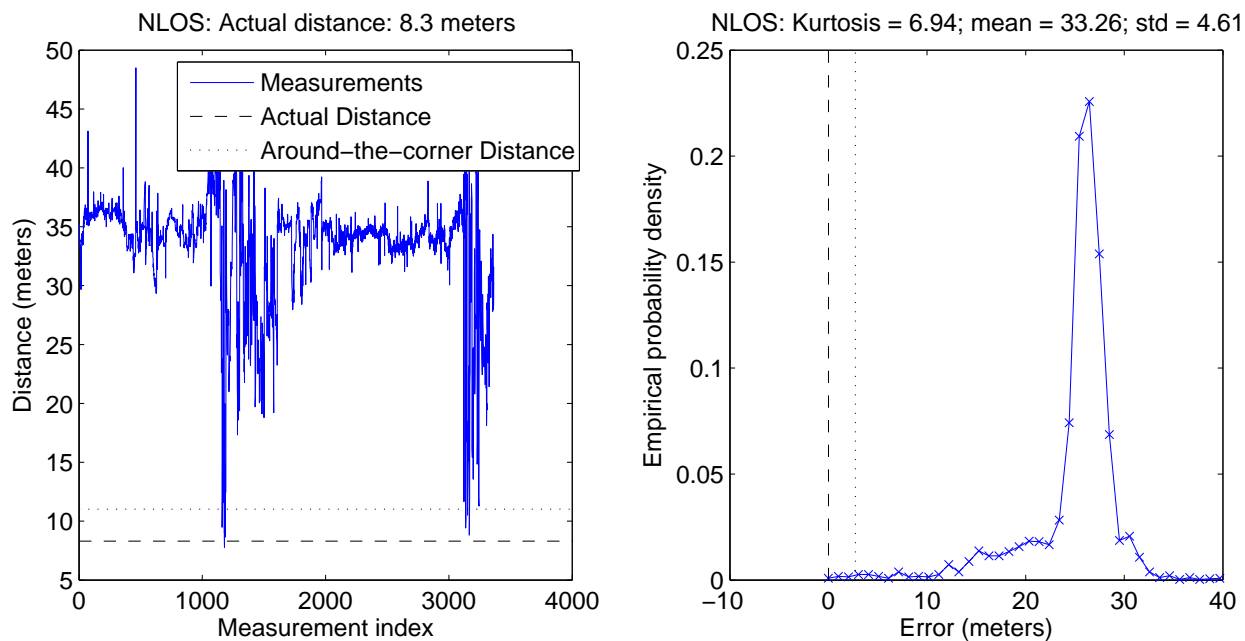


Figure B.93: MPRG lab, location pair T5, group # 1

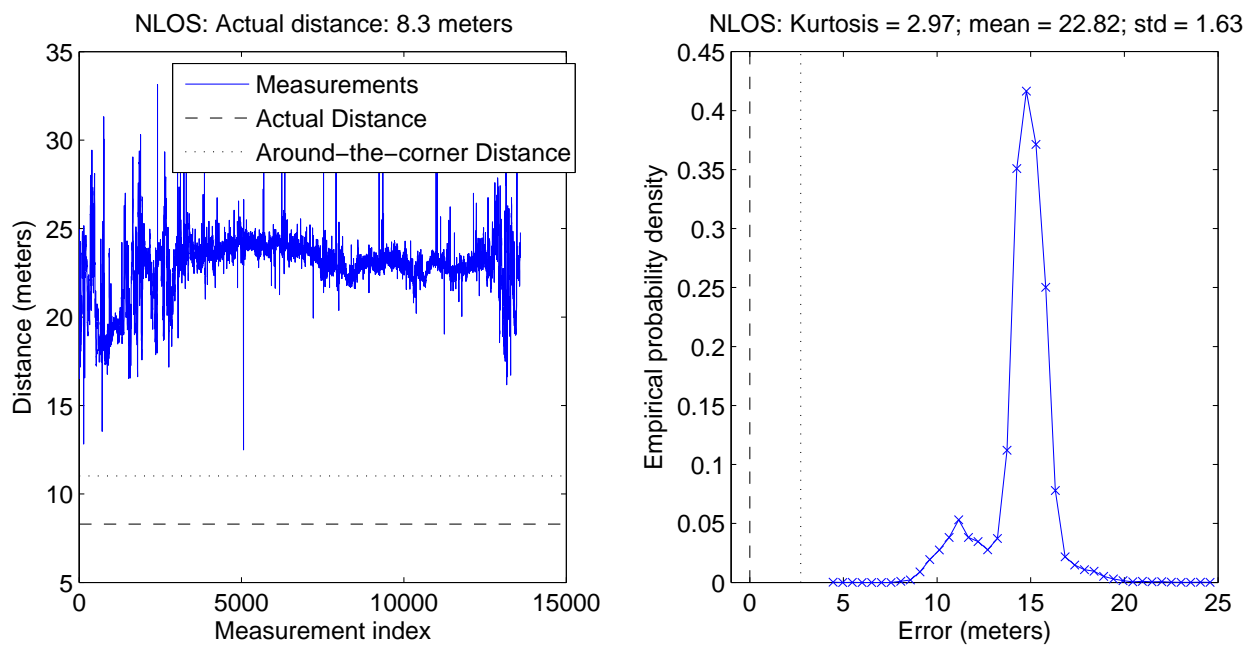


Figure B.94: MPRG lab, location pair T5, group # 2

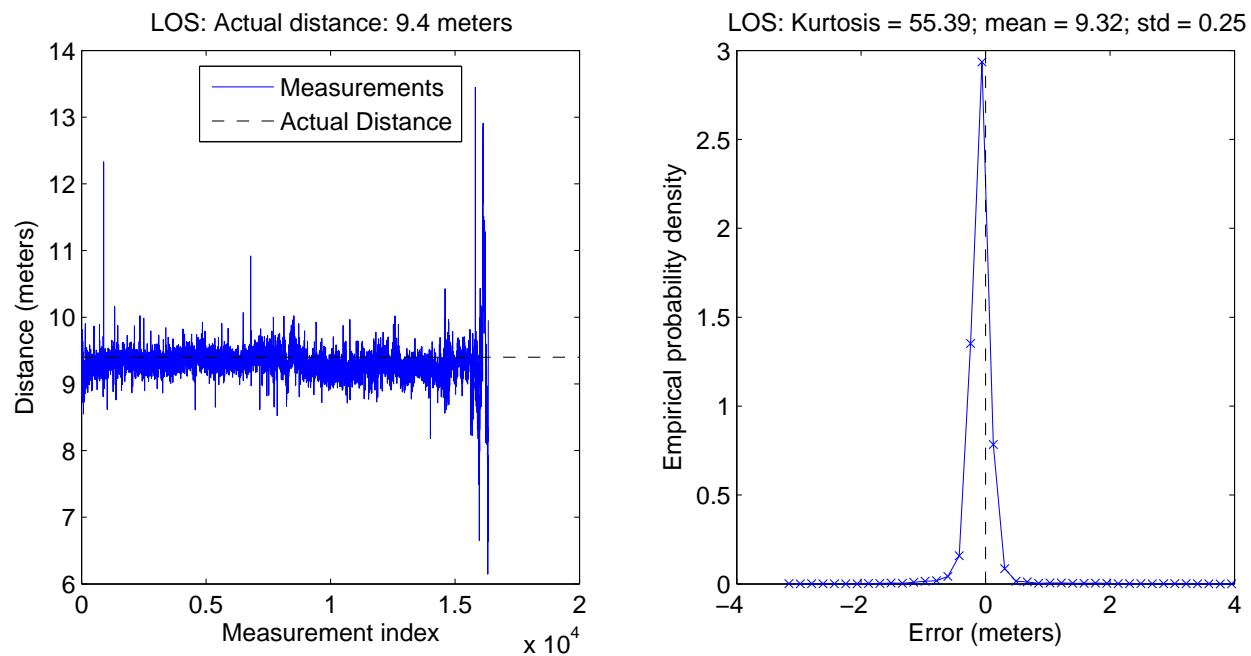


Figure B.95: MPRG lab, location pair T6, group # 1

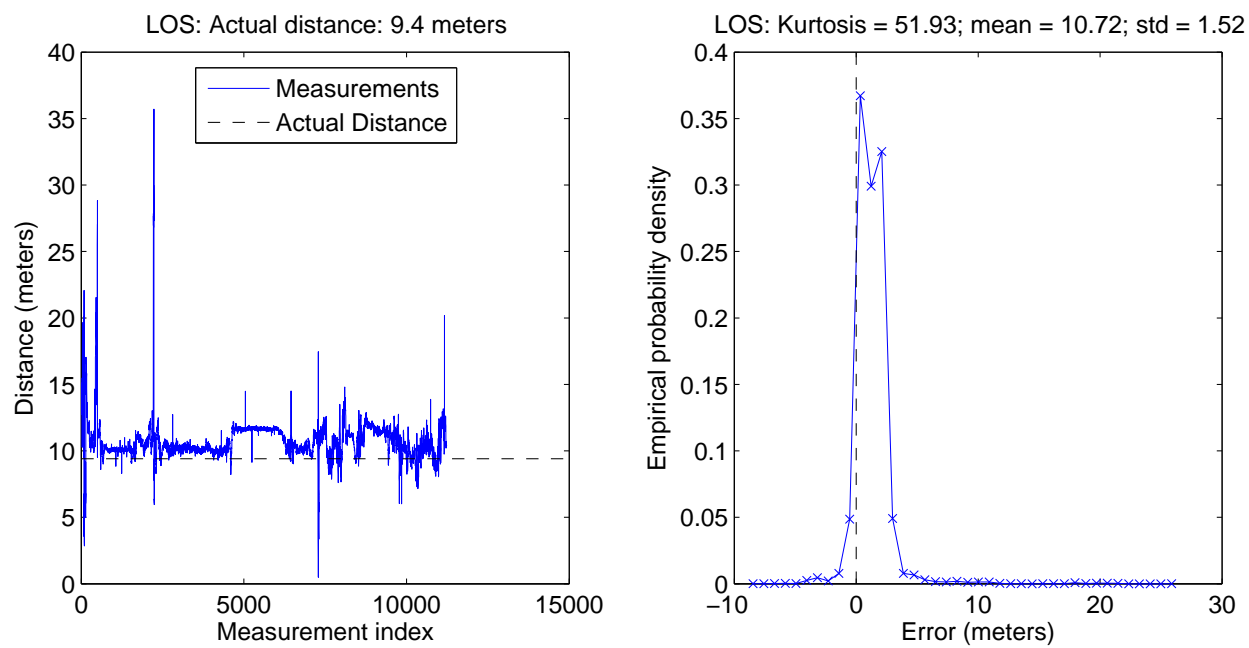


Figure B.96: MPRG lab, location pair T6, group # 2

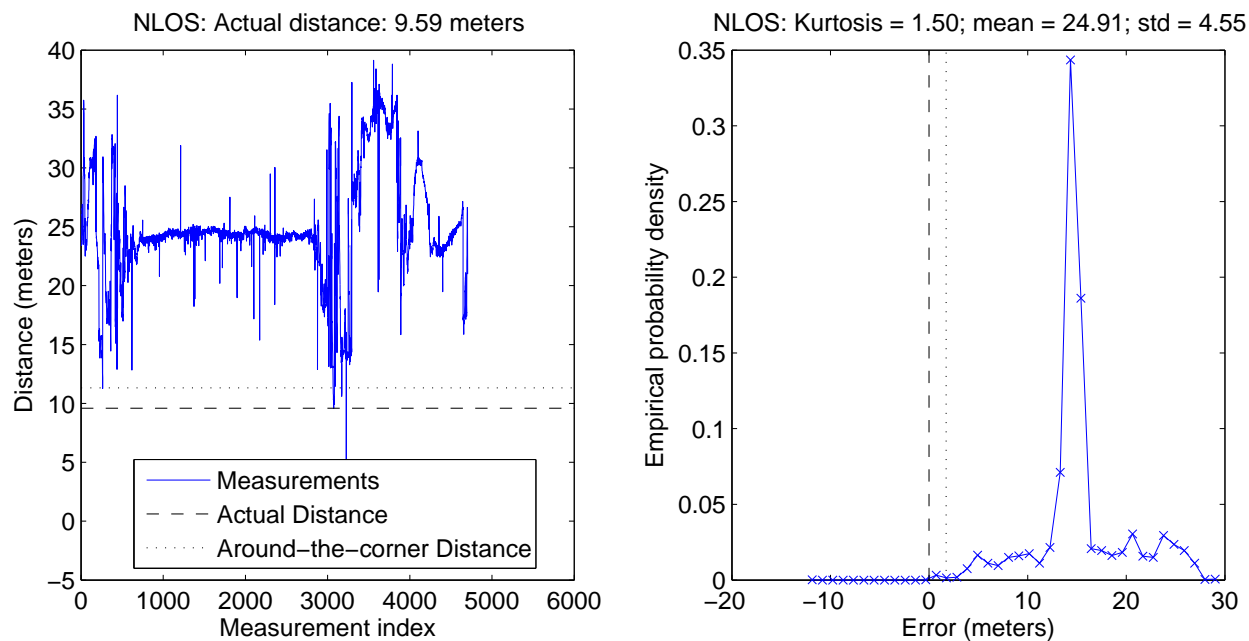


Figure B.97: MPRG lab, location pair T7, group # 1

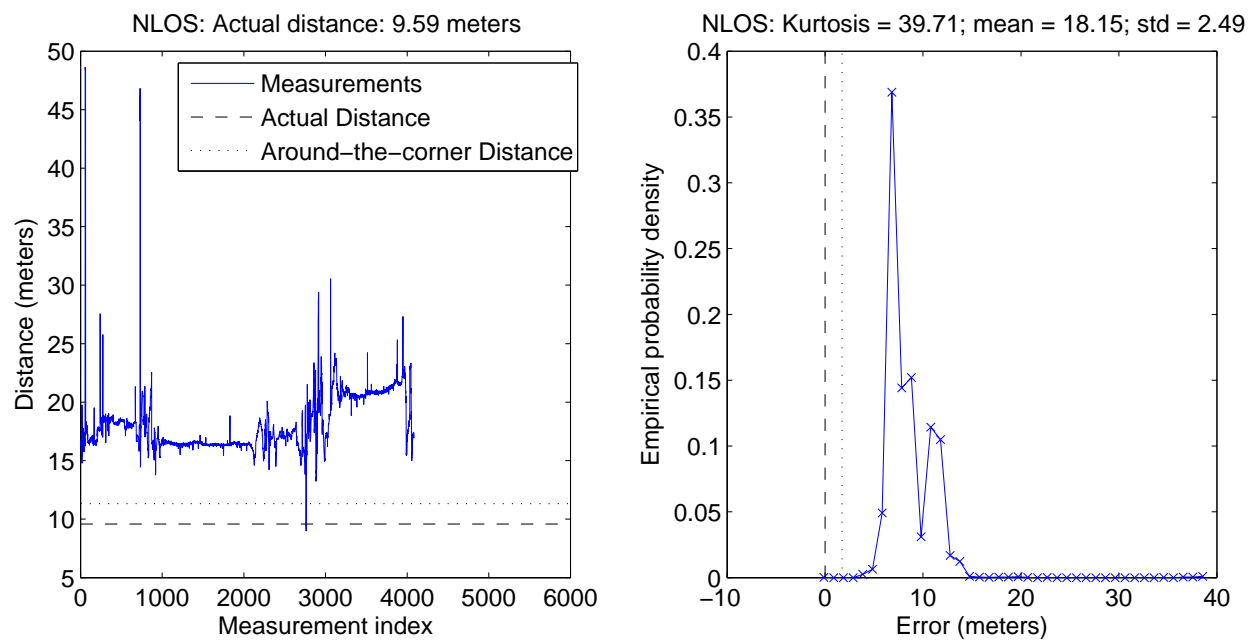


Figure B.98: MPRG lab, location pair T7, group # 2

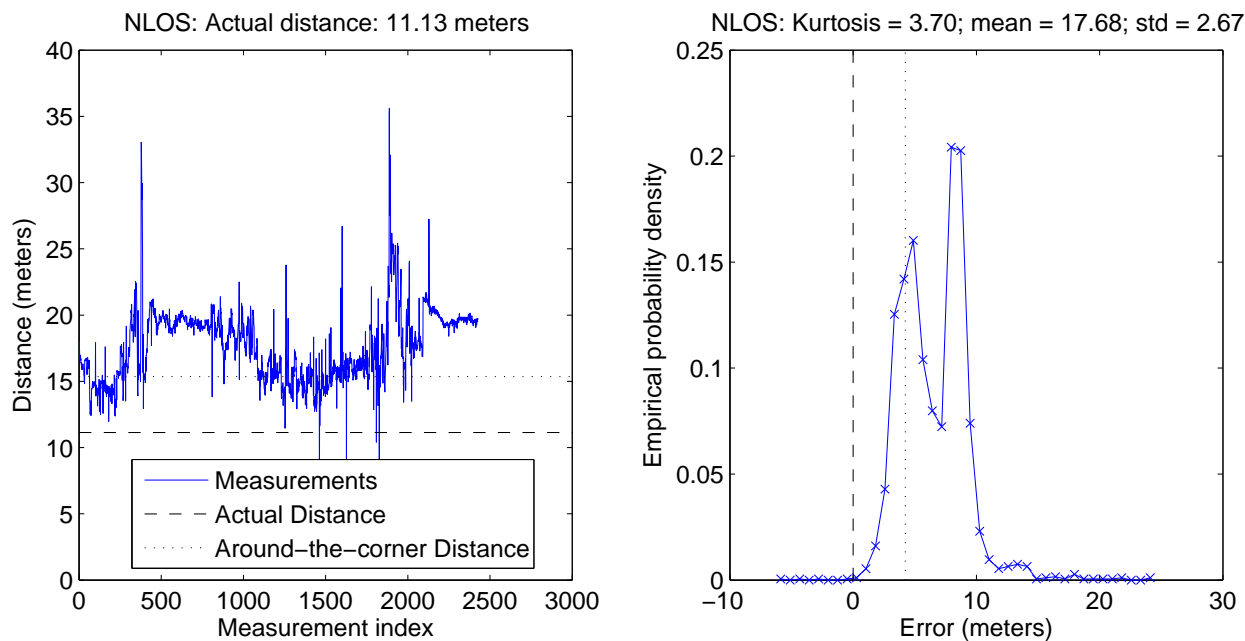


Figure B.99: MPRG lab, location pair T8, group # 1

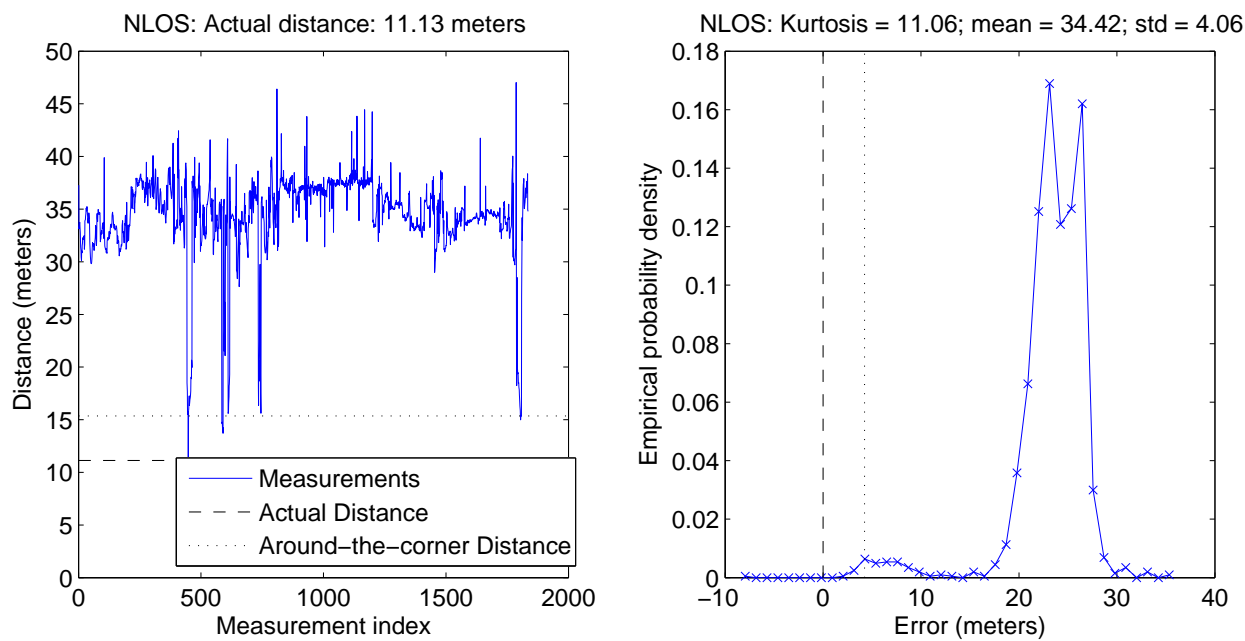


Figure B.100: MPRG lab, location pair T8, group # 2

# Bibliography

- [1] M. Bourimi, G. Mau, S. Steinmann, D. Klein, S. Templin, D. Kesdogan, and H. Schramm-Klein, "A privacy-respecting indoor localization approach for identifying shopper paths by using end-users mobile devices," in *Eighth International Conference on Information Technology: New Generations, (ITNG)*, pp. 139–144, Apr. 2011.
- [2] F. Calabrese, M. Colonna, P. Lovisolo, D. Parata, and C. Ratti, "Real-time urban monitoring using cell phones: A case study in rome," *IEEE Transactions on Intelligent Transportation Systems*, vol. 12, pp. 141–151, Mar. 2011.
- [3] C.-Y. Chong and S. Kumar, "Sensor networks: evolution, opportunities, and challenges," *Proceedings of the IEEE*, vol. 91, pp. 1247–1256, Aug. 2003.
- [4] C. Arthur, "iPhone keeps record of everywhere you go," *The Guardian*, Apr. 2011.
- [5] L. Doherty, K. Pister, and L. El Ghaoui, "Convex position estimation in wireless sensor networks," in *Proceedings of IEEE Conference on Computer Communications (INFOCOM)*, vol. 3, pp. 1655–1663, 2001.
- [6] P. Biswas and Y. Ye, "Semidefinite programming for ad hoc wireless sensor network localization," *International Symposium on Information Processing in Sensor Networks (IPSN)*, pp. 46–54, 2004.
- [7] P. Tseng, "Second-order cone programming relaxation of sensor network localization," *SIAM Journal on Optimization*, vol. 18, no. 1, pp. 156–85, 2008.

- [8] J. Albowicz, A. Chen, and L. Zhang, "Recursive position estimation in sensor networks," in *Ninth International Conference on Network Protocols*, pp. 35–41, Nov. 2001.
- [9] D. Niculescu and B. Nath, "Ad hoc positioning system (APS)," in *IEEE Global Telecommunications Conference (GLOBECOM)*, vol. 5, pp. 2926–2931, 2001.
- [10] A. Savvides, "The bits and flops of the n-hop multilateration primitive for node localization problems," *Proceedings of the ACM International Workshop on Wireless Sensor Networks and Applications*, pp. 112–121, 2002.
- [11] J. Liu, "Robust distributed node localization with error management," in *Proceedings of the Seventh ACM International Symposium on Mobile Ad Hoc Networking and Computing*, (New York, New York, USA), pp. 250–261, 2006.
- [12] S. Srirangarajan, A. Tewfik, and Z.-Q. Luo, "Distributed sensor network localization using SOCP relaxation," *IEEE Transactions on Wireless Communications*, vol. 7, pp. 4886–4895, Dec. 2008.
- [13] T. Jia and R. M. Buehrer, "Collaborative position location," in *Position Location - Theory, Practice and Advances*, ch. 23, Wiley-IEEE Press, Nov. 2011.
- [14] N. Patwari, J. Ash, S. Kyperountas, I. Hero, A.O., R. Moses, and N. Correal, "Locating the nodes: cooperative localization in wireless sensor networks," *Signal Processing Magazine, IEEE*, vol. 22, pp. 54–69, July 2005.
- [15] G. Mao, "Wireless sensor network localization techniques," *Computer networks (Amsterdam, Netherlands : 1999)*, vol. 51, no. 10, 2007.
- [16] T. Jia and R. M. Buehrer, "Collaborative position location for wireless networks using iterative parallel projection method," in *IEEE Global Telecommunications Conference (GLOBECOM)*, pp. 1–6, Dec. 2010.

- [17] T. Jia and R. M. Buehrer, "A set-theoretic approach to collaborative position location for wireless networks," *IEEE Transactions on Mobile Computing*, vol. 10, no. 9, pp. 1264–1275, 2011.
- [18] P. Combettes, "Inconsistent signal feasibility problems: least-squares solutions in a product space," *IEEE Transactions on Signal Processing*, vol. 42, pp. 2955–2966, Nov. 1994.
- [19] N. Patwari, I. Hero, A.O., M. Perkins, N. Correal, and R. O'Dea, "Relative location estimation in wireless sensor networks," *IEEE Transactions on Signal Processing*, vol. 51, pp. 2137–2148, Aug. 2003.
- [20] T. Jia and R. M. Buehrer, "On the optimal performance of collaborative position location," *IEEE Transactions on Wireless Communications*, vol. 9, pp. 374–383, Jan. 2010.
- [21] H. D. Sherali and W. P. Adams, *A Reformulation-Linearization Technique for Solving Discrete and Continuous Nonconvex Problems*. Boston, MA: Kluwer Academic Publishers, 1999.
- [22] S. Rump, "INTLAB - INTerval LABoratory," in *Developments in Reliable Computing* (T. Csendes, ed.), pp. 77–104, Dordrecht: Kluwer Academic Publishers, 1999. <http://www.ti3.tu-harburg.de/rump/>.
- [23] G. I. Hargreaves, "Interval analysis in MATLAB," tech. rep., Department of Mathematics, University of Manchester, Manchester, 2002.
- [24] S. Uwamusi, "Modified-accelerated Krawczyk's algorithm," *International Journal of Physical Sciences*, vol. 4, no. 2, 2009.
- [25] A. Neumaier, *Interval Methods for Systems of Equations*. Cambridge, England: Cambridge University Press, 1990.

- [26] D. Blatt and A. Hero, "Energy-based sensor network source localization via projection onto convex sets," *IEEE Transactions on Signal Processing*, vol. 54, pp. 3614–3619, Sep. 2006.
- [27] S. Zhu and Z. Ding, "Distributed cooperative localization of wireless sensor networks with convex hull constraint," *IEEE Transactions on Wireless Communications*, vol. 10, pp. 2150–2161, July 2011.
- [28] C. Comsa, A. Haimovich, S. Schwartz, Y. Dobyys, and J. Dabin, "Time difference of arrival based source localization within a sparse representation framework," in *5th Annual Conference on Information Sciences and Systems (CISS)*, pp. 1–6, Mar. 2011.
- [29] G. Destino and G. Abreu, "Reformulating the least-square source localization problem with contracted distances," in *Conference Record of the Forty-Third Asilomar Conference on Signals, Systems and Computers*, pp. 307–311, Nov. 2009.
- [30] U. Khan, S. Kar, and J. Moura, "Distributed sensor localization using barycentric coordinates," in *3rd IEEE International Workshop on Computational Advances in Multi-Sensor Adaptive Processing (CAMSAP)*, pp. 65–68, Dec. 2009.
- [31] N. Wang and L. Yang, "A semidefinite programming approach for cooperative localization," in *Conference Record of the Forty Fourth Asilomar Conference on Signals, Systems and Computers (ASILOMAR)*, pp. 487–491, Nov. 2010.
- [32] M. Stojmenovic, A. Nayak, and J. Zunic, "Measuring linearity of planar point sets," *Pattern Recognition*, vol. 41, no. 8, pp. 2503–2511, 2008.
- [33] D. P. Bertsekas, *Nonlinear Programming*. P.O. Box 391, Belmont, MA 02478-9998: Athena Scientific, second ed., 1995.
- [34] B. Farnsworth and D. Taylor, "High Precision Narrow-Band RF Ranging." Presentation at International Technical Meeting of the Institute of Navigation, Jan. 2010.

- [35] B. Farnsworth and D. Taylor, "High Precision Narrow-Band RF Ranging," *Proceedings of the 2010 International Technical Meeting of the Institute of Navigation*, pp. 161–166, Jan. 2010.
- [36] T. S. Rappaport, *Wireless Communications: Principles and Practice*. Upper Saddle River N.J.: Prentice Hall PTR, 2nd ed., 2002.